# University of Southampton

Faculty of Engineering and Physical Sciences

School of Chemistry


# Preparation of Glass Nanopores for the Coulter Counting of Transient Nanobubbles


by

**Steven Linfield**


Thesis for the degree of Doctor of Philosophy

22nd January, 2020

# University of Southampton

## Abstract

Faculty of Engineering and Physical Sciences

School of Chemistry

Doctor of Philosophy

**Preparation of Glass Nanopores for the Coulter Counting of Transient Nanobubbles**

by Steven Linfield

Conventional characterisation techniques have so far provided insufficient explanations for the existence of bulk nanobubbles. This thesis proposes an alternative Coulter counting approach that has not yet been applied to nanobubbles and could help elucidate the reasons for their stability. The work herein details the procedure used to obtain glass nanopores and to apply them to the Coulter counting of ultrasonically generated bulk nanobubbles. Tungsten nanoelectrodes are prepared from the electrochemical etching of microwires and the electrochemistry of tungsten is explored in order to characterise and size these electrodes. Nanoelectrodes prepared in this fashion give reproducible diameters of $\approx$ 100 nm and show electrochemical traits similar to those seen with microelectrodes. Chemical etching of the nanoelectrodes yields glass nanopores that are sized and compared to the nanoelectrodes using voltammetry, simulations, and the Coulter counting of polystyrene nanoparticles. Using a unique differential approach, the sensitivity of the Coulter counting apparatus is shown to increase dramatically. Nanopores are then used to detect and size the transient bulk nanobubbles that are generated during the ultrasonication of potassium chloride solutions with a piston-like emitter. These nanobubbles are distinguished apart from nanoparticles, which are detected in the absence of a local acoustic environment, and microbubbles, which are shown to oscillate in the presence of a local acoustic environment.

# Contents

# List of Tables

# List of Figures

## Research Thesis: Declaration of Authorship

Print Name: STEVEN LINFIELD

Title of Thesis: Preparation of Glass Nanopores for the Coulter Counting of Transient Nanobubbles

I declare that this thesis and the work presented in it are my own and has been generated by me as the result of my own original research. I confirm that:

1. This work was done wholly or mainly while in candidature for a research degree at this University;
2. Where any part of this thesis has previously been submitted for a degree or any other qualification at this University or any other institution, this has been clearly stated;
3. Where I have consulted the published work of others, this is always clearly attributed;
4. Where I have quoted from the work of others, the source is always given. With the exception of such quotations, this thesis is entirely my own work;
5. I have acknowledged all main sources of help;
6. Where the thesis is based on work done by myself jointly with others, I have made clear exactly what was done by others and what I have contributed myself;
7. Parts of this work have been published as:
    - P. R. Birkin, S. Linfield, G. Denuault, R. Jones, J. J. Youngs and E. Wain, *ACS Sensors*, 2019, **4**, 2190-2195
    - P. R. Birkin, S. Linfield and G. Denuault, *Phys. Chem. Chem. Phys.*, 2019, **21**, 24802-24807

Signature:

Date: 22nd January, 2020

# Acknowledgements

I would like to express my gratitude to both Guy and Pete for giving me the opportunity to study for my postgraduate degree under their supervision. Their advice, feedback, and guidance throughout my project has been invaluable and I am proud to have been part of their groups.

For their continuous friendship and useful advice, I'd like to give a huge thanks to Ana, Tammy, and Oliver from the Denuault group. This gratitude also extends to all of the undergraduate project students and visiting students that joined the Denuault group throughout my time here and provided useful discussion and feedback during group presentations.

For their advice and help, I'd like to thank Tom, Hannah and Laura from the Birkin group. I would particularly like to thank Jack for his contribution to nanoelectrode fabrication during his Masters project, throughout which his hard work and his company were much appreciated.

Special thanks must go to David Cook and Alistair Clark for their help in recording electron microscope images during the project. I would also like to acknowledge past colleagues Nawal and Charlie who supervised me during my undergraduate research projects, and convinced me to study for my postgraduate degree.

Last but not least, I would like to thank my parents for all their love and support throughout my undergraduate and postgraduate degrees, without which I would never have got as far as I have.

# List of Symbols

| | |
|---|---|
| $\ddot{R}_s$ | Radial acceleration of the sphere of incompressible liquid around a bubble during expansion/collapse |
| $\ddot{r}$ | Radial acceleration of a bubble interface during expansion/collapse |
| $\Delta A$ | Change in the surface area of a bubble |
| $\Delta E$ | Change in the enthalpy of a bubble caused by a change in the surface area |
| $\Delta P$ | Pressure differential applied across a pore |
| $\Delta R$ | Change in resistance during particle translocation |
| $\dot{R}_s$ | Radial velocity of the sphere of incompressible liquid around a bubble during expansion/collapse |
| $\dot{r}$ | Radial velocity of a bubble interface during expansion/collapse |
| $\eta_g$ | Dynamic viscosity of a gas |
| $\eta_l$ | Dynamic viscosity of a liquid |
| $\gamma$ | Surface tension of a liquid |
| $\kappa$ | Conductivity of an electrolyte solution |
| $\mu$ | Kinematic viscosity of the liquid surrounding a bubble |
| $\omega$ | Angular frequency of an acoustic wave |
| $\omega_r$ | Resonance frequency of a bubble oscillating under a sinusoidal acoustic pressure |
| $\phi$ | Velocity potential of a bubble interface |
| $\rho$ | Resistivity of the solution in a pore |
| $\rho_g$ | Density of a gas |

| | |
|---|---|
| $\rho_l$ | Density of a liquid |
| $\rho_{eff}$ | Effective resistivity of the solution in a pore during particle translocation |
| $\sigma$ | Ratio of specific heats of a gas |
| $\theta$ | Half cone angle of a W nanotip or a glass nanopore |
| $\theta_R$ | Combined resistance of the resistor bridge used in the resistor bridge differential system |
| $\xi$ | Correction factor for loss of instrument sensitivity in the differential systems |
| $A$ | Cross-sectional area of a cylindrical micropore |
| $a$ | Radius of an electrode exhibiting steady state voltammetry |
| $c$ | Concentration of a redox compound |
| $c_g$ | Concentration of a dissolved gas |
| $D$ | Diffusion coefficient of a redox compound |
| $D_g$ | Diffusion coefficient of a gas in a liquid |
| $D_p$ | Diameter of a cylindrical micropore |
| $d_p$ | Diameter of a particle |
| $E_{1/4}, E_{3/4}$ | Electrode potential at current values of 1/4 and 3/4 of the limiting current |
| $F$ | Faraday constant |
| $f$ | Volume fraction of particle in a pore |
| $F_{buoyancy}$ | Buoyancy force acting upon a rising bubble |
| $F_{drag}$ | Frictional force acting against a rising bubble |
| $F_{excess}$ | Force pushing the bubble apart due to excess internal pressure |
| $F_{surface}$ | Force imposed on the bubble by surface tension |
| $g$ | Acceleration due to gravity |
| $H$ | Henry's Law solubility constant |

| | |
|---|---|
| $i_{lim}$ | Limiting current of a steady state voltammogram |
| $K$ | Henry's Law volatility constant |
| $k_m$ | Rate of mass transport |
| $k_s$ | Rate of electron transfer |
| $L$ | Length of a cylindrical micropore |
| $n$ | Number of electrons transferred in a redox reaction |
| $n_{(t)}$ | Number of moles of gas in a bubble at time $t$ |
| $P_0$ | Hydrostatic pressure in a liquid |
| $P_A$ | Additional external pressure |
| $P_B$ | Blake threshold pressure required for explosive growth of a bubble |
| $p_g$ | Partial pressure of the gas in a bubble |
| $P_H$ | Pressure recorded at a hydrophone |
| $P_i$ | Total internal pressure of a bubble |
| $P_L$ | Pressure of the liquid at the interface of the bubble |
| $p_v$ | Partial pressure of the vapour in a bubble |
| $P_\gamma$ | External pressure acting on a bubble as a result of surface tension |
| $P_\infty$ | Pressure of the liquid at infinite distance from the bubble |
| $p_{g*}$ | Partial pressure of the gas in a bubble under the additional external pressure, $P_A$ |
| $Q$ | Flow rate of liquid through a pore |
| $R$ | Ideal gas constant |
| $r$ | Radius of a bubble |
| $r^*$ | Blake threshold radius for a bubble to experience explosive growth |
| $r_0$ | Equilibrium radius of a bubble |
| $r_A$ | Radius of a bubble under the additional external pressure, $P_A$ |

| | |
|---|---|
| $R_d$ | Value of the dummy resistor in the resistor bridge differential system |
| $R_p$ | Background resistance of a pore |
| $r_p$ | Radius of a pore |
| $r_r$ | Resonance radius of a bubble oscillating under a sinusoidal acoustic pressure |
| $R_s$ | Radius of the sphere of incompressible liquid around a bubble |
| $R_t$ | Resistance of a pore during particle translocation |
| $r_{(t)}$ | Radius of bubble at time $t$ |
| $R_{CF}$ | Value of the resistor in the feedback loop of a current follower |
| $T$ | Temperature |
| $t_d$ | Time required for complete dissolution of a bubble |
| $v$ | Rise velocity of a bubble |
| $v_T$ | Terminal rise velocity of a bubble |
| $V_{app}$ | Voltage applied to the Coulter counting apparatus |
| $V_{DiS}$ | Output voltage of the current differential system |
| $V_{out}$ | Output voltage of the resistor bridge differential system |
| $V_{sen}$ | Sensing voltage at the point in between the pore and dummy resistor of the resistor bridge differential system |
| $X_{DiS}$ | Gain of the differential amplifier in both the resistor bridge and current differential systems |
| Ø | General symbol for the diameter of an object |

# 1 Introduction

## 1.1 Motivations behind nanobubble research

The unique properties of bubbles are exploited for numerous industrial processes. For example, the size distribution of bubbles has been shown to affect the texture of foods and beverages[1], whilst the nucleation of bubbles in polymers is relevant to the formation of lightweight plastic foams[2]. Removal of wastewater contaminants by froth flotation is also reliant on the buoyancy of bubbles[3].

Other processes can be disrupted by the presence of bubbles, creating the need to avoid their formation. The material integrity of setting glasses/metals can be compromised by bubble formation[4] and damage to ship propellers can be caused by bubble cavitation[5]. Bubbles have even been reported to pose health risks when formed in certain parts of the body[6]. Due to the wide range of areas that are affected by bubbles and their properties, it is essential to conduct research that can shed light on how bubbles are formed and how they behave.

The properties and uses of macrobubbles ($\geq$ 1 mm Ø) have been extensively studied, but the focus of bubble research has more recently shifted to microbubbles (1–1000 $\mu$m Ø). The reduced size of microbubbles has allowed for improvements to existing processes and even the proposal of new applications. For example, their small dimensions enable microbubbles to be safely inserted into the body, where they can be used to deliver drugs or act as ultrasound contrast agents[7]. Microbubbles have also had success in cleaning proteins from fouled membranes[8]. The attractive qualities of microbubbles have led to recent discussions on the possibility of using nanobubbles ($\leq$ 1 $\mu$m Ø), which could offer even more improvements and could open up the pathway to even more discoveries. However, the apparent stability of nanobubbles contradicts bubble dynamics and needs to be investigated in more detail.

## 1.2 Bubble dynamics

Bubbles are thermodynamically unstable and therefore can never be in equilibrium with their surroundings[9]. For example, enthalpy is needed for the establishment of the liquid-gas interface of a bubble and the maintenance of this interface against the surface tension of the liquid. The change in enthalpy required for bubble growth can therefore be calculated by multiplying the surface tension of the liquid with the change in the surface area of the bubble, as shown in Equation 1.1[9].

$$\Delta E = \gamma \times \Delta A \tag{1.1}$$

where $\Delta E$ is the change in enthalpy; $\gamma$ is the surface tension of the liquid; and $\Delta A$ is the change in the surface area of the bubble. The enthalpy cost incurred by bubble formation is unfavourable and the system will always act to reduce the surface area of the bubble, either through dissolution of the gas into the surrounding liquid, or through the bubble rising out of the liquid under buoyancy. Bubbles are also entropically unfavourable, as their formation represents a more ordered system compared to the gas being equally dissolved across a liquid. The high partial pressure of the gas in a bubble results in the establishment of a concentration gradient across the bubble interface, which causes the gas to diffuse from the bubble into the liquid. Henry's Law, which is shown by Equation 1.2, describes the relationship between the partial pressure of gas in a bubble and the concentration of the gas in the liquid[10].

$$c_g = H \times p_g \tag{1.2}$$

where $c_g$ is the concentration of dissolved gas; $H$ is the Henry's Law solubility constant; and $p_g$ is the partial pressure of gas in a bubble. The only way to prevent gas diffusion from the bubble would be to saturate the liquid with gas, so that the concentration of gas in the liquid countered the partial pressure of the gas. However, this would then cause the liquid to be out of equilibrium with the atmosphere, which is also entropically unfavourable[9]. Whilst these relationships explain why bubbles are thermodynamically unstable, they do

not describe how the size of a bubble affects its stability. In order to understand why the stability and lifetime of smaller bubbles differs to that of larger bubbles, the pressures and forces acting upon the bubble need to be considered.

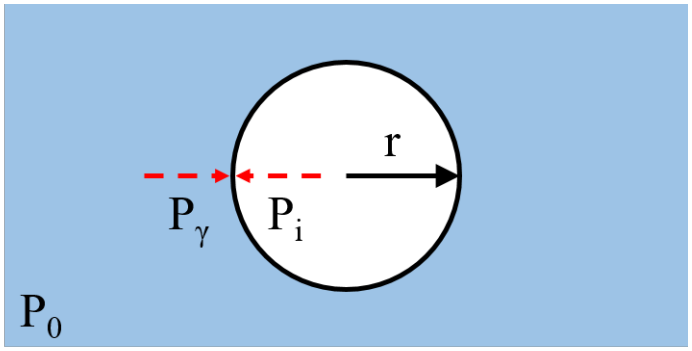


**Figure 1.1:** Various internal and external pressures that are constantly acting upon a bubble of radius $r$. The internal pressure of the bubble, $P_i$, is determined by the partial pressures exerted by the gaseous/vapourous contents of the bubble on its interface. This is countered externally by the hydrostatic pressure of the liquid, $P_0$, and the pressure exerted by the surface tension of the liquid, $P_\gamma$. Note that in this use, the atmospheric pressure is included in hydrostatic pressure.

Figure 1.1 illustrates the pressures that constantly act on a bubble and would have to be balanced in order for the bubble to be in equilibrium, ignoring the enthalpy and entropy costs required for this to occur[11,12]. The bubble contains an unknown ratio of gas and vapour, both of which exert a partial pressure from the inside of the bubble. These partial pressures are combined to give the total internal pressure, $P_i$ . The liquid surrounding the bubble has an external hydrostatic pressure that opposes the total internal pressure. However, the internal pressure is constantly increasing due to the squeezing of the bubble by the surface tension of the liquid. In order for the internal and external pressures to balance out, the surface tension must also impose its own external pressure on the bubble. Equation 1.3 summarises the pressures acting on a bubble in equilibrium[11,12].

$$p_v + p_g = P_0 + P_\gamma \tag{1.3}$$

where $p_v$ is the partial pressure of vapour in the bubble; $p_g$ is the partial pressure of gas in the bubble; $P_0$ is the hydrostatic pressure of the liquid; and $P_\gamma$ pressure acting on the bubble due to surface tension.

If the excess internal pressure and the pressure induced by surface tension are required to balance out in order to keep the bubble in equilibrium (*i.e.* $P_\gamma = P_i - P_0$), then the forces imposed by these two pressures must also balance each other out. The force imposed by the excess internal pressure acts to expand the bubble and, if the bubble was cut in half, would push the two halves of the bubble apart. Therefore, this force can be calculated by multiplying the pressure exerted by surface tension, which is equal to the excess internal pressure, by the cross-sectional area of half of the bubble, as described in Equation 1.4[11].

$$F_{excess} = \pi r^2 P_\gamma \tag{1.4}$$

where $F_{excess}$ is the force pushing the bubble apart and $r$ is the radius of the bubble. The force imposed by the surface tension opposes this expansion and can be calculated by multiplying the surface tension with the circumference of bubble, as shown in Equation 1.5[11].

$$F_{surface} = 2\pi r\gamma \tag{1.5}$$

where $F_{surface}$ is the force imposed by surface tension. Since the bubble is in equilibrium, these two forces balance out to give Equation 1.6, which is known as the Young-Laplace equation[9,11]. In this context, $P_\gamma$ is sometimes referred to as the Laplace pressure.

$$P_\gamma = \frac{2\gamma}{r} \tag{1.6}$$

The Young-Laplace equation relates the pressure induced by surface tension to the radius of the bubble. By substituting the Laplace pressure into Equation 1.3, a relationship can be established between the internal pressure of a bubble in equilibrium and the equilibrium radius of the bubble[11,12]. In order to simplify the relationship, the partial

pressure of vapour in the bubble is assumed to be negligible, as shown in Equation 1.7.

$$p_g = P_0 + \frac{2\gamma}{r_0} \tag{1.7}$$

where $r_0$ is the equilibrium radius of the bubble. However, the thermodynamic instability of the bubble means that it cannot remain in equilibrium, and the radius of the bubble will have to change from its equilibrium value. If the radius decreases ($r < r_0$), then the Laplace pressure term becomes larger than the excess internal pressure, causing the bubble to collapse. Conversely, if the bubble radius increases ($r > r_0$), then the Laplace pressure term becomes smaller than the excess internal pressure, causing the bubble to expand. Therefore, there are four ways in which the stability of a bubble can be compromised[12].

1. It can rise out of the liquid due to buoyancy.
2. It can dissolve due to diffusion of gas across the bubble interface.
3. It can collapse due to surface tension.
4. It can expand due to the internal partial pressure of the gas.

In the following sections, the dynamics behind each of these scenarios will be discussed, with particular focus on how nanobubbles and their lifetimes are affected.

### 1.2.1 Buoyancy

When the gas inside a bubble is less dense than the liquid surrounding it, the bubble will tend to rise out of solution. The rate of this process is controlled by the terminal rise velocity of the bubble, where any motional forces are equal to the opposing frictional forces (*i.e.* acceleration = 0). The motional force of a bubble is determined by the effect of gravity on the liquid column above it and is referred to as the buoyancy force, calculated

using Equation 1.8.

$$F_{buoyancy} = \frac{4}{3}\pi r^3(\rho_l - \rho_g)g \tag{1.8}$$

where $F_{buoyancy}$ is the buoyancy force of the bubble; $r$ is the bubble radius; $\rho_l$ is the density of the liquid; $\rho_g$ is the density of the gas; and $g$ is the gravity that accelerates the bubble. Any buoyant motion of the bubble is opposed by a frictional force from the laminar flow of liquid. This frictional (drag) force can be calculated using the Rybczynski formula, shown in Equation 1.9, which is a variant of Stoke's Law that accounts for the viscosity of the gas.

$$F_{drag} = 6\pi\eta_l r v \frac{2\eta_l + 3\eta_g}{3\eta_l + 3\eta_g} \tag{1.9}$$

where $\eta_l$ is the dynamic viscosity of the liquid; $\eta_g$ is the dynamic viscosity of the gas; and $v$ is the rise velocity of the bubble. The dynamic viscosity of the liquid is often greater than that of the gas (*i.e.* $\eta_l \gg \eta_g$), simplifying the Rybczynski formula. The terminal rise velocity of the bubble is achieved when the two forces are balanced ($F_{buoyancy} = F_{drag}$), which gives the formula shown in Equation 1.10.

$$v_T = \frac{r^2\rho_l g}{3\eta_l} \tag{1.10}$$

where $v_T$ is the terminal rise velocity of the bubble. This formula is known as the Hadamard-Rybczynski equation and links the radius of a bubble to its terminal rise velocity[9,13]. As shown in Figure 1.2, the terminal rise velocity decreases as the radius of the bubble is reduced, meaning nanobubbles are less likely to escape the solution than microbubbles and macrobubbles.

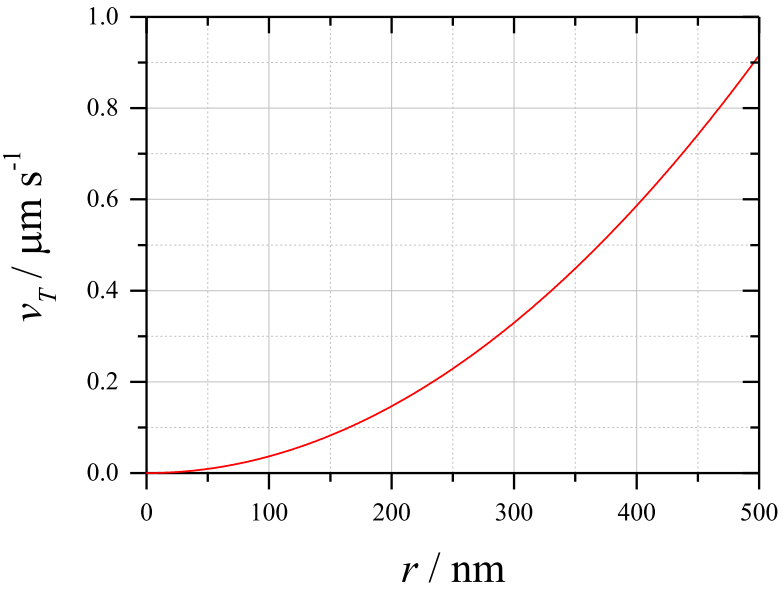


**Figure 1.2:** Terminal rise velocity of an air nanobubble in water, plotted as a function of the bubble radius using the Hadamard-Rybczynski equation (Equation 1.10). The density of water was taken as 997 kg m$^{-3}$ and the dynamic viscosity of water was taken as $8.9 \times 10^{-4}$ Pa s.

### 1.2.2 Mass diffusion

In order to determine the rate at which the gas in a bubble fully dissolves into the surrounding liquid, it is first essential to determine the number of moles of the gas from the bubble radius. This can be done by combining Equation 1.7 with the ideal gas equation ($pV = nRT$), which gives Equation 1.11[14] .

$$\frac{3n_{(t)}RT}{4\pi {r_{(t)}}^3} = P_0 + \frac{2\gamma}{r_{(t)}} \tag{1.11}$$

where $n_{(t)}$ is the number of moles of gas in the bubble at time $t$; $R$ is the ideal gas constant; $T$ is the temperature; $r_{(t)}$ is the radius of the bubble at time $t$; $P_0$ is the hydrostatic pressure of the liquid; and $\gamma$ is the surface tension of the liquid. By assuming that $2\gamma/r_{(t)} \gg P_0$ and then rearranging the remainder of Equation 1.11, the number of moles of gas at a

given time is found by Equation 1.12.

$$n_{(t)} = \frac{8\pi\gamma r_{(t)}^2}{3RT} \tag{1.12}$$

The rate of change in the number of moles over time must then be considered. Since $\frac{dn_{(t)}}{dr_{(t)}} = \frac{dn_{(t)}}{dt} \times \frac{dt}{dr_{(t)}}$, Equation 1.12 can be differentiated with respect to $r_{(t)}$ in order to obtain Equation 1.13.

$$\frac{dn_{(t)}}{dt} = \frac{16\pi\gamma r_{(t)}}{3RT} \times \frac{dr_{(t)}}{dt} \tag{1.13}$$

Ficks first (Equation 1.14) and second (Equation 1.15) laws of diffusion are then applied to the diffusion of gas from a bubble into the surrounding liquid, allowing the change in concentration at a distance from the bubble interface to be determined. Incorporating these laws into Equation 1.13 gives a formula that describes the rate of change in the radius of a bubble that is dissolving over time, as shown in Equation 1.16.

$$\frac{dn_{(t)}}{dt} = 4\pi {r_{(t)}}^2 D_g \frac{\partial c_g}{\partial x} \tag{1.14}$$

$$\frac{\partial c_g}{\partial x} = \frac{-2\gamma}{K \times r_{(t)}} \times \left(\frac{1}{r_{(t)}} + \frac{1}{(\pi D_g t)^{\frac{1}{2}}}\right) \tag{1.15}$$

$$\frac{dr_{(t)}}{dt} \times r_{(t)} = \frac{-3RTD_g}{2K} \times \left(1 + \frac{r_{(t)}}{(\pi D_g t)^{\frac{1}{2}}}\right) \tag{1.16}$$

where $D_g$ is the diffusion coefficient for a gas in a liquid; $c_g$ is the concentration of gas in a liquid; and $K$ is the Henry's Law volatility constant. As time progresses, $r_{(t)} \ll (\pi D_g t)^{1/2}$ and Equation 1.16 is simplified to Equation 1.17[14].

$$\frac{{r_{(t)}}^2}{2} - \frac{r^2}{2} = \frac{-3RTD_g t}{2K} \tag{1.17}$$

where $r$ is the initial radius of the bubble. When the bubble is fully dissolved, $r_{(t)} = 0$. Subsequent rearrangement of Equation 1.17 yields Equation 1.18.

$$t_d = \frac{r^2 K}{3RTD_g} \tag{1.18}$$

where $t_d$ is the time required for complete dissolution of the bubble. This is known as the Epstein-Plesset equation and describes the relationship between the radius of a bubble and the complete diffusion of gas from the bubble. As shown in Figure 1.3 the time required for complete dissolution decreases as the radius of the bubble decreases, making nanobubbles particularly susceptible to the loss of their gaseous contents. Whilst this theory was first published by Epstein and Plesset[15], it has been used extensively in recent years to express doubt in the reported stability of nanobubbles, most notably by Ljunggren *et al.*[14].

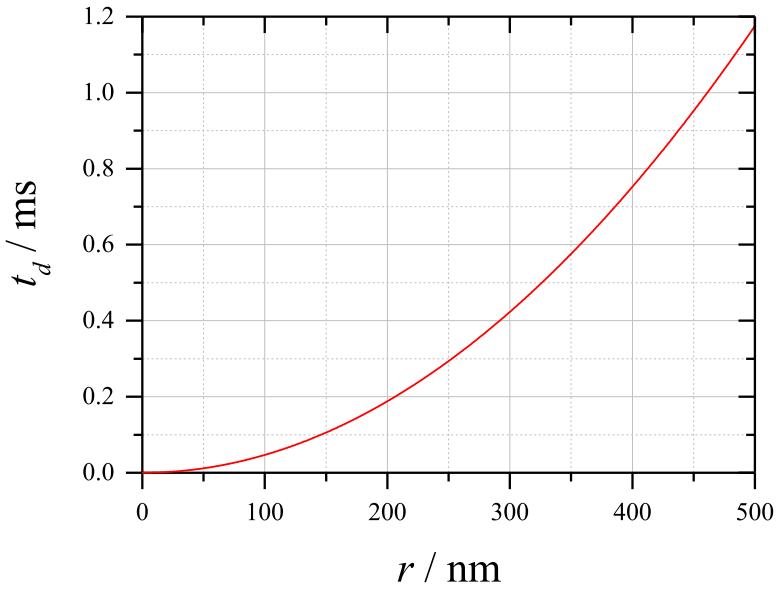


**Figure 1.3:** Time required for the complete dissolution of an $O_2$ bubble, plotted as a function of the bubble radius using the Epstein-Plesset equation (Equation 1.18). The Henry's constant of $O_2$ in water was taken from reference 10 as $1.3 \times 10^{-5}$ mol m$^{-3}$ Pa$^{-1}$ and the diffusion coefficient of $O_2$ in water was taken from reference 16 as $2.2 \times 10^{-9}$ m$^2$ s$^{-1}$.

### 1.2.3 Bubble growth and collapse

The growth or collapse of a bubble can be induced by the application of a suitable external pressure, which causes the radius of the bubble to deviate from its equilibrium

value[12]. This external pressure can be added to Equation 1.7 so that it produces a formula that describes the new stability conditions of the bubble. This is shown in Equation 1.19 for an additional negative pressure, which causes the growth of a bubble from its equilibrium radius. However, the collapse of bubbles can also be studied by application of a positive external pressure instead.

$$p_{g*} = P_0 - P_A + \frac{2\gamma}{r_A} \tag{1.19}$$

where $P_A$ is the additional external pressure; $p_{g*}$ is the partial pressure of gas in the bubble under the additional external pressure; $P_0$ is the hydrostatic pressure of the liquid; $\gamma$ is the surface tension of the liquid; and $r_A$ is the radius of the bubble under the additional external pressure. If this growth process is assumed to be isothermal (*i.e.* $P_1V_1 = P_2V_2$), then Equations 1.7 and 1.19 can be used to create Equation 1.20.

$$\left(P_0 + \frac{2\gamma}{r_0}\right)\left(\frac{4\pi {r_0}^3}{3}\right) = \left(P_0 - P_A + \frac{2\gamma}{r_A}\right)\left(\frac{4\pi {r_A}^3}{3}\right) \tag{1.20}$$

where $r_0$ is the equilibrium radius of the bubble. This formula is used to determine the minimum static external pressure value needed to expand a bubble from its equilibrium radius to $r_A$ (*i.e.* $\frac{\partial(P_A - P_0)}{\partial r_A} = 0$). Any static pressure significant enough to expand the bubble to a radius of $r_A$ will also be sufficient to expand the bubble beyond this radius, causing the indefinite, explosive growth of the bubble. Therefore, the value of $r_A$ at this minimum static pressure can be thought of as the threshold radius required for the indefinite, explosive growth of the bubble, as shown in Equation 1.21.

$$r^* = \left(\frac{3{r_0}^3\left(P_0 + \frac{2\gamma}{r_0}\right)}{2\gamma}\right)^{\frac{1}{2}} \tag{1.21}$$

where $r^*$ is the threshold radius for explosive growth of the bubble. Substituting the threshold radius into Equation 1.20 gives the minimum static pressure required to cause the explosive growth of the bubble[11,12]. This minimum pressure value is known as the

Blake threshold pressure, which can be calculated using Equation 1.22.

$$P_B = P_0 + \frac{4\gamma}{3}\Big(\frac{2\gamma}{3r_0^3(P_0 + \frac{2\gamma}{r_0})}\Big)^{\frac{1}{2}} \tag{1.22}$$

where $P_B$ is the Blake threshold pressure. In this relationship the applied pressure needed to overcome the Blake threshold becomes higher as the bubble radius decreases. This implies that nanobubbles would be harder to influence with external pressures, which might contribute to their supposed stability.

Equation 1.22 can be used to determine whether a bubble will experience explosive growth/collapse based on the value of the additional external pressure, but it does not describe the dynamics of any growth/collapse process. This is instead provided by the Rayleigh-Plesset equation, which contains terms for any parameters that might affect bubble motion. The inertial terms are derived from the continuity of flow rate in an incompressible liquid (*i.e.* $\rho_1 A_1 \dot{r}_1 = \rho_2 A_2 \dot{r}_2$). If the interface of a bubble moves, then its radial velocity can be related to the radial velocity of a larger sphere of incompressible liquid surrounding the bubble, using Equation 1.23[17].

$$\dot{r} = \frac{R_s^2 \dot{R}_s}{r^2} \tag{1.23}$$

where $r$ is the radius of the bubble; $\dot{r}$ is the radial velocity of the bubble interface; $R_s$ is the radius of a sphere of incompressible liquid around the bubble; and $\dot{R}_s$ is the radial velocity of this sphere of liquid. Integrating the radial velocity of the bubble with respect to its radius determines the velocity potential as shown by Equation 1.24.

$$\phi = -\int_r^\infty \dot{r} dr = -\frac{R_s^2 \dot{R}_s}{r} \tag{1.24}$$

where $\phi$ is the velocity potential of the bubble interface. Equations 1.23 and 1.24 can then be used in the Bernoulli equation to connect the inertial terms to the effect of a pressure difference between the liquid at the bubble wall and the liquid at an infinite distance from

the bubble, as shown in Equation 1.25.

$$\frac{P_L - P_\infty}{\rho_l} = -\frac{\partial \phi}{\partial t} - \frac{\dot{r}^2}{2} = \frac{2R_s\dot{R_s}^2 + R_s^2\ddot{R}_s}{r} - \frac{R_s^4\dot{R_s}^2}{2r^4} \tag{1.25}$$

where $P_L$ is the pressure of the liquid at the bubble interface; $P_\infty$ is the pressure of the liquid at infinite distance from the bubble $\rho_l$ is the density of the liquid; and $\ddot{R}_s$ is the radial acceleration of the sphere of liquid around a bubble. By replacing $R_s$ with the radius of the bubble, Equation 1.25 can be used to characterise the motion of the bubble interface[5,12,18]. Furthermore, the pressure of the liquid at the bubble interface can be substituted with the hydrostatic pressure from Equation 1.7 to include the effects of surface tension. After introducing a term for the effect of liquid viscosity, the Rayleigh-Plesset equation for a bubble in an incompressible liquid is obtained, as shown in Equation 1.26.

$$\underbrace{r\ddot{r} + \frac{3\dot{r}}{2}}_{Inertial\ Terms} + \underbrace{\frac{4\mu\dot{r}}{\rho_l r}}_{Viscosity} + \underbrace{\frac{2\gamma}{\rho_l r}}_{Surface\ Tension} + \underbrace{\frac{P_\infty - p_g}{\rho_l}}_{Pressure} = 0 \tag{1.26}$$

where $\ddot{r}$ is the radial acceleration of the bubble interface and $\mu$ is the kinematic viscosity of the liquid surrounding a bubble. The small radius of nanobubbles would cause the surface tension and viscosity terms to dominate. Note that the Rayleigh-Plesset equation reverts back to the Young-Laplace equation when the bubble interface is stationary (*i.e.* $\dot{r} = 0$).

### 1.2.4 Assumptions

Several assumptions have been made throughout the derivation of the bubble dynamics described above. Most of the derivations assume that the bubble is always spherical, that its contents are uniform, and that the liquid surrounding the bubble is incompressible and denser than the gas. These assumptions are reasonable for explaining the effect of bubble radius for each dynamic. However, each of the dynamics have been derived independently of each other, whereas they would be occurring simultaneously in a real system. For example, the dissolution of a bubble will affect its terminal rise velocity and the Blake

threshold required for explosive growth. Likewise the concentration gradient around the bubble will be disturbed by the buoyant motion of the bubble. These interactions may therefore cause some deviation from the described dynamics.

In all the derivations, it was assumed that the bubble was solitary, which might not allow for the dynamics to be applied to clusters of bubbles. For example, the dissolution of a bubble will increase the local concentration of dissolved gas, which may affect the dissolution process of nearby bubbles. Other interactions between bubbles have not been considered, such as coalescence, where two or more bubbles combine to make a larger bubble. The influence of multiple bubbles is far more complicated to define, and the dynamics described here may not be sufficient for explaining such scenarios.

## 1.3 Summary of nanobubble literature

In theory, the rapid diffusion of gas from a nanobubble should give it a lifetime that is far too short to allow for experimental observation. However, mounting evidence for the existence of stable nanobubbles has been published in recent years, seemingly contradicting their theoretical lifetime. In these publications, two types of nanobubble are reported to have been observed[19]. These are bulk and surface nanobubbles, as illustrated in Fig. 1.4.

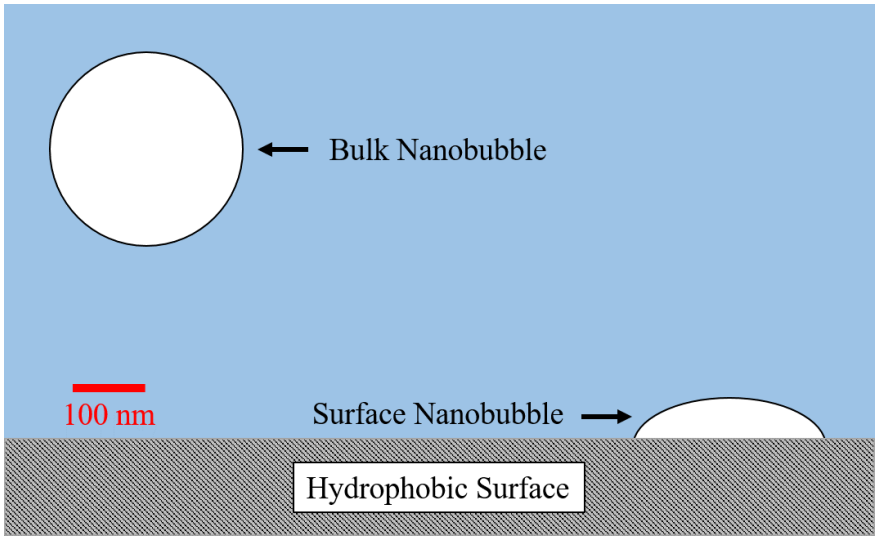


**Figure 1.4:** Illustration showing the two main types of nanobubble that have been reported in the literature. Bulk nanobubbles have a spherical shape and can move freely around the bulk of a solution. Conversely, surface nanobubbles are spherical caps that are often found pinned in place onto hydrophobic surfaces.

Bulk nanobubbles are suspended in the body of a solution and can move about freely like nanoparticles. Their internal gas pressure causes them to adopt a perfectly spherical shape. Surface nanobubbles are confined to an immersed surface, often reported to be hydrophobic. The interaction between the gas and the surface causes them to be immobile, with a spherical cap shape. Much is still unknown about these nanobubble types, especially how they can be so stable against diffusion, and whether there is a mechanism by which bulk nanobubbles become surface nanobubbles and *vice versa*. However, reports of their existence have led to several proposals of new applications, generation methods and characterisation techniques. In this section, the literature concerning each nanobubble type is discussed and compared.

### 1.3.1 Bulk nanobubbles

The existence of bulk nanobubbles was first proposed in 1962, when Sette and Wanderlingh found that the energy threshold for acoustic cavitation was lower in aqueous solutions that had been exposed to cosmic radiation[20]. They believed the radiation was generating localised H and OH radicals, which then reacted to form $O_2$ and $H_2$ nanobubbles that acted as precursors to cavitation. Lead shielding of the solution resulted in a slow increase in the threshold, as the remaining nanobubbles gradually dissolved. Gas oversaturation also increased the threshold, due to the increased solution pressure acting to hasten the nanobubble dissolution. Later work by Bunkin *et al.* found that the threshold also increased after application of an electric field to the solution[21]. They claimed this was caused by a negative charge on the nanobubbles, given by adsorbed hydroxide ions in a similar effect to that seen with microbubbles. Higher salt concentrations decreased the threshold, which they attributed to the stabilisation of negatively charged nanobubble clusters.

Bulk nanobubbles were later identified as key components in the evolution of algae in Lake Kivu, Kenya[22]. Sediment from the lake was examined using electron microscopy, revealing the presence of hollow spheres of ZnS. These spheres, shown in Figure 1.5, were 800–1000 nm Ø, and identified as catalysts for algae evolution in the area. The spheres were said to have originated from volcanic activity, where methane nanobubbles in the lake attracted volcanic sediment, which then coated the bubbles and allowed them to settle on the lake bed.

In 1981, Cooke *et al.* offered the first piece of direct evidence, with microscope images of microbubbles in seawater[23]. The microbubbles quickly dissolved, with the rate of dissolution increasing as the bubble radius decreased. Particles under 1 $\mu$m Ø were then seen in place of the bubble after dissolution, but application of a pressure to the solution seemed to make these particles change in size. These were thought to be nanobubbles originating from the microbubbles, but stabilised against complete dissolution.

Research into bulk nanobubbles has increased dramatically since their discovery, and nanobubble technology has started being implemented into many unique and exciting applications. For example, Ebina *et al.* showed how the generation of $O_2$ nanobubbles could

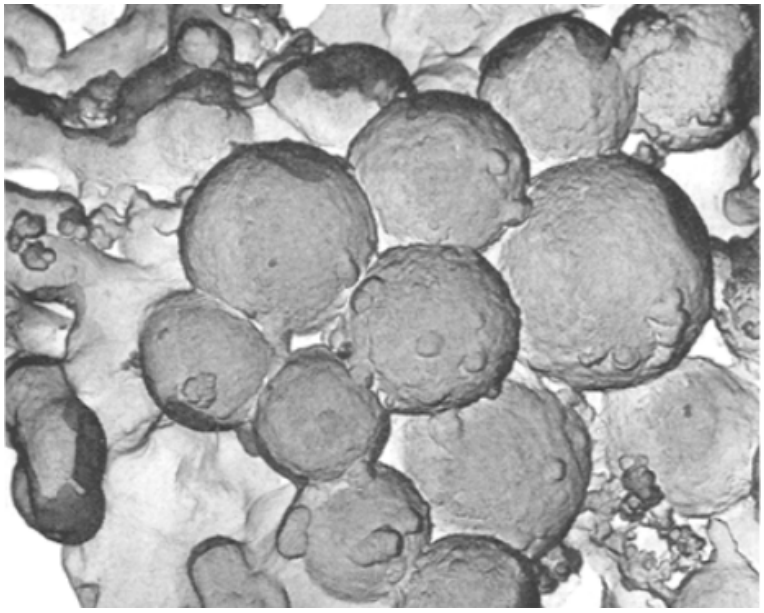

**Figure 1.5:** Transmission electron microscope image of ≈ 800–1000 nm Ø hollow spheres collected from the sediment of Lake Kivu, Kenya. The spheres were composed of ZnS, and were attributed to volcanic sediment coating the surface of bulk methane nanobubbles. Reprinted with permission from Reference 22. Copyright 1973, Springer Nature.

result in a 4× increase in the $O_2$ concentration of distilled water[24]. They then demonstrated the effects of nanobubbles on hydroponically grown rapeseed plants and also on mice, as shown in Figure 1.6. Rapeseed grown in air-nanobubble water grew approximately 14% higher and had 35% more mass compared to distilled water. Mice fed with $O_2$-nanobubble water grew approximately 6% longer and had 7% more mass compared to distilled water. The plant growth was attributed to increased levels of nutrients attracted by the negative nanobubble charge, whilst the mice growth was credited to the higher metabolism rates induced by the increased oxygen content.

Bulk nanobubbles also have potential applications in medicinal research. Recent studies have suggested the use of surfactant stabilised nanobubbles as advanced drug delivery agents[25,26]. Nanoparticles are capable of delivering anti-tumour drugs to specific sites by exploiting the porosity of tumour cells (380–780 nm Ø), but they can also accumulate in the organs and cause damage. Nanobubbles can be modified to carry the same anti-tumour drugs, but have been shown to have a higher delivery efficiency, with ≈ 20% greater concentration of drug delivered to a cell compared to nanoparticles, as shown in Figure 1.7[27]. They can then be acoustically destroyed to prevent accumulation. Tumours

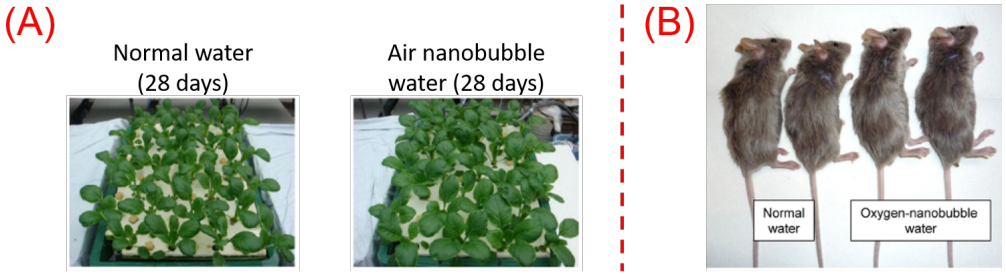


**Figure 1.6:** Visual observations made on the increased size of (A) rapeseed plants grown hydroponically in air-nanobubble water and (B) mice that were fed oxygen-nanobubble water over several weeks. Reprinted (adapted) with permission (open access) from Reference 24. Copyright 2013, Ebina *et al.*.

are also difficult to detect with ultrasound, due to the tissue structures giving low resolution images. Surfactant stabilised nanobubbles can be used as ultrasound contrast agents that are capable of increasing the signal detection by 25 dB[25].

Improvements to numerous cleaning processes could also benefit from nanobubble research. Surfactant free solutions containing bulk nanobubbles could be used to clean membrane surfaces, which are prone to fouling with protein contamination during continuous use[28,29]. Nanobubbles could also improve froth flotation, where they could increase attachment and decrease detachment probabilities of particles, compared to microbubbles[30,31]. There are countless other applications for bulk nanobubbles, but the exciting possibilities have led to rushed research and conflicting literature[32]. In order to better use bulk nanobubbles, it is essential to understand how they can be reliably generated and why they appear to be so stable.

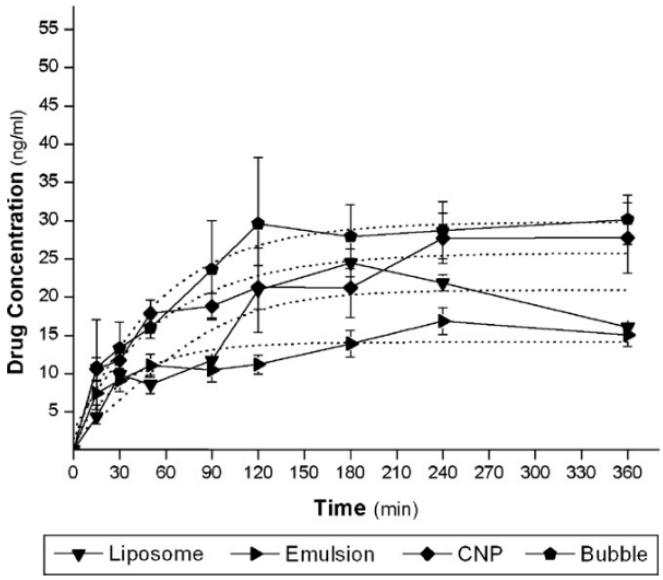


**Figure 1.7:** Absorption of an anti-tumour drug (coumarin-6) into cancerous cells (MCF-7) over time. The anti-tumour dug was delivered using liposome suspensions, emulsions, nanoparticles, and bulk nanobubbles. The solid lines with symbols shows the drug concentration over time, whilst the dashed lines show the fitting to this data. Reprinted with permission from Reference 27. Copyright 2010, Elsevier B.V.

#### 1.3.1.1 Methods of generating bulk nanobubbles

Reported methods of creating bulk nanobubbles are often similar to the methods used to create microbubbles. In general, a liquid is supersaturated with gas, then subjected to a change in conditions which encourages nanobubble formation. Separation of the nanobubbles from a polydisperse suspension is often required before further use. Some of the most commonly reported generation methods are listed below.

***Hydrodynamic cavitation*:** In this process, mixtures of gas and liquid are pumped through a series of components designed to divide existing bubbles[33]. Examples of components include Venturi tubes, where sudden pressure changes induce nanobubble formation, and swirl flow generators, where liquid vortexes create high shear forces that further shrink bubbles[34]. Hydrodynamic cavitation is highly cost effective and requires little upkeep, but component design requires a deep knowledge of hydrodynamics[35,36]. Most commercial

nanobubble generators rely on hydrodynamic cavitation, but are not adequately tested and can give unpredictable results[32].

***Acoustic cavitation*:** An alternative method is acoustic cavitation, where a sinusoidal pressure wave is applied to a liquid in order to create nanobubbles[37,38]. When the amplitude of the pressure wave is low enough, bubbles of vapour and dissolved gas are formed. Large nanobubble populations ($10^9$ bubbles $mL^{-1}$) can be generated with this method, with longer sonication times giving even more bubbles[39]. However, there is concern that the acoustic cavitation also damages the ultrasonic horn, releasing nanoparticles into the solution that may then be mistaken for nanobubbles[9].

***Solvent exchange*:** Gases have different solubilities depending on which solvent is being used. For example, $CO_2$ is more soluble in ethanol than it is in water[40]. Solvent exchange exploits this by replacing a highly solvating liquid with a poorly solvating liquid, thereby creating local supersaturation which can then lead to nanobubble formation. Qui *et al.* showed that ethanol-water solvent exchange resulted in nanobubbles, but not in solvents that had been previously degassed, as shown in Figure 1.8[41]. Solvent exchange is simple and produces large quantities of nanobubbles ($10^8$ $mL^{-1}$), but the use of organic solvents is controversial as they could stabilise the bubbles unnaturally. Habich *et al.* found no evidence that suggested solvent exchange bubbles contained gas, suggesting they could even be nanoparticles instead[42]. However, it should also be noted that Najafi *et al.* have showed bulk nanobubble formation without solvent exchange, by manipulating the temperature and pressure of the solution to induce supersaturation[43].

***Electrolysis*:** Application of a sufficient potential between two electrodes can split water in a process known as electrolysis. In a series of publications, Kikuchi *et al.* showed how the electrolysis reaction was capable of producing bulk $H_2$ and $O_2$ nanobubbles[44–47]. In acidic solutions, the bubbles adhered to the electrode surface, but in alkaline conditions they detached as freely moving nanobubbles. Electrolysis provides finer control over the nanobubble dimensions through the duration of the applied potential[48]. However, electrolysis also limits the nanobubbles to only $H_2$ and $O_2$ and in alkaline solutions.

Acoustic cavitation and electrolysis are the most promising methods of bulk nanobubble generation, since they are easy to use and potentially provide more control over the

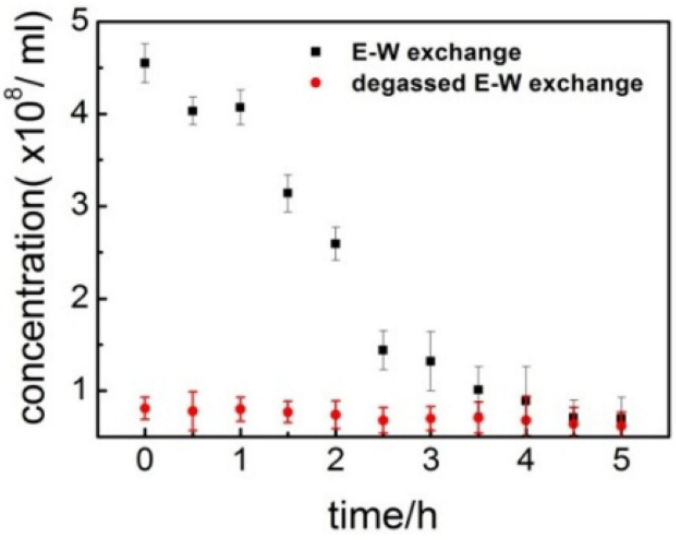


**Figure 1.8:** Concentration of bulk nanobubbles generated in solutions that had recently undergone ethanol-water solvent exchange procedures, measured by dynamic light scattering. Regular solvent exchange resulted in nanobubbles that disappeared over time, as shown by the black symbols, whilst solvent exchange performed with degassed solvents showed no apparent nanobubble generation, as shown by the red symbols. Reprinted with permission from Reference 41. Copyright 2017, WileyVCH Verlag GmbH and Co.

bubble size. Solvent exchange offers a simple method for creating large quantities of nanobubbles, but the role of the organic solvents in bubble stability is unclear and there are conflicts in the literature. Hydrodynamic cavitation is an attractive technique, but requires too much expertise to design the components. However, regardless of the generation method used, ways of detecting and sizing the nanobubbles are needed.

#### 1.3.1.2 Techniques for characterising bulk nanobubbles

Characterisation techniques are essential for confirming the production of bulk nanobubbles by the generation methods seen previously. The information given by characterisation could also help explain the properties of nanobubbles and the cause of their apparent stability. Some of the most popular techniques used in the literature are listed below.

***Light scattering techniques*:** Dynamic light scattering (DLS) is the most commonly used technique for bulk nanobubble characterisation. In this technique, laser light is scattered by the suspended nanobubbles, forming a detectable interference pattern. Over short timescales, the bubbles move under Brownian motion and the intensity of the interference pattern fluctuates. The frequency of the fluctuations is correlated to the diffusion coefficient of the bubbles, allowing the hydrodynamic radius to be calculated through the Stokes-Einstein equation. Kikuchi *et al.* used DLS to characterise $O_2$ nanobubbles over a period of several days[46]. As shown in Figure 1.9, a high scattering intensity was seen immediately after generation, but the signal soon shifted to higher diameters and lower intensities as the nanobubbles slowly coalesced together.

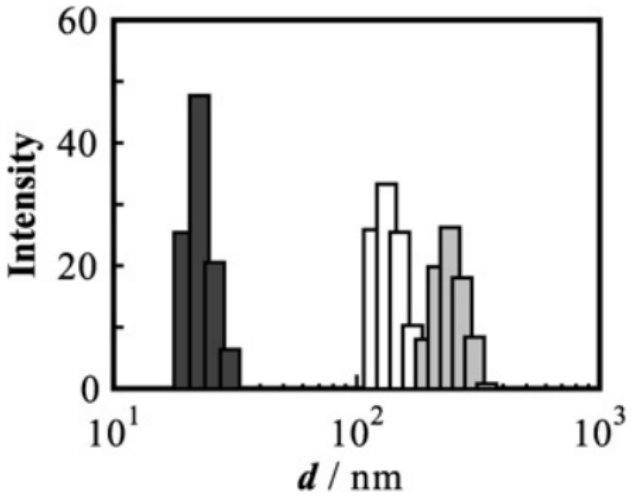


**Figure 1.9:** Dynamic light scattering of $O_2$ nanobubbles produced by electrolysis of 33 mM $Na_2SO_4$. The particle size and concentration was observed to change over (BLACK) 1, (WHITE) 2, and (GREY) 3 days after electrolysis. Reprinted with permission from Reference 46. Copyright 2009, Elsevier Inc.

DLS could offer a convenient method of sizing bulk nanobubbles and monitoring their population over time. However, this assumes that the laser light is more likely to be scattered than it is to refract through the bubble, and that the nanobubbles are subjected to the influence of Brownian motion. There is not much evidence to support these assumptions, which casts doubt on the use of DLS for nanobubble characterisation. Further concern was expressed by Okhagi *et al.*, who found inconsistencies between three different DLS apparatus when characterising $N_2$ and methane nanobubbles[49].

***ζ-potential measurements*:** In this technique, a potential is applied between two electrodes in a solution containing bulk nanobubbles. The electric field causes the electrophoretic movement of the nanobubbles, which supposedly have a negative charge due to OH adsorption. The electrophoretic velocity is monitored by the scattering of laser light, allowing the ζ-potential between the solution and the bubble to be calculated. Kim *et al.* recorded a negative ζ-potential after acoustic cavitation was used to generate bulk nanobubbles[37]. The potential value was consistent with that of microbubbles and not the value of any nanoparticles that could have been also generated. Surfactants appeared to stabilise the bubbles, making the potential more negative, with the effect more noticeable when using longer surfactant chains. Other research suggested that an alkaline pH also stabilised the nanobubbles, due to the increased adsorption of OH ions on the bubble surface[43]. Measurement of the ζ-potential provides a way of determining whether nanobubbles or nanoparticles are present. However, there is still very little evidence to suggest nanobubbles are capable of scattering light efficiently.

***Microscopy*:** Neither light scattering nor ζ-potential measurements are capable of giving direct evidence of bulk nanobubbles. An alternative is optical microscopy, which has already been used to identify sub-micron bubbles as shown in Figure 1.10[50]. However, visible light has a diffraction limit of ≈ 300 nm, which means optical microscopy is restricted to the identification of nanobubbles larger than this value.

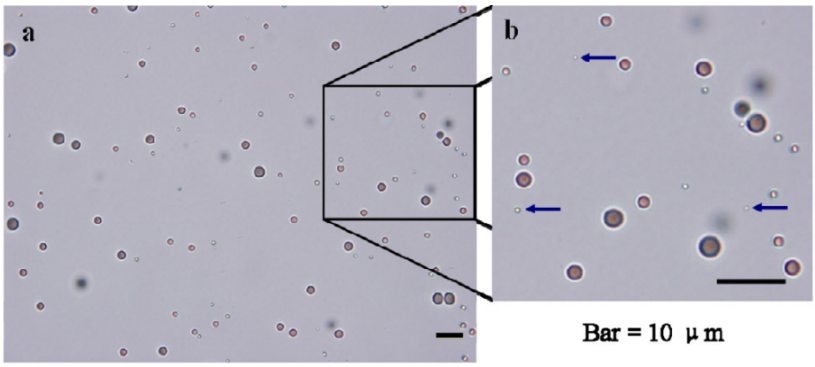


**Figure 1.10:** Optical microscope image (LEFT) of a polydisperse suspension of bulk microbubbles and nanobubbles, produced by acoustic cavitation. An enhanced section of the image (RIGHT) was used to identify large bulk nanobubbles, as indicated by the arrows. Reprinted (adapted) with permission from Reference 50. Copyright 2010, IOP Publishing Ltd.

Scanning electron microscopy (SEM) uses an electron beam to study the sample

instead of visible light, allowing for greater resolution. However, the low pressures required for SEM would destroy any nanobubbles in direct observation, so freeze-fracture replica imaging is used instead. To do this, the nanobubble suspension is rapidly frozen and then cut in half, giving a surface that is coated with a metal to create a replica for imaging. This technique has been used to identify several sites attributed to $\approx 140$ nm oxygen bubbles in the solution, as shown in Figure 1.11[51,52]. No bubble sites were witnessed on the replicas of degassed solutions, but in wastewater there was evidence of nanobubbles coated in a skin of nanoparticles. Similar results have been seen for replicas of nitrogen, methane and argon nanobubbles[49]. Replica imaging gives convincing evidence of bulk nanobubbles, but cannot be performed *in situ*. This raises the possibility that the sites are not bubbles, but defects caused during the preparation of the replica.

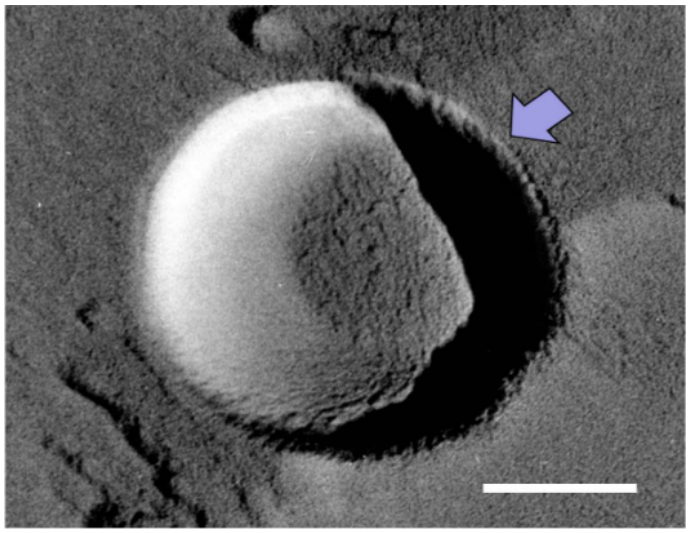

**Figure 1.11:** Transmission electron microscope image of a buk nanobubble site found in the freeze-fracture replica of a 1% wt. NaCl solution that had been subjected to hydrodynamic cavitation. After nanobubble generation, the solution was rapidly frozen in liquid $N_2$, cut in half, and then replicated by evaporating Pt/C onto the surface. The scale bar represents 100 nm. Reprinted with permission (open access) from Reference 52. Copyright 2016, Uchida *et al.*.

***Electrochemical techniques*:** Kikuchi *et al.* performed potential step experiments that showed the oxidation of electrochemically generated $H_2$[53]. When the cathodic potential used for $H_2$ generation was increased, the slope of the $H_2$ oxidation current became steeper. This change was attributed to the formation of $H_2$ nanobubbles, which increased the mass transfer to the electrode during oxidation. Cyclic voltammetry was also performed, showing a $H_2$ oxidation peak in solutions containing $H_2$ nanobubbles, but not in

solutions bubbled with $H_2$ gas[45]. The peak magnitude increased during electrolysis, but then dissipated over time as the nanobubbles dissolved. Electrochemistry is a promising, but underused tool for nanobubble characterisation and it could help elucidate the properties of nanobubbles as well as detect them in solution. A powerful electrochemical technique that has not yet been used for nanobubble characterisation is Coulter counting, which will be discussed in more detail later.

***Spectroscopy methods*:** Spectroscopic methods have also been successfully used to analyse bulk nanobubbles, providing a way of distinguishing between dissolved gas and freely moving gas molecules. Ushikubo *et al.* measured the nuclear magnetic resonance (NMR) proton spin relaxation time in a 10 mM $MnCl_2 \cdot 4\,H_2O$ solution containing $O_2$ nanobubbles[54]. As shown in Figure 1.12, the paramagnetism of the $Mn^{2+}$ ions resulted in more efficient relaxation of the control solution, but the presence of $O_2$ nanobubbles increased the relaxation time. The negative charges on the nanobubbles were thought to attract $Mn^{2+}$ ions, reducing the paramagnetic effect on the solution. The same effect was observed with Xe nanobubbles, but not with $O_2$ saturated solutions.

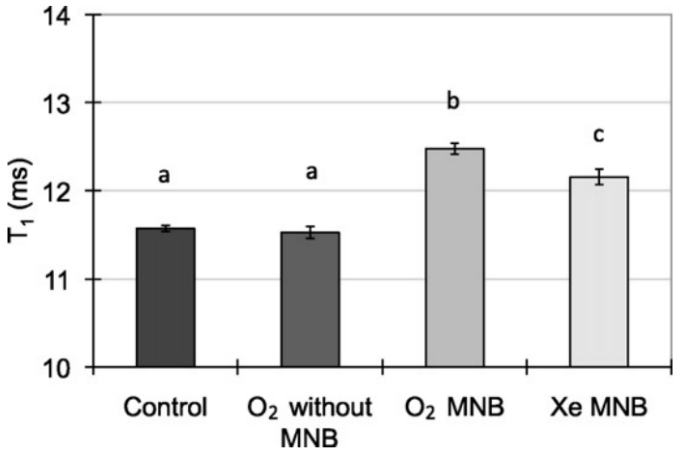


**Figure 1.12:** Measurements of the proton spin relaxation time recorded in 10 mM $MnCl_2 \cdot 4\,H_2O$ solutions containing bulk nanobubbles. The presence of negatively charged nanobubbles attracted $Mn^{2+}$ ions, increasing the proton spin relaxation time in the process. Reprinted with permission from Reference 54. Copyright 2010, Elsevier B.V.

Raman and infrared spectroscopy have been used to study bond environments in $N_2$ nanobubbles[49]. The N–N Raman band was shown to shift from values for dissolved $N_2$ to a position indicative of a gaseous $N_2$, which indicated the growth of nanobubbles. The

O−H infrared band also possessed one of the four possible H-bond modes, suggesting the presence of a rigid H-bonding network. Similar results by Habich *et al.* showed a difference in the infrared rotation mode for dissolved $CO_2$ and nanobubbles[42]. Spectroscopic techniques could provide crucial information on the state of the gas in a nanobubble, but are not capable of distinguishing between nanobubbles and microbubbles on their own.

***Other characterisation techniques*:** Some less common techniques have also been used to study nanobubbles. Kobayashi *et al.* have detected nanobubbles using a unique microchannel mass resonator method[55]. In this technique, a bulk nanobubble suspension is flowed through the internal microfluidic channel of a cantilever. The cantilever is electrostatically driven by a sinusoidal electric field, causing it to vibrate. Figure 1.13 shows that when a bubble enters the channel, the density of the cantilever decreases and the frequency of the vibration shifts higher, which is detected by a laser-photodetector as a change in resonance[56]. Higher density objects shift the vibration to lower frequencies, allowing discernment between nanobubbles and nanoparticles.

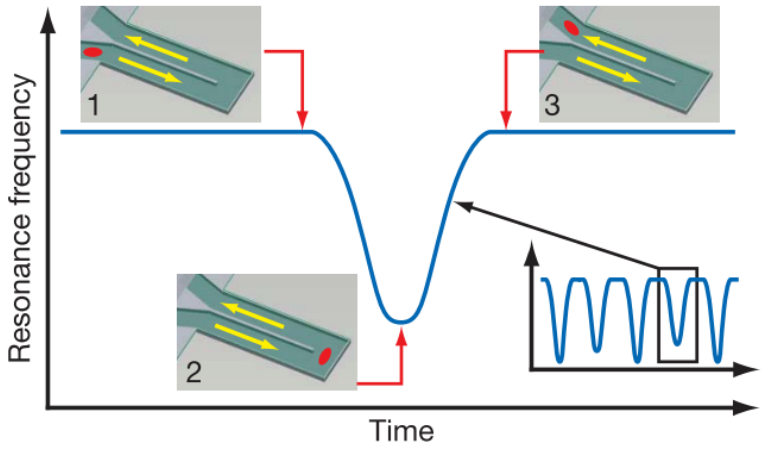


**Figure 1.13:** Principle behind the mass resonance characterisation technique. As the particle or bubble enters the microchannel of the cantilever, the resonance of the cantilever oscillation varies in response to the change in density. This effect reaches its maximum at the apex of the cantilever. Reprinted (adapted) with permission from Reference 56. Copyright 2007, Springer Nature.

Leroy *et al.* suggested using ultrasound to detect the presence of bulk nanobubbles in water[32]. Ultrasound is usually attenuated in water, but in the presence of gas the ultrasound can be picked up by a transducer. The size of the bubble can be determined from

the maximum of the attenuation. This technique also has the advantage of distinguishing between bubbles and solid particles, which would not cause the same effect.

#### 1.3.1.3 Theories for the stability of bulk nanobubbles

Epstein and Plesset predicted that rapid gas diffusion from nanobubbles would prevent them from existing long enough for experimental observation[15]. Bulk nanobubbles follow this theory, with simulations showing that a 100 nm Ø air bubble in saturated water would dissolve in 75 $\mu$s (assuming the surface of the bubble was clean)[57,58]. Nevertheless, various characteristion techniques have provided evidence of bulk nanobubbles that appear stable against diffusion. Some of the properties of nanobubbles may help explain this stability.

Surfactants can help stabilise against the diffusion of gas from microbubbles by lowering the surface tension acting upon the bubble interface. A similar effect is observed using nanobubbles, with the $\zeta$-potential becoming more negative as surfactant concentration increased (linear under the critical micellar concentration) and smaller bubbles being obtained[38]. In solutions without surfactant, this stabilisation could be achieved by organic molecules or particles in the water. Water-miscible organic molecules were shown to stabilise nanobubbles and alter their predicted internal pressure to $\approx 2$ atm[59]. Slower diffusion due to lower surface tension might explain the apparent lifetime of bulk nanobubbles, and it is possible that the small size of the bubbles enhances the attraction of contaminants.

However, others argue that surface bound contamination would only slow down the diffusion of gas from a bubble, not prevent it. The alternative is that the negative charge of nanobubbles offers stability from the diffusion of gas. The adsorbed $OH^-$ ions repel each other, minimising the surface tension of the bubble interface and stabilising against diffusion. Yurchenko *et al.* tried to prove this by increasing the temperature to desorb the $OH^-$ ions[60]. Bunkin *et al.* even proposed that nanobubbles could exist in clusters, with the negative charges preventing coalescence[21,61]. This theory is supported by experiments that showed larger electrolyte concentrations decreased the Debye length and increased coalescence[52].

Another theory suggests that the gas in a nanobubble is never stable against diffusion, but that initial gas diffusion results in the local supersaturation of the solution, establishing an equilibrium. This effect would be enhanced in nanobubble clusters, where the network of nanobubbles would lead to widespread supersaturation. However, it is worth noting that any supersaturation would be out of equilibrium with the atmosphere and the dissolved gas would therefore dissipate quickly, making this option less likely[62].

#### 1.3.1.4 Conclusion on bulk nanobubbles

There is still no consensus on why bulk nanobubbles should appear stable for so long, but there is a lot of evidence for their existence. The most popular theory for bulk nanobubble stability involves contamination of the bubble interface, but further characterisation is needed to confirm this. Most characterisation techniques are unsuitable for nanobubble detection, often because they fail to distinguish between bubbles and particles, but some ingenious detection technologies are now being used, and the combination of techniques could improve the evidence. Many attractive applications can be found for bulk nanobubbles, but generation methods are currently much less developed, although electrolysis and acoustic cavitation methods are promising.

### 1.3.2 Surface nanobubbles

In 1982, Israelachvili *et al.* reported a long range attractive interaction between hydrophobic surfaces in water[63]. This interaction was 10× stronger than Van der Waals forces, but decayed exponentially as the surfaces were brought within 10 nm of each other. The gap between the surfaces was later shown to have a different refractive index to water, which was attributed to the formation of stable cavities[64]. Parker *et al.* recorded force curves of this interaction which featured several steps, as shown in Figure 1.14[65]. The steps appeared to be related to the cavities, which they claimed were actually gaseous nanobubbles on the hydrophobic surfaces. Weaker interactions were observed in degassed solutions[66]. However, the idea of surface nanobubbles was heavily criticised, most prominently by Ljunggren *et al.*, who voiced their concern over the apparent contradiction to the Epstein-Plesset theory[14].

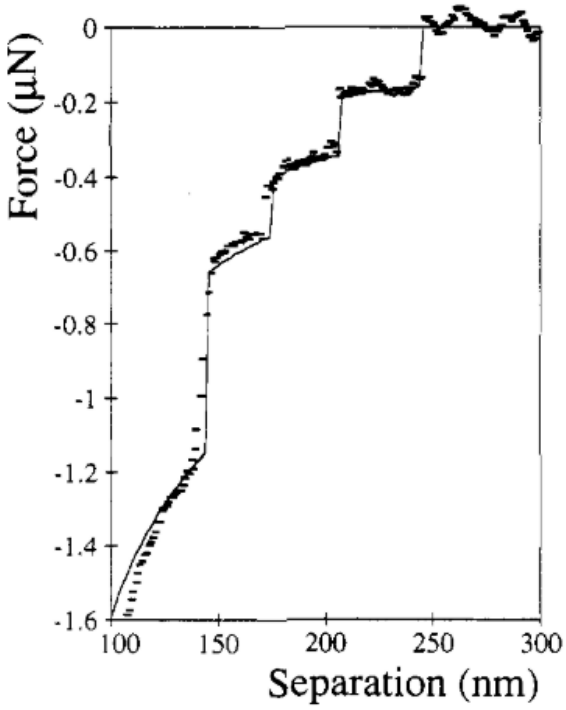


**Figure 1.14:** Force curves recorded during the separation of two silanised glass surfaces under water. The steps in the curve were said to correspond to six identical surface nanobubbles that bridged the two surfaces. Reprinted with permission from Reference 65. Copyright 1994, American Chemical Society.

Debate over these publications continued until images appearing to show surface

nanobubbles were recorded using tapping-mode atomic force microscopy (AFM). Lou *et al.* imaged both hydrophobic mica and highly ordered pyrolitic graphite surfaces, and found nanobubbles that lasted for several hours until coalescence[67]. In the same year, Ishida *et al.* observed nanobubbles on an octadecyltrichlorosilane coated Si surface[68]. They recorded height maps and phase images which gave the dimensions of the nanobubbles, as shown in Figure 1.15. Contact with the AFM tip was noted to deform these bubbles, while surfaces that had not been exposed to air showed no bubbles. While the use of AFM was deemed to be intrusive by critics, this research accelerated interest in both bulk and surface nanobubbles.

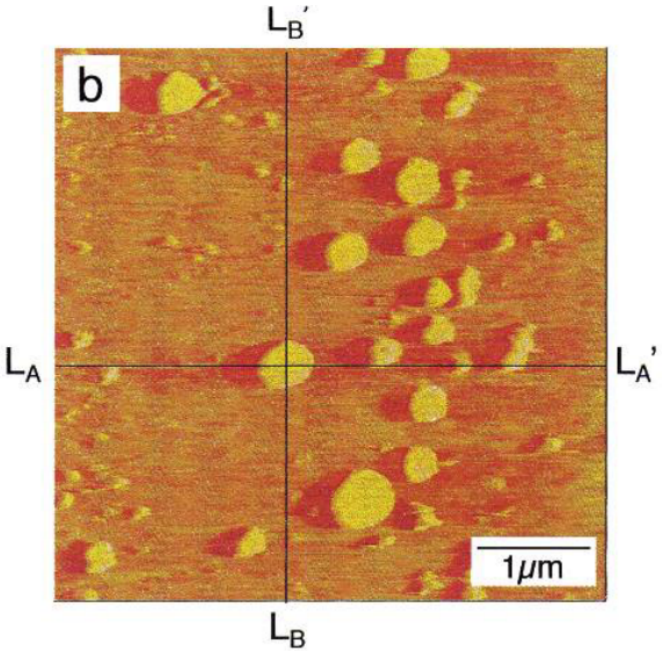


**Figure 1.15:** Tapping-mode atomic force microscope phase images showing surface nanobubbles on an octadecyltrichlorosilane coated Si surface after an ethanol-water solvent exchange process. Reprinted (adapted) with permission from Reference 68. Copyright 2000, American Chemical Society.

More recently, the case for surface nanobubbles has been strengthened with spectroscopic methods. Zhang *et al.* have studied $CO_2$ surface nanobubbles with infrared spectroscopy, showing peaks for gaseous $CO_2$ but not dissolved $CO_2$[69]. Similarly, Seo *et al.* examined air nanobubbles with fluorescence, by coating their hydrophobic surface with a fluorophore. They showed nanoscale objects in reflective interference contrast microscopy images with a fluorescence emission wavelength of air and not water, as well as showing the lack of such objects in degassed water[70].

The strong adhesion of surface nanobubbles to their solid interface has been exploited for several applications, including the enhanced cleaning of membranes. Membranes are heavily used in many industrial processes like water purification, and often are fouled by protein build-up through regular use. Surface nanobubbles could present a new way of cleaning membranes, with 10 s of nanobubble treatment having been shown to remove adsorbed proteins more efficiently than 20 mins of surfactant cleaning, as seen in Figure 1.16[71,72]. Proteins that adsorb more strongly were more resistant to nanobubbles, but easily removed using nanobubble/surfactant mixtures[73]. Preadsorbed surface nanobubbles have also been shown to reduce the adsorption of proteins by $\approx 30\%$[74].

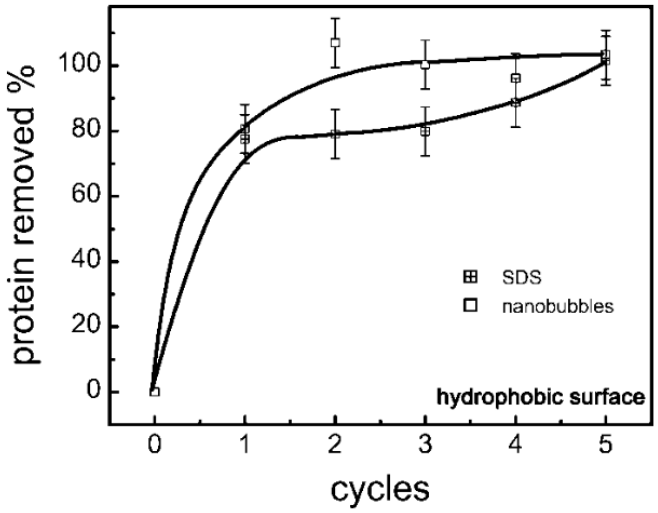


**Figure 1.16:** Comparison of the techniques used to clean the surface of a fouled hydrophobic quartz crystal microbalance. The plot shows the percentage of protein (bovine serum albumin) removed with each cycle of a conventional cleaning treatment and a nanobubble cleaning treatment. The conventional cleaning cycle was comprised of 20 min of washing with SDS, whilst the nanobubble cleaning cycle involved a 10 s electrolysis procedure to produce large quantities of surface nanobubbles. Reprinted with permission from Reference 71. Copyright 2008, American Chemical Society.

Surface nanobubbles are also relevant to the improvement of microfluidic devices. In such devices, the fluid near the microchannel wall is assumed to be stationary, in what is known as the no-slip boundary condition. This introduces a frictional drag force to the microfluidics, but recent use of surface microbubbles has shown to produce a $\approx 20\%$ reduction in this drag by allowing slip of the liquid at the interface[75]. Surface nanobubbles show a 500 nm increase in the slip length, which could reduce drag in nanofluidics[76–78]. Additional uses of surface nanobubbles are possible, but often they are unwanted as their

presence interferes with other process such as electrodeposition and surface studies[9].

#### 1.3.2.1 Methods of generating surface nanobubbles

Surface nanobubbles are often generated using the same techniques as bulk nanobubbles, but they need a surface which nearby dissolved gas can nucleate onto[79]. This surface is typically made hydrophobic to improve nanobubble stability, which limits the generation methods that can be used. Since their discovery, literature reports of surface nanobubbles have been mostly generated by electrochemical and solvent exchange methods[80].

***Solvent exchange*:** Surface nanobubbles are often generated by an ethanol-water exchange in the presence of a hydrophobic surface. Most procedures expose the surface to air before adding it to pre-saturated ethanol[81,82]. This is due to the observations of Ishida *et al.*, in which no nanobubbles were obtained on surfaces made hydrophobic *in situ*[68]. However, this need for exposure is not consistent with the bulk nanobubble generation mechanism, where the bubbles nucleate from gas dissolved in the solvent. Furthermore, the addition of saturated water to a pre-exposed surface has been shown to produce no bubbles[82]. It is therefore more likely that Ishida *et al.* had erroneous data on the pre-exposure of the surface, which is not needed to produce nanobubbles.

The solvent exchange method produces local supersaturation in the solvent which causes the nucleation of nanobubbles. While ethanol-water remains the most prevalent system, surface nanobubbles have also been made with other methods of supersaturation. These include swapping cold water for warm water[83], replacing weak electrolyte solutions for a more concentrated solution[84], and even adding cold water to a preheated surface[85].

***Electrochemical generation*:** Nanoelectrodes have recently been used to reduce $H^+$ to $H_2$ gas, causing local saturation near to the electrode surface, which then leads to nucleation of a nanobubble[86]. In cyclic voltammetry, the formation of $H_2$ is observed as a reduction wave, whilst the nucleation is seen by a sudden drop in the current, as shown in Figure 1.17. After nucleation, a steady current is obtained through equilibrium of the $H_2$ diffusing from the bubble and the $H_2$ generated at the edge of the nanoelectrode[87]. Stable populations of surface nanobubbles have also been created by electrolysis on large

hydrophobic HOPG electrodes[88]. Other gases can be obtained by different reactions, such as the oxidation of $N_2H_4$ to $N_2$[89] and $H_2O_2$ to $O_2$[90]

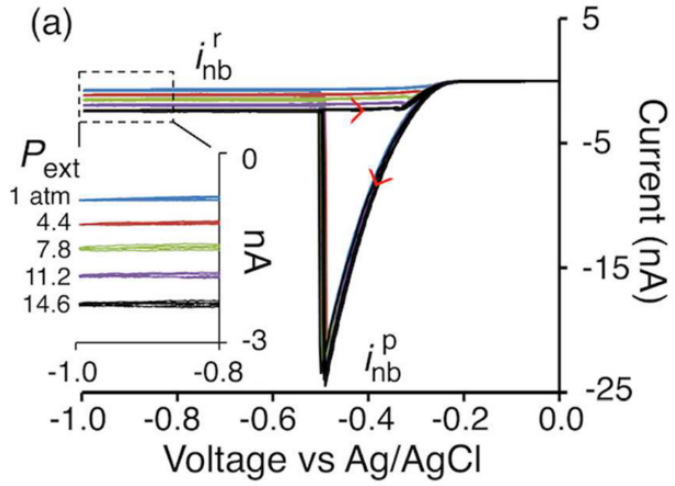


**Figure 1.17:** Cyclic voltammograms showing a dynamic equilibrium of $H_2$ surface nanobubbles on a Pt nanoelectrode. The reduction wave indicates the production of $H_2$, whilst the sudden drop in current is related to the nucleation of a surface nanobubble that blocks the electrode. The current after nucleation was maintained by a dynamic equilibrium between $H_2$ diffusing from the bubble and $H_2$ being produced at the electrode edge. Increased external pressures reduced the bubble size, which increased the exposed electrode area and therefore the background current. Reprinted (adapted) with permission from Reference 87. Copyright 2016, American Chemical Society.

There have been significantly fewer generation methods reported for surface nanobubbles, in part due to the need for a hydrophobic surface. Solvent exchange is the most prevalent method, but the procedures are not well-defined and there is still concern over the regular use of ethanol. Electrochemical generation is more reliable, but is limited to conductive and hydrophobic electrode materials. Alternative generation methods may provide an answer to these problems. For example, the use of microwaves to heat HOPG surfaces has been shown to cause supersaturation and nanobubble formation[91].

#### 1.3.2.2 Techniques for characterising surface nanobubbles

Techniques to characterise surface nanobubbles are also limited by the presence of a surface. Unlike bulk nanobubbles, particle sizing techniques are often unsuitable and surface characterisation techniques are instead used. Generally, this has led to the same techniques being used repeatedly.

***Atomic force microscopy*:** Tapping-mode AFM has been used extensively to study nanobubbles adhered to surfaces. In this mode, the cantilever is electrostatically oscillated to create a tapping motion, which reduces tip damage to soft objects. Tapping-mode AFM has been used to identify nanobubbles on hydrophobic surfaces, revealing information about their dimensions and contact angles[92]. However, the dimensions recorded using this mode are often smaller than in reality[93] and the technique has issue with distinguishing between bubbles and contaminants like oil[94]. Furthermore, there has been some concern that the oscillation causes pressure variation which affects the bubbles. These issues could be addressed by contact-mode AFM, in which the cantilever tip is dragged across the surface to determine the topography. Recently, contact-mode AFM has been used to distinguish between nanoparticles/droplets and nanobubbles. Nanobubbles do not appear to move after gentle pushing from the tip, or even strong dragging motions, whilst particles and droplets are more easily displaced[95,96].

***Microscopy*:** Optical microscopy can provide direct observation of nanobubbles and has been reported using a reflective interference contrast (RICM) technique. Polarised light is reflected by any films or oxide layers on a surface and by the surface itself, causing the reflected light to form an interference pattern. Surface nanobubbles cause a phase shift in the reflected light, which alters the interference pattern and can be observed by the contrast in reflectivity. RICM has given similar results to AFM measurements of surface nanobubbles above the diffraction limit, but has the advantage of being non-intrusive[93]. An alternative microscopy technique is total internal reflection microscopy (TIRM), in which a laser is used to excite fluorophores on the surface[97,98]. The fluorophore has different emission wavelengths depending on if it is in a gaseous or liquid environment, allowing the presence of a nanobubble to be confirmed. This has been used to distinguish between oil droplets and surface nanobubbles. As shown in Figure 1.18, both of these microscopy techniques can be combined with each other and even with AFM, allowing for

extensive characterisation[70].

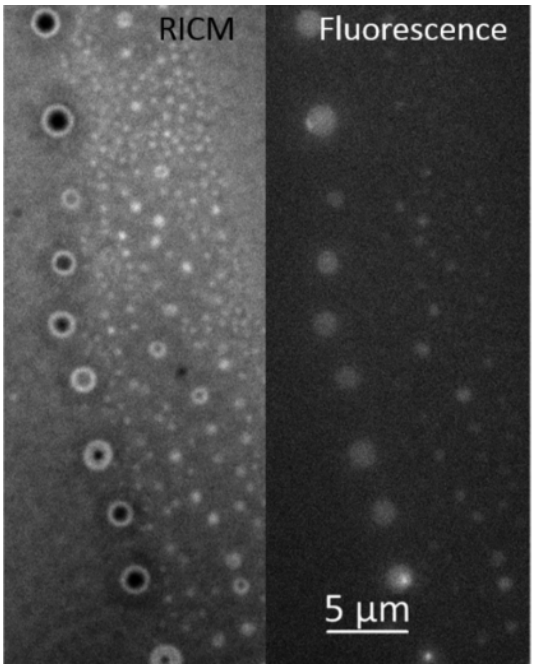


**Figure 1.18:** Identification of surface nanobubbles produced by a solvent exchange method, using advanced optical microscopy methods. Reflective interference contrast microscopy (LEFT) detects changes to a reflected interference pattern, whilst total internal reflection microscopy (RIGHT) uses the excitation of fluorophores to distinguish surfaces in gaseous and aqueous environments. Reprinted with permission from Reference 70. Copyright 2015, American Chemical Society.

Less common microscopy techniques could also provide information on surface nanobubbles. Scanning transmission soft X-ray microscopy has been shown to size nanobubbles with a resolution of 15 nm. The technique is not intrusive and can even distinguish between some gases[99]. Scanning transmission electron microscopy has also been used to observe the growth and decline of electrochemically generated nanobubbles over short timescales[100]. However, the use of these techniques for nanobubble characterisation is in its infancy, and both have been shown to alter the bubbles with long exposure times.

AFM and microscopy are routinely used for surface nanobubble characterisation, but different techniques could provide different perspectives on their apparent stability. Quartz crystal microbalances have been used to detect changes in mass after nanobubble nucleation, which could help prove that the bubbles contain gas[71]. Furthermore, the deliberate electrodeposition of metals onto surfaces around the nanobubbles can cause a templating

effect which can be observed by AFM/SEM[101]. Cyclic voltammetry has also been used to reveal information on the dissolution rate of surface nanobubbles by altering scan rate, and can also be used to estimate size[102]. Simulations are also being more frequently used to investigate the factors affecting surface nanobubble stability[103,104]. While microscopy is probably the most reliable technique at the moment, these newer techniques could improve surface nanobubble research.

#### 1.3.2.3 Theories for the stability of surface nanobubbles

The stability of surface nanobubbles is better understood than that of bulk nanobubbles. It is clear the presence of a surface stabilises the nanobubble, as detachment from the surface would increase the surface area and therefore be more energetically unfavourable[9]. However, this does not explain the long life of the surface nanobubbles that is observed experimentally.

Many theories of surface nanobubble stability are shared with those for the stability of bulk nanobubbles[105] . Contaminants or surfactants found on the bubble interface could reduce surface tension and therefore slow down the diffusion of gas from the bubble, making it appear more stable[105,106]. A similar effect has been proposed with hydroxide ions adsorbed at the surface of the bubble, which repel each other and therefore reduce the surface tension. The saturation of gas near the bubble is also cited as a possible mechanism for stabilising bubbles, with initial diffusion creating a saturated layer of gas which then establishes an equilibrium to stop further diffusion, but again this is only temporary[105,107].

Both of these ideas explain slower diffusion, but not the apparent long term stability that has been observed. One theory is that the escape of gas by diffusion is countered by the gas entering at the intersection of the solid-liquid-gas interfaces. However, the consensus is that this needs an external driving force and has not been confirmed by experimental results.[108–110]

Examination of surface nanobubbles by AFM has revealed a lower contact angle than in predictions based on macroscopic bubbles. For a given bubble diameter, a smaller contact angle would correlate to a larger radius of curvature. It has been argued that for

a surface nanobubble with a spherical cap geometry, the Young-Laplace equation relies more on the radius of curvature than the apparent radius[111,112]. This would mean the pressure difference is much smaller for surface nanobubbles. Hydrophobicity of the surface is related to the contact angle, so this stability is in a way provided by the surface. A similar argument to this is the contact line pinning of surface nanobubbles[113]. At the boundary on the surface where the gas and liquid interfaces meet, there is a three-phase boundary at which the bubble is pinned[114]. The gas can expand past this point, but the liquid cannot push the line back due to insufficient wetting of the hydrophobic surface[115]. Contact-mode AFM has been used to drag the nanobubbles away from this boundary, but they are clearly pinned, with the bubbles returning to their original position[98]. When gas diffuses from the bubble, the boundary lines are unchanged, so the height profile of the bubble is reduced, which results in a lower contact angle and therefore a larger radius of curvature that reduces the internal pressure and prevents further diffusion[116] .

The most likely case for the stability of surface nanobubbles is a mixture of contact angle/pinning effects and the local saturation of gas near the top of the bubble[117,118].

#### 1.3.2.4 Micropancakes

Micropancakes have been recently proposed as a different type of nanobubble with similarities to surface nanobubbles. They are flat quasi-2D layers of gas with small height profiles and are found at solid-liquid interfaces. Tapping-mode AFM images recorded on HOPG after an ethanol-water exchange have shown micropancakes present alongside surface nanobubbles[83]. These micropancakes had an average thickness of $\approx$ 2 nm and were observed to coalesce into wider micropancakes rather than increase in thickness. Ethanol removed the micropancakes but not the surface nanobubbles, suggesting a stronger dependence on the local saturation. Micropancakes were also obtained by injecting hot water onto hydrophobic silicon surfaces[119] and *ex situ* AFM has been used to identify areas of a polystyrene surface that were protected from water swelling by micropancakes[120]. AFM height maps have also shown surface nanobubbles sitting on micropancakes[121] and even other micropancakes stacking[122].

Micropancakes do not appear to share the stabilising features of surface nanobubbles,

such as boundary pinning or low contact angles. Simulations have suggested that their low height profiles could cause a stabilising reduction in their internal pressure, but there are still doubts as to their existence[123]. Solvent exchange procedures that produce micropancakes have not worked for different research groups and many have not witnessed the coexistence of surface nanobubbles and micropancakes[124]. An *et al.* have suggested that micropancakes are actually a polydimethylsilane (PDMS) lubricant from the plastic syringes used in solvent exchange processes[125]. Use of these syringes resulted in micropancake formation, with more micropancakes seen after longer times of leaving ethanol in the syringe, whilst the use of sterile glass syringes did not produce micropancakes. Direct application of PDMS also gave pancake like objects and the pancakes were still present after the surface was removed and dried[125]. Reports of micropancakes are now discounted, but the findings have also cast doubt onto surface nanobubble research. Characterisation techniques are able to discern between oils and nanobubbles, but it is not clear how much of the literature examples could be caused by PDMS contamination[78,126].

#### 1.3.2.5 Conclusion on surface nanobubbles

Surface nanobubbles have been researched far more than bulk nanobubbles, but despite this the field is still is in its infancy. There are only a few generation methods that have been used to create surface nanobubbles and there are concerns over the use of solvent exchange, in which the use of ethanol is thought to provide stability to the nanobubble. Likewise, characterisation techniques are not as varied, with AFM and microscopy being the most common. Tapping-mode AFM is controversial for its possible pressure fluctuations that may cause bubble formation. Furthermore, the evidence for PDMS contamination casts doubt on the reports of surface nanobubbles. However, many publications have proved the presence of gas filled nanobubbles on hydrophobic surfaces and the theory for their stability is a combination of boundary pinning and local saturation.

## 1.4 Project Aims

Theory dictates that nanobubbles should completely dissolve into the surrounding liquid in under a millisecond. However, there is mounting evidence for the existence of stable nanobubbles, both in the bulk of a solution and at solid-liquid interfaces. Current research is no longer concerned with proving that nanobubbles exist, but understanding why they appear stable enough for experimental observation.

To date, surface nanobubbles have received far more attention in the literature than bulk nanobubbles. Despite there being fewer applications of surface nanobubbles, as well as fewer techniques for their generation and detection, there are more explanations for their apparent stability. Conversely, far more interesting applications and unique characterisation techniques have been reported for bulk nanobubbles, but the cause of their stability is still unknown. However, the recent use of innovative characterisation techniques, such as mass resonance, shows promise for future insight into bulk nanobubble stability.

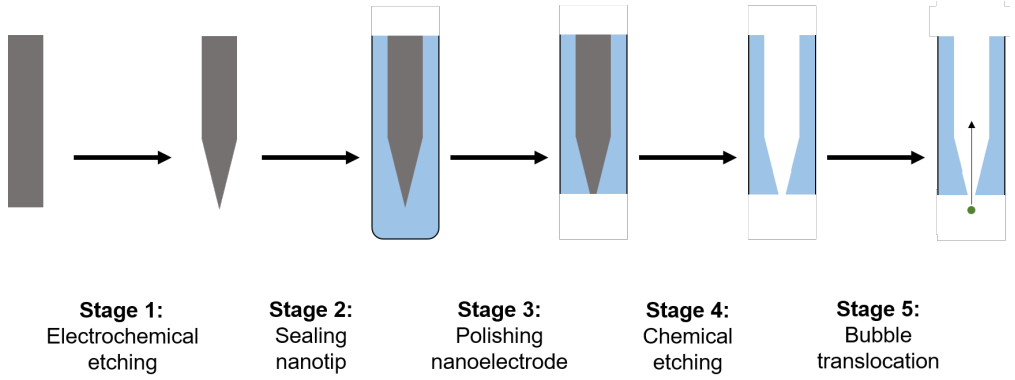


**Figure 1.19:** Proposed method of recording the Coulter counting of ultrasonically generated bulk nanobubbles. The electrochemical etching of W microwires will be used to make W nanoelectrodes, which will then be etched to produce glass nanopores suitable for use in Coulter counting.

The aim of the work shown in this thesis was to utilise a Coulter counting technique for the detection and characterisation of bulk nanobubbles. This electrochemical technique is commonly employed for nanoparticle characterisation, but has not yet been applied to the detection of bulk nanobubbles. This method could provide a better understanding of the concentration, charge, and size distribution of bulk nanobubbles, especially when

combined with existing characterisation techniques. Nanopores are required for the effective Coulter counting of nanobubbles, so a procedure for obtaining these nanopores is proposed, as illustrated in Figure 1.19. In this procedure, nanoelectrodes are first prepared from tungsten microwires using an electrochemical wire etching method. These nanoelectrodes are then chemically etched to produce glass nanopores, which can be characterised by the Coulter counting of nanoparticle standards. Finally, the Coulter counting of bulk nanobubbles through the nanopore will be recorded during the ultrasonication of electrolytes.

The remainder of this chapter will be dedicated to introducing the relevant theory needed to achieve this aim, including the literature on nanoelectrode fabrication, the principles behind Coulter counting, and the influence of acoustic waves on bubble dynamics.

## 1.5 Nanoelectrodes

Nanoelectrodes are generally defined as having at least one dimension in the range of 1–1000 nm. Their small dimensions cause their electrochemical behaviour to differ from macroelectrodes (> 50 $\mu$m Ø) and they share more similarities with microelectrodes (1–50 $\mu$m Ø). However, many of their electrochemical properties can be thought of as improvements to microelectrodes, such as the dramatic increase in the rate of mass transport towards the electrode[127–129]. This property allows hemispherical diffusion fields to rapidly form around nanoelectrodes, allowing the establishment of a steady state at shorter timescales, as illustrated in Figure 1.20[130]. Other improvements offered by nanoelectrodes include a lower charging current and a greater resilience to additional external resistances.

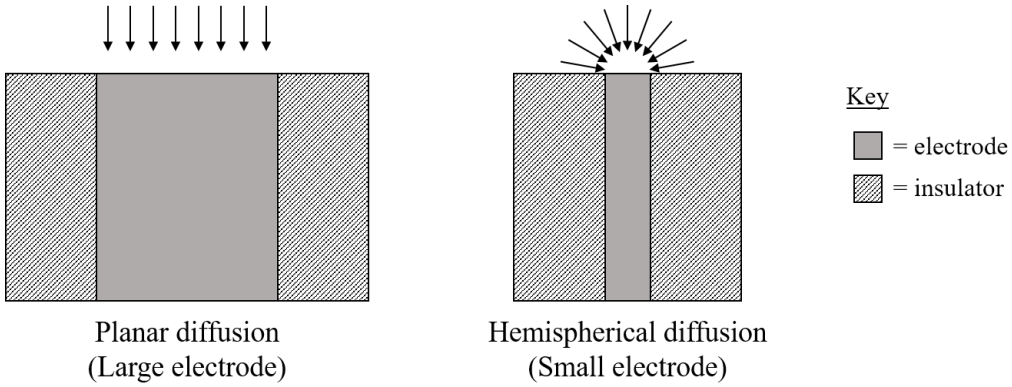


**Figure 1.20:** Example of the mass transport regimes that can be encountered during a diffusion controlled redox reaction at the surface of an electrode. At short timescales, the thin diffusion layer causes the mass transport to be dominated by planar diffusion. This is inefficient at providing the electrode with more reactant, causing the diffusion layer to grow and provide diffusion from the side of the disc. Macroelectrodes (LEFT) are large enough that the majority of the mass transport still comes from planar diffusion. Conversely, microelectrodes and nanoelectrodes (RIGHT) are small enough that the diffusion from the side of the disc makes a significant contribution, eventually establishing a more efficient hemispherical diffusion field around the electrode.

Over the past few decades, nanoelectrodes have emerged as advanced tools for analytical electrochemistry, with their small dimensions particularly suited for applications requiring high spatial resolution, such as SECM[128,131–133] and electrochemical measurements inside biological cells[128,134,135]. Furthermore, the rapid establishment of a hemispherical

diffusion field means that the steady state voltammetry of nanoelectrodes can be used in the study of fast electrochemical processes[136]. Nanoelectrodes can also serve as precursors to the nanopores required for Coulter counting[69]. This method of nanopore preparation provides the benefit of using the nanoelectrode characterisation to assess the dimensions of the subsequent nanopores. However, their small dimensions mean more complex fabrication and characterisation techniques are often required for the study of nanoelectrodes.

### 1.5.1 Methods of fabricating nanoelectrodes

The first reported methods of nanoelectrode preparation involved sputtering layers of gold onto cleaved mica surfaces. These surfaces were then sealed in an epoxy resin to yield single gold nanoband electrodes[137]. Such nanoelectrodes were simple to make and the principle was later adapted with lithography to make nanoband arrays, allowing higher currents to be recorded whilst maintaining the advantages of the individual nanoelectrodes[138,139]. However, nanoband electrodes were limited in their usefulness, being unsuitable for applications requiring high spatial resolution and for nanopore fabrication.

This led to the widespread use of nanodisc electrodes, which were more suited for such applications. Two methods for the fabrication of nanodisc electrodes are commonly reported: pipette pulling and wire etching[127,140,141]. In pipette pulling, a heating element or laser is used to soften a glass capillary containing a microwire. As the heat softens the glass, a gentle pulling force is simultaneously applied to both ends of the capillary. When the glass has softened enough, the two ends of the capillary are drawn apart, causing the glass/microwire to stretch and thin in the centre. The capillary is continuously drawn apart, tapering down until the pulling force causes the two ends become separated. This yields two pipette nanoelectrodes, each surrounded by a thin shroud of glass[129,142]. The small dimensions of the pipettes make them particularly useful for SECM, where lower glass-to-electrode ratios enable higher currents to be recorded near to surfaces[143], and in bioelectrochemistry, where it can be inserted into cells with minimal damage[144]. However, pipettes are more fragile than conventional electrodes, and the pulling procedures used are difficult to establish and generally irreproducible between other lab environments.

Wire etching uses a corrosive etching procedure to shape a microwire into a nanotip,

before it is manually sealed in an insulator. Methods of sealing include coating the electrode in paint, pushing the end of the electrode into molten glass[140], and covering the electrode with an epoxy or a wax[145,146]. Polishing any excess insulator away reveals an inlaid nanodisc electrode, set in a thick shroud of insulator. Nanoelectrodes made by wire etching tend to be sturdier and therefore easier for repeated use. However, some of the etching procedures can require the use of toxic materials (e.g. 6 M NaCN/0.1 M NaOH), complicating the use of this fabrication method.

Arrays of nanodiscs can also be prepared through electrodeposition into porous membranes (*e.g.* anodized aluminum oxide films or ion beam track etched films)[147,148]. However, nanodisc arrays are unsuitable for many of the applications detailed above, including the preparation of single nanopores.

### 1.5.2 Methods of characterising nanoelectrodes

Electrochemical techniques are commonly used to assess the dimensions and the surface properties of nanoelectrodes. For example, the steady state cyclic voltammetry of a redox compound can be recorded with nanoelectrodes and then assessed using Equation 1.27[130,149].

$$i_{lim} = 4nFDca \tag{1.27}$$

where $n$ is the number of electrons transferred in the redox reaction; $F$ is the Faraday constant; $D$ is the diffusion coefficient of the redox compound; $c$ is the bulk concentration of the redox compound; and $a$ is the radius of the electrode. This can be used to determine the radius of an unknown electrode, or to calculate the concentration and diffusion coefficient of an unknown redox compound. Without the presence of a redox compound, cyclic voltammetry can also reveal the nature of the surface in various conditions, showing currents associated with oxide formation and removal reactions, as well as any gas evolution reactions that can take place. Currents associated with the formation of monolayers and with double layer charging can help ascertain the electrochemical area of the nano-

electrode. Chronoamperometry can also be used to characterise nanoelectrodes, allowing the establishment of the hemispherical diffusion field to be studied, whilst scanning electrochemical microscopy can be used to distinguish between the conductive and insulative parts of the nanoelectrode surface.

Nanoelectrodes are also commonly characterised with microscopy techniques, such as electron microscopy, which can be used to take high resolution images of the nanoelectrode surface, and atomic force microscopy, which can generate a surface map for the nanoelectrode, featuring information about recesses, protruding wires, and poor glass-to-metal sealing.

## 1.6 Principles behind Coulter counting

Coulter counting (also known as resistive pulse sensing) is an electrochemical technique that uses a pore filled with electrolyte to detect and count particles suspended in solutions of the same electrolyte[150]. The principle behind this technique is that a particle entering the pore displaces the electrolyte and therefore reduces the possible ionic pathways through the pore[151]. The decrease in current caused by this event is used to identify when a particle has translocated through the pore. In order to record the current change induced by particle translocation, a potential is applied between electrodes in two reservoirs of electrolyte, which are separated by the electrolyte-filled pore. An example of this typical Coulter counting set-up is shown in Figure 1.21.

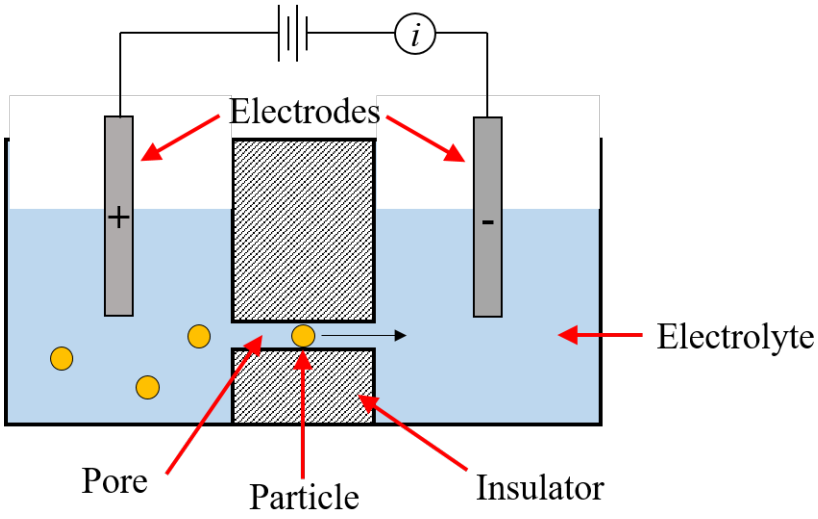


**Figure 1.21:** Typical design for a Coulter counting apparatus, in which two reservoirs of electrolyte are separated by a channel/pore, which is filled with the same electrolyte. The reduced dimensions of the pore cause it to restrict the current that can be passed between electrodes in each of the reservoirs. Particles are often kept in one of the reservoirs and are encouraged to translocate through the pore towards the other reservoir by means of a driving force.

The current that can be passed through a pore is already limited by its reduced dimensions, which give the pore its characteristic background resistance. The reduction of the ionic pathways induced by the presence of a particle increases the apparent resistance of the pore from its background value for the duration of a translocation. The decrease in current observed during particle translocation is a result of this temporary change in the

pore resistance, as illustrated in Figure 1.22.

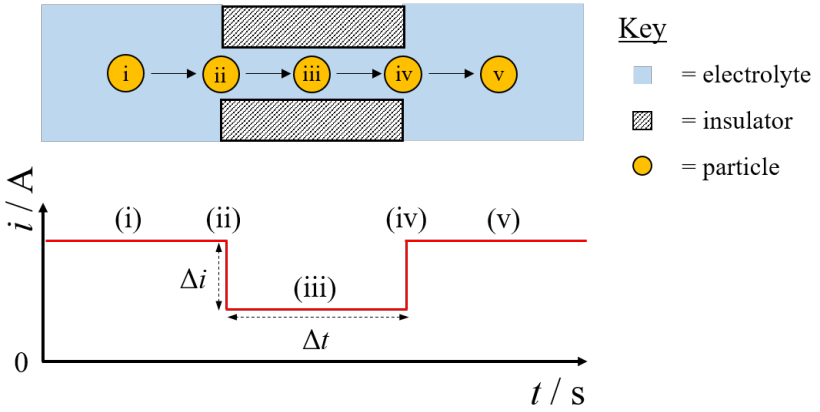


**Figure 1.22:** Example of how the signal obtained during particle translocation is observed in the current measured through a cylindrical pore. The background current is determined by the restrictive dimensions of the pore without the presence of a particle. However, upon entry of a particle into the pore, the electrolyte within the pore is displaced and the effective pore resistance increases. This results in a drop in the measured current, which is observed throughout the duration of the translocation. When the particle exits the pore, the resistance of the pore returns to its background value.

Changes in the pore resistance can be avoided by tuning the electrolyte conductivity so that it matches the conductivity of the particle. In this scenario, the particle will displace the electrolyte, but will not reduce the ionic pathways through the pore. This principle can also be used to increase the magnitude of the resistive change, making translocation events easier to observe. Furthermore, the number of translocations can be increased by applying a suitable driving force that forces particles to travel from one reservoir to the other. Common choices for this driving force include the use of a pressure differential across the pore to induce liquid flow[152], and the electrophoretic movement of charged particles under the applied potential[153]. The quantity and magnitude of translocation events can be used to characterise the particle suspension, as well as the pore.

### 1.6.1 Extracting information from particle translocations

Since the displacement of the electrolyte is based on the volume fraction of the particle in the pore, the magnitude of the change in pore resistance can be used to determine the particle size. The background resistance of a cylindrical pore can be calculated using Equation 1.28[154].

$$R_p = \rho \frac{L}{A} \tag{1.28}$$

where $R_p$ is the background pore resistance; $\rho$ is the solution resistivity; $L$ is the pore length; and $A$ is the cross-sectional area of the pore. The presence of a particle in the pore leads to an effective increase in the solution resistivity, so the resistance of the pore during translocation can be expressed as Equation 1.29.

$$R_t = \rho_{eff} \frac{L}{A} \tag{1.29}$$

where $R_t$ is the pore resistance during translocation and $\rho_{eff}$ is the effective resistivity of the electrolyte with a particle in the pore, which can be estimated using Maxwell's approximation, Equation 1.30.[154]

$$\rho_{eff} = \rho(1 + 3f/2 + \dots) \tag{1.30}$$

where $f$ is the volume fraction of the particle in the cylindrical pore. This can be calculated by dividing the volume of the particle by the volume of the pore, as shown in Equation 1.31.

$$f = \frac{2{d_p}^3}{3{D_p}^2 L} \tag{1.31}$$

where $d_p$ is the particle diameter and $D_p$ is the pore diameter. Equations 1.28 – 1.31 can

be combined to calculate the change in the pore resistance during translocation, as seen in Equation 1.32.

$$\Delta R = R_t - R_p = \frac{4\rho {d_p}^3}{\pi {D_p}^4} \tag{1.32}$$

where $\Delta R$ is the change in the pore resistance during translocation. This equation is not applicable when the particle diameter becomes comparable to the pore diameter, since the distortions in the electric field around the particle cause inaccuracies when in close proximity to the pore wall. DeBlois *et al.* modified Equation 1.32 to include a correction factor that modelled these distortions more accurately, as shown in Equation 1.33[154].

$$\Delta R = \left(\frac{4\rho {d_p}^3}{\pi {D_p}^4}\right)[1 + 0.73\left(\frac{{d_p}^3}{{D_p}^3}\right)] \tag{1.33}$$

This assumes that particles translocate exactly through the centre of the pore, and does not account for translocations when the particle is closer to one side of the pore[155]. Off-axis translocations would cause a slightly larger increase in the resistance change, but Equation 1.33 is a good approximation for the average translocation signal[156].

The concentration of a particle suspension can be determined from the number of translocations observed under the influence of a pressure differential driving force. The pressure applied to the pore induces a laminar flow of electrolyte, which for a cylindrical channel can be calculated by the Hagen-Poiseuille equation, a shown in Equation 1.34[157].

$$Q = \frac{\pi {r_p}^4 \Delta P}{8\mu L} \tag{1.34}$$

where $Q$ is the flow rate; $r_p$ is the channel radius; $\Delta P$ is the pressure differential across the channel; $\mu$ is the solution viscosity; and $L$ is the channel length. The number of translocations (particles $s^{-1}$) is divided by the flow rate (mL $s^{-1}$) calculated by Equation 1.34 in order to estimate the particle concentration. However, the chance of multiple particles translocating simultaneously increases at high particle concentrations and longer

pore lengths, limiting the application of this counting method.

The appearance of the translocation signal can also be used to provide further characterisation. The timescale of a translocation can reveal information about the particle speed (under pressure control) and particle charge (under electrophoretic control), whilst the shape of a translocation signal can provide details on the pore geometry.

### 1.6.2 Effects of the pore geometry

The shape and dimensions of a pore can severely impact the detection of translocating particles. For example, the change in pore resistance predicted by Equation 1.33 is proportional to the volume of the particle and inversely proportional to the volume of the pore. This means that a particle with a significantly smaller diameter than the pore it translocates through causes a negligible change in the pore resistance, presenting a lower detection limit for Coulter counting. Conversely, particles with diameters much larger than that of the pore cannot translocate, instead blocking the ionic pathways completely. Therefore, the greatest sensitivity in Coulter counting is achieved with pores that have slightly wider diameters than the particle of interest, as depicted in Figure 1.23

Nanopores are therefore required for the effective Coulter counting of nanoparticles and nanobubbles. The complete etching of nanoelectrodes is one method of obtaining suitable nanopores, but both the wire etching and the pipette pulling methods of fabricating nanoelectrodes result in the formation of nanopores with conical and exponential geometries[69,158]. Different geometries can affect the relationship between particle size and the change in pore resistance, as well as the shape of particle translocations. For example, the background resistance of a conical pore is determined by a different formula, which is shown in Equation 1.35[159].

$$R_p = \frac{1}{\kappa r_p}\left(\frac{1}{\pi \tan(\theta)} + \frac{1}{4}\right) \tag{1.35}$$

where $R_p$ is the pore resistance; $\kappa$ is the solution conductivity; $r_p$ is the pore radius; and

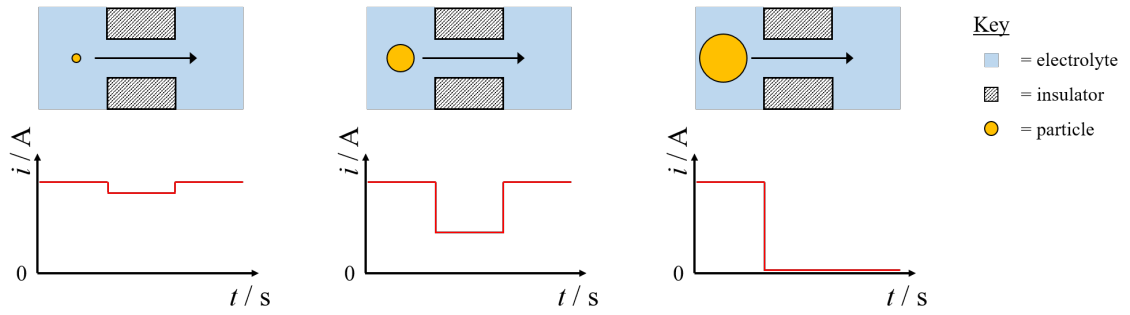


**Figure 1.23:** Example of how the signal obtained during particle translocation through a cylindrical pore can vary as a result of differing particle diameters. Particles that are much smaller than the pore (LEFT) result in a smaller volume fraction during translocation, which makes the change in the pore resistance negligible. Particles that are larger than the pore (RIGHT) block the pore rather than translocate through it, preventing current from being passed across the pore. In Coulter counting, the best sensitivity is obtained with a particle that is only slightly smaller than the pore (MIDDLE), resulting in a large volume fraction and ensuring the change in the pore resistance is large enough to be observed.

$\theta$ is the cone angle of the pore. Note that since this equation does not account for the length of the pore, it can only be used to estimate the magnitude of the background pore resistance. Furthermore, the change in pore resistance during translocation is more complicated to calculate for conical geometries, since the resistance of the pore changes as the particle travels through the pore. This is consistent with the observation of asymmetrical translocation shapes, as illustrated in Figure 1.24[160].

Therefore, the analysis of any particle translocations through a conical/exponential pore is more easily performed by comparison with simulations of the process. The number of translocations observed is also affected by the pore geometry, with conical geometries providing different flow rates, as estimated by Equation 1.36[161].

$$Q = \frac{3\pi r_p^3 \Delta P}{8\eta_l \cot(\theta)} \tag{1.36}$$

where $Q$ is the flow rate; $r$ is the pore radius; $\Delta P$ is the pressure differential; $\eta_l$ is the electrolyte viscosity; and $\theta$ is the cone angle of the pore. The smaller dimensions of nanopores

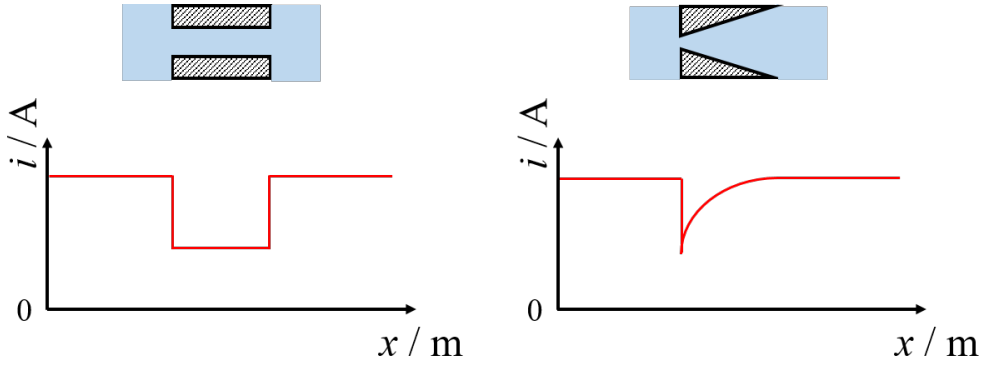


**Figure 1.24:** Example of how the signal obtained during particle translocation through a pore can vary as a result of differing pore geometries. Cylindrical pores (LEFT) have a large sensing zone spread out over the whole pore, which means the effective resistance of the pore remains constant throughout the duration of the translocation. Conversely, pores with conical and exponential geometries (RIGHT) have a smaller sensing zone concentrated at the mouth of the pore, meaning the effective resistance of the pore during translocation is greatest when the particle first enters the pore.

can result in significantly reduced flow rates, which can cause fewer translocations to be observed. Further complications come from the ion rectification near nanopores, which can result in electroosmotic flow that detracts from the flow induced by applied pressure. This effect becomes more significant when the cone angle of the conical pore becomes more acute. However, it should also be noted that small errors in the cone angles can result in the propagation of larger errors in Equations 1.35 and 1.36.

## 1.7 Influence of acoustic waves on nanobubbles

In Section 1.2, it was shown that the stability of a bubble could be compromised by the growth of the bubble due to internal gas pressure and the collapse of the bubble due to surface tension[12]. The growth of the bubble requires work to be done against the liquid, and would therefore need a driving force in order to occur[157]. Applying a sufficiently negative external static pressure to the liquid can drive the explosive growth of a bubble, provided the pressure exceeds the Blake threshold pressure for the bubble.

Acoustic waves can be applied to a liquid in order to induce sinusoidal pressure fluctuations rather than static pressure changes. If the pressure amplitude of the negative half cycle of the acoustic wave is sufficiently large enough that it exceeds the Blake threshold, then the explosive growth of existing bubbles, and the spontaneous formation of bubbles from pre-dissolved nuclei, can occur[12]. This process is known as acoustic cavitation and the minimum pressure amplitude of the acoustic wave required for this process is referred to as the cavitation threshold[12]. This process is exploited by ultrasonication, in which acoustic waves with frequencies typically above 20 kHz are applied to the liquid, allowing for the formation of microbubbles in the liquid[162,163]. However, the presence of acoustic waves also affects the bubble dynamics determined in Section 1.2.

### 1.7.1 Changes to the dynamics of a bubble under acoustic pressure

The presence of an ultrasonic acoustic wave changes the total pressure in the liquid, according to the relationship shown in Equation 1.37[12,164].

$$P_L = P_0 - P_A \sin(\omega t) \tag{1.37}$$

where $P_L$ is the pressure in the liquid at the bubble interface; $P_0$ is the hydrostatic pressure of the liquid; $\omega$ is the angular frequency of the acoustic wave; and $P_A$ is the pressure amplitude of the acoustic wave. When the terms inside the sine function are equal to zero (*i.e.* $t = 0$), the acoustic wave adds no pressure to the liquid, leaving the hydrostatic

pressure to keep the bubble at its equilibrium size. As the time progresses, the pressure amplitude reaches its minimum value during the negative half cycle of the acoustic wave, causing the total pressure of the liquid to drop below the cavitation threshold, and enabling the explosive growth of the bubble. Continued ultrasonication causes the pressure amplitude to reach its maximum value during the positive half cycle of the acoustic wave.

This pressure fluctuation causes the radius of a bubble to oscillate around its equilibrium value. If the frequency of the acoustic wave is high enough, or the pressure amplitude is low enough, then the distance amplitude of the bubble oscillation is small. In this case the bubble oscillates at the same frequency of the acoustic wave (*i.e.* linear oscillation). This is known as non-inertial cavitation, because the inertial forces of the liquid do not affect the bubble oscillation. If the distance amplitude of the bubble oscillation is large, then the inertial forces of the liquid oppose the bubble growth and the frequency of this oscillation starts to deviate from the frequency of the acoustic wave (*i.e.* non-linear oscillation). This is referred to as inertial cavitation and can result in the violent collapse of the bubble, typically occurring over one cycle of the acoustic wave. The dynamics of each of these processes can be determined by combining Equation 1.37 with Equation 1.25, which provides an updated version of the Rayleigh-Plesset equation that accounts for the pressure induced by the acoustic wave, as shown in Equation 1.38[12].

$$r\ddot{r} + \frac{3\dot{r}}{2} + \frac{4\mu\dot{r}}{\rho_l r} + \frac{2\gamma}{\rho_l r} + \frac{P_\infty + P_A \sin(\omega t) - p_g}{\rho_l} = 0 \tag{1.38}$$

where $r$ is the radius of the bubble; $\dot{r}$ is the radial velocity of the bubble interface; $\ddot{r}$ is the radial acceleration of the bubble interface; $\rho_l$ is the density of the liquid; $\mu$ is the kinematic viscosity of the liquid; $\gamma$ is the surface tension of the liquid; $P_\infty$ is the pressure in the liquid at an infinite distance from the bubble; and $p_g$ is the partial pressure of the gas in the bubble.

### 1.7.2 Non-inertial and inertial cavitation processes

The contraction experienced during the positive half cycle of the acoustic wave causes the compression of the gas inside the bubble, resulting in the diffusion of the gas out into the surrounding liquid. Similarly, the expansion during the negative half cycle causes gas to diffuse from the liquid into the bubble. Since the surface area of the bubble is greater when it is expanded, the total diffusion of gas between bubble and the liquid is rectified[12]. During the continuous application of acoustic pressure waves to the liquid, the bubble will expand and contract repeatedly, resulting in the increase of the gaseous contents of the bubble, and therefore an increase in the size[12,18]. This causes the equilibrium radius of the bubble to grow during the non-inertial cavitation process.

As this growth continues, the equilibrium radius of the bubble gets closer to its resonance radius, where the distance amplitude of the bubble oscillation will be at its greatest. For a given acoustic frequency, the resonance radius of a bubble can be determined using Equation 1.39

$$\rho_l {\omega_r}^2 {r_r}^2 = 3\sigma\left(P_0 + \frac{2\gamma}{r_r}\right) - \frac{2\gamma}{r_r} \tag{1.39}$$

where $\omega_r$ is the resonance frequency of the bubble; $r_r$ is the resonance radius of the bubble; and $\sigma$ is the ratio of specific heats of a gas. The large amplitude of the oscillations of a bubble at its resonance radius can provide conditions for the easier formation of surface waves on the bubble, which can cause phenomena such as microstreaming in the liquid and ejection of finer bubbles from the crests of the surface waves[12,18]. However, it can also cause an increase in the inertial forces acting on the bubble, causing the bubble to cross over the threshold for inertial cavitation.

A bubble transitioning from non-inertial to inertial cavitation will expand dramatically, often up to twice the size of its equilibrium radius, before violently collapsing, all within the timeframe of one full cycle of the acoustic wave. This event occurs when the bubble grows to an unstable radius or when the pressure amplitude of the acoustic wave is too large, as shown in Figure 1.25. Bubbles that can grow by rectified diffusion with-

out encountering their resonance radius are able to escape the solution by buoyancy, in a process known as degassing.

The collapse of inertial cavities causes energy from the acoustic wave to become localised in one area, resulting in the formation of large shockwave pressures and high gas temperatures. These extreme conditions cause interesting phenomena such as erosion, sonoluminescence and localised heating[12]. During the collapse, there is insufficient time for mass diffusion out of the bubble, meaning gaseous bubbles are slightly cushioned against their own collapse. Conversely, the rapid condensation of vapour means the collapse of vapour bubbles is generally more violent. The use of ultrasonication to form non-inertial cavities could result in the generation of observable bulk nanobubbles[37,38].

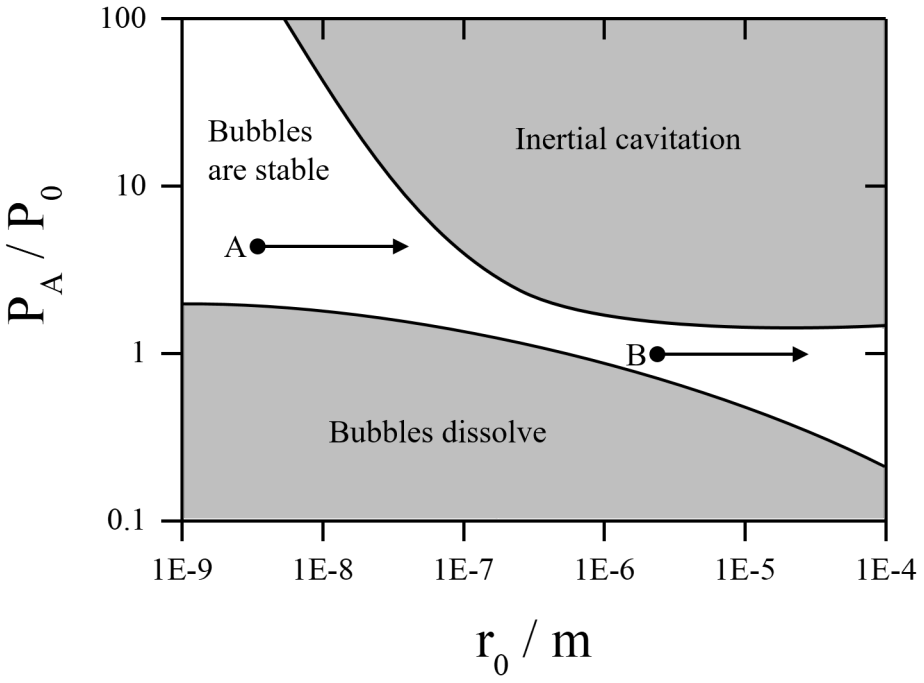


**Figure 1.25:** Relationship between the equilibrium radius of an air bubble in air-saturated water and the pressure amplitude of an acoustic wave driving the bubble at a frequency of 20 kHz. Sufficient pressure amplitudes will stabilise the bubble against dissolution, allowing it to undergo non-inertial cavitation. The rectified diffusion that occurs during this process causes the bubble to grow in size over several oscillation cycles. For a bubble at point B, this growth continues until the bubble escapes the liquid. However, for a bubble at point A, the growth will only continue until it reaches the inertial cavitation threshold, upon which the bubble will expand to several times its original size, then collapse into numerous smaller bubbles. Reproduced (adapted) from Reference 12 with permission from the original author, Reference 18. Copyright 1980, Elsevier B. V.

## 1.8 Structure of thesis

The remainder of this thesis consists of six chapters. Chapter 2 summarises the conditions used to record all of the experimental data and also details the procedures used to fabricate and characterise W microelectrodes, W nanoelectrodes and glass nanopores. The various apparatus used to record W electrochemistry and the Coulter counting of ultrasonically generated nanobubbles is also described, with reference to simplified circuit diagrams.

Chapters 3 – 5 present and discuss the experimental results obtained throughout the project. In Chapter 3, the electrochemical behaviour of W is examined using microelectrodes. This is used to design a procedure for fabricating W nanoelectrodes, which are then characterised using electrochemical techniques and electron microscopy. This chapter concludes with a discussion on the possible applications of W micro/nanoelectrodes.

Chapter 4 shows the characterisation of the apparatus designed to measure Coulter counting. Particle translocation through well-defined micropores is used to assess the abilities of the apparatus under various conditions. Several methods of recording translocations are described, including a differential method designed to increase sensitivity towards smaller particles/bubbles. The Coulter counting apparatus is later used to measure nanoparticle translocation through glass nanopores, prepared by the chemical etching of the W nanoelectrodes shown in Chapter 3.

In Chapter 5, the Coulter counting apparatus is applied to the study of ultrasonically generated nanobubbles through the nanopores prepared in Chapter 4. Translocations observed during the ultrasonication of electrolytes are attributed to transient nanobubbles, a claim which is supported by high-speed camera images of bubble motion around the pore. The oscillation of the bubbles during translocation is observed with the Coulter counter, and is linked to the acoustic waves within the electrolyte.

Chapter 6 gives a conclusion on the results shown in this thesis and highlights some possible future work. This is then followed by the references and an appendix.

# 2 Experimental details

## 2.1 Chemicals and materials

The following table lists the chemicals and materials that were used throughout the project. All chemicals were used as received unless noted otherwise.

**Table 2.1:** List of the chemicals and materials used throughout the project.

| Name | Formula | Purity | Supplier |
|---|---|---|---|
| **Electrolytes** | | | |
| Hydrochloric acid | HCl | 37% | Fisher Scientific |
| Hydrogen peroxide in $H_2O$ | $H_2O_2$ | 30% w/w | Fisher Scientific |
| Orthophosphoric acid | $H_3PO_4$ | 85% | Fisher Scientific |
| Potassium chloride | KCl | 99% | Fisher Scientific |
| Potassium persulphate | $K_2S_2O_8$ | 98% | Lancaster Synthesis |
| Potassium sulphate | $K_2SO_4$ | 99.5% | Fisher Scientific |
| Sodium hydroxide | NaOH | 97% | Fisher Scientific |
| Strontium nitrate | $Sr(NO_3)_2$ | 99% | Sigma Aldrich |
| Sulphuric acid | $H_2SO_4$ | 95–98% | Sigma Aldrich |
| Triton$^{TM}$ X-100 | $C_{14}H_{22}O(C_2H_4O)_{9-10}$ | 100% | Sigma Aldrich |
| **Redox Compounds** | | | |
| Potassium ferricyanide | $K_3Fe(CN)_6$ | 99% | Sigma Aldrich |
| Ruthenium hexaammine chloride | $Ru(NH_3)_6Cl_3$ | 99% | Strem Chemicals |

| Name | Formula | Purity | Supplier |
|---|---|---|---|
| **Micro/nanoparticles (all non-functionalised polystyrene spheres in $H_2O$)** | | | |
| $18.8 \pm 1.5$ $\mu$m Ø | | 2.6% w/v | Polysciences |
| $11 \pm 1.1$ $\mu$m Ø | | 2.5% w/v | Polysciences |
| $4.99 \pm 0.04$ $\mu$m Ø | | 0.3% w/v | ThermoFisher Scientific |
| $903 \pm 12$ nm Ø | | 1% w/v | ThermoFisher Scientific |
| $600 \pm 9$ nm Ø | $[-CH_2CH(C_6H_5)-]n$ | 1% w/v | ThermoFisher Scientific |
| $370 \pm 14.8$ nm Ø | | 2.5% w/v | Polysciences |
| $220 \pm 17.6$ nm Ø | | 2.5% w/v | Polysciences |
| $100 \pm 15$ nm Ø | | 2.5% w/v | Alfa Aesar |
| **Electrodeposition Solutions** | | | |
| ECF-60 with E3 Brightener | N/A | 99.99% | Metalor |
| **Microwires and Foils** | | | |
| Copper 40, 50 and 64 $\mu$m Ø | Cu | 99.9% | Advent Research Materials |
| Platinum 25 $\mu$m Ø | Pt | 99.99% | Advent Research Materials |
| Stainless steel AISI 316 (500 $\mu$m Ø) | $Fe/Cr_{18}/Ni_{10}/Mo_3$ | 99.9% | Advent Research Materials |
| Single core electrical wire 600 $\mu$m Ø | Sn/Cu | N/A | Rapid Electronics |
| Silver 500 $\mu$m Ø | Ag | 99.99% | Advent Research Materials |
| Tungsten 250 $\mu$m Ø | W | 99.95% | Advent Research Materials |
| Tungsten 25 $\mu$m Ø | | 99.95% | Advent Research Materials |
| Copper 12.5 $\mu m$ thick | Cu | 99.9% | Advent Research Materials |
| **Gases** | | | |

| | | | |
|---|---|---|---|
| Pureshield Argon | Ar | 99.998% | BOC |

The following consumables were also used in the preparation of W nanoelectrodes/glass nanopores:

**Polishing materials:** Silicon carbide paper (P80–1200) and alumina lapping film (5, 1, and 0.3 $\mu$m Ø) was purchased from 3M. Alumina polishing powders were purchased from Buehler (5 $\mu$m Ø and 0.05 $\mu$m Ø) and Struers (1 $\mu$m Ø and 0.3 $\mu$m Ø). Felt polishing pads were also purchased from Buehler.

**Glass capillaries**: Soda glass capillaries with an outer diameter of 2 mm and an internal diameter of 1.8 mm (G119/02) were purchased from S Murray and Co.. Borosilicate glass capillaries (PG52165-4) and 22% PbO glass capillaries (PG10165-4) with an outer diameter of 1.65 mm and an internal diameter of 1.1 mm were purchased from World Precision Instruments.

## 2.2 Preparation of tungsten microelectrodes

In order to examine the electrochemical properties of W surfaces, a procedure for fabricating W microelectrodes was developed. In this procedure, a portion of 25 $\mu$m W microwire was soldered into a Cu tube, which was made by rolling up a 1 cm$^2$ square of Cu foil (12.5 $\mu m$ thickness). The supporting 600 $\mu$m Ø single core electrical wire was soldered into the other side of the Cu tube, forming the electrical connection to the microwire. Note that directly soldering the W microwire to the supporting wire produced a less stable electrical connection. After this connection was tested with a continuity detector, the microwire ensemble was threaded through an open-ended soda glass capillary, until the end of the microwire was slightly protruding from the end of the capillary. Using a butane microtorch, the end of the capillary was heated until it melted around the microwire, sealing it in the process. The steps of this microelectrode fabrication procedure are illustrated in Figure 2.1.

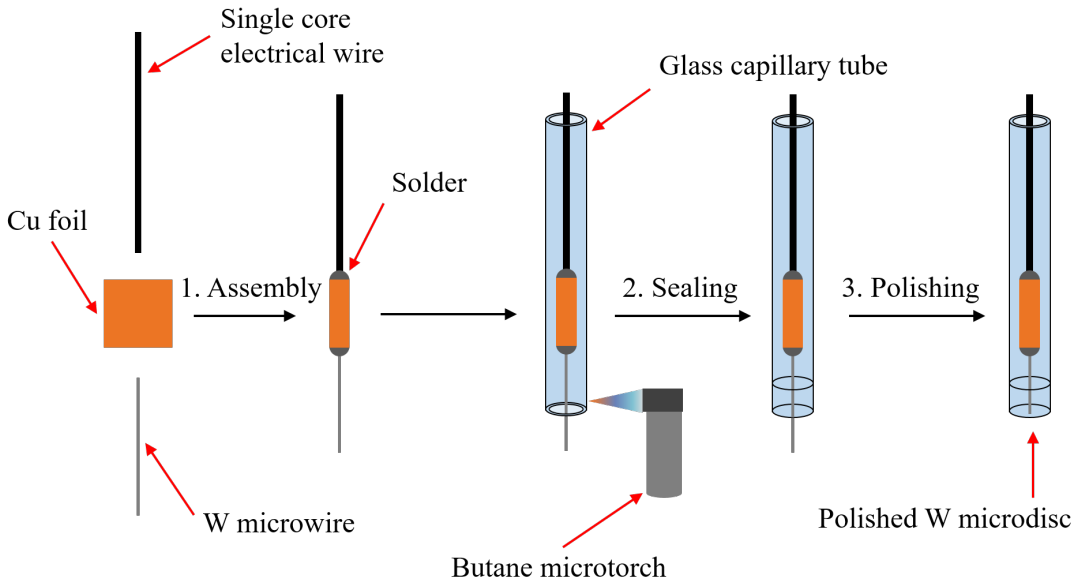


**Figure 2.1:** Procedure for fabricating W microelectrodes. A 25 $\mu$m Ø W microwire was soldered into one end of a copper tube, whilst a 600 $\mu$m Ø single core electrical wire was soldered into the other end. After inserting into an open ended glass capillary, the W microwire was sealed with a microtorch flame, then exposed by polishing on silicon carbide paper and alumina powder.

Subsequent polishing of the capillary removed the protruding W microwire and exposed an inlaid W microdisc electrode, set in a thick surround of glass. High grade silicon carbide paper (P600–P1200) was used roughly polish the capillary back to a desired area, whilst aqueous alumina slurries on felt pads (5, 1, and 0.3 $\mu$m Ø) were used to further minimise surface roughness of the electrode.

## 2.3 Preparation of tungsten nanoelectrodes

Nanoelectrodes were prepared using a wire etching procedure, in which the same 25 $\mu$m Ø W microwire/Cu tube ensemble prepared in section 2.2 was instead electrochemically etched in 2 M NaOH[158]. By applying a potential of +3.3 V to the W microwire, *vs.* a stainless steel ring counter electrode, the corrosive oxidation of the W microwire was encouraged. The loss of the $WO_4^{2-}$ ion during this oxidation allowed for the shaping of the microwire[158]. This eventually resulted in the formation of an unstable hourglass shape,

which was then transformed into a sharp W tip when the lower portion of the hourglass snapped in a so-called 'drop-off' event. The length of W microwire immersed in the NaOH solution was ≈ 3.5 cm, which provided enough weight to ensure that the lower portion of the microwire would detach properly in the 'drop-off' event.

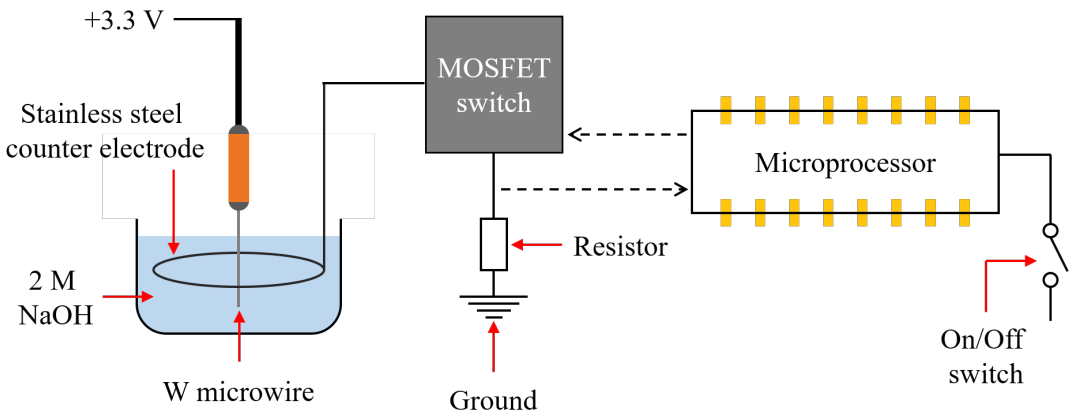


**Figure 2.2:** Illustration showing a basic view of the electrochemical W microwire etching circuit. The W microwire was held at +3.3 V *vs.* a stainless steel ring in a solution of 2M NaOH. The current recorded at the stainless steel counter electrode was passed through a MOFSET and then read by a microprocessor. After reaching a certain current value, the microprocessor sent a signal to the MOSFET, breaking the circuit and prevented further etching.

Etching of the W microwire after the 'drop-off' event would result in the blunting of the tip. In order to avoid this, a circuit was developed so that the etching was stopped once the 'drop-off' had occurred. In this circuit, the current from the counter electrode was passed through a MOSFET switch and read by a microprocessor, before going to ground through a resistor. This current was produced by the corrosive oxidation of the W microwire, which gradually declined as the surface area changed due to the dissociation of the $WO_4^{2-}$ ions. However, a large sudden drop in current was observed during the 'drop-off' event. This caused the current to pass through the cut-off value of 0.3 mA set on the microprocessor, which in turn rapidly switched off the MOSFET and prevented any more current from passing through the circuit. This resulted in the procurement of conical and exponential (tapering) W tips at their sharpest, where their tip diameters reached the nanometre scale. An illustration of the apparatus used to obtain these sharp W nanotips is shown in Figure 2.2.

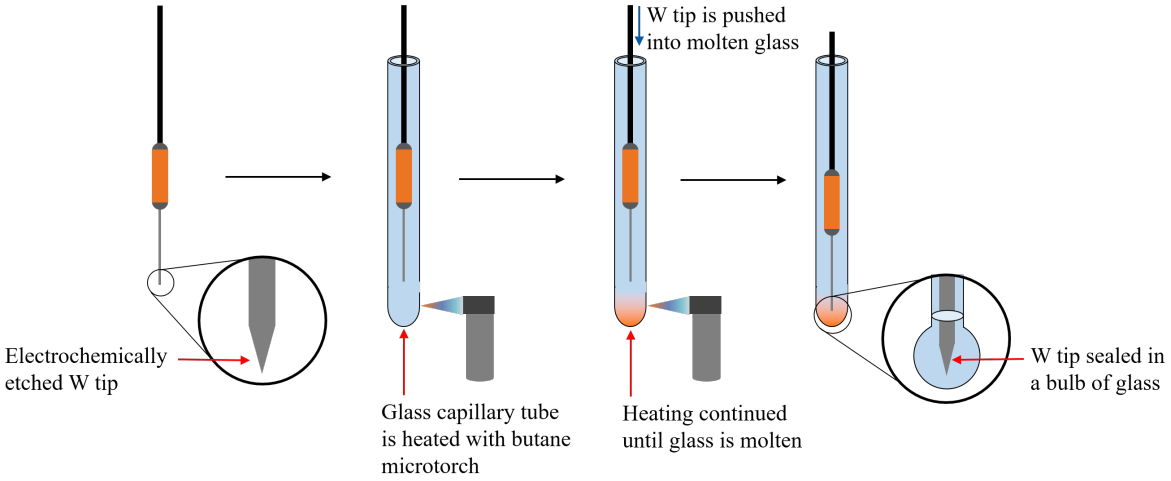


**Figure 2.3:** Procedure for fabricating W nanoelectrodes. After the electrochemical etching of W microwires had been used to prepare W nanotips, the nanotip-copper tube assembly was placed inside one half of a closed-end glass capillary. With the nanotip a safe distance away, the end of the capillary was heated with a microtorch flame until molten. This was indicated by an orange glow in the glass. At this point, the W nanotip was pushed into the molten glass with minimal damage, then allowed to cool before polishing.

After washing with deionised water and leaving to dry for 5 mins, the W tips were used to fabricate W nanoelectrodes, as shown by the procedure illustrated in Figure 2.3. In this procedure, the tip was carefully inserted into one half of a close-ended glass capillary, ensuring the tip was kept away from the sides and bottom of the capillary in order to avoid collision damage. A butane microtorch was used to heat the end of the capillary until it had become molten. At this point, the W tip was slowly pushed into the molten glass, sealing it in the process. Care was needed for this sealing step, as pushing the tip in too fast resulted in bubble entrapment in the glass, whilst pushing it in too slowly resulted in collision with the rapidly cooling glass, which blunted the tip.

Polishing away the excess glass yielded an inlaid W nanodisc electrode, surrounded by a thick shroud of glass. Low grade silicon carbide paper (P120 - P240) was used to remove the bulk of the excess glass, whilst the higher grade papers were used to finish the rough polish so that only a small layer of glass covered the nanodisc. The distance between the nanodisc and the polishing surface was assessed by optical microscopy of the electrode in water (this reduces the change in refractive index), which showed the reflection of the W

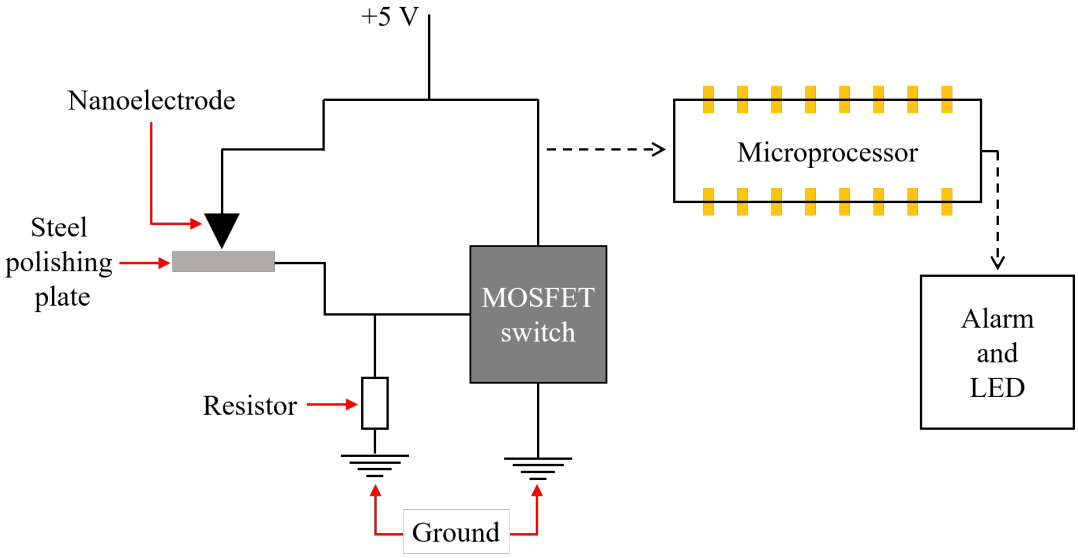


**Figure 2.4:** Illustration showing a basic view of the breakthrough circuit used to polish W nanoelectrodes until exposure. The W nanoelectrode is held at +5 V *vs.* a steel polishing plate, allowing current to be passed across the glass surface covering the W nanodisc. This current goes to ground through a resistor, until it is large enough to activate a MOSFET switch. Upon doing so, the current passes through the MOSFET switch, which has a lower resistance, and in doing so, a microprocessor reads the current and activates an alarm.

tip in the surface of the glass. When this distance was indistinguishable under a microscope, the polishing was finished on a 50 nm Ø alumina slurry in 1 M KCl. In order to determine the exact breakthrough moment in which the nanodisc was exposed, the polishing pad was mounted on a stainless steel plate and a continuity tester was attached to the nanoelectrode. The circuit which allowed this breakthrough to be monitored was based of the work by Zhang *et al.*, and is illustrated in Figure 2.4[69]. During the breakthrough polishing, all equipment and users were grounded in order to avoid any static discharge that could damage the nanoelectrode[165].

## 2.4 Tungsten electrode characterisation

Characterisation of the W micro/nanoelectrodes was mostly performed with electrochemical techniques, such as cyclic voltammetry. Most of the cyclic voltammetry exper-

iments were recorded with a custom built potentiostat, capable of recording down to a 1 pA current range. Cyclic voltammetry recorded at higher scan rates (0.2 – 5 V $s^{-1}$) was instead recorded on an Autolab PGSTAT30 from Metrohm, equipped with an ECD module that lowered the current range of this potentiostat to 100 pA. This potentiostat was also used to record the chronoamperometry of W micro/nanoelectrodes in 5 mM $Ru(NH_3)_6Cl_3$, as well as linear sweep voltammograms of the W microelectrodes in NaOH solutions. Chronoamperometry was also used to monitor the electrochemical W wire etching procedure, using an EA161 potentiostat connected to an ED201 current recorder (both from eDAQ).

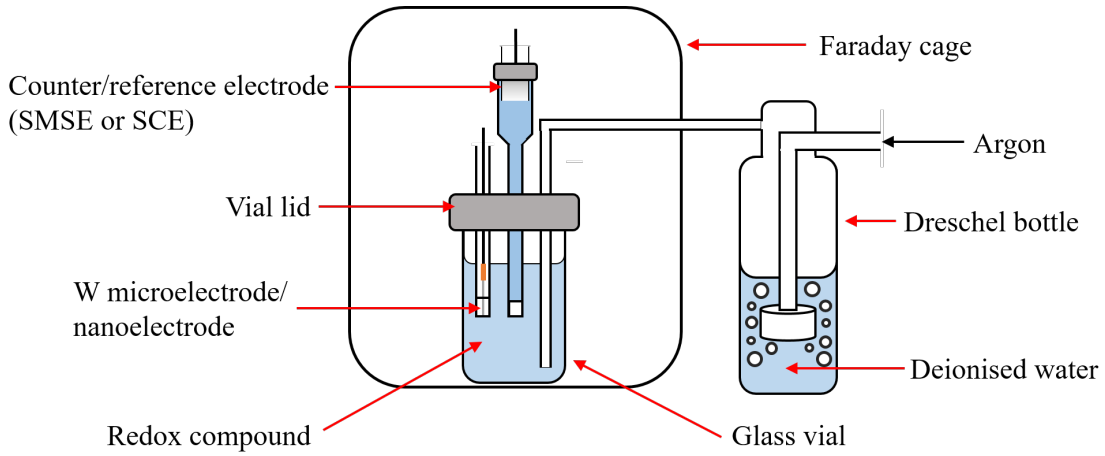


**Figure 2.5:** Design of the set-up used to record electrochemical measurements. A two electrode system was used, with a W working electrode and the counter/reference either being an SMSE, an SCE or an Ag/AgCl wire. These electrodes were placed into a vial containing the solution being examined, and secured in the lid of the vial. The solution was degassed using Ar gas that had been passed through a Dreschel bottle, filled with water. All measurements were taken inside a Faraday cage.

All electrochemical characterisation of the W electrodes was performed within a Faraday cage. This reduced the influence of nearby electrical noise, which was most significant at the lowest currents being recorded. Note that in order to exclude its own electrical noise, the potentiostat was kept on the outside of the Faraday cage. In the case of extremely small nanoelectrodes, the precautions taken were insufficient at minimising noise, providing the need to employ low-pass filters that removed the noise. The characterisation of W electrodes was recorded with a two electrode system, with the counter/reference being either a homemade saturated mercury/mercurous sulphate electrode (SMSE) in saturated $K_2SO_4$, or a homemade saturated calomel electrode (SCE) in saturated KCl. Solutions

being studied were purged with Ar in order to remove any oxygen. This Ar was first passed through a Dreschel bottle filled with deionised water in order to remove any particulates. An example of the set-up used to perform electrochemical characterisation is illustrated in Figure 2.5

Various microscopy methods were also used to study the W micro/nanoelectrodes. During microelectrode polishing, the surface roughness was monitored using a Nikon Eclipse LV100D optical microscope with 2–100× lens. Further characterisation was provided with a Jai digital camera attached to a 12× Navitar lens with 0.58–7× variable zoom and a 2× Navitar adaptor, which was used to examine the appearance of freshly etched W microwires and monitor the polishing progress of W microelectrodes and nanoelectrodes. During this process, the W electrodes were immersed in water in order to reduce the change in refractive index. Electron microscopy was used to study the fabrication of W nanoelectrodes at higher resolution. A JSM59 field emission gun scanning electron microscope (FEGSEM) from JEOL was used to characterise the dimensions of several electrochemically etched W tips, whilst an XL30 scanning electron microscope from Phillips was used to image the surface of W nanoelectrodes immediately after breakthrough.

## 2.5 Preparation and characterisation of pores

Glass nanopores were prepared through the complete chemical etching of W nanoelectrodes in a solution of 250 mM $K_2S_2O_8$ + 2 M NaOH. The corrosive oxidation of the W to $WO_4{}^{2-}$ removed the electrode material from the glass, leaving in its place a nanopore with a conical/exponential (tapering) geometry. This chemical etching step was used so that the W could be removed from both directions, by adding the solution into the capillary. The same chemical etching process was used on W microelectrodes in order to prepare 25 $\mu$m Ø cylindrical pores. However, larger micropores were prepared from a Cu chemical etching procedure (1 : 3 $H_2O_2$/HCl) on Cu microelectrodes. These Cu microelectrodes were prepared using the same procedure as detailed in section 2.2, but with 40, 50, and 64 $\mu$m Ø Cu microwires.

Pores generated by this chemical wire etching procedure were compared to pulled

pipettes, prepared using a PUL-100 vertical pipette puller from World Precision Instruments. This apparatus used a Pt heating element to soften the centre of a glass capillary, before pulling the ends of the capillary apart to create two identical pipettes. The dimensions of the resulting pore could be controlled through adjustment of the parameters on the puller, which included: the temperature of the heating element; the pulling force applied to the ends of the capillary; and the delay between the heating element stopping and the application of the pulling force.

Pores prepared through either method were characterised with both electrochemical and microscopy techniques. Electrochemical characterisation comprised of cyclic voltammetry in electrolyte solutions, which allowed the characteristic background resistance of the pore to be determined from the gradient of the resulting plot. This was performed in the same set-up as shown in Figure 2.5, except that the potential was instead applied between Ag/AgCl electrodes on the inside and outside of the pore. These Ag/AgCl electrodes were prepared by oxidation of 500 $\mu$m Ø Ag wires in 1 M KCl. Optical microscopy recorded with the Jai digital camera was used to examine the dimensions of micropores and to monitor the chemical etching progress of both micropores and nanopores. Simulations of the pores in COMSOL Multiphysics were compared with the voltammetry and microscopy, allowing the dimensions of micropores and nanopores to be confirmed. Examples of how these simulations were performed can be found in the appendix.

## 2.6 Apparatus for Coulter counting

Custom apparatus was required in order to record Coulter counting with glass micro/nanopores. This apparatus secured the pore in the sealed screw joint of a microelectrode holder, allowing the pore to be filled with electrolyte and held in a suspension of particles in the same electrolyte. Negative pressure differentials were applied to the pore using an inverted syringe, which drove the translocation of particles. Weights could be added onto a basket attached to the syringe plunger, allowing the magnitude of the pressure differential to be controlled. This pressure differential was gauged with a resolution of 1 mBar using an EBRO VM 2000 vacuum meter. Potentials of up to $\pm$5 V were applied by a direct voltage generator between Ag/AgCl electrodes inside the microelectrode holder

and in the particle suspension. All measurements were recorded within a Faraday cage, preventing any electrical noise from influencing the current recorded across the pore. An example of this apparatus is illustrated in Figure 2.6.

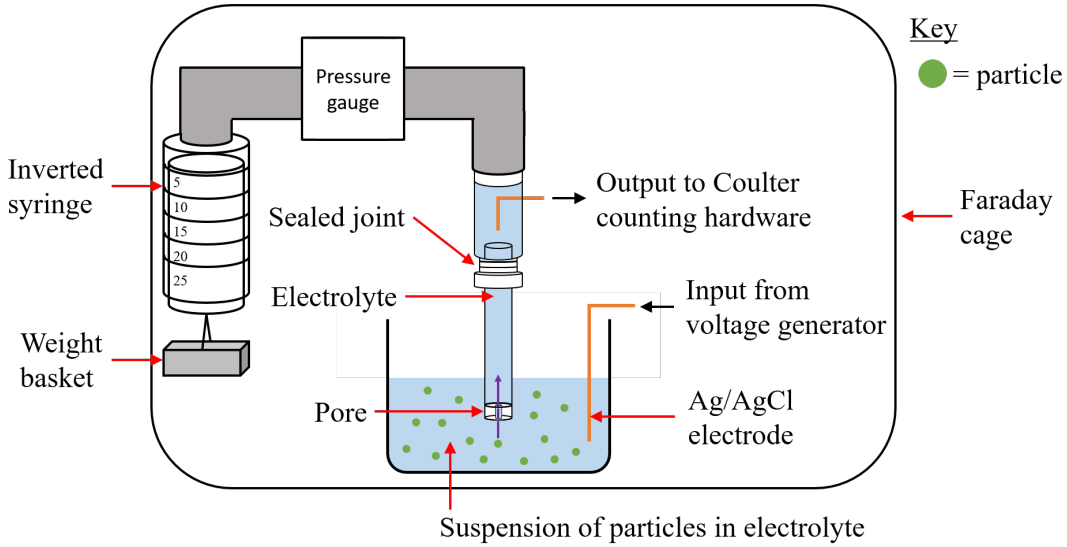


**Figure 2.6:** Illustration of the Coulter counting apparatus used to detect particle and bubble translocations. The pore is filled with electrolyte and placed in a particle suspension made with the same electrolyte. A screw joint is used to attach the pore to a pressure differential system. This consisted of an inverted syringe, with a small basket on the plunger allowing weights to be added for more pressure. Two Ag/AgCl wires are placed on either side of the pore, allowing a current to be passed across the pore.

The change in pore resistance induced by particle translocation was monitored using one of several homemade hardware systems. Each of these systems were battery powered, so as to avoid electrical noise from the mains power supply. The data from each of these systems was recorded using a 16 bit USB1608FS Plus 100 data acquisition card from Measurement Computing, which was capable of sampling data with a rate of 100 kHz. Data was then analysed using a program written for Microsoft Visual Basic 2010 software. The three hardware systems that were used to record Coulter counting signals are described below.

1. *Current follower system*: In this system, particle translocations were monitored using the change in current recorded across the pore. This current was fed into a simple current follower circuit, in which the output voltage could be amplified using a feedback loop in the operational amplifier. The value of the resistor in the feedback loop determined

the magnitude of this amplification, with gains of $10^4$ – $10^7 V/A$ available. Figure 2.7 shows the circuit for such a current follower system.

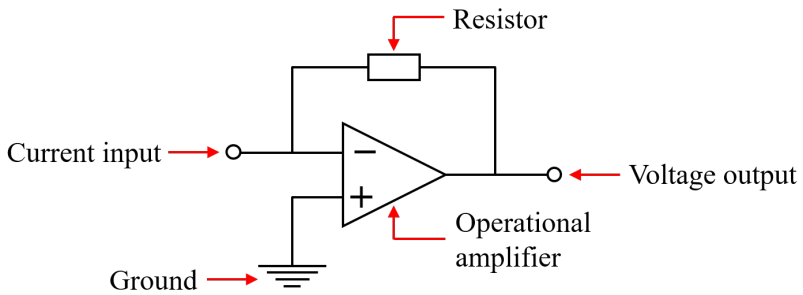


**Figure 2.7:** Illustration showing the basic view of a current follower circuit, used to record current transients through a pore during translocation. The current recorded through the pore is inputted into an operational amplifier, giving a voltage output that is converted back to current for viewing. A feedback loop is built by adding a resistor between the input and output, allowing the signal to be amplified by the gain of the resistor.

2. *Resistor bridge differential system*: This system differed in that the particle translocations were not monitored by the change in current, but by the effective change in the pore resistance. In order to record this change in pore resistance, a dummy resistor was placed in series with the pore, creating a resistor bridge. When the dummy resistor was similar in value to the background resistance of the pore, then the amount of applied voltage that was dropped over each resistor was the same, and the sensing voltage in between the resistor bridge was half that of the applied voltage. During particle translocation, the effective resistance of the pore increased, causing the sensing voltage to temporarily drop[151]. This sensing voltage signal was directed to a differential signal generator, as shown in Figure 2.8.

In the differential signal generator, the sensing voltage signal was split into two channels, A and B. Channel B was deliberately delayed using a low-pass bandwidth filter, causing the high frequency components of the signal to appear rounded. Meanwhile, the signal in channel A was left unfiltered, causing it to retain its high frequency components. When the signal from the delayed channel was subtracted from the signal of the unfiltered channel (*i.e.* $V_A - V_B$), a characteristic differential signal was obtained, as shown in Figure 2.9. This signal could be amplified by up to $10^3$ V/V, but this also amplified any offset and background noise. Therefore, a self-servoing system was used to subtract a heavily filtered

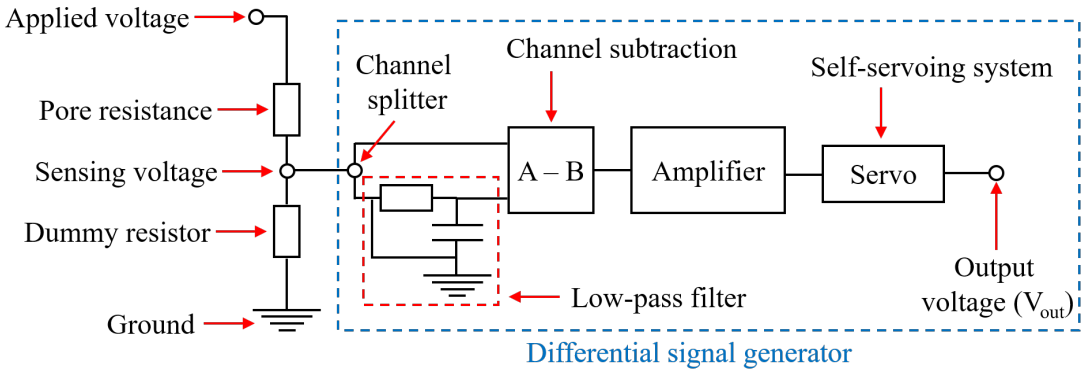


**Figure 2.8:** Illustration showing the basic view of the resistor bridge differential system circuit, used to record differential transients through a pore during translocation. The applied voltage goes to ground, passing through the pore and a dummy resistor on its way. By matching the dummy resistor to the resistance of the pore, half of the applied voltage is dropped over the pore, but in the case of a particle translocation, almost all the voltage is dropped over the pore. This results in a voltage pulse between the two resistors, which is then split into two channels. One of these channels is filtered to slow it down and then subtracted from the other. After amplification and subtraction of a heavily filtered pulse to remove noise, the output signal is obtained.

differential signal from the amplified differential signal, reducing the noise and centering the signal around 0 V.

The conversion of this differential voltage signal into the change in pore resistance can be accomplished using Equation 2.1.

$$\Delta R = \frac{{\theta_R}^2 V_{out}}{\xi V_{app} R_d X_{DiS}} \tag{2.1}$$

where $\Delta R$ is the change in pore resistance; $R_d$ is the resistance of the dummy resistor; $\theta_R$ is the combined resistance of the resistor bridge; $V_{app}$ is the voltage applied to the electrodes; $X_{DiS}$ is the gain of the differential signal amplification; $\xi$ is a factor to correct for loss in instrument sensitivity, and was estimated to be 1.36 in this work[151]; and $V_{out}$ is the output voltage of the differential system. The derivation of Equation 2.1 can be found in the appendix and in Reference 151. The correction factor, $\xi$, was estimated by

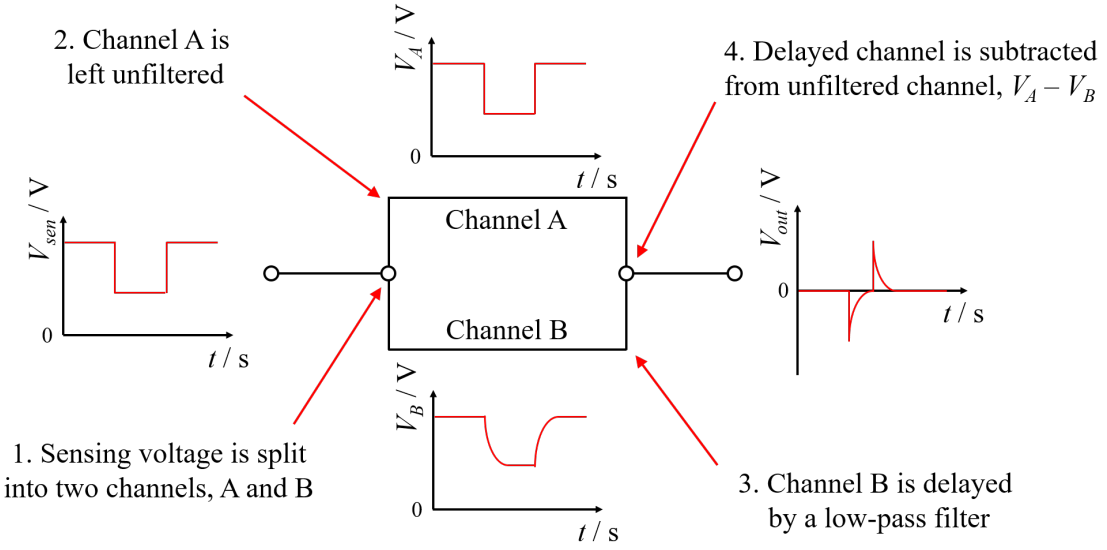


**Figure 2.9:** Process by which a square wave voltage signal is transformed into an amplified differential voltage signal. The voltage signal is split into a fast and a slow channel, the latter of which consists of a low-pass filter that distorts the high frequency components of the square wave. Subtraction of the slow wave from the fast wave results in a voltage signal with the differential shape.

dividing the expected $V_{out}$ value by the actual $V_{out}$ value obtained during calibration with a waveform generator. Note that in all the cases shown in this work, a 470 kΩ dummy resistance was used.

3. *Current differential system*: This system combined the other two systems, allowing both the current and the differential signal to be recorded. Instead of using a resistor bridge, the output voltage of a current follower was directly fed into the differential signal generator. The differential signal could be amplified up to $10^3$ V/V, and the current follower signal could be amplified by $10^6$, $10^7$ and $10^9$ V/A. However, the use of the $10^9$ V/A amplification resulted in the electronic filtering of the signal, causing the high frequency components to become slightly delayed. As this would interfere with the differential channel subtraction, a circuit for correcting this delay was included, as shown in Figure 2.10[166].

In this correction circuit, the output voltage of the current follower was split into two channels. In one of the channels, the signal was left unaltered, whilst the signal in

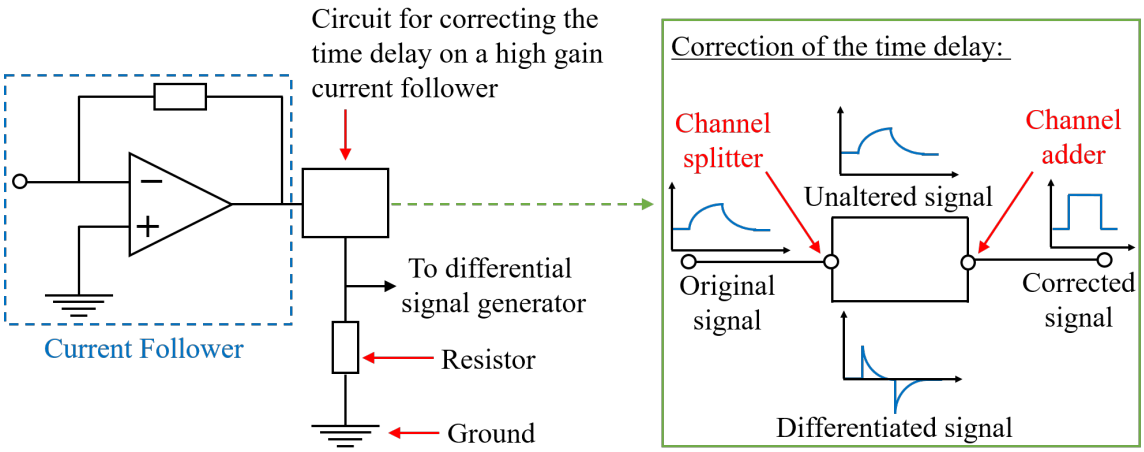


**Figure 2.10:** Illustration showing the basic view of the current differential system circuit, used to record differential transients through a pore during translocation. In this circuit, the signal inputted into the differential signal generator comes from a current follower rather than a resistor bridge. In the cases of high current follower amplifications, the signal may already be delayed. This is corrected by splitting the channel into two, differentiating one of the channels and then adding it to the other to return the expected undelayed voltage pulse.

the other channel was differentiated. Adding the two signals together corrected the time delay so that the output of the current follower could be fed into the differential signal generator. The output differential voltage signal could then be converted into the change in pore resistance using Equation 2.2.

$$\Delta R = \frac{R_p{}^2 V_{DiS} \xi}{V_{app} R_{CF} X_{DiS}} \tag{2.2}$$

where $\Delta R$ is the change in pore resistance; $R_p$ is the background resistance of the pore; $\xi$ is a factor to correct for loss in instrument sensitivity, and was taken to be as 1.21; $V_{app}$ is the voltage applied to the electrodes; $R_{CF}$ is the value of the resistor in the current follower feedback loop; $X_{DiS}$ is the gain of the differential signal amplification; and $V_{DiS}$ is the output voltage of the differential system. The derivation of Equation 2.2 can be found in the appendix. The correction factor, $\xi$, was estimated by dividing the expected $V_{DiS}$ value by the actual $V_{DiS}$ value obtained during calibration with a waveform generator. However, it should be noted that an error in the design of this system occasionally caused

misalignment between the gain of the amplification and the value of the dial used to select this gain. As a result, the gains reported for several figures were an order of magnitude smaller than the gains that were actually used. This error was easily identified by comparison to the current output, but a note of this error is made in each of the appropriate figure captions.

## 2.7 Ultrasonication generation of nanobubbles

The application of ultrasonic waves to electrolyte solutions was used to generate microbubbles and nanobubbles. The ultrasonic waves were provided using a 3.2 mm Ø titanium piston-like emitter (PLE) which was powered using a Microson XL2007 ultrasonic cell disruptor from Misonix Inc.. Ultrasonication of the electrolytes was driven at $22-24$ kHz, using various output powers as reported in the appropriate figure captions. An ABS thread between the tip and transducer of the PLE was used to minimise electrical noise from the ultrasonication. The tip of the PLE was usually immersed in the electrolyte solution by 5 mm, and a glass reflector was placed typically 2.5 mm below the tip of the PLE. This reflector was found to increase the quantity and reproducibility of microbubbles generated below the PLE. The height of the reflector could be adjusted using a SQ16 joint in the bottom of the cell containing the electrolyte. An illustration of this ultrasonication cell is shown in Figure 2.11

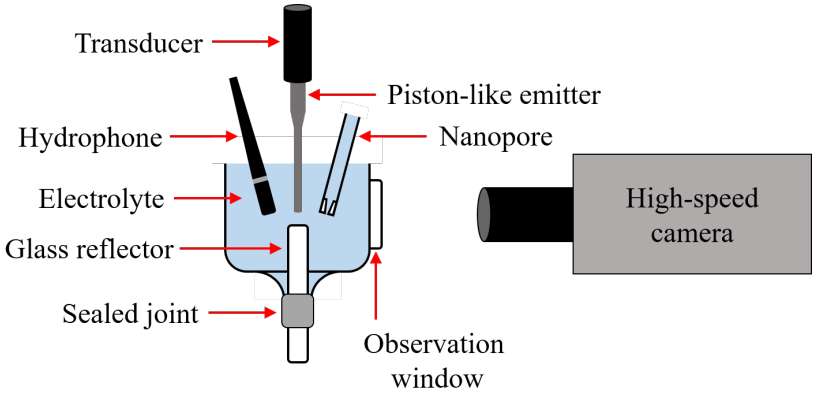


**Figure 2.11:** Illustration showing the set-up for recording the Coulter counting of ultrasonically generated nanobubbles. An ultrasonic piston like emitter is held above a glass reflector in electrolyte, and by applying electrical power to the transducer, generates bubbles that are trapped onto the reflector surface. The ultrasonication process can be recorded using a hydrophone held level with the PLE and the translocation of nanobubbles can be monitored using a nanopore held near the PLE. An observation window allowed images to be recorded with a high-speed camera.

Translocation of bubbles was achieved using the same Coulter counting apparatus shown in Figure 2.6. Micropositioners were used to place the micro/nanopore level with the horn, at a horizontal distance of 1–4 mm. A Reson TC4013 hydrophone, held level with the horn at a horizontal distance of $\approx$ 5 mm, was used to monitor the acoustic pressures within the cell during ultrasonication. High-speed camera videos of the bubble formation and translocation were recorded through a flat quartz window in the cell using a Fastcam-APX RS high-speed camera from Photron. This camera was fitted with a 12$\times$ Navitar lens with 0.58–7$\times$ variable zoom and a 67$\times$ Navitar adaptor. Images from the camera were analysed using Photron Fastcam Viewer ver. 3391 software.

# 3 Fabrication of tungsten nanoelectrodes

The complete etching of nanoelectrodes is a convenient route to obtaining the nanopores required for Coulter counting[127,128,167], making the fabrication of nanoelectrodes an important step in the detection of nanobubbles. For eventual conversion to nanopores, it is preferable to fabricate nanoelectrodes with a wire etching method rather than a pipette pulling method, since the thick surround of glass makes the nanopores prepared in this way sturdier and therefore easier for repeated use. The formation of such nanopores has been demonstrated by Zhang *et al.*, who produced well-defined Pt nanoelectrodes from an electrochemical wire etching procedure, then electrochemically etched the Pt away to obtain robust glass nanopores[167]. They used the wire etching procedure to form conically shaped Pt tips, which were shown in electron microscope images to have diameters as low as 20 nm. After sealing these tips in molten glass and then polishing until exposure, they obtained an inlaid Pt nanodisc electrode. The electrochemical response of this electrode was assessed before formation of the nanopore, providing an opportunity to characterise the electrode dimensions for later comparison with the nanopore characterisation. An illustration of how the wire etching procedure leads to the formation of nanopores is shown in Figure 3.1.

Electrochemical etching of Pt nanoelectrodes has been reported with both aggressive conditions (*i.e.* 6 M NaCN + 0.1 M NaOH)[69], and relatively benign conditions (*i.e.* 15–20% $CaCl_2$)[160,168]. Similar wire etching procedures are available for other noble metals, but could also be used to obtain W nanoelectrodes. Since W is not a noble metal, it is more susceptible to dissociative corrosion and therefore requires less aggressive etching conditions[169]. The electrochemical etching mechanism of W has been extensively studied and is often used in the preparation of scanning tunneling microscopy tips[158]. W also offers desirable physical properties for nanoelectrode fabrication, such as a high mechanical strength, a high melting point and a low thermal expansion coefficient[170]. These factors make W an attractive alternative to the use of Pt in wire etching procedures.

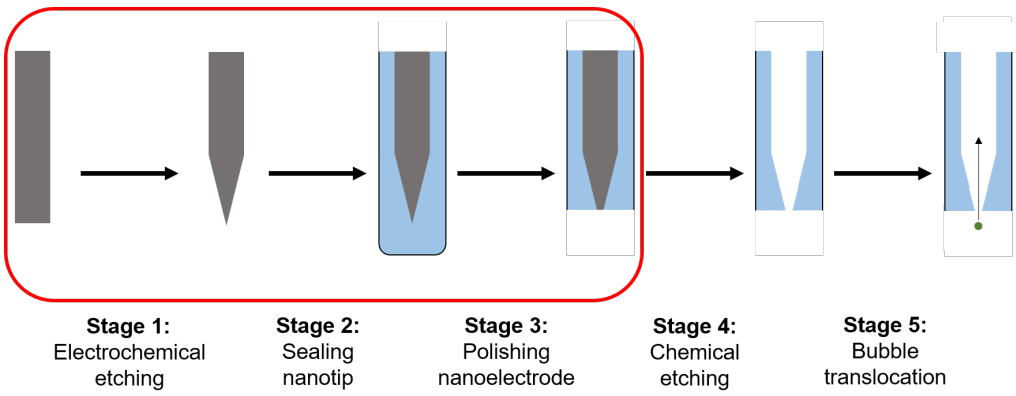


**Figure 3.1:** Stages in the project required to record the Coulter counting of nanobubbles. The focus of this chapter, highlighted by the red box, is a discussion on the preparation of W nanoelectrodes, and their subsequent characterisation, as a precursor to the nanopores needed for Coulter counting.

In this chapter, the fabrication of W nanoelectrodes is reported and the subsequent characterisation of these nanoelectrodes is shown. The properties of the W nanoelectrodes are discussed, and some possible applications for W electrodes are also examined. This discussion is accompanied by a basic study of W electrochemistry, covering the surface processes and potential limits exhibited by W microelectrodes.

## 3.1 Electrochemical stability of tungsten and its oxides

Metals form oxides through either passive or corrosive oxidation reactions[169]. Passivation leaves the surface of the metal intact, allowing the metal to be regenerated by the subsequent reduction of the oxides. On the other hand, corrosion results in the irreversible loss of material, due to the dissociation of the oxides from the surface. For this reason, wire etching procedures often involve the use of chemical or electrochemical corrosion reactions. Since W is not a noble metal, it is more susceptible to corrosion, which is more convenient for wire etching procedures[169]. The electrochemical corrosion and passivation reactions of W are described in the Pourbaix diagram of W, shown in Figure 3.2[171].

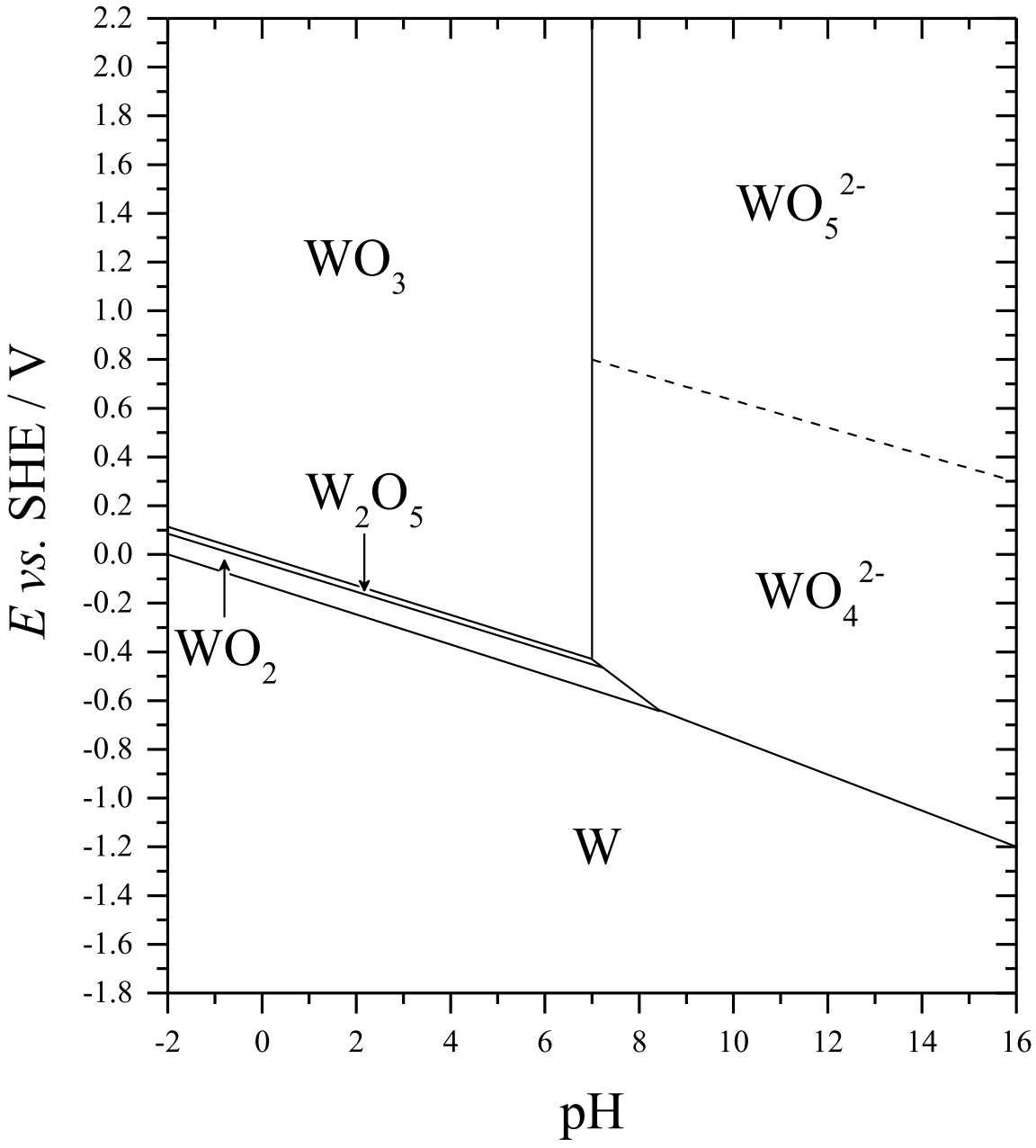


**Figure 3.2:** Pourbaix diagram of W in aqueous solutions, showing the electrochemical stability of W and its oxides with respect to the applied potential and the solution pH. Each region of the diagram depicts a different phase of W, with the boundaries between the regions indicating the conditions for an electrochemical reaction. The existence of the $WO_5^{2-}$ state has not been confirmed, but the dashed boundary predicts the conditions required for its formation. Reproduced (adapted) using the original Pourbaix diagram from reference 171.

The Pourbaix diagram in Figure 3.2 can be used to describe the electrochemical stability of W and its oxides in aqueous solutions. Each region of the diagram represents a different phase of W and the conditions where each phase is stable. At the boundary between two regions, the electrochemical surface reaction between the two corresponding phases will occur. The conditions for such a reaction, and therefore the stability of each phase, varies with the solution pH and the potential applied to the W surface.

With the application of sufficiently negative potentials, a W surface can be constantly kept in its reduced phase. Note that this occurs regardless of the solution pH, but that the potential needed to keep W in its reduced phase becomes more negative as the solution becomes more alkaline. However, the application of more positive potentials can cause oxidation of the W surface, and the solution pH then dictates the nature of the oxide formation. In solutions below pH 7, the oxidation of W is passive and can result in the formation of several different oxide compounds depending on the applied potential.

$$\mathrm{W} + 2\,\mathrm{H_2O} \rightleftharpoons \mathrm{WO_2} + 4\,\mathrm{H^+} + 4\,\mathrm{e^-} \tag{3.1}$$

$$2\,\mathrm{WO_2} + \mathrm{H_2O} \rightleftharpoons \mathrm{W_2O_5} + 2\,\mathrm{H^+} + 2\,\mathrm{e^-} \tag{3.2}$$

$$\mathrm{W_2O_5} + \mathrm{H_2O} \rightleftharpoons 2\,\mathrm{WO_3} + 2\,\mathrm{H^+} + 2\,\mathrm{e^-} \tag{3.3}$$

The W metal is initially passivated to form $WO_2$, as shown in Equation 3.1. This oxide is only stable over a short potential window, but its stability does extend slightly above pH 7. Further oxidation of $WO_2$ yields the $W_2O_5$ compound, as shown in Equation 3.2. This compound is unstable and is quickly oxidised to form the final passivation product, $WO_3$, as shown in Equation 3.3. $WO_3$ is a metal oxide semiconductor, with a highly tuneable structure and an ability to withstand large oxygen vacancies, making it appropriate for applications in photocatalysis and electrochromic devices[172,173]. The overall passivation of W is displayed in Equation 3.4. Each of the passivation products has slightly different physical properties, which could affect the electrochemical response of W electrodes, but the processes shown in Equations 3.1-3.4 are reversible, and the W

electrode can be regenerated through application of a reduction potential.

$$\mathrm{W} + 3\,\mathrm{H_2O} \rightleftharpoons \mathrm{WO_3} + 6\,\mathrm{H^+} + 6\,\mathrm{e^-} \tag{3.4}$$

In solutions above pH 7, the oxidation of W is corrosive, resulting in the dissociative formation of the $\mathrm{WO_4}^{2-}$ ion, as shown in Equation 3.5. Further oxidation may yield another corrosion product, the $\mathrm{WO_5}^{2-}$ ion, but details around the formation of this compound were omitted from Pourbaix's research, due to difficulties in confirming its existence. The process shown in Equation 3.5 is irreversible and results in the loss of material, which is then exploited in electrochemical etching procedures.

$$\mathrm{W} + 4\,\mathrm{OH^-} \longrightarrow \mathrm{WO_4}^{2-} + 4\,\mathrm{H^+} + 6\,\mathrm{e^-} \tag{3.5}$$

Any of the passivation products formed in Equations 3.1-3.4 can also react further to form the corrosion product, $\mathrm{WO_4}^{2-}$. This is usually brought about by a change in the solution pH and can be expressed by Equations 3.6-3.7. These processes are also irreversible, due to the dissociation of the $\mathrm{WO_4}^{2-}$ ion.

$$\mathrm{WO_2} + 2\,\mathrm{OH^-} \longrightarrow \mathrm{WO_4}^{2-} + 2\,\mathrm{H^+} + 2\,\mathrm{e^-} \tag{3.6}$$

$$\mathrm{W_2O_5} + 3\,\mathrm{OH^-} \longrightarrow 2\,\mathrm{WO_4}^{2-} + 3\,\mathrm{H^+} + 6\,\mathrm{e^-} \tag{3.7}$$

$$\mathrm{WO_3} + \mathrm{OH^-} \longrightarrow \mathrm{WO_4}^{2-} + \mathrm{H^+} \tag{3.8}$$

Other oxides are possible, including hydrated oxides such as $\mathrm{WO_3 \cdot H_2O}$ and $\mathrm{H_2WO_4}$, but these have also been omitted from Pourbaix's research due to a lack of data.

## 3.2 Electrochemical characterisation of tungsten

The properties of W electrodes need to be well understood before attempting to fabricate nanoelectrodes. The Pourbaix diagram shown in Figure 3.2 describes some of the surface processes that can occur on W electrodes, but does not provide information on characteristics such as the electrical properties of each phase, or the potential range over which W can be used in various solvents. These properties have an important effect on the electrochemical characterisation of W and need to be studied further, in this case with cyclic voltammetry on W microelectrodes.

The potential range of an electrode material is usually limited by the breakdown of the solvent, which occurs at the electrode under application of a sufficiently high potential[174]. In aqueous solvents, this process results in the electrolysis of water and the evolution of $H_2$ and $O_2$ gas at opposing electrodes, as show in Equations 3.9 + 3.10[130]. Gas evolution forms bubbles that can roughen the surface of the electrode and also results in large currents which overshadow the electrochemistry of interest, so electrodes are often only used within the potential limits set by this process.

$$2\,H^+ + 2\,e^- \longrightarrow H_2 \tag{3.9}$$

$$2\,H_2O \longrightarrow O_2 + 4\,H^+ + 4\,e^- \tag{3.10}$$

The potential limits set by gas evolution differ for each electrode material, with some metals showing catalytic behaviour towards these processes[175]. Cyclic voltammetry was recorded in various aqueous solutions on W microelectrodes in order to determine the potential limits of the electrode material and establish the relationship between gas evolution and solution pH.

In each of the solutions, $H_2$ evolution was observed at cathodic potentials. The onset potential of this process varied with the pH value, in accordance with the Nernst equation[130]. At acidic pH values, shown in Figure 3.3A, the onset of $H_2$ evolution was seen at $-1$ V *vs.* SMSE, which is far more negative than the onset of $H_2$ evolution recorded

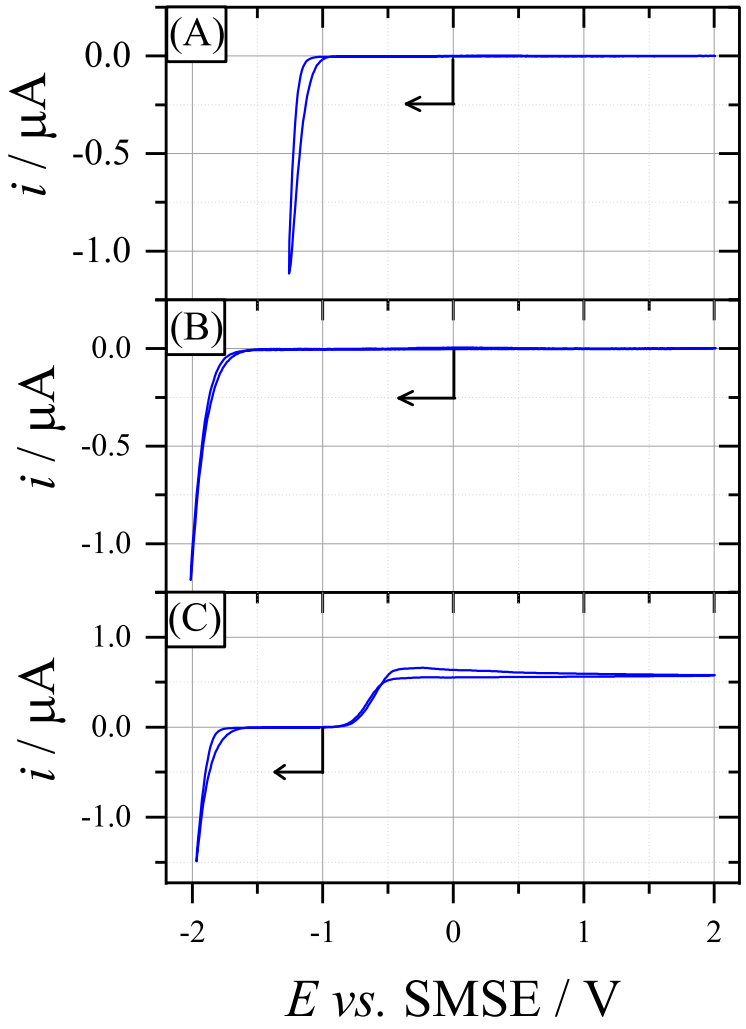


**Figure 3.3:** Cyclic voltammograms recorded at 50 mV $s^{-1}$ with a 25 $\mu$m Ø W microelectrode in anaerobic solutions of: (A) 100 mM $H_2SO_4$ (pH 1); (B) 100 mM $K_2SO_4$ (pH 7); and (C) 100 mM NaOH (pH 13). The arrows indicate the initial potential and the scan direction of each voltammogram.

on Pt electrodes (−0.7 V *vs.* SMSE). As shown in Figure 3.3B+C, similar observations were made at neutral and alkaline pH values, with the onset of $H_2$ evolution starting at −1.5 V *vs.* SMSE. No evidence of $O_2$ evolution was seen in any of the solutions, even after cycling to potentials of +4 V *vs.* SMSE. One possible explanation is that upon increasing the positive potential, the W electrode was oxidised to $WO_3$, which has a much lower conductivity and therefore detracts from the voltage applied to drive the $O_2$ evolution process. This gives W a much wider potential window than is seen on Pt electrodes.

The voltammograms recorded in alkaline solutions exhibited an oxidation wave starting at −0.7 V *vs.* SMSE, which coincided with the boundary between the W and $WO_4^{2-}$

phases observed in Figure 3.2. This oxidation wave appeared to plateau, but after closer inspection the current of the plateau seemed to decrease over time. Subsequent cycles had similar oxidation waves, but with lower currents. This suggested that the oxidation wave was caused by the corrosion of the W microelectrode, with the dissociative loss of material responsible for the declining current. The electrochemical corrosion reaction in Equation 3.5 relies on the transport of hydroxide ions to the electrode surface, which has been observed to be a diffusion controlled process on Au, Pt and Ni microdisc electrodes[174,176]. The limiting current of the oxidation wave, $i_{lim}$, can therefore be used to calculate the concentration of hydroxide ions in solution, using Equation 3.11[130,149].

$$i_{lim} = 4nFDca \tag{3.11}$$

where $n$ is the number of electrons transferred; $F$ is Faraday's constant; $D$ is the diffusion coefficient; $c$ is the concentration; and $a$ is the electrode radius. Using the limiting current of the oxidation wave in Figure 3.3C, and assuming that $n = 1$, $D = 5.6 \times 10^{-5}$ cm$^2$ s$^{-1}$[174], and $a = 12.5$ $\mu$m, the concentration of $OH^-$ ions was calculated as $\approx 25$ mM. This value was 4$\times$ smaller than the real concentration of NaOH (100 mM), which was possibly a result of damage to the electrode during cycling in the $H_2$ evolution region. As will be shown later, the limiting currents recorded without cycling in the $H_2$ evolution region showed good agreement with the theoretical currents derived from Equation 3.11, confirming the oxidation process was indeed W corrosion. The electrochemical detection of this corrosion process has been reported on rotating W disc electrodes[175], and linked to the diffusion of $OH^-$ ions towards the W surface[177]. However, the steady state oxidation of $OH^-$ ions on W microelectrodes has not been reported, and could be exploited to measure the pH of alkaline solutions, which will be discussed in more detail later.

The electrochemical characterisation of W electrodes was therefore performed in acidic solutions and confined to within the negative potential limit set by $H_2$ evolution ($-1$ V *vs.* SMSE in pH 1). The background surface processes of W microelectrodes under these conditions were recorded by cyclic voltammetry in 100 mM $H_2SO_4$, as shown in Figure 3.4.

The W microelectrodes were cycled between $-1$ and $+1$ V *vs.* SMSE until repro-

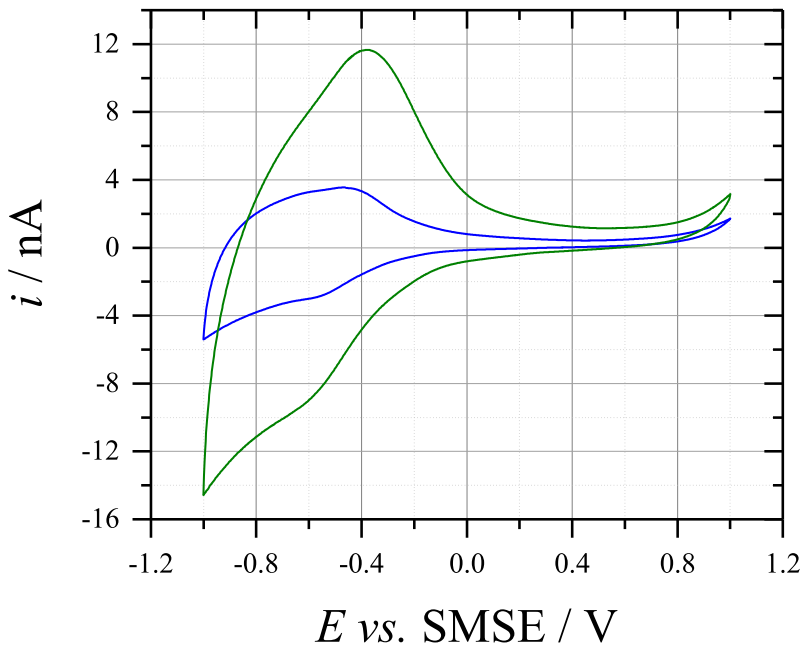


**Figure 3.4:** Cyclic voltammograms recorded at (BLUE) 50 mV $s^{-1}$ and (GREEN) 200 mV $s^{-1}$ with a 25 $\mu$m Ø W microelectrode in anaerobic 0.1 M $H_2SO_4$ (pH 1). The arrow indicates the initial potential and the scan direction of both voltammograms.

ducible voltammetry was obtained. The voltammetry was mostly featureless, except for a poorly defined reduction wave starting around −0.2 V *vs.* SMSE, and a broad oxidation peak on the reverse scan at −0.4 V *vs.* SMSE. The Pourbaix diagram suggests that the redox potentials for the oxidation of W should be −0.83 V *vs.* SMSE for the formation of $WO_2$, −0.73 V *vs.* SMSE for the formation of $W_2O_5$, and −0.7 V *vs.* SMSE for the formation of $WO_3$. Whilst no well defined peaks were seen for any of these processes, the close proximity of the redox potentials could explain the broad oxidation peak seen in Figure 3.4. Furthermore, the proximity of the $H_2$ evolution region could be the reason for the poor definition on the reduction wave. This result implies that the potential window of W electrodes will feature the formation of $WO_3$ at potentials above −0.4 V *vs.* SMSE, and the reduction of the $WO_3$ to W and lower oxides below this potential. This may have important consequences, given the varying physical properties of W and its oxides[172]. Of note is the magnitude of the background currents, which decreased at slower scan rates and therefore should not interfere with the further characterisation of W electrodes using redox compounds.

Both nanoelectrodes and some microelectrodes have small enough dimensions for a

hemispherical diffusion field to be rapidly established around the electrode, which allows the steady state of an electrochemical reaction to be reached[130]. This increases the diffusion of a reactant towards the electrode and, in the presence of a redox compound, produces a sigmoidal cyclic voltammogram with a steady state limiting current that can be assessed using Equation 3.11. The $Ru(NH_3)_6Cl_3$ redox compound is commonly used to assess electrode dimensions, due to its high rate of electron transfer[178,179] and its reversible behaviour, as shown in Equation 3.12.

$$[Ru(NH_3)_6]^{3+} + e^- \rightleftharpoons [Ru(NH_3)_6]^{2+} \tag{3.12}$$

This redox compound contains a ruthenium complex which starts in a 3+ oxidation state, but is then reduced to the 2+ oxidation state at a sufficiently negative potential. The potential window of this redox reaction coincides with the potential limits of W, making it ideal for the characterisation of W microelectrodes.

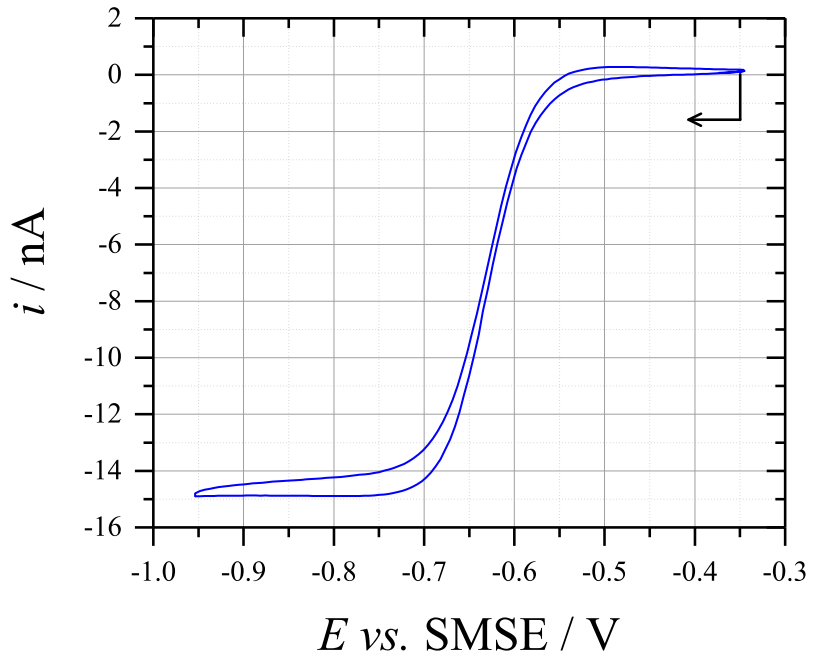


**Figure 3.5:** Cyclic voltammogram recorded at 5 mV $s^{-1}$ with a 25 $\mu$m Ø W microelectrode in anaerobic 5 mM $Ru(NH_3)_6Cl_3$ + 0.1 M $K_2SO_4$ (pH 3.5). The arrow indicates the initial potential and the scan direction.

Figure 3.5 shows the steady state sigmoidal voltammogram of a W microelectrode recorded in $Ru(NH_3)_6Cl_3$. By assuming $D = 5.71 \times 10^{-6}$ cm$^2$ s$^{-1}$[178], the limiting current was used to calculate an electrode diameter of $\approx 13.5$ $\mu$m, which was in good agreement with the diameter observed by optical microscopy. Despite the ongoing background processes, the W electrode appeared to be stable, with little hysteresis between the forward and backward scans. Furthermore, the gradient of the reduction wave met the Tomeš criterion ($E_{3/4} - E_{1/4} \approx 56$ mV), suggesting the reversibility was not hindered by the properties of the W electrode[180].

The establishment of the hemispherical diffusion field can be examined through the current-time response of the W microelectrode in $Ru(NH_3)_6Cl_3$. At short times, only the $[Ru(NH_3)_6]^{3+}$ close to the electrode surface is reduced, resulting in a steep concentration gradient of $[Ru(NH_3)_6]^{3+}$ near the electrode, and therefore a thin diffusion layer[130]. In this region, the mass transport of $[Ru(NH_3)_6]^{3+}$ towards the electrode is dominated by planar diffusion, which is inefficient at supplying the electrode with enough $[Ru(NH_3)_6]^{3+}$ to reach the steady state. Over time, the diffusion layer extends further into the solution, causing $[Ru(NH_3)_6]^{3+}$ from all surrounding directions to diffuse towards the microelectrode, eventually establishing a hemispherical diffusion field at long times. Chronoamperometry allows for examination of these different diffusion regimes and of any intermediary stages. The response of a W microelectrode was analysed by stepping from $-0.49$ V to $-0.95$ V *vs.* SMSE and then fitting to the theoretical Mahon and Oldham model[181].

The current transient of a W microelectrode in 5 mM $Ru(NH_3)_6Cl_3$ is shown in Figure 3.6, linearised by plotting the current *vs.* the inverse square root of time. Note that, although the first few data points were not included due to what appears to be an instrumentation error, the time intervals of 1.3 ms were too large to record the planar diffusion regime anyway. Instead, only the hemispherical diffusion regime and the intermediary regime were recorded. At the start of the current transient, the thin diffusion layer resulted in a large flux of $[Ru(NH_3)_6]^{3+}$ towards the electrode, giving high currents. Over time, the growth of the diffusion layer resulted in the decline in current, as well as a shift towards the hemispherical diffusion regime. After longer times, when the hemispherical diffusion field had been established, the current from the W microelectrode had reached the steady state value seen in Figure 3.5. The recorded current was in good agreement with the theoretical fitting, but there was slightly less current in the experimental data

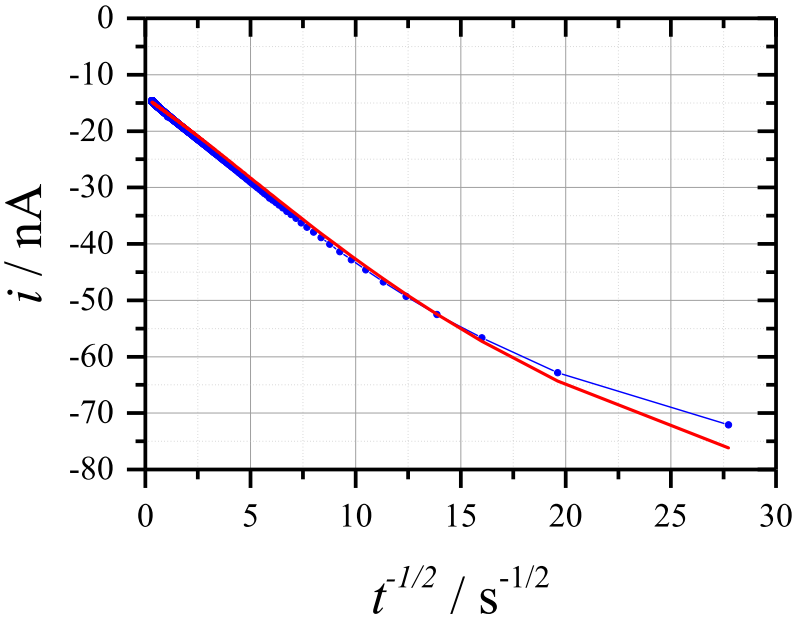


**Figure 3.6:** Current transient (BLUE) recorded at −0.95 V *vs.* SMSE, at time intervals of 1.3 ms, with a 25 $\mu$m Ø W microelectrode in anaerobic 5 mM $Ru(NH_3)_6Cl_3$ + 0.1 M $K_2SO_4$ (pH 3.5) and the theoretical transient (RED) calculated from Equation 6 in reference 181, by using: $n = 1$; $D = 5.7 \times 10^{-6}$ cm$^2$ s$^{-1}$; $a = 12.5$ $\mu$m; and $c = 5$ mM.

at shorter times. It seems likely that this lower current was caused by the presence of $WO_3$, which increased the resistance of the electrode material and reduced the overpotential experienced at the electrode surface during the start of the transient. This oxide would have been formed in the rest period before the potential step and then reduced over short timescales. This would be consistent with the observations from Figure 3.4, since the resting potential of −0.49 V *vs.* SMSE coincided with the formation of $WO_3$, whilst the stepping potential of −0.95 V *vs.* SMSE coincided with the reduction of this oxide. These characterisation techniques demonstrate the ability to use W as a microelectrode material, and set a precedent for characterising W nanoelectrodes.

## 3.3 Electrochemical etching of tungsten microwires

Whilst the formation of $WO_4^{2-}$ by Equation 3.12 was intentionally avoided during electrochemical characterisation, it is essential for the electrochemical etching of W. This

procedure involves the oxidation of a W substrate in highly alkaline solutions, with control over the dissociative corrosion dictating the substrate geometry. Recently, Ju *et al.* showed how this process could be used to prepare tips from W microwires, with exponential geometries obtained by static etching, and conical geometries obtained by gradual removal of the microwire (dynamic etching)[158]. A mechanism explaining how the exponential shape was obtained during static etching was proposed by Ju *et al.*, and is illustrated in Figure 3.7.

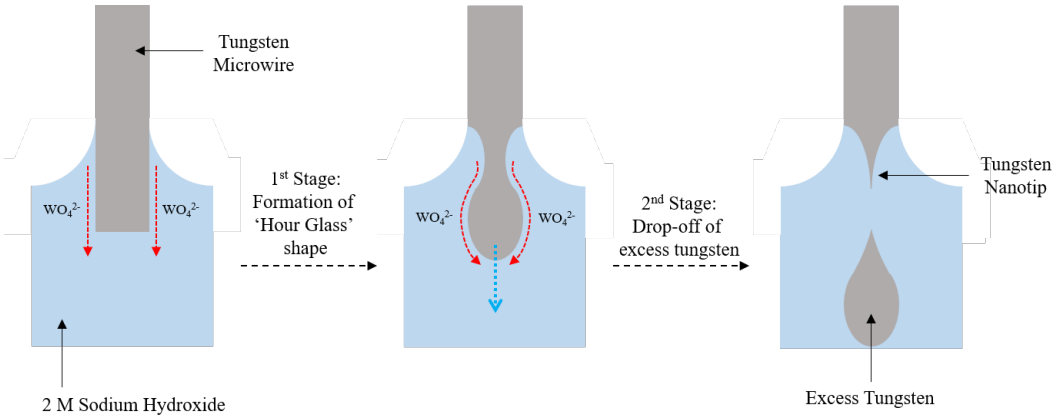


**Figure 3.7:** Hypothesised mechanism for the electrochemical etching of W microwires in alkaline solutions. Selective etching near the meniscus, caused by the flow of $WO_4^{2-}$ ions around the lower part of the microwire, results in the formation of an hourglass shape. After sufficient etching, the etched section near the meniscus becomes too thin to support the weight of the lower part of the microwire, which then breaks away in a 'drop-off' process. This causes the formation of a sharp, exponentially shaped W tip. The red dashed arrows depict the flow of $WO_4^{2-}$ ions around the microwire, whilst the blue dashed arrow shows the 'drop-off' process. Adapted from the proposed mechanism shown in reference 158.

Upon applying a sufficiently positive potential to the W microwire, corrosion takes place over all regions of the microwire in contact with the alkaline solution. The concentration of $OH^-$ ions in the meniscus around the wire is rapidly depleted, resulting in a decreased rate of etching in this region. Immediately below the meniscus, the etching process begins to produce $WO_4^{2-}$ ions, which then flow down past the lower part of the microwire, protecting it from further corrosion. As these simultaneous processes persist, the region immediately below the meniscus is continuously etched, eventually forming an hourglass shape. After some time, this region becomes too thin to support the weight of the lower portion of the microwire, which then detaches from the bulk of the microwire. In

this 'drop-off' event, the thin section of the microwire is drawn out and eventually snaps to create a W tip. By monitoring the current of a W microwire during corrosion, the formation of a tip can be examined.

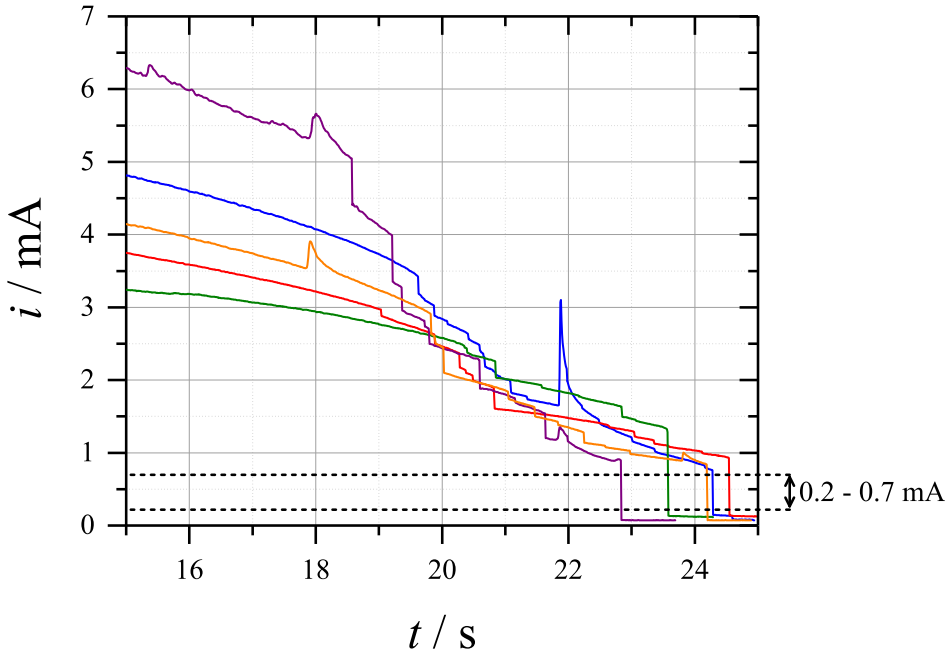


**Figure 3.8:** Selected region of the current transients recorded with five separate 25 $\mu$m Ø W microwires during electrochemical etching in 2 M NaOH. Each microwire was held at +1.9 V *vs.* SCE until the current suddenly decreased, signifying the formation of the tip by the 'drop-off' event. The dashed lines represent the current range (0.2 – 0.7 mA) in which this 'drop-off' typically occurred.

Figure 3.8 shows the chronoamperometry of several W microwires in 2 M NaOH. By stepping to +1.9 V *vs.* SCE, the recorded current showed the rate of the W corrosion process. This current steadily decreased as the surface area of the microwire was reduced by the dissociative oxidation. Note that there were occasional increases in the current, believed to be caused by the detachment of bubbles from the microwire. A sudden decline in current was observed near the end of each transient and was attributed to the 'drop-off' event and the formation of a W tip. The time required for this event varied, but the current range over which it took place ($0.2 - 0.7$ mA) was consistent. Continued etching after this event resulted in small currents associated with the blunting of the tip. It was necessary to avoid this in order to obtain the sharpest tips possible, which are required for nanoelectrode fabrication. In order to etch the microwires without risking the blunting of any possible nanotips, a circuit was designed to cut off the potential during the end of the

drop-off event, after the current of the microwire had passed through 0.3 mA.

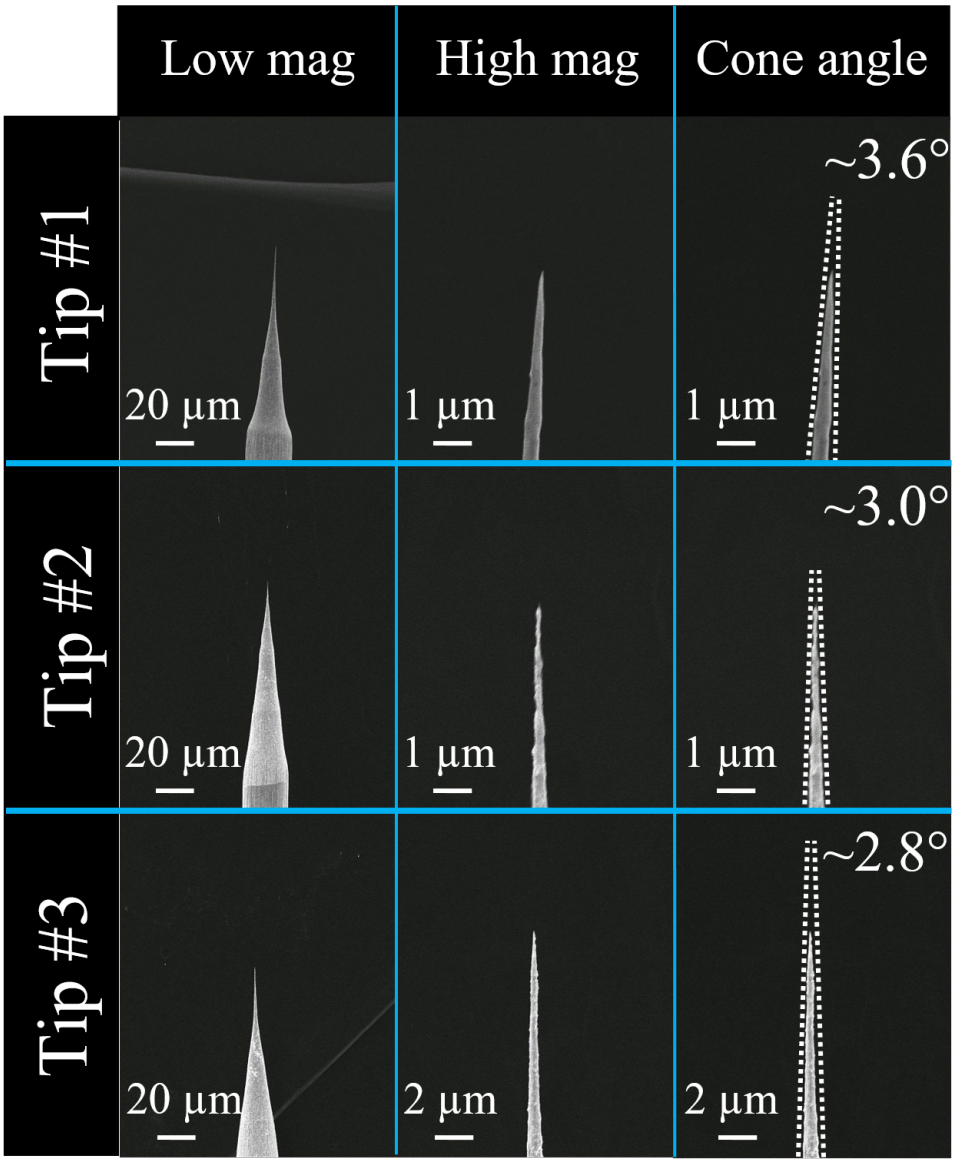


**Figure 3.9:** Field emission gun scanning electron microscope (FEGSEM) images of three separate 25 $\mu$m Ø W microwires after electrochemical etching in 2 M NaOH. The first column shows low magnification (500×) images of each microwire, whilst the second column shows higher magnification (5000× and 10000×) images of the tip ends. The third column shows the full cone angle values estimated from the high magnification images using ImageJ software.

FEGSEM images of three separate etched W microwires are shown in Figure 3.9. The electrochemical etching procedure using the cut-off circuit was shown to produce sharp W tips, with diameters around 250 nm and some of the FEGSEM images showed diameters as low as 13 nm. Near the base of the microwire, the tips often exhibited an exponential geometry, but as the tip was tapered in, the geometry became more conical, with full cone angles ranging between $2 - 4°$.

## 3.4 Characterisation of tungsten nanoelectrodes

After using the wire etching of W microwires to prepare nanotips, inlaid W nanodisc electrodes were fabricated by sealing the nanotips in glass and polishing until exposure. The breakthrough of the W nanodisc, in which the W was first exposed during the polishing, was monitored using a custom device that tested for continuity between the electrode and the polishing slurry[167]. Following this breakthrough event, the dimensions of each electrode were characterised with various techniques, such as electron microscopy.

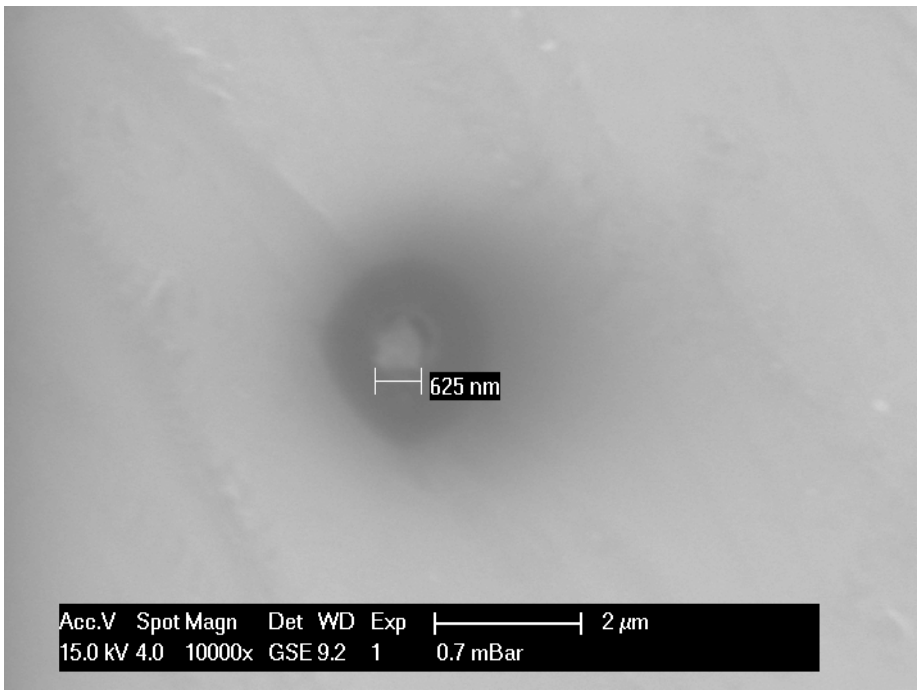


**Figure 3.10:** Scanning electron microscope image of the surface of a recently exposed ≈ 600 nm Ø W nanoelectrode.

Figure 3.10 shows an electron microscope image of the surface of a W nanoelectrode.

The W nanodisc was determined to be ≈ 625 nm Ø and was surrounded by an insulating shroud of glass. A dark region was observed in the glass around the nanodisc, and was possibly caused by the conductive W offering the electrical charge built up on the glass a path to ground. Locating and imaging the W nanodisc proved challenging, since the nanodisc was identified by its high conductivity in high vacuum mode, but then imaged in low vacuum mode in order to minimise charging of the glass. This complication, paired with the necessary destruction of the nanoelectrode for entry into the microscope stage, made SEM unsuitable for routine characterisation. Instead, the electrochemical characterisation described for W microelectrodes was employed.

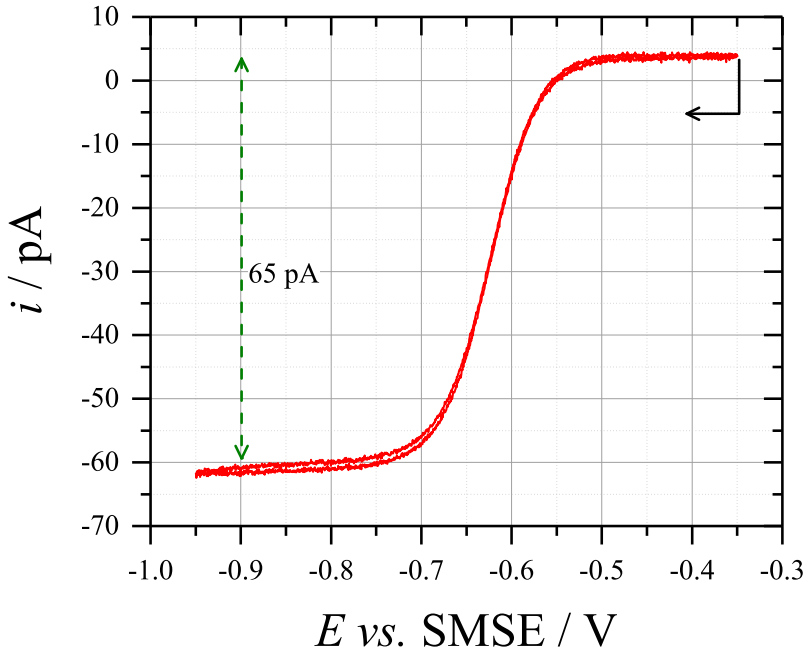


**Figure 3.11:** Cyclic voltammogram recorded at 5 mV $s^{-1}$ with a 116 nm Ø W nanoelectrode in anaerobic 5 mM $Ru(NH_3)_6Cl_3$ + 0.1 M $K_2SO_4$ (pH 3.5). The dashed green arrow indicates the magnitude of the reduction plateau, taking the +5 pA current offset from the potentiostat into account. The black arrow indicates the initial potential and the scan direction.

The steady state voltammetry of a W nanoelectrode in $Ru(NH_3)_6Cl_3$ is shown in Figure 3.11. Many of the features observed on W microelectrodes were also seen on nanoelectrodes, including the low hysteresis that indicated the stability of the electrode surface, and the reduction plateau that could be analysed using Equation 3.11. The nanoelectrode that gave the voltammogram shown in Figure 3.11 was calculated to be 116 nm Ø, after taking a positive current offset from the potentiostat into account. Additionally, the nanoelectrode shown in the electron microscope image of Figure 3.10 was calculated to

be ≈ 600 nm Ø, which is in agreement with the observations from the microscope image. Furthermore, the gradient of the reduction wave in these voltammograms still met the Tomeš criterion ($E_{3/4} - E_{1/4} \approx 56$ mV) due to the high rate of electron transfer offered by the $[Ru(NH_3)_6]^{3+}/[Ru(NH_3)_6]^{2+}$ redox couple.

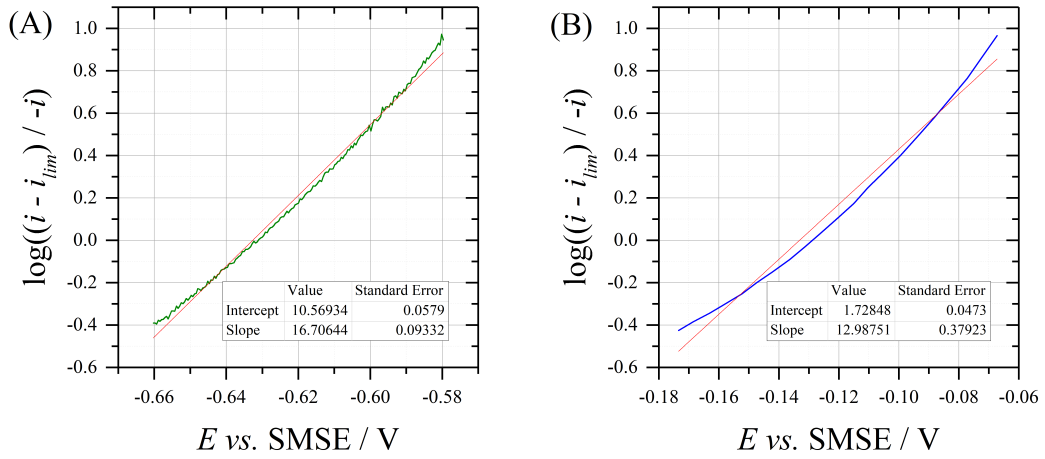


**Figure 3.12:** $log\left(\frac{i-i_{lim}}{-i}\right)$ *vs.* $E$ plots from the linear section of the cyclic voltammograms recorded at 5 mV $s^{-1}$ with: (A) a 116 nm Ø W nanodisc in an anaerobic solution of 5 mM $Ru(NH_3)_6Cl_3$ + 100 mM $K_2SO_4$ (pH 3.5); and (B) a 400 nm Ø W nanodisc in an anaerobic solution of 10 mM $K_3Fe(CN)_6$ + 200 mM $Sr(NO_3)_2$ (pH 6.5)[182]. Linear fitting was used to determine the gradient of the line, and the results of this fitting are shown in the boxes on each plot.

The reversibility of the redox reaction was further investigated by plotting $log((i-i_{lim})/-i)$ *vs.* the applied potential over the linear region of the reduction wave. The inverse gradient of this plot should also be ≈ 56 mV for a reversible reaction, and any deviation from this value would indicate the loss of electrochemical reversibility. $Ru(NH_3)_6Cl_3$ was chosen due to its ability to undergo a fast outer sphere electron transfer ($k_s > 17$ cm $s^{-1}$), ensuring that the redox reaction remains limited by the rate of mass transport. This is even the case when using nanoelectrodes, where a 116 nm Ø disc in $Ru(NH_3)_6Cl_3$ is estimated to have a steady state mass transfer coefficient ($k_m$) of 1.5 cm $s^{-1}$, using Equation 3.13 and assuming D = $5.7 \times 10^{-6}$ $cm^2$ $s^{-1}$.

$$k_m = \frac{4D}{\pi a} \tag{3.13}$$

Since this value is lower than the rate of electron transfer, $k_s$, the reduction of $[Ru(NH_3)_6]^{3+}$ remains reversible, an observation which is confirmed by the gradient of the plot seen in Figure 3.12A. Comparatively, $[Fe(CN)_6]^{3-}/[Fe(CN)_6]^{3-}$ undergoes a slower electron transfer ($k_s \approx 0.1$ cm s$^{-1}$[1183]) and, under the increased rate of mass transport offered by nanoelectrodes, the reduction of $[Fe(CN)_6]^{3-}$ instead becomes affected by the rate of electron transfer. This causes the redox reaction to become irreversible, which is evident from the gradient of the plot in Figure 3.12B. These observations confirm the high rate of mass transport offered by nanoelectrodes, a feature which could be used to investigate the kinetics of redox reactions which are deemed too fast to observe on microelectrodes.

However, the ideal sigmoidal voltammetry exhibited by Figure 3.11 was not always obtained immediately after breakthrough, with the W nanoelectrodes often showing voltammograms with various distortions instead.

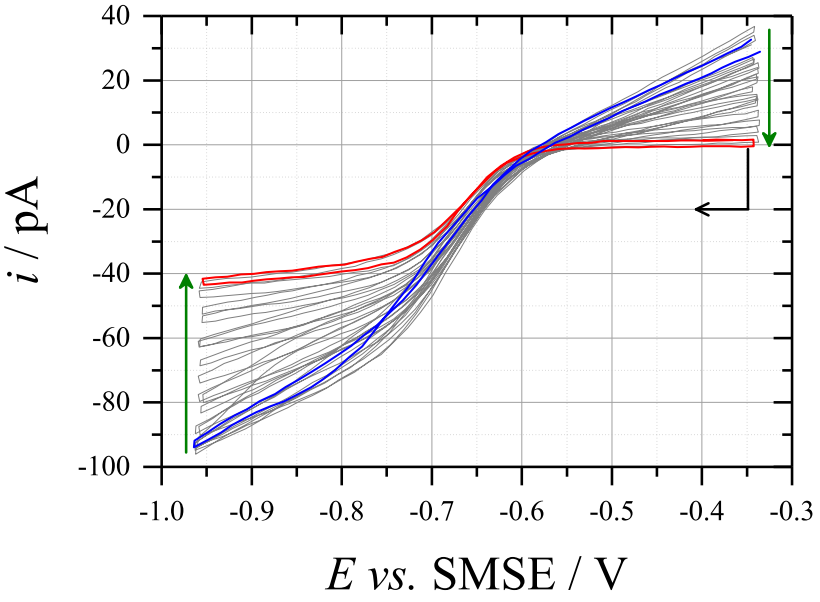


**Figure 3.13:** Continuous cyclic voltammogram recorded at 100 mV s$^{-1}$ with a ≈ 60 nm Ø W nanoelectrode in anaerobic 5 mM $Ru(NH_3)_6Cl_3$ + 0.1 M $K_2SO_4$ (pH 3.5). The blue outline shows the initial voltammogram obtained after breakthrough, the grey traces show subsequent cleaning scans, and the red outline shows the stable voltammogram obtained after sufficient cycling. The green arrows show the direction in which the grey traces progressed over time. The black arrow indicates the initial potential and the scan direction.

A distortion often seen on W nanoelectrodes that had recently been polished to break-

through was the presence of additional current slopes at the start of the voltammogram and at the reduction plateau, as exhibited in Figure 3.13. Upon continuous cycling in $Ru(NH_3)_6Cl_3$, the additional current started to decline, until the slopes eventually disappeared and the voltammetry returned to the expected steady state response. The presence of extra currents indicated that this effect was not caused by $iR$ drop, and was due to an additional Faradaic process occurring on the W surface. The most likely cause was the reduction of $WO_3$ that had formed on the W surface under the highly positive potentials used in the breakthrough circuit. This $WO_3$ was then repeatedly reduced and reoxidised during the voltammetry, resulting in the eventual conditioning of the W surface. This is consistent with the observations from Figure 3.4, where the formation of $WO_3$ was seen at $-0.4$ V *vs.* SMSE and the reduction of this oxide was seen at more negative potentials. The reduction of $WO_3$ is reported to occur through the formation of oxygen vacancies, changing the stoichiometry of the oxide to $WO_{3-x}$[172]. The gradual decline in the additional current suggests the eventual stability of the electrode surface, possibly through the permanent reduction of $WO_3$ to $WO_{3-x}$ during cycling. After this continuous cycling, the nanoelectrode could be used as normal and did not require further conditioning, unless it was polished again or left to rest for long periods. The effect of $WO_3$ formation/reduction was further studied using the deliberate passivation of a W nanoelectrode, as seen in Figure 3.14.

After $\approx$ 12 hours of resting in $Ru(NH_3)_6Cl_3$, W nanoelectrodes gave no trace of the steady state voltammetry expected from the reduction of $[Ru(NH_3)_6]^{3+}$. Instead, Faradaic currents caused by the reduction of the $WO_3$ to $WO_{3-x}$ were observed. The large magnitude of these currents (*i.e.* in the nA range) where possibly a result of the complete passivation of the electrode surface. The reduction of $WO_3$ would not be diffusion controlled, possibly explaining why these currents were several orders of magnitude higher than the currents obtained by reduction of $[Ru(NH_3)_6]^{3+}$. Furthermore, the complete passivation of 25 $\mu$m Ø microelectrodes would take much longer, which might explain why no such effect was seen with the W microelectrodes. This additional current complicated the use of W nanoelectrodes, but with sufficient conditioning to remove this oxide, the nanoelectrodes could be used as normal.

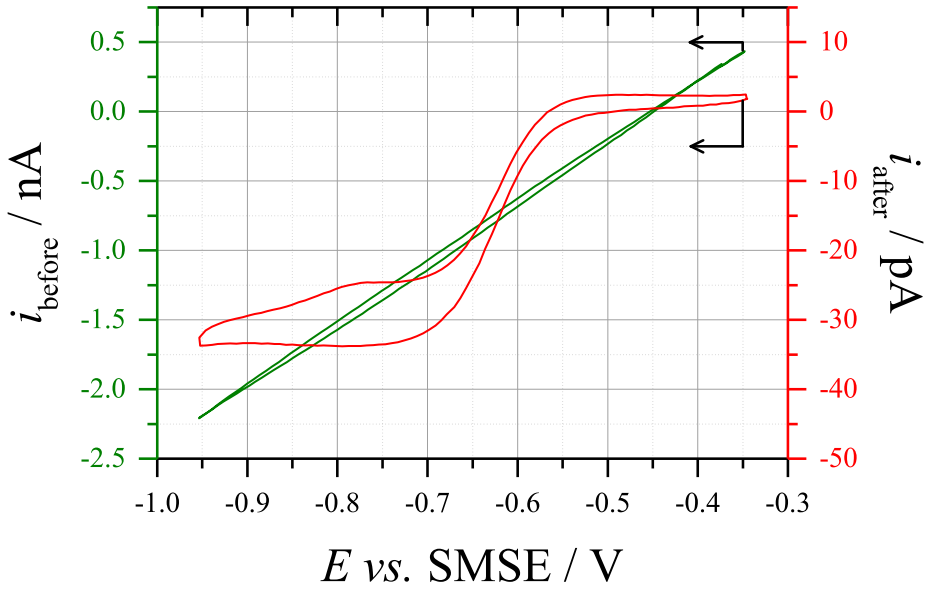


**Figure 3.14:** Initial (GREEN) and final (RED) cyclic voltammograms from the continuous cyclic voltammetry recorded at 20 mV $s^{-1}$ with a deliberately passivated ≈ 50 nm Ø W nanoelectrode in anaerobic 5 mM $Ru(NH_3)_6Cl_3$ + 0.1 M $K_2SO_4$ (pH 3.5). The electrode was passivated by leaving it in the same redox solution (aerobic) overnight. The arrows indicate the initial potential and the scan direction.

Other peculiar effects were observed in the voltammetry of W nanoelectrodes, even after conditioning. Often, the polishing of nanoelectrodes was continued beyond the breakthrough event, allowing the electrode to be widened to a desired diameter. In order to avoid overpolishing, the diameter of each nanoelectrode was routinely characterised by cyclic voltammetry in $Ru(NH_3)_6Cl_3$. However, the recorded voltammetry of polished W nanoelectrodes varied between the steady state response seen in Figure 3.13 and an Ohmic response. Unlike nanoelectrodes that had been deliberately passivated, the voltammetry of the nanoelectrodes exhibiting this response did not improve after continuous cycling, suggesting a permanent change in the electrode surface. However, further polishing caused the voltammetric response to alternate between the two extremes, with the periods in which sigmoidal voltammetry was observed becoming more frequent and longer lasting. After sufficient polishing, the steady state voltammetry of the electrodes became reproducible.

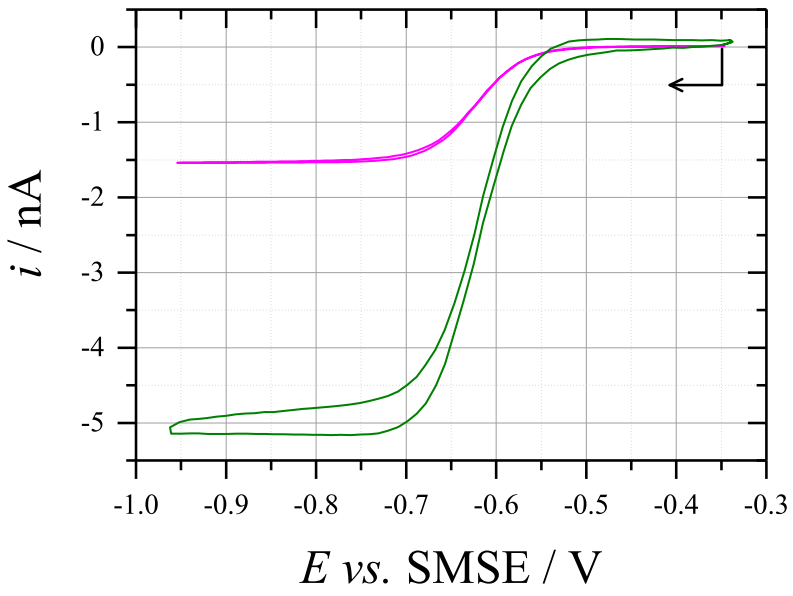


**Figure 3.15:** Cyclic voltammograms recorded at 50 mV $s^{-1}$ with W nanoelectrodes in anaerobic 5 mM $Ru(NH_3)_6Cl_3$ + 0.1 M $K_2SO_4$ (pH 3.5). Each nanoelectrode was polished until it gave reproducible voltammetry, using either (PINK) 50 nm alumina, or (GREEN) 300 nm alumina. The arrow indicates the initial potential and the scan direction.

As shown in Figure 3.15, the point at which voltammetry became reproducible depended on the grade of the polishing material being used. Electrodes polished with 0.3 $\mu$m and 50 nm Ø alumina showed reproducibility at diameters of 9.3 $\mu$m and 2.7 $\mu$m respectively. This suggested a connection between the roughness of the electrode surface and the size of the W disc. It was theorised that if the polishing material was comparable in size to the electrode diameter, then the relatively high surface roughness would result in cases where the W disc was obscured within a groove on the surface. This would reduce the rate of mass transport of $[Ru(NH_3)_6]^{3+}$ towards the electrode, resulting in lower currents. This could be exacerbated by polishing material blocking the grooves of the surface, which might explain the Ohmic response. Deviation from steady state voltammetry has been reported on Pt nanoelectrodes before cleaning procedures[184]. On the other hand, when the W disc was not obscured by the surface roughness, the rate of mass transport would increase, allowing the steady state voltammetry to be observed. Polishing nanoelectrodes until they started to exhibit reproducibility often resulted in larger diameters than desired, so the possibility of cleaning the electrode surface instead was examined.

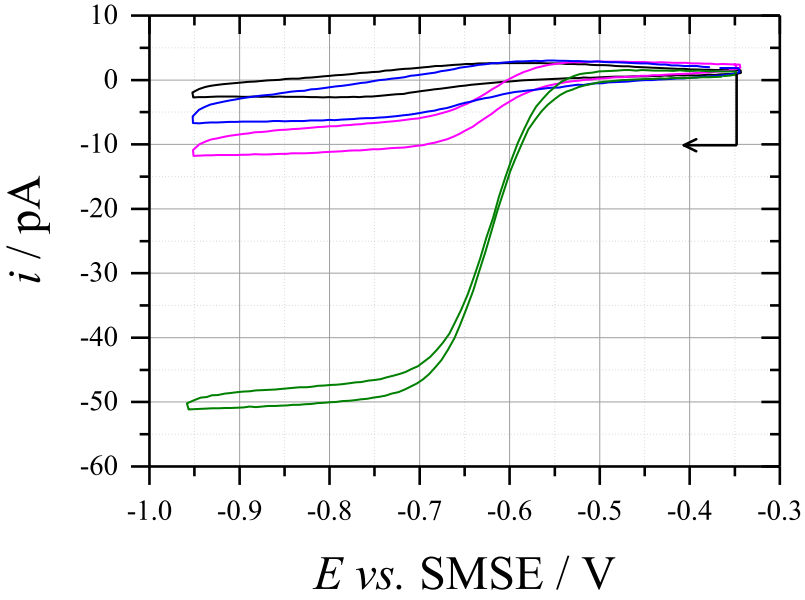


**Figure 3.16:** Cyclic voltammograms recorded at 20 mV $s^{-1}$ with a ≈ 80 nm Ø W nanoelectrode in anaerobic 5 mM $Ru(NH_3)_6Cl_3$ + 0.1 M $K_2SO_4$ (pH 3.5). The voltammograms were recorded (BLACK) immediately after breakthrough, and then after: (BLUE) 10 min; (PINK) 20 min; and (GREEN) 30 min of resting in stirring 10% $H_3PO_4$. The arrow indicates the initial potential and the scan direction.

When an Ohmic response was obtained, the nanoelectrode was left to rest in a stirring 10% $H_3PO_4$ solution, thereby removing any alumina from the surface of the electrode. Figure 3.16 shows cyclic voltammograms of a W nanoelectrode after successive periods of exposure to this cleaning procedure. A gradual increase in the current was seen, with the full steady state response obtained after 30 minutes in the $H_3PO_4$. This cleaning procedure did not always result in the return of steady state voltammetry, but was occasionally capable of reclaiming nanoelectrodes that had ceased to do so.

Another type of distortion was witnessed on conditioned nanoelectrodes that were giving reproducible steady state voltammetry. As shown in Figure 3.17, this was another case of additional current slopes at the start of the voltammogram and at the reduction plateau. However, these slopes did not decline after continuous cycling and were seen on both W and Au-plated W nanoelectrodes (the preparation of Au-plated nanoelectrodes will be discussed more later). Similar observations have been reported for Pt nanoelectrodes, and have been shown to result from small currents passing across the glass body of the

nanoelectrode[167].

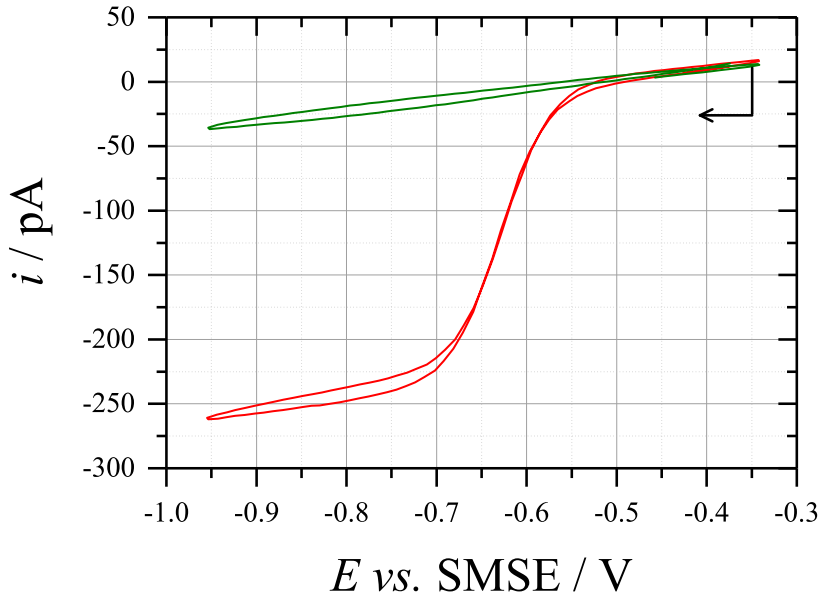


**Figure 3.17:** Cyclic voltammograms recorded at 50 mV $s^{-1}$ with a ≈ 300 nm Ø Au-plated W nanoelectrode, sealed in soda glass, in (RED) anaerobic 5 mM $Ru(NH_3)_6Cl_3$ + 0.1 M $K_2SO_4$ (pH 3.5) and (GREEN) anaerobic 0.1 M $K_2SO_4$ (pH 3.5). The arrow indicates the initial potential and the scan direction.

The additional current was therefore an Ohmic response derived from the conductivity of the glass, and was superimposed onto the steady state voltammetry of the Au-plated W nanodisc in $Ru(NH_3)_6Cl_3$. The resistive slope of the voltammetry recorded in the absence of $Ru(NH_3)_6Cl_3$ can be seen in Figure 3.17, and is consistent with the additional current superimposed onto the steady state voltammogram. Current recorded through the glass has been attributed to the mobility of cations within the glass, which allows charge to be carried across from the solution to the electrode material[167]. The use of glass with lower conductivities than soda glass, such as 50% lead oxide glass, has been shown to minimise this additional current. This is because Na ions are smaller than Pb ions and their mobility is therefore greater, allowing more charge to be carried across the glass. Note that this additional current was observed more often on smaller electrodes, since the Faradaic currents recorded from $[Ru(NH_3)_6]^{3+}$ reduction on larger electrodes often eclipsed the small contribution from glass conductivity.

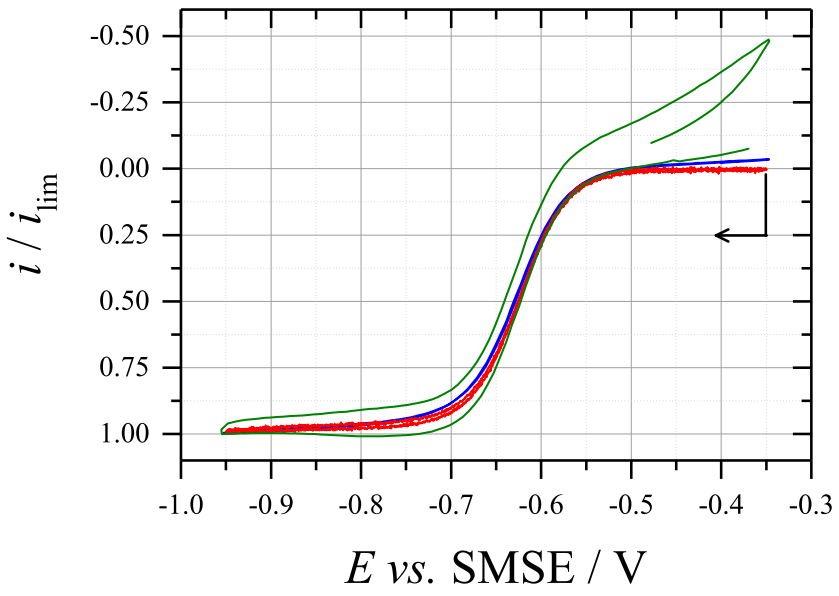


**Figure 3.18:** Normalised cyclic voltammograms recorded at 50 mV $s^{-1}$ with: (BLUE) a ≈ 250 nm Ø W nanoelectrode, sealed in soda glass; (RED) a 116 nm Ø W nanoelectrode, sealed in 22% PbO glass; and (GREEN) a 25 $\mu$m Ø W microelectrode, sealed in high resistance borosilicate glass, in anaerobic 5 mM $Ru(NH_3)_6Cl_3$ + 0.1 M $K_2SO_4$ (pH 3.5) . Each voltammogram was normalised with respect to its limiting current at −0.95 V *vs.* SMSE. The arrow indicates the initial potential and the scan direction.

Alternative types of glass were therefore examined for use in W nanoelectrode fabrication. As shown in Figure 3.18, the cyclic voltammetry of a W nanoelectrode sealed in soda glass was still seen to exhibit this additional current. However, low-conductivity borosilicate and 22% lead oxide glass minimised the resistive effect on the reduction plateau, confirming the role of glass cation migration on the steady state voltammetry of nanoelectrodes. The use of borosilicate glass also resulted in an oxidation process at the start of the voltammogram. This process was witnessed on both W microelectrodes and nanoelectrodes and, as it did not scale with the electrode size, it completely obscured the current from the reduction of $[Ru(NH_3)_6]^{3+}$ on nanoelectrodes. The use of 22% lead oxide glass did not show any such oxidation processes, allowing the steady state voltammetry to be more readily analysed. Therefore, 22% lead oxide glass was routinely used to prepare W nanoelectrodes. Note that the use of 22% lead oxide glass did not alter the need for conditioning and/or cleaning of the W nanoelectrodes.

After sufficient conditioning and cleaning of the W surface, and after implementing the use of 22% lead oxide glass, the characterisation of W nanoelectrodes using cyclic voltammetry was routinely used to obtain the same steady state responses as seen in Figure 3.13. However, the characterisation of the W nanoelectrodes by chronoamperometry, which is shown in Figure 3.19, displayed even more unique surface effects.

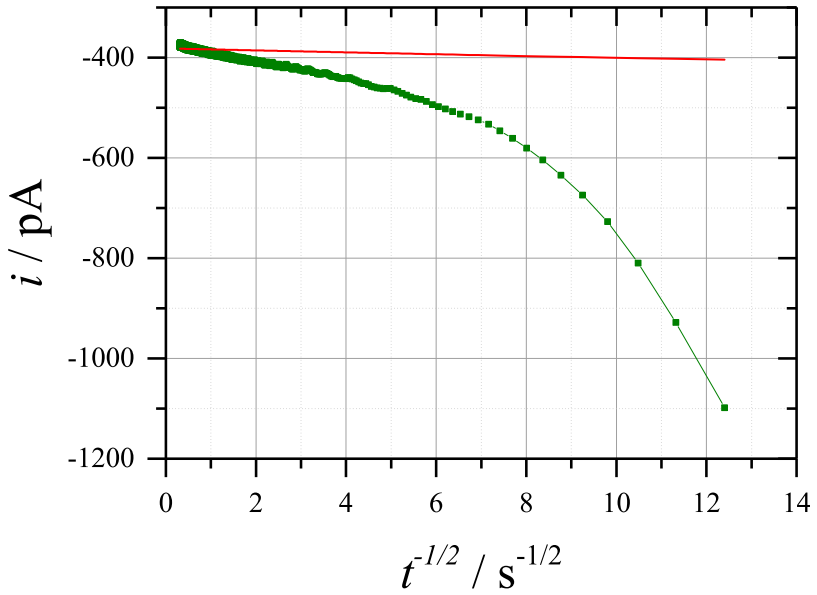


**Figure 3.19:** Current transient (GREEN) recorded at −0.95 V *vs.* SMSE, at time intervals of 1.3 ms, with a 800 nm Ø W nanoelectrode in anaerobic 5 mM $Ru(NH_3)_6Cl_3$ + 0.1 M $K_2SO_4$ (pH 3.5) and the theoretical transient (RED) calculated from Equation 6 in reference 181, by using: $n = 1$; $D = 5.7 \times 10^{-6}$ cm$^2$ s$^{-1}$; $a = 400$ nm; and $c = 5$ mM.

Chronoamperometry recorded with W nanoelectrodes did not agree well with the theoretical Mahon and Oldham fitting, particularly at shorter timescales. Despite removing the first few data points due to an instrumentation error, large currents were obtained as a result of possibly two additional processes. The first process took place over short times and resulted in a large current magnitude. The second process took place over much longer times and can be identified as a deviation from the expected gradient. These observations were reproducible on the same electrode over several successive transients, and the voltammetry recorded between each transient was consistent and showed no evidence of any surface changes. Several possible explanations exist for each process, but the exact cause for the disagreement is unknown. As a similar effect was not witnessed during the reduction of $WO_3$ on W microelectrodes, the first process is more likely an instrumentational error resulting from the use of the lowest current sensitivity on the potentiostat.

Note that the value of the time steps was too large for planar diffusion, also ruling out increased currents from sealing inconsistencies or shape deviations caused by electrode damage[165]. The cause of the second process is unknown, although the linearity of the deviation suggests a diffusion controlled reaction. However, the gradient of this process was 10× larger than that of the fitting, suggesting the process involved a reactant with a diffusion coefficient of $\approx 10^{-5}$ cm$^2$ s$^{-1}$. This was inconsistent with the formation of oxygen vacancies, which would be limited by diffusion of oxygen and cations through the $WO_3$ surface. The reduction of $O_2$ was also ruled out, as the voltammetric response of the electrode did not change after further degassing. At sufficiently long times, the steady state limiting current was obtained and was in agreement with the theoretical value and the voltammetry. These observations indicate the incompatibility of W nanoelectrodes at faster timescales and the chronoamperometry of W nanoelectrodes needs to be investigated in further detail in order to understand this.

## 3.5 Applications of tungsten electrodes

In addition to the conventional uses of microelectrodes and nanoelectrodes, many unique applications for the electrodes described above can be derived from the use of W as an electrode material. For example, the ability to corrode W surfaces in alkaline solutions allows W nanoelectrodes to be etched in a procedure to generate glass nanopores. These nanopores can be used for the Coulter counting of nanobubbles, which will be discussed more in the following chapters. Meanwhile, some other possible applications of W electrodes will be discussed.

In Figure 3.3C, the corrosion of a W microelectrode in NaOH was observed using cyclic voltammetry. Under steady state conditions, the oxidation wave associated with this process had a plateau that was found to be dependent on the concentration of $OH^-$ ions. This portion of the voltammogram was repeated at different NaOH concentrations, using linear sweep voltammetry on W microelectrodes. Figure 3.20 compares the theoretical limiting current, determined using Equation 3.11, with the experimental values determined from the linear sweep voltammetry. The recorded currents closely followed the theoretical trend, but appeared to be slightly lower at each of the NaOH concentrations

used. Equation 3.11 did not account for the ongoing corrosion of the W surface during the onset of the oxidation wave, which would have had resulted in lower currents at the plateau. This observation was most significant in the highest concentration NaOH solution, where the plateau current was seen to decline during the voltammetry. Minimising the discrepancy between the experimental and theoretical currents would require higher scan speeds, which would remove the steady state conditions, but a correction factor could be applied to the recorded current instead. This would allow the pH of alkaline solutions to be accurately determined, which is an ongoing issue with conventional soda glass pH meters.

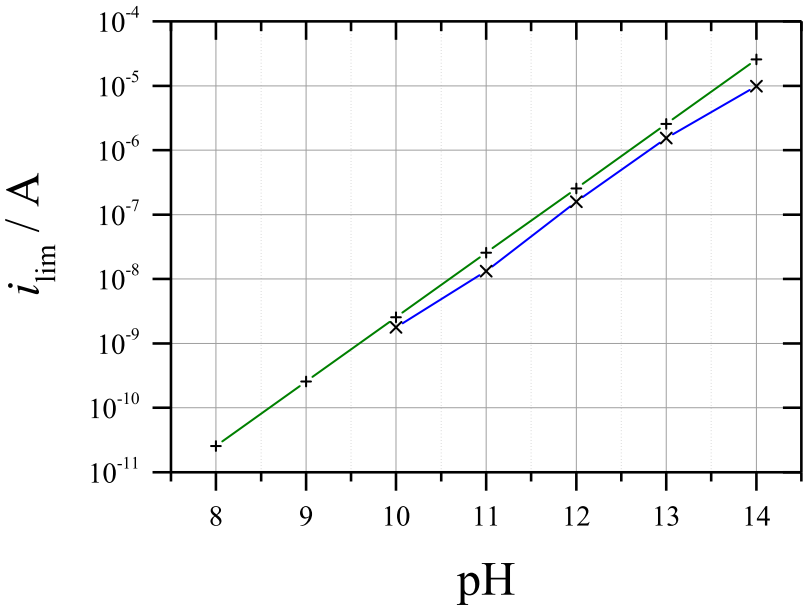


**Figure 3.20:** Comparison between (BLUE, ×) the experimentally recorded limited currents of a 25 $\mu$m Ø W microelectrode in different NaOH solutions, obtained with linear sweep voltammograms recorded at 25 mV $s^{-1}$, and (GREEN, +) the theoretical relationship between $i_{lim}$ and pH, calculated from Equation 3.11, using $n = 1$ and $D = 10^{-5}$ $cm^2$ $s^{-1}$.

The complete etching of a nanoelectrode yields a glass nanopore, but the partial etching has been shown to instead produce recessed nanoelectrodes[185]. The less aggressive conditions required for the corrosion of W could therefore offer a simpler method of obtaining these recessed nanoelectrodes. The electrodeposition of other materials into recesses generated in this way is an alternative route towards obtaining noble metal nanoelectrodes[186]. The use of noble metals might be preferable to that of W, especially in cases where passivation must be avoided. Therefore, W nanoelectrodes were partially

etched in a chemical etching solution of 250 mM $K_2S_2O_8$ + 2 M NaOH, then Au was electrodeposited into the recess. A brief polish was then used to remove any excess Au from the surface of the nanoelectrode. Note that the exact depth of the recess was not measurable using chemical etching, and estimations from the amount of Au that had been deposited also included Au which had overfilled from the recess. Nevertheless, the Au-plated W nanoelectrodes were characterised in $Ru(NH_3)_6Cl_3$, as shown in Figure 3.21. The voltammogram shared many similarities with the voltammetry of the preceding W nanoelectrode, but there was a slope on the reduction plateau. This could be an indication of porosity in the Au deposit, or gaps between the deposit and the surrounding glass.

The Au-plated W nanoelectrodes were also characterised by cyclic voltammetry in $H_2SO_4$. Numerous publications report the various surface processes that can occur on Au electrodes in acidic solutions. In the voltammetry shown in Figure 3.22, peaks attributed to these processes were indeed seen on Au-plated W nanoelectrodes. These include the formation of Au oxides at +0.7 V *vs.* SMSE and the subsequent reduction of these oxides at +0.4 *vs.* SMSE. However, broad oxidation and reduction peaks at −0.5 V *vs.* SMSE were also seen and were not consistent with voltammetry of pure Au microelectrodes. Comparison with the voltammetry in Figure 3.4 suggested that these peaks were related to the formation and reduction of $WO_3$, confirming the presence of either a porous deposit or a poor seal. Whilst the electrodeposition process shows promise, this apparent leaking effect needs to be addressed in order to fully exploit this method of fabricating noble metal nanoelectrodes.

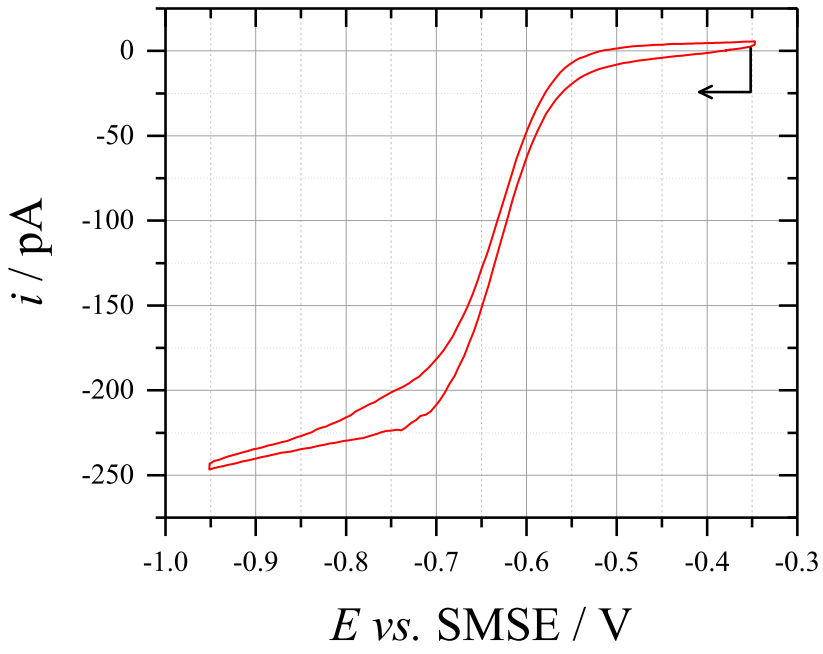


**Figure 3.21:** Cyclic voltammogram recorded at 5 mV $s^{-1}$ with a 400 nm Ø Au-plated W nanoelectrode in anaerobic 5 mM $Ru(NH_3)_6Cl_3$ + 0.1 M $K_2SO_4$ (pH 3.5). The arrow indicates the initial potential and the scan direction.

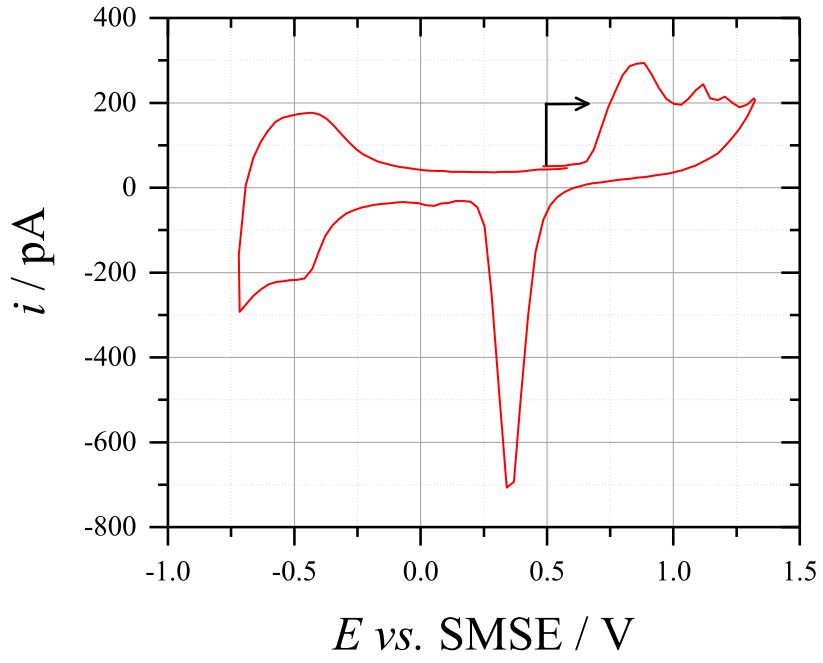


**Figure 3.22:** Cyclic voltammogram recorded at 200 mV $s^{-1}$ with a 400 nm Ø Au-plated W nanoelectrode in anaerobic 0.1 M $H_2SO_4$ (pH 1). The arrow indicates the initial potential and the scan direction.

## 3.6 Chapter 3 conclusions

The use of W as an electrode material was investigated using the characterisation of W microelectrodes. These microelectrodes were shown to give well-behaved steady state voltammetry, with little hysteresis and no interference from background surface processes. The wire etching of W microwires was also shown to be successful, providing sharp nanotips with controllable geometries that could then be used to fabricate W nanoelectrodes. This route towards nanoelectrodes was less aggressive compared to literature examples of Pt wire etching. Characterisation of W nanoelectrodes revealed they had similar properties to the W microelectrodes, but in many cases the steady state voltammetry could only be obtained after sufficient conditioning and cleaning. However, the chronoamperometric response of the W nanoelectrodes did not follow theoretical fittings, suggesting other processes were taking place at shorter timescales. The cause of these processes was not determined and is of interest to future work, but the W nanoelectrodes are still effective for use at longer timescales. Moreover, the W nanoelectrodes present a convenient route to obtaining glass nanopores, which can be used for the Coulter counting of nanobubbles. Other applications for W electrodes were also investigated, including the determination of solution pH from the current of $OH^-$ oxidation, and the electrodeposition of Au into recessed nanoelectrodes.

# 4 Coulter counting of particles and nanopore characterisation

In Coulter counting, the greatest sensitivity is obtained with pores that are only slightly wider than the diameter of the particles/bubbles being analysed. This means nanopores are required for the effective characterisation of nanobubbles. Numerous methods for preparing single nanopores for Coulter counting have been reported, and include pipette pulling[153], track etching of polymer membranes[187], and the sealing of carbon nanotubes[188]. However, the method employed in this chapter involves the complete removal of the electrode material from a nanoelectrode, which provides sturdier nanopores that are more suited for repeated use[167]. This method of preparing nanopores could offer several advantages if applied to the W nanoelectrodes shown in Chapter 3. Since the corrosion of W is more readily achievable than that of noble metals, the W metal can be removed from the nanoelectrodes with a relatively benign chemical etching procedure. Additionally, the electrochemical characterisation of the W nanoelectrode prior to the chemical etching can be used to predict the diameter of the subsequent nanopore. Polishing of the nanoelectrode after its initial breakthrough also allows the diameter of the subsequent pore to be widened to a desired value. Furthermore, the geometry of the glass nanopore is influenced by the shape of the W nanotip, which can in turn be controlled through the electrochemical wire etching procedure[158]. Figure 4.1 illustrates how the preparation of nanopores through the etching of W nanoelectrodes could be used in the Coulter counting of nanoparticles and nanobubbles.

This chapter discusses the preparation and characterisation of single glass nanopores, prior to their use in the Coulter counting of nanobubbles. Methods for nanopore characterisation include cyclic voltammetry and microscopy, but also the Coulter counting of polystyrene nanoparticle standards. This practice provides key information on the geometry of the nanopore and the signal magnitude given by a particle/bubble with a particular diameter, which will be useful in the later analysis of any nanobubble translocations.

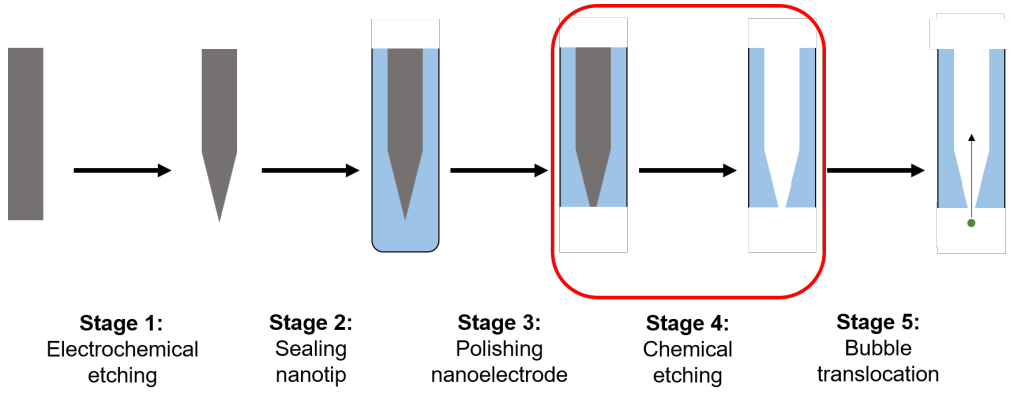


**Figure 4.1:** Stages in the project required to record the Coulter counting of nanobubbles. The focus of this chapter, highlighted by the red box, is the establishment of a Coulter counting system and the study of this system using micropores. This is followed by the preparation of conical glass nanopores from the W nanoelectrodes of Chapter 3, which are then characterised by the Coulter counting of nanoparticles.

Therefore, a large portion of this chapter discusses the establishment of the apparatus needed to record Coulter counting, the different approaches to recording particle translocations, and the effect of various parameters on the translocation signal. Well-defined micropores were first used to test the abilities of the Coulter counting apparatus, with comparisons to the shape and magnitude of simulated particle translocations.

## 4.1 Micropore preparation and characterisation

Cylindrical micropores were prepared through the complete removal of the microwires from Cu and W microelectrodes. In both cases, the electrode material was removed with a chemical etching procedure, as detailed in Chapter 2. By using various microwires, micropores with diameters ranging from 25 to 64 $\mu$m Ø were obtained. After the chemical etching was complete, the micropores were assessed by optical microscopy.

Figure 4.2 shows an example of an optical microscope image recorded with a cylindrical microelectrode before and after chemical etching. In the case shown, the electrode/pore had a diameter of 40 $\mu$m and a length of $\approx$ 800 $\mu$m. These are ideal dimensions for Coulter counting, since the micropore is long enough to allow the apparatus to record faster moving

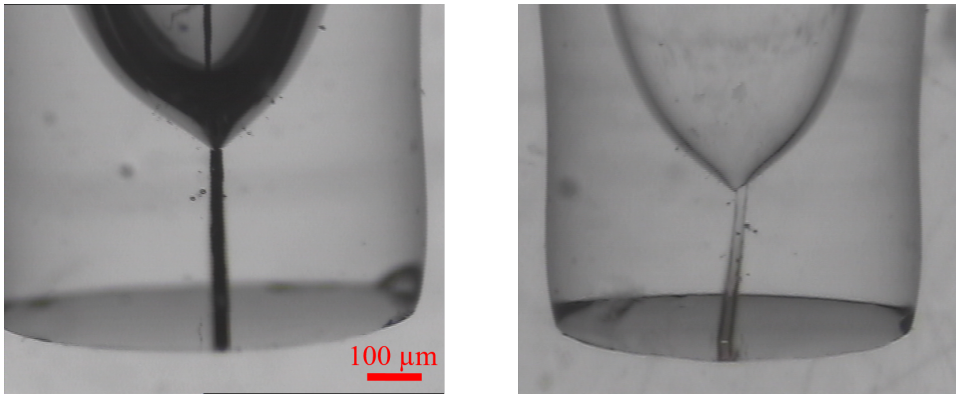


**Figure 4.2:** Optical microscope images of a 40 $\mu$m Ø Cu microelectrode before (LEFT) and after (RIGHT) complete chemical etching in 1 : 3 1 M HCl: 30% $H_2O_2$. Each image was recorded at 2× magnification, with the electrode/pore submerged in $H_2O$ to minimise the distortion from the refractive index of the glass.

particles, but not so long that it exhibits more frequent blocking and a higher background resistance. The dimensions derived for this microscope image were then confirmed using the electrochemical characterisation of the micropore.

Cyclic voltammetry was recorded between two Ag/AgCl wires in an electrolyte solution of 10 mM KCl. One of the Ag/AgCl wires was placed on the inside of a cylindrical micropore, with the restrictive channel of the micropore structure limiting the current that could be passed between the wires. As a result, the cyclic voltammetry, as shown in Figure 4.3, exhibited an Ohmic response. This allowed the micropore to be analysed using the formula for the resistance of a pipe, Equation 4.1.

$$R_p = \frac{\rho L}{A} \tag{4.1}$$

where $R_p$ is the background resistance of the pore; $\rho$ is the resistivity of the electrolyte; $L$ is the length of the pore; and $A$ is the cross-sectional area of the pore. Given the resistance of the micropore, calculated from Figure 4.3 as 4.5 MΩ, the length of the micropore was estimated from Equation 4.1 as 804 $\mu$m[189]. It should be noted that this same resistance was also obtained when cycling to greater potentials of ±5 V. This was in good agreement with the pore length measured from the microscope images in Figure 4.2, although the

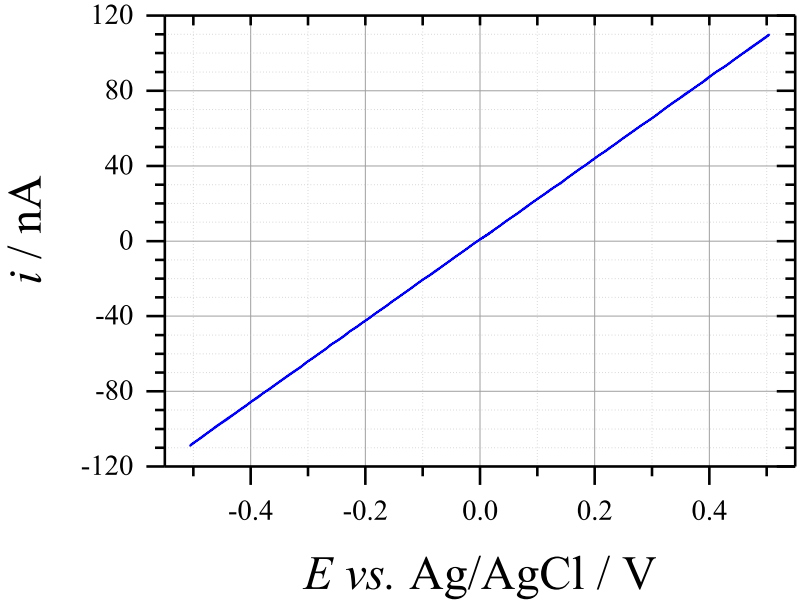


**Figure 4.3:** Cyclic voltammogram recorded at 50 mV $s^{-1}$ with a 40 $\mu$m Ø cylindrical micropore in aerobic 10 mM KCl.

length derived from Equation 4.1 will vary with any changes in the resistivity of the electrolyte and with the inclusion of any end effects from additional resistance at the openings of the micropore channel. The dimensions of the micropore calculated from Equation 4.1 can be used to simulate particle translocations and predict the background resistance of the micropore during a Coulter counting experiment.

## 4.2 Characterisation of the Coulter counting apparatus

The translocation of polystyrene microparticle standards through the cylindrical micropores was used to test the Coulter counting apparatus described in Chapter 2. During the translocation of a particle through a pore, the electrolyte in the pore is displaced and the ionic pathways through the pore are reduced, resulting in a change in the pore resistance from its background value. The magnitude of this resistance change is highly dependent on the particle volume and the pore geometry. After the particle exits the pore, the resistance of the pore returns to its background value. This temporary change in pore resistance can be monitored in several ways. The most common way to measure a particle translocation signal is to use chronoamperometry, which can be recorded between an Ag/AgCl wire in an electrolyte solution and an Ag/AgCl wire inside the micropore[190].

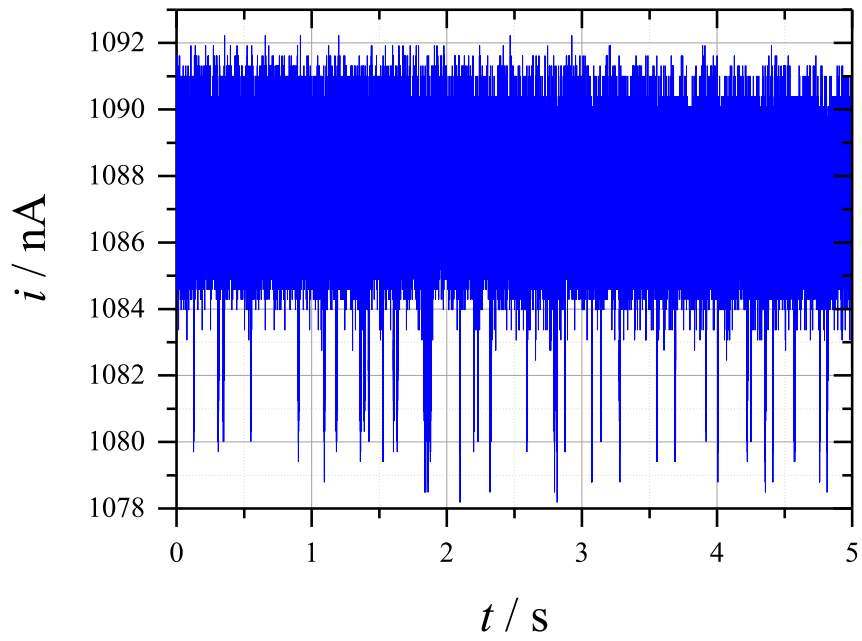


**Figure 4.4:** Current transient recorded at −5 V *vs.* Ag/AgCl with a 40 $\mu$m Ø cylindrical micropore in aerobic 10 mM KCl. The plot shows the translocation of 18.8 ± 1.5 $\mu$m Ø microparticles ($7.2 \times 10^4$ particles mL$^{-1}$), recorded with the low gain ($10^6$ V/A) current follower system. The pressure differential applied to the micropore was −43 mBar and the temperature during the experiment was 30.9 °C.

The current transient in Figure 4.4 shows the translocation of 18.8±1.5 $\mu$m Ø particles through a 40 $\mu$m Ø cylindrical pore. A stable background current of 1088 ± 4 nA was observed, which was consistent with the background pore resistance calculated from Figure 4.3. Changes in the resistance caused by the translocation of the microparticles can be seen throughout the transient, with a typical translocation lowering the pore current to 1083 ± 4 nA (taking the noise into account). This corresponds to a change in resistance of 21 ± 34 kΩ. This large error is a result of the low signal to noise ratio being carried through the calculation of change in resistance (see appendix). However, using the ratio of particle diameter to pore diameter (including errors on particle diameter) to calculate the theoretical change in resistance with the equation given by DeBlois and Bean[154,157] gives a value of 24.4 ± 7.4 kΩ, showing the experimentally obtained value is similar. The sign of the background current was dependent on the polarity of the applied voltage, but the direction of the signal was always towards 0 A (*i.e.* a drop in current), since the translocation of polystyrene particles resulted in a temporary increase in the pore resistance. Slight variations on the signal magnitude were most likely due to the off-axis

translocation of particles, which give larger than expected resistance changes[191]. However, the large background electrical noise seen throughout the transient could have also altered the signal magnitude. The signal-to-noise ratio of the current transient was particularly poor, with the noise around 8 nA and the average signal magnitude around 8 nA. Whilst this noise could possibly obscure signals produced by the translocation of smaller particles, the Coulter counting apparatus was clearly shown to be operating properly for the analysis of larger particles.

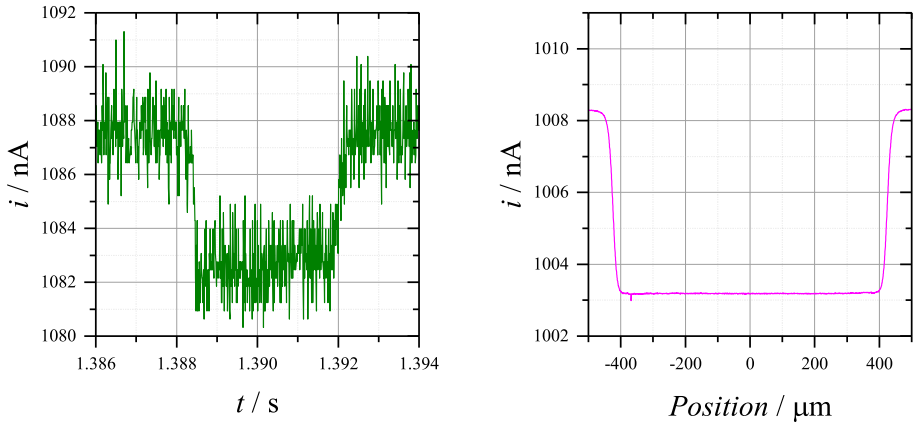


**Figure 4.5:** Experimental (LEFT) and simulated (RIGHT) current transients recorded at −5 V *vs.* Ag/AgCl with a 40 $\mu$m Ø cylindrical micropore in aerobic 10 mM KCl. The plots compare the signal shape observed during the translocation of $18.8 \pm 1.5$ $\mu$m Ø microparticles ($7.2 \times 10^4$ particles mL$^{-1}$), recorded with the low gain ($10^6$ V/A) current follower system. For the experimental transient, the pressure differential applied to the micropore was −43 mBar and the temperature during the experiment was 30.9 °C.

Information on the pore geometry and the translocation time can be obtained by analysis of the translocation signal shape. Figure 4.5 shows an expanded view of a microparticle translocation from Figure 4.4 and compares it to a simulated translocation. In this case, the simulated translocation was obtained by incrementally stepping the particle position through a pore that had been built with the dimensions determined from Figure 4.3, and was independent of the time or liquid flow through the pore. The cylindrical geometry of the pore was evident in both cases, with the sharp decline/incline at each end of the event corresponding to the pore openings, and the stable current during translocation indicative of the constant diameter of the pore. Particles were observed to translocate over a period of ≈ 4 ms. The translocation time can reveal information about the particle velocity under the influence of a pressure differential, or if using an

electrophoretic driving force, can describe the charge of the particle[153]. The background current of both transients, as well as the signal magnitude of the particle translocations, were in close agreement, although the simulated transient returned slightly lower values. This was most likely due to an overestimation in the pore length as assessed by Figure 4.3.

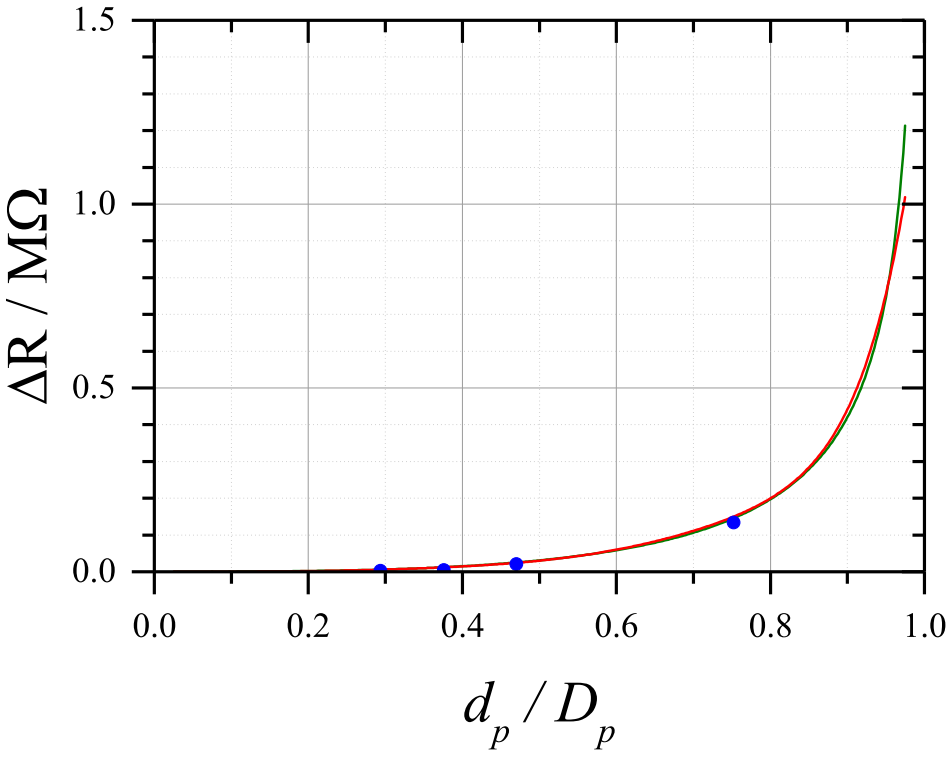


**Figure 4.6:** Signal magnitude ($\Delta R$) observed during the translocation of a microparticle through a cylindrical micropore as a function of the ratio of the particle ($d_p$) and pore ($D_p$) diameters. The green line was obtained by the simulation of an expanding spherical microparticle in the centre of a 40 $\mu$m Ø cylindrical micropore in 10 mM KCl. The red line was derived from Equation 1.32 using a polynomial correction factor[154,157]. The blue dots show the signals observed from experimental current transients recorded at −5 V *vs.* Ag/AgCl during the translocation of 18.8 ± 1.5 $\mu$m Ø microparticles ($7.2 \times 10^4$ particles $mL^{-1}$) through 25, 40, 50, and 64 $\mu$m Ø cylindrical micropores in anaerobic 10 mM KCl. For each of these experimental transients, the pressure differential applied to the micropore was −44 mBar and the temperature during the experiments was 28.8 °C.

The translocation of $18.8 \pm 1.5$ $\mu$m Ø particles was recorded through micropores with various diameters, and the change in resistance measured for these translocations was compared to both theoretical and simulated trends, as shown in Figure 4.6. This comparison revealed that the signal magnitude declined exponentially as the particle diameter was decreased and established a method for converting the signal magnitude to a particle diameter. The simulated and theoretical trends agreed well with each other, except at large particle-to-pore ratios, where Equation 1.32 fails to account for interactions between the particle and the insulating pore boundary[154]. The experimental translocation signals also appeared to agree with the other trends, but the exact change in resistance was difficult to determine due to the large background electrical noise. This effect obscured the signals given by small particle translocations, and could even become worse if the background current was further reduced (*i.e.* during the use of nanopores, the application of lower voltages, or the use of longer micropores). An alternative method for recording translocations in these conditions was necessary, and so a differential method was devised in order to improve the signal-to-noise ratio. In this method, the translocation signal was split into two channels, one of which was deliberately delayed using bandwidth filters[151]. The delayed channel was subtracted from the unfiltered channel to give a characteristic differential signal. Amplification of this signal made the translocations much easier to identify, whilst the subtraction of a second heavily filtered transient minimised the electrical noise.

Figure 4.7 shows an example differential transient used to record the translocation of $18.8 \pm 1.5$ $\mu$m Ø particles through a 40 $\mu$m Ø cylindrical pore. Differential signals attributed to particle translocations can be clearly seen throughout the transient, with changes in resistance of $21 \pm 2.5$ k$\Omega$. Whilst this agreed with the values determined in Figure 4.4, it should be noted that the conversion of the differential voltage to the change in resistance was performed using an amplification gain 10× higher than that used in the experiment. This was because of a design error which caused misalignment between the actual gain value and the value shown on the dial of the differential hardware. Therefore, the transient in Figure 4.7 was recorded with an amplification gain of 1000 V/V, rather than the reported 100 V/V. Whilst the data shown in Figure 4.7 is still correct, further work is needed to address this error and ensure the differential system works with the correct amplification. Regardless of the magnitude, the amplification of the signal and the subsequent subtraction of the heavily filtered transient gave the significantly larger signal-to-noise ratio of $\approx 6$ and also centered the output signal around 0 $\Omega$. Each translocation

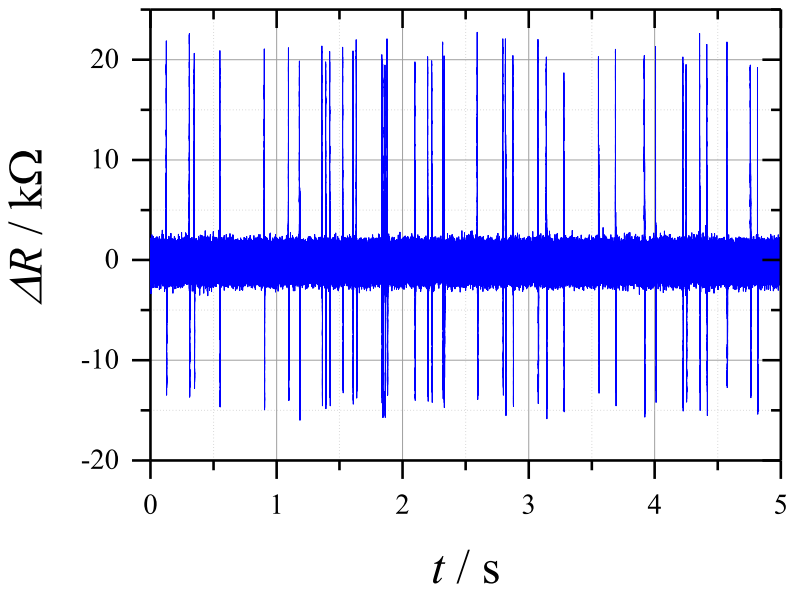


**Figure 4.7:** Differential transient recorded at −5 V *vs.* Ag/AgCl with a 40 $\mu$m Ø cylindrical micropore in aerobic 10 mM KCl. The plot shows the translocation of $18.8 \pm 1.5$ $\mu$m Ø microparticles ($7.2 \times 10^4$ particles mL$^{-1}$), recorded with the current-differential system. The pressure differential applied to the micropore was −43 mBar, the amplification of the differential signal was 100 V/V, and the temperature during the experiment was 30.9 °C. The conversion of differential voltage to change in resistance was performed assuming the real gain of the amplification was 1000 V/V.

gave both a positive and a negative signal, which aided in observation of the translocations and also distinguished them from high frequency noise spikes and permanent changes in the background current, which were both filtered out.

Figure 4.8 compares the signal shape of particle translocations recorded with both current and differential transients. The unique signal shape observed in the differential transient was closely related to the signal recorded with chronoamperometry, but differed as a result of the channel subtraction. Sharp peaks, both positive and negative, were seen during the entry/exit of the particle and were caused by the rapid response of the unfiltered channel. After each peak, the signal declined exponentially as the delayed response of the filtered channel caught up with, and was subtracted from, the unfiltered channel. Whenever the signal magnitude of the two channels was equal, the differential signal returned to 0 Ω. The magnitude of the first peak can be used to calculate particle diameter and the separation of the two peaks can be related to the translocation time.

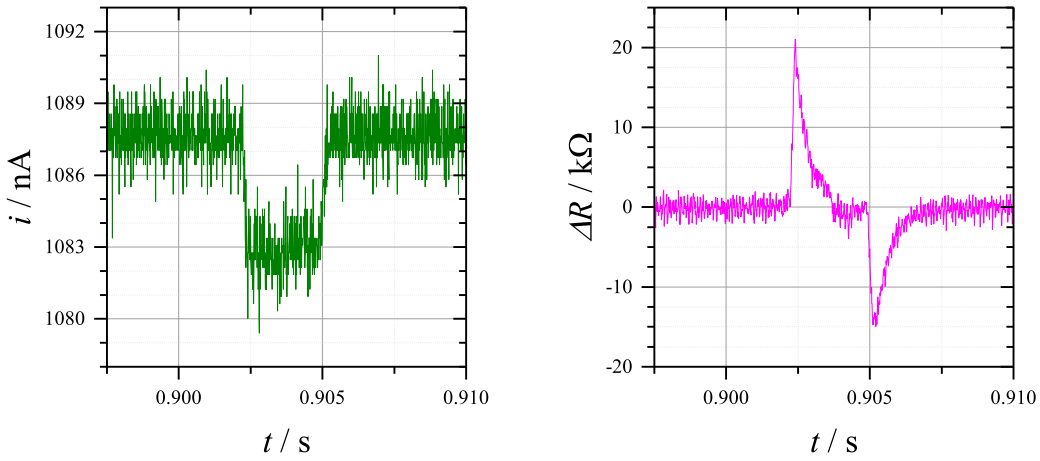


**Figure 4.8:** Current (LEFT) and differential (RIGHT) transients recorded at $-5$ V *vs.* Ag/AgCl with a 40 $\mu$m Ø cylindrical micropore in aerobic 10 mM KCl. Each plot shows the translocation of $18.8 \pm 1.5$ $\mu$m Ø microparticles ($7.2 \times 10^4$ particles mL$^{-1}$). The differential transient was recorded using the current-differential system, with a signal amplification of 100 V/V. The pressure differential applied to the micropore was $-43$ mBar, and the temperature during the experiment was 30.9 °C. The conversion of differential voltage to change in resistance was performed assuming the real gain of the amplification was 1000 V/V.

However, in the case of extremely fast translocations, the filtered channel would not have time to catch up with the unfiltered channel before the particle would exit the pore. As a result, the peaks would move closer together and the second peak would start before the first peak had relaxed to 0 Ω, causing the second peak to appear smaller.

Particle translocation through micropores had shown that the Coulter counting apparatus was operational and could be used for nanopore characterisation. Furthermore, the use of chronoamperometry and the new differential system to record translocation signals was successful. Throughout the project, several variations of these recording systems were devised, included current followers with different amplification gains, and differential systems that could be recorded independently (resistor bridge differential system) or in conjunction with a current follower (current differential system). These different recording systems were used interchangeably during the Coulter counting of nanopores, as will be shown later. However, during particle translocation through micropores, these different recording systems were also able to show where each parameter of the Coulter counting apparatus had the most impact.

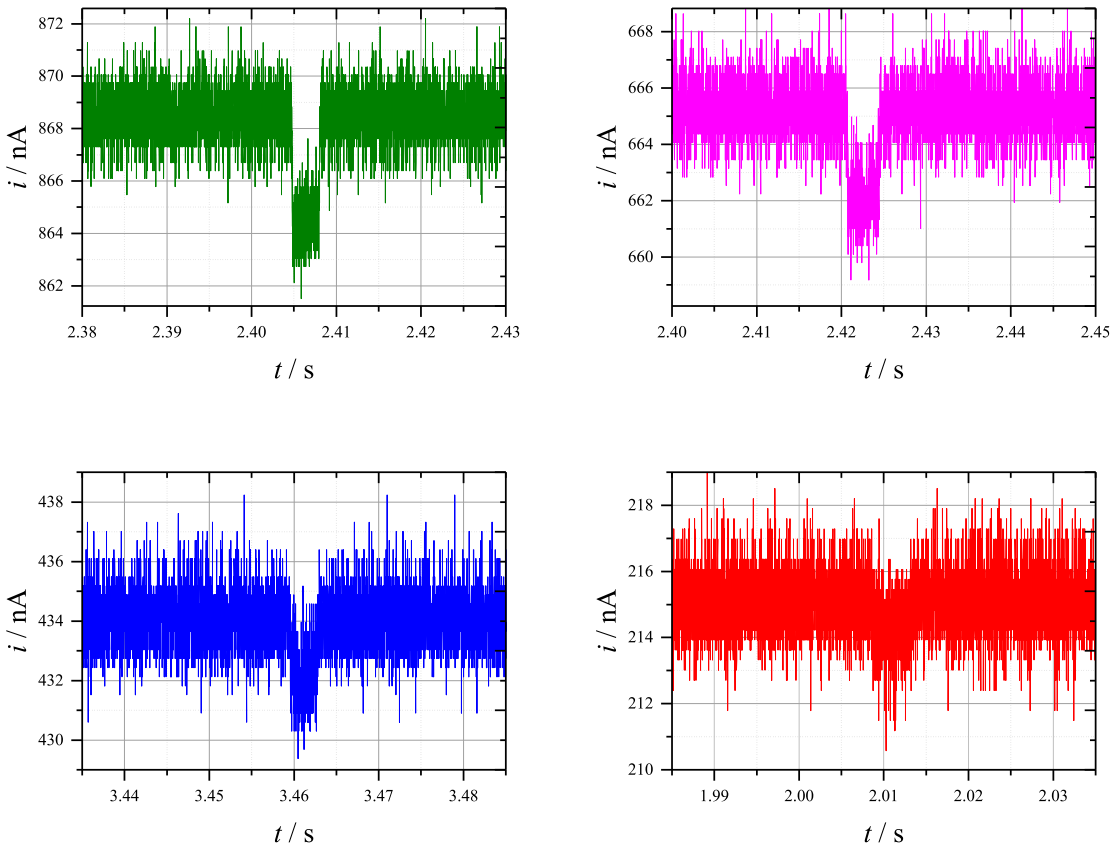


**Figure 4.9:** Current transients recorded at (GREEN) −4, (PINK) −3, (BLUE) −2, and (RED) −1 V *vs.* Ag/AgCl with a 40 $\mu$m Ø cylindrical micropore in aerobic 10 mM KCl. Each plot shows the translocation of an 18.8 ± 1.5 $\mu$m Ø microparticle ($7.2 \times 10^4$ particles $mL^{-1}$), recorded with the low gain ($10^6$ V/A) current follower system. The pressure differential applied to the micropore was −38 mBar and the temperature during the experiment was 26.1 °C.

One parameter that had a drastic effect on translocation signal was the applied voltage. Figure 4.9 shows the effect of different applied voltages on the current transients of an $18.8 \pm 1.5$ $\mu$m Ø particle translocating through a 40 $\mu$m Ø cylindrical pore. As the voltage was reduced, both the background current of the transients and the magnitude of the translocation signal decreased. This made the translocations more difficult to identify, despite the relatively large particle-to-pore ratio. Note that this effect was not a result of varying pore resistances, as there were no alterations to either the background resistance of the pore or the change in resistance incurred by particle translocation. The effect of voltage was more visible on the current transients rather than the differential transients, which could compensate for the poor signal-to-noise ratio using the amplification and second subtraction procedure.

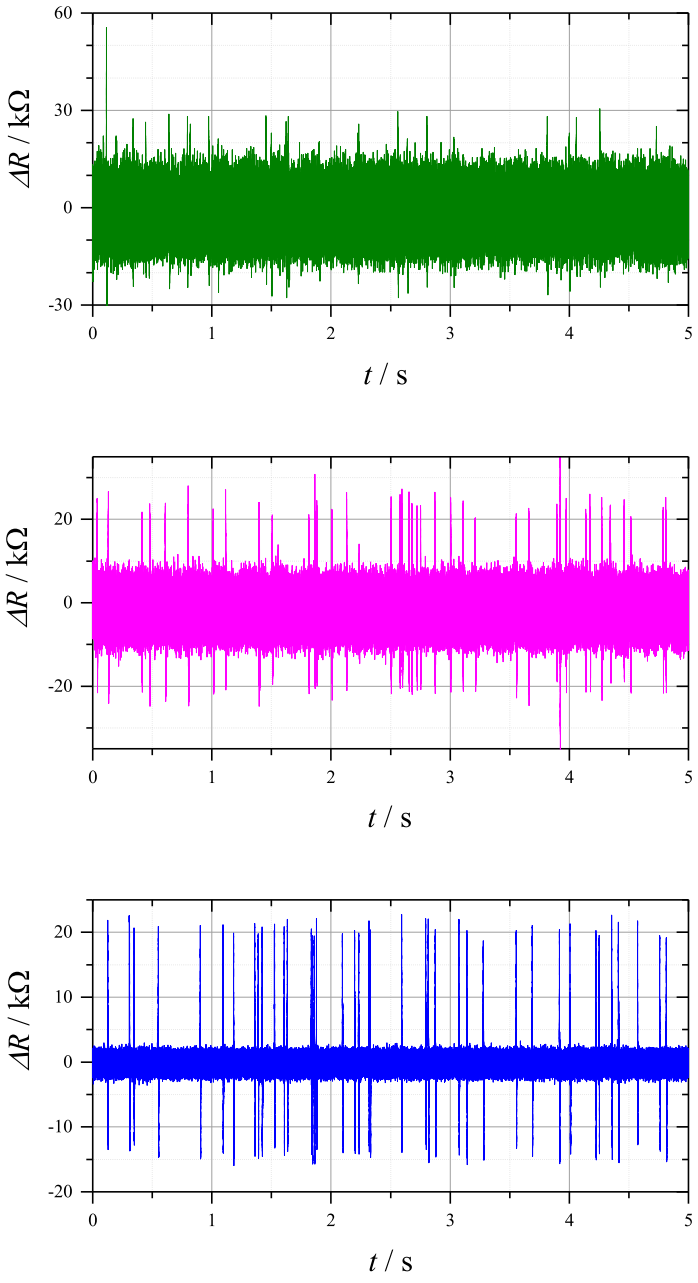


**Figure 4.10:** Differential transients recorded at −5 V *vs.* Ag/AgCl with a 40 $\mu$m Ø cylindrical micropore in aerobic 10 mM KCl. Each plot shows the translocation of $18.8 \pm 1.5$ $\mu$m Ø microparticles ($7.2 \times 10^4$ particles mL$^{-1}$), recorded with the current-differential system. The pressure differential applied to the micropore was −39 mBar, the amplification of the differential signal was: (TOP) 1 V/V; (MIDDLE) 10 V/V; and (BOTTOM) 100 V/V, and the temperature during the experiment was 25.3 °C. The conversion of differential voltage to change in resistance was performed assuming the real gain of the amplification was 10× higher than stated.

The improvement to the signal-to-noise ratio offered by the differential system was highly dependent on the gain of the amplification procedure. As shown in Figure 4.10, higher gain settings increased the magnitude of the translocation signals. Electrical noise was not amplified by the same factor, due the second subtraction of the heavily filtered transient. This resulted in the higher gain settings giving a larger signal-to-noise ratio. Again, these plots suffered from the design error described above, and each of these transients were in fact recorded with amplification gain 10× higher than that reported. This is accounted for in the conversion of the signals into change in resistance. Observation of particle translocations was simplified by higher amplification, but this parameter needed to be used in moderation. Too much amplification resulted in signal saturation, where the signal magnitude was limited to the battery voltage of the differential system, and time response delays, where high frequency components of the signal were lost.

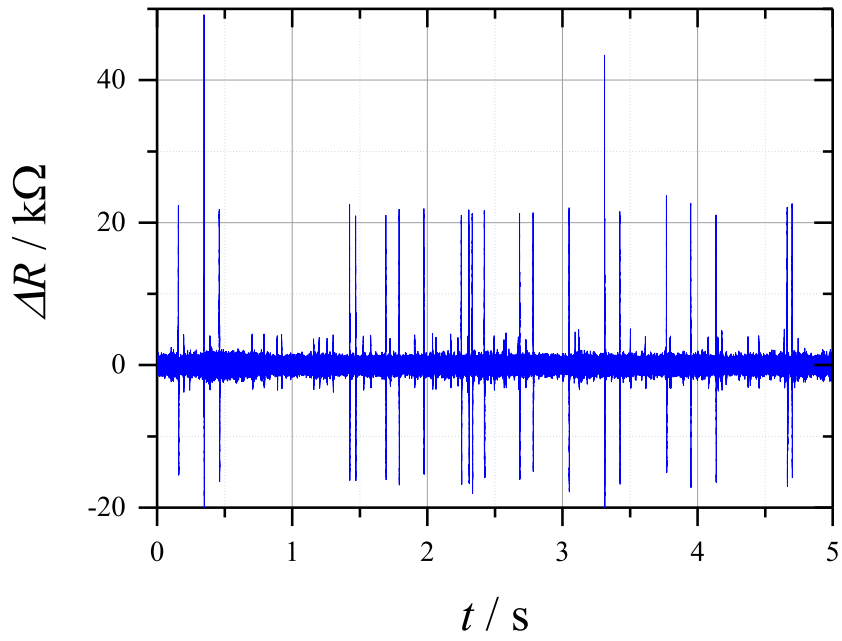


**Figure 4.11:** Differential transient recorded at −5 V *vs.* Ag/AgCl with a 40 $\mu$m Ø cylindrical micropore in aerobic 10 mM KCl. The plot shows the simultaneous translocation of 11 ± 1.1 and 18.8 ± 1.5 $\mu$m Ø microparticles, recorded with the current-differential system. The pressure differential applied to the micropore was −46 mBar, the amplification of the differential signal was 100 V/V, and the temperature during the experiment was 28.5 °C. The conversion of differential voltage to change in resistance was performed assuming the real gain of the amplification was 1000 V/V.

Used correctly, the amplification of a differential signal can enhance the observation of smaller particles and can also allow polydisperse particle suspensions to be analysed. To

illustrate this, the differential system was used to record the simultaneous translocation of 18.8 ± 1.5 $\mu$m and 11 ± 1.1 $\mu$m Ø particles through a 40 $\mu$m Ø cylindrical pore, as shown in Figure 4.11. The translocation of both particles was visible on the same gain setting, with the characteristic differential signal aiding in the identification of events. Smaller signals of 5 ± 2.1 kΩ were attributed to the translocation of the 11 ± 1.1 $\mu$m Ø particles, whilst the larger signals of 21 ± 2.1 kΩ were assigned to the translocation of 18.8 ± 1.5 $\mu$m Ø particles. Double events, caused by the translocation of more than one 18.8 ± 1.5 $\mu$m Ø particle at a time, were also visible. Conversely, the translocation of 11 ± 1.1 $\mu$m Ø particles was difficult to observe with chronoamperometry, as any translocation signals were obscured by the large electrical noise.

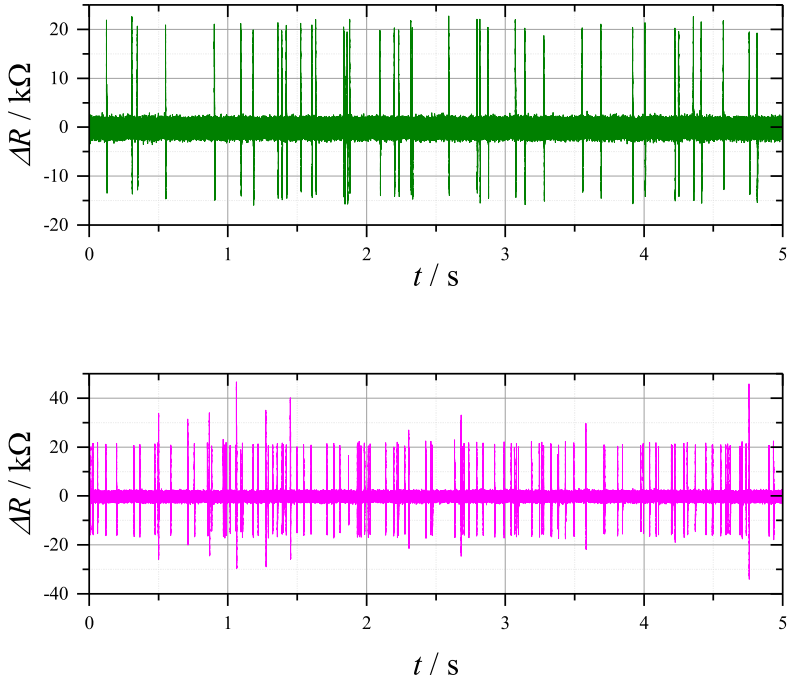


**Figure 4.12:** Differential transients recorded at −5 V *vs.* Ag/AgCl with a 40 $\mu$m Ø cylindrical micropore in aerobic 10 mM KCl. Each plot shows the translocation of 18.8 ± 1.5 $\mu$m Ø microparticles ($7.2 \times 10^4$ particles mL$^{-1}$), recorded with the current-differential system. The pressure differentials applied to the micropore were (TOP) −38 mBar and (BOTTOM) −93 mBar, the amplification of the differential signal was 100 V/V, and the temperature during the experiment was 26.1 °C. The conversion of differential voltage to change in resistance was performed assuming the real gain of the amplification was 1000 V/V.

Other parameters that influenced the translocation of particles were the pressure applied to the pore and the particle/bubble concentration. Figure 4.12 shows how the

application of increased pressures resulted in a greater number of particle translocation events. The higher pressure resulted in an increased flow rate, which caused more particles to translocate through the pore over a given period. The same effect can be obtained by increasing the particle concentration instead. The advantage of using higher pressures/greater particle concentrations is that it increases the number of events, leading to better analysis of the particles size distribution. This effect is particularly important for smaller pores, where the reduced dimensions can minimise the flow rate. However, it also increases the chance of double events and of a particle partially or completely blocking the pore, which results in a dramatic and permanent drop in current. Blocking also becomes more frequent when using longer channels and larger pore-to-particle ratios. The effect of higher pressures and greater concentrations was more visible with the differential system, but the partial and complete blocking events were easier to spot with chronoamperometry.

## 4.3 Coulter counting through conical micropores

The particle translocations used to test the Coulter counting apparatus were recorded using a cylindrical micropore. However, the nanopores prepared by the etching of W nanoelectrodes will have a conical/exponential geometry. This geometry will produce translocation signals with different shapes and may also affect the signal magnitude[153,160,192]. In order to observe the expected signal shape for translocation through a nanopore, and to test if the Coulter counting apparatus was able to record such signals, the translocation of microparticles was also recorded through conical micropores. In order to obtain conical micropores, W nanoelectrodes were polished until they were several micrometres in diameter, then the W metal was completely removed with a chemical etching solution of 250 mM $K_2S_2O_8$ + 2 M NaOH. This etching was more gentle, albeit slower than electrochemical etching, and was used in an effort to avoid any damage to the resulting pores.

After the chemical etching procedure was complete, the conical micropore was characterised by cyclic voltammetry and optical microscopy. Figure 4.13 shows an example optical microscope image of a conical W microelectrode before and after chemical etching. The image before etching showed both the W tip and its reflection in the highly polished glass surface. This was used alongside voltammetry in $Ru(NH_3)_6Cl_3$ to determine when

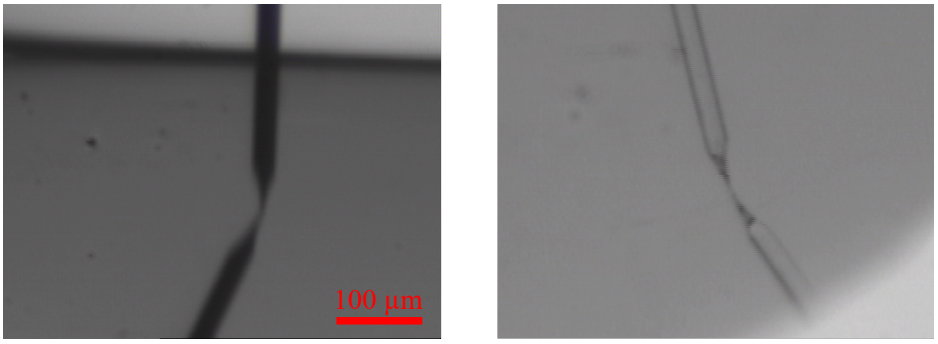


**Figure 4.13:** Optical microscope images of a 2 $\mu$m Ø W microelectrode before (LEFT) and after (RIGHT) complete chemical etching in a solution of 250 mM $K_2S_2O_8$ + 2 M NaOH. Each image was recorded at 6× magnification, with the electrode/pore submerged in $H_2O$ to minimise the distortion from the refractive index of the glass.

the electrode had been polished to the desired diameter. The image after etching showed the outline of the micropore in the glass, and was used to confirm the complete removal of the W metal. The images were focussed on the conical part of the electrode/pore, since the dimensions of this part cause more current restriction than the cylindrical channel behind it. The half cone angle of the micropore shown in Figure 4.13 was determined to be $\approx 11°$, which agreed well with the values derived from the cyclic voltammetry of the pore recorded in an electrolyte solution. The dimensions derived from these images are important for explaining the shape of a translocation signal and for calculating the background resistance of the pore.

Figure 4.14 shows the translocation of $4.9 \pm 0.04$ $\mu$m Ø particles through an $\approx 8$ $\mu$m Ø conical micropore. Particle translocations were observed throughout the transient, and were identified by $75 \pm 2.5$ nA signals. This corresponds to a resistance change of $2 \pm 0.13$ kΩ, which was an order of magnitude smaller than the signal recorded using a cylindrical micropore. The change in resistance calculated by Equation 1.32 is directly proportional to the solution resistivity, which explains the smaller change in resistance recorded in 1 M KCl. Furthermore, the relationship between the resistance change and the particle-to-pore ratio may vary to the one shown in Figure 4.6 as a result of the conical geometry. High concentrations of electrolyte were used to increase the background pore current, which allowed the current to be more easily recorded with low gain amplifications and resulted in larger current changes being observed. However, the excessive use of electrolyte may also result in the agglomeration of charged particles.

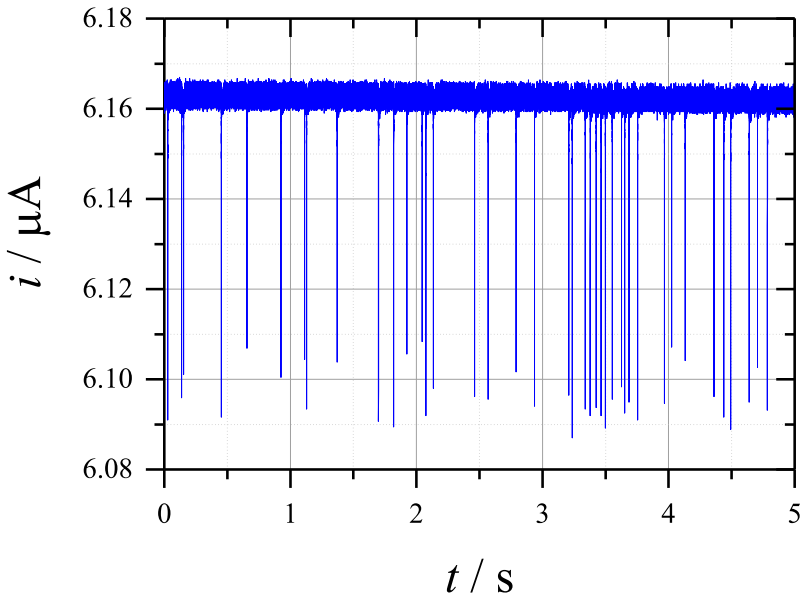


**Figure 4.14:** Current transient recorded at −1 V *vs.* Ag/AgCl with an ≈ 8 $\mu$m Ø conical micropore in aerobic 1 M KCl. The plot shows the translocation of 4.9 ± 0.04 $\mu$m Ø microparticles ($7.2 \times 10^4$ particles $mL^{-1}$), recorded with the low gain ($10^6$ V/A) current follower system. The pressure differential applied to the micropore was −36 mBar and the temperature during the experiment was 26.2 °C.

The conical geometry of the micropores also affected the shape of the translocation signals. Figure 4.15 shows an expanded view of a microparticle translocation from Figure 4.14 and compares it to a simulated translocation. This simulation was obtained independently of time and liquid flow, by stepping the position of the particle through a pore that was built using the estimated dimensions from Figure 4.13. As opposed to the symmetrical signals observed with cylindrical pores, highly asymmetric signals were obtained with conical geometries, which was consistent with reported observations[153,160,192]. Entry of the particle into the pore caused a sharp drop in current, since the mouth of the pore was where the most voltage was dropped and therefore where the sensing of particles occurred[193]. The subsequent exponential decline was attributed to the varying particle-to-pore ratio as the particle translocated through the remainder of the pore. This is in contrast to the cylindrical pores, in which the entire channel was a sensing zone, giving signals as the particle entered and exited the pore. Despite there being no peak at the moment the particle exited the pore, the differential signals recorded with a conical micropore exhibited both positive and negative peaks. The negative peak originated from the filtering of the particle entry signal, which caused the high frequency data from this process to appear at

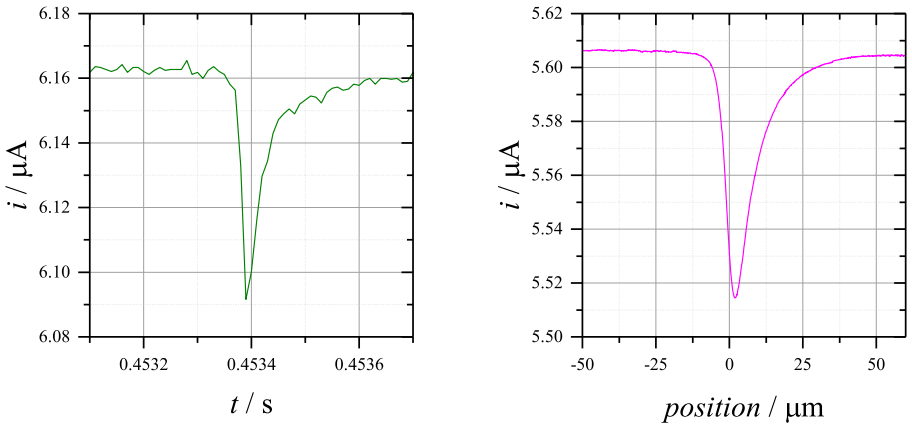


**Figure 4.15:** Experimental (LEFT) and simulated (RIGHT) current transients recorded at −1 V *vs.* Ag/AgCl with an ≈ 8 $\mu$m Ø conical micropore in aerobic 1 M KCl. The plots compare the signal shape observed during the translocation of 4.9 ± 0.04 $\mu$m Ø microparticles ($7.2 \times 10^4$ particles $mL^{-1}$), recorded with the low gain ($10^6$ V/A) current follower system. For the experimental transient, the pressure differential applied to the micropore was −34 mBar and the temperature during the experiment was 26.2 °C.

later timescales in the delayed channel. When subtracted from the unfiltered channel, this caused the output signal to temporarily drop below 0 Ω, resulting in the appearance of a small negative peak. Particle translocation took place over ≈ 0.3 ms, which was an order of magnitude faster than with cylindrical micropores. The faster time was a result of the increased flow velocities required to maintain mass continuity through the smaller pore diameter and the smaller sensing area focussed around the mouth of the nanopore[161,193]. Similarities between the shapes of the experimental and simulated signals indicated the Coulter counting apparatus had sufficient time resolution to record the faster translocations. However, slight discrepancies between the two examples, such as the simulated signal displaying a larger magnitude and a smaller background current, suggested either the underestimation of experimental peak height due to the bandwidth of the electronics or inaccuracies in the simulation due to incorrect estimations of the pore dimensions[153].

## 4.4 Characterisation of glass nanopores

After the Coulter counting apparatus had been sufficiently tested using microparticle translocations, it could be employed in the characterisation of the glass nanopores pre-

pared by the complete etching of W nanoelectrodes. As with the W nanoelectrodes, the diffraction limit of visible light prevented the nanopores from being characterised by optical microscopy, and the lack of a conductive surface made electron microscopy unsuitable for routine characterisation. Therefore, the dimensions of the pores were instead assessed using electrochemical techniques.

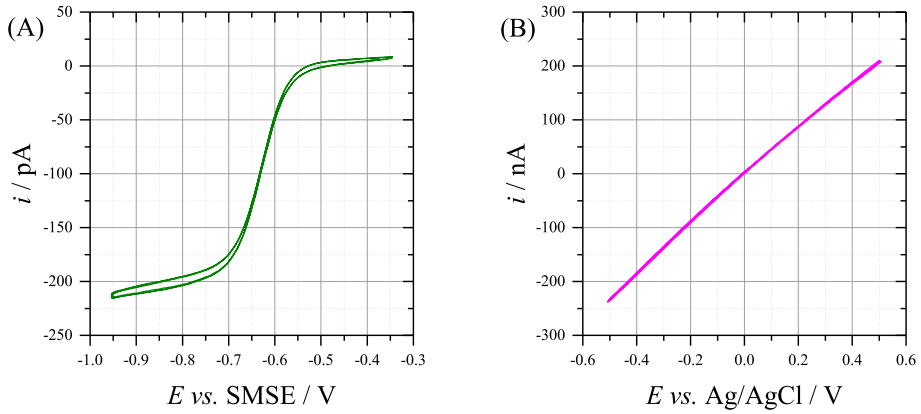


**Figure 4.16:** Cyclic voltammograms recorded at 50 mV $s^{-1}$ with: (LEFT) a ≈ 360 nm Ø W nanoelectrode in anaerobic 5 mM $Ru(NH_3)_6Cl_3$ + 100 mM $K_2SO_4$ (pH 3.5); and (RIGHT) the subsequent ≈ 360 nm Ø conical nanopore in aerobic 1 M KCl (pH 6.5).

Figure 4.16 shows an example of the cyclic voltammetry recorded with a W nanoelectrode before chemical etching and with the subsequent nanopore after chemical etching. The voltammetry of the W nanoelectrode showed a steady state response, with the limiting current being used to calculate an electrode diameter of ≈ 360 nm. Conversely, the voltammetry of the nanopore gave an Ohmic response, defined by the background resistance of the restrictive pore dimensions. The diameter derived from the voltammetry of the nanoelectrode was used to estimate the dimensions of the nanopore, using Equation 4.2[159].

$$R_p = \frac{1}{\kappa r_p}\left(\frac{1}{\pi \tan(\theta)} + \frac{1}{4}\right) \tag{4.2}$$

where $R_p$ is the background resistance of the pore; $\kappa$ is the conductivity of the electrolyte; $r_p$ is the radius of the pore; and $\theta$ is the half cone angle of the pore. In the case of Figure 4.16, the half cone angle of the nanopore was estimated as $\approx 5°$, which was slightly larger than the full cone angle of the W nanotips assessed by electron microscopy. However,

it should be noted that errors in the cone angle can propagate into large errors in the estimated radius. Therefore, the formula in Equation 4.2 should only be used to estimate the pore radius. The Ohmic response of the nanopore was slightly rectified, with the negative currents appearing larger than the positive currents. Similar observations reported for glass nanopores have been attributed to the negative charge of OH groups on the surface of the glass[194,195]. In low conductivity electrolytes, this charge extends far into the mouth of the pore, excluding anions from passing through. Depending on the polarity of the applied voltage, this can cause the apparent electrolyte concentration in the pore to either increase or decrease. Whilst this effect is usually only observed on much smaller nanopores, the rectification effect seen in Figure 4.16 was consistently seen on the nanopores generated in this work, even in high conductivity electrolytes. Modification of the OH groups of the glass surface has been reported to reduce this rectification effect, but attempts to do so with the nanopores made by W nanoelectrode etching gave mixed results[160].

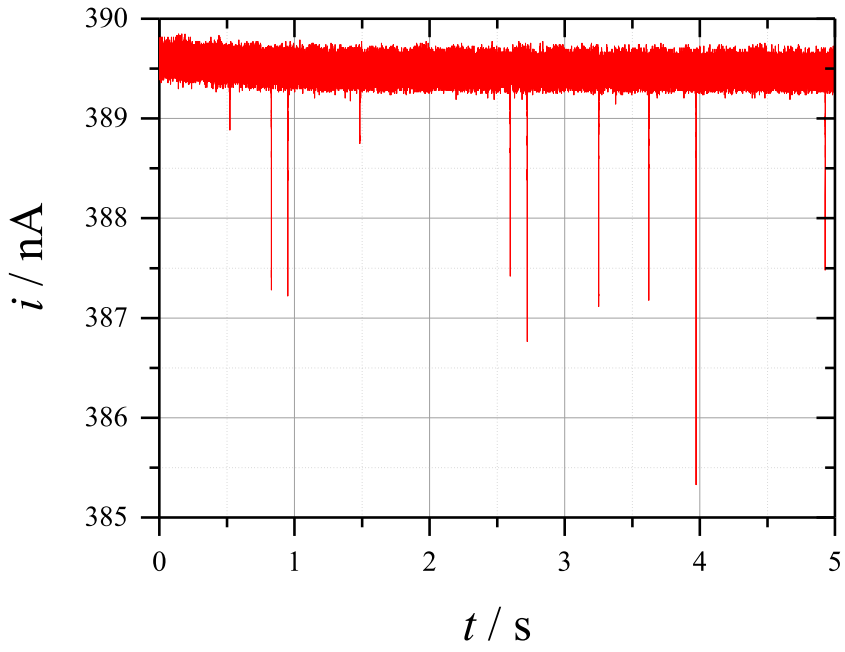


**Figure 4.17:** Current transient recorded at −1 V *vs.* Ag/AgCl with an ≈ 800 nm Ø conical nanopore in aerobic 1 M KCl. The plot shows the translocation of 600 ± 9 nm Ø nanoparticles ($1 \times 10^7$ particles $mL^{-1}$), recorded with the low gain ($10^7$ V/A) current follower system. The pressure differential applied to the nanopore was −34 mBar and the temperature during the experiment was 27.2 °C.

Further characterisation was performed by recording the translocation of 600 ± 9 nm

Ø particles through an ≈800 nm Ø nanopore, as shown by the current transient in Figure 4.17. The magnitude of the stable background current of 38.95 ± 0.25 nA was consistent with the resistance of an 800 nm Ø nanopore with a half cone angle of 1.25°. During the transient, several 2 ± 0.25 nA signals were observed, indicating the translocation of the nanoparticles. This signal magnitude corresponded to a resistance change of 13.3 ± 0.3 kΩ. A possible double event was also recorded, but in general there were very few translocations observed throughout the transient. This was a result of the small nanopore dimensions, which drastically reduced the flow rate through the nanopore[161]. High concentrations of electrolyte were used to avoid the problems encountered at small pore diameters, such as difficulty in recording the low currents and increased ion rectification and electroosmotic flow effects[153]. A higher current follower amplification gain was also used to better observe the low currents recorded with the nanopore. This had the added benefit of reducing the background electrical noise (0.5 nA) compared to previous current transients.

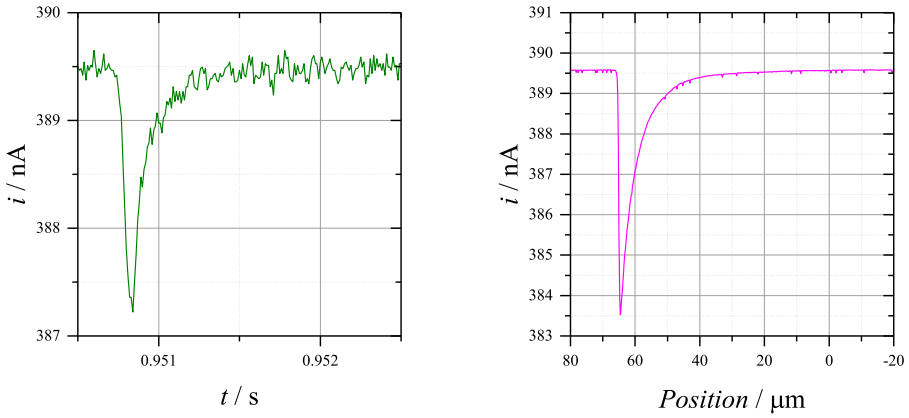


**Figure 4.18:** Experimental (LEFT) and simulated (RIGHT) current transients recorded with an ≈800 nm Ø conical nanopore in aerobic 1 M KCl. The plots compare the translocation of 600 ± 9 nm Ø nanoparticles ($1 \times 10^7$ particles $mL^{-1}$), recorded with the low gain ($10^7$ V/A) current follower system. The experimental transient was recorded at −1 V *vs.* Ag/AgCl with a pressure differential of −34 mBar applied to the nanopore. The simulated transient was obtained by moving the nanoparticle by 200 nm increments through the centre of the nanopore, assuming a half cone angle of 1.25° and a pore diameter of 900 nm (see appendix for more details).

Insight into the geometry and dimensions of the nanopore were provided by analysis of the translocation signal shape. Figure 4.18 shows an expanded view of a nanoparticle translocation from Figure 4.17 and compares it to a simulated translocation. This simulation was obtained independently of time and liquid flow, by stepping the position of the

particle through a modelled pore. The asymmetric shape of the particle translocation was similar to that seen with conical micropores, with a sharp increase in resistance, followed by an exponential decline returning to the background resistance. Similarly, the particle translocation took place over $\approx 0.5$ ms. Since the exact geometry of the nanopore was unknown, the simulation shown in Figure 4.18 was obtained by varying the geometry parameters until the result best fitted that of the experimental translocation. This fitting gave a nanopore diameter of 900 nm and half cone angles of 1.25° at the pore of the mouth, and 10° at the transition between exponential and conical geometry. Such fitting of simulations could be used in the future to provide further nanopore characterisation. However, fitting was complicated by the often contradictory effects each geometry parameter had on the signal magnitude and the background resistance. In the case of Figure 4.18, the background resistance was similar to experimental observations, but the signal magnitude was much greater than expected. This could be due to inaccuracies in the simulation, which assumed conical rather than exponential geometries, or an issue with the apparatus, such as underestimation of the signal magnitudes due to data loss from the bandwidth of the electronics[153].

The effect of geometry on the translocation shape was demonstrated with simulations of a $600 \pm 9$ nm Ø particle translocating through 800 nm Ø nanopores with different half cone angles. The comparison between these simulations is shown in Figure 4.19. Despite each simulation sharing the same nanopore/nanoparticle diameters, smaller changes in current were observed with the most acute nanopores. This was due to the decreased background current at acute angles, caused by the more restrictive pore dimensions. Broader signals were also observed with more acute nanopores, causing the exponential decay to be drawn out over longer distances. This was a result of the pore geometry approaching that of a cylinder, meaning the sensing zone would be spread out more over the pore, and the particle-to-pore ratio would be higher for longer periods[193]. The half cone angle is one of the many parameters that can influence the translocation signal shape and magnitude relationship, and can be used to fit simulations to experimental translocations for further characterisation. However, it is worth noting that these simulations were recorded using a fixed pore length. In reality the effect would be much more dramatic, with the more acute nanopores giving signals approaching those observed with cylindrical pores. Furthermore, the half cone angle has been shown to affect the degree of ion rectification and electroosmotic flow seen with the nanopores[194] and the flow of liquid through the pore[161].

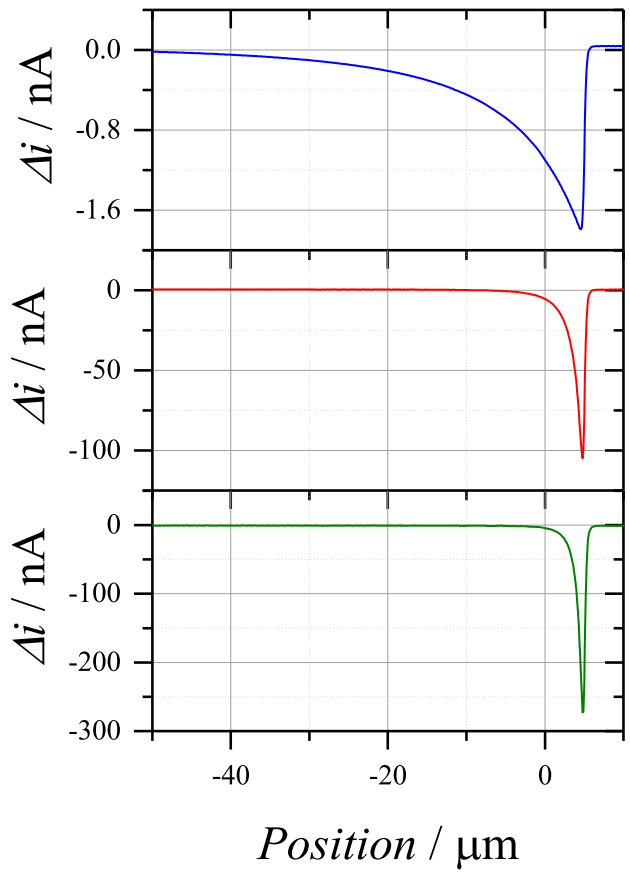


**Figure 4.19:** Simulated current transients showing the translocation of a 600 nm Ø nanoparticle through 800 nm Ø conical nanopores with half cone angles of (TOP) 0.5°, (MIDDLE) 5°, and (BOTTOM) 10°. The transients were simulated in 100 mM KCl with an applied voltage of −1 V *vs.* Ag/AgCl.

The differential system was also used to measure the translocation of 600 ± 9 nm Ø particles through an ≈ 800 nm Ø nanopore. Several differential signals attributed to particle translocation were observed during the transient, shown in Figure 4.20. These signals were 16 ± 1 kΩ in magnitude, which was in close proximity to the magnitude observed in Figure 4.17. The shape of the differential signal was also similar to that observed with conical micropores, with a large positive peak and a small negative peak, the latter of which was a result of the subtraction of the delayed channel. Whilst the number of translocations recorded was still low, the translocations were much easier to observe, with an excellent signal-to-noise ratio of ≈ 16. This was a result of the resistor bridge differential system that was employed, which was more suitable than chronoamperometry for the measurement of smaller nanoparticles/nanobubbles.

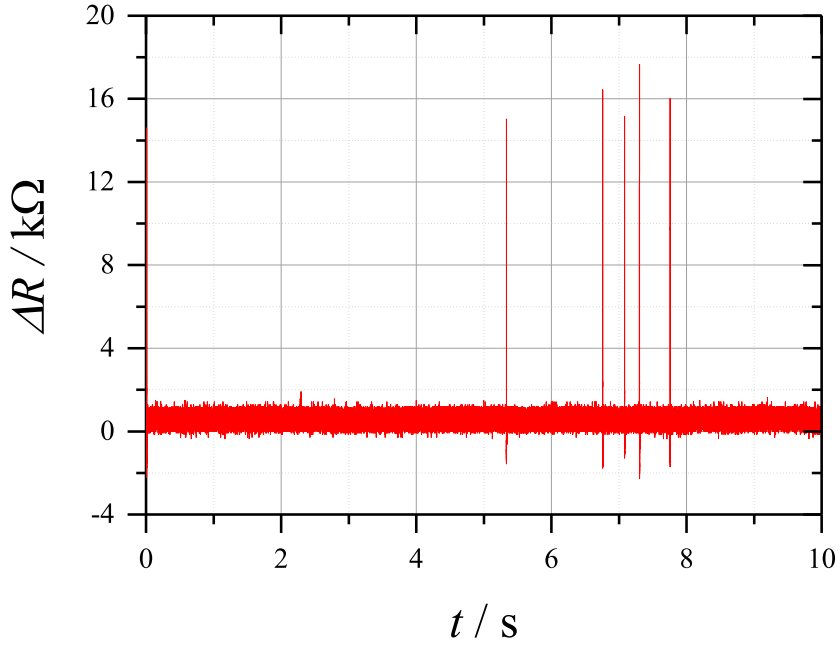


**Figure 4.20:** Differential transient recorded at −1 V *vs.* Ag/AgCl with a ≈ 800 nm Ø conical nanopore in aerobic 1 M KCl. The plot shows the translocation of 600 ± 1.5 nm Ø nanoparticles ($1 \times 10^7$ particles $mL^{-1}$), recorded with the resistor bridge differential system. The pressure differential applied to the micropore was −49 mBar, the amplification of the differential signal was 1000 V/V, and the temperature during the experiment was 27.5 °C.

Figure 4.21 shows the differential transient used to record the translocation of 100 ± 15 nm Ø particles through an ≈ 800 nm Ø nanopore. The number of translocations observed was far greater than in the transient shown in 4.20, which is due to the dramatic increase in the particle concentration, in turn caused by the large decrease in particle volume. However, the signal magnitudes were varied, indicating the simultaneous translocation of several particles[152]. This was believed to be caused by use of 1 M KCl, which neutralised the slight charges on the surface of the nanoparticles, resulting in their agglomeration. Whilst this transient shows that smaller nanoparticles can be sized with the differential method, accurate measurements of the nanoparticles would require less agglomeration. This could be achieved by lowering the electrolyte concentration and using a smaller pore diameter, but both of these precautions would also reduce the background current of the nanopore, making translocations more difficult to observe and creating a demand for more sensitive apparatus.

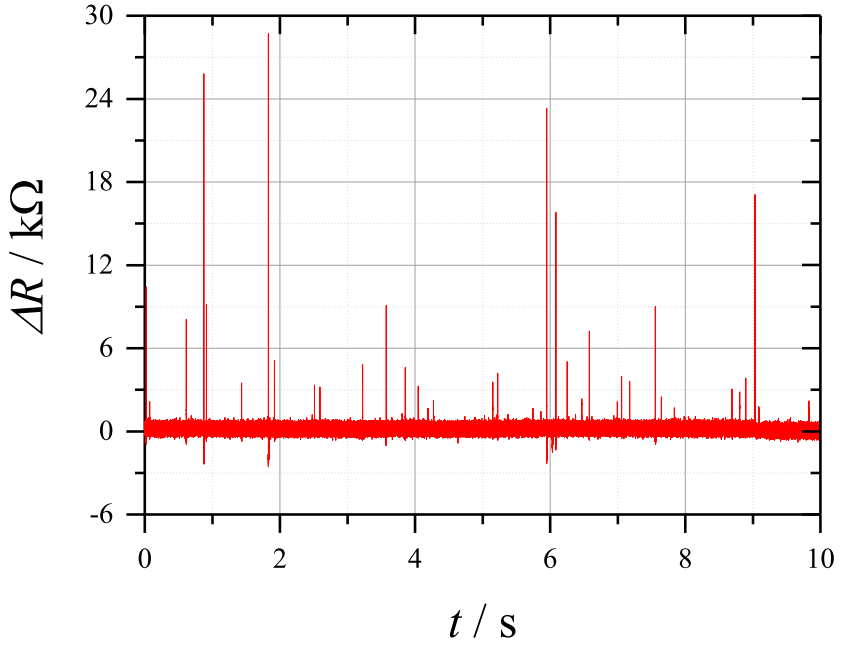


**Figure 4.21:** Differential transient recorded at −1 V *vs.* Ag/AgCl with a ≈ 800 nm Ø conical nanopore in aerobic 1 M KCl. The plot shows the translocation of 100 ± 15 nm Ø nanoparticles ($2.1 \times 10^9$ particles $mL^{-1}$), recorded with the resistor bridge differential system. The pressure differential applied to the micropore was −77 mBar, the amplification of the differential signal was 1000 V/V, and the temperature during the experiment was 27.5 °C.

The increased signal magnitude given by translocation through smaller diameter nanopores could be used to better observe smaller nanoparticles and nanobubbles. Figure 4.22 shows the transients used to record the translocation of 220 ± 17.6 nm Ø particles through a ≈ 520 nm Ø nanopore. Despite the high particle concentration, there were very few translocations observed through the nanopore. This was due to the decreased flow rate through the reduced dimensions of the pore[161]. Note that electroosmotic flow in the opposite direction was not expected in this scenario, due to the use of high electrolyte concentrations[153]. Methods to resolve the low number of translocations have been reported, and include exerting fine control over the pressure[196] or electroosmotic flow[153,197] to cause a single particle to repeatedly translocate. Attempts to increase the number of translocations by applying a greater pressure differential did not work, contrary to reports on the translocation of nanoparticles under different pressures[152,195]. Furthermore, the translocations were still relatively varied, suggesting the particles were still agglomerating in the high electrolyte concentrations.

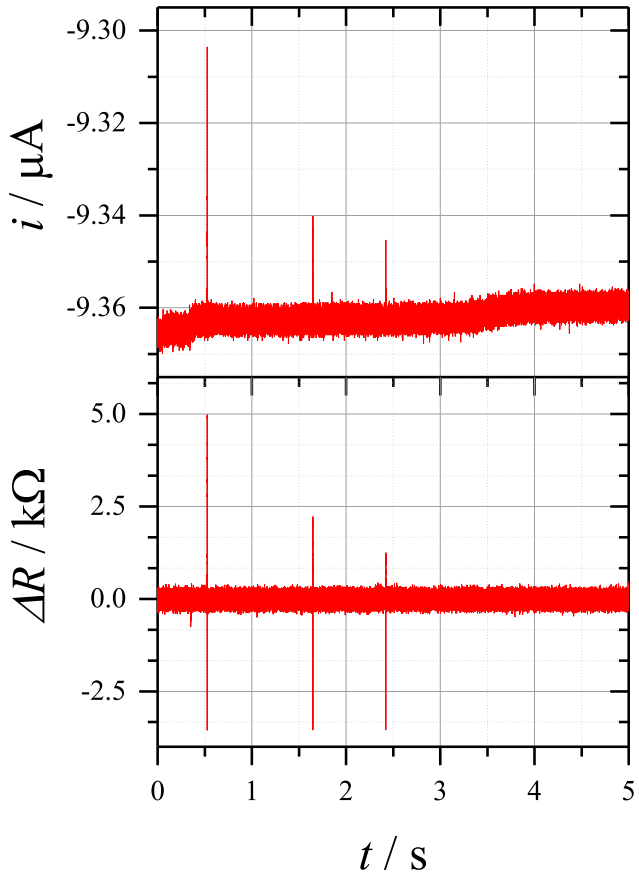


**Figure 4.22:** Current and differential transients recorded at −5 V *vs.* Ag/AgCl with a ≈ 520 nm Ø conical nanopore in aerobic 1 M KCl. The plots show the translocation of 220 ± 17.6 nm Ø nanoparticles ($1.4 \times 10^{10}$ particles $mL^{-1}$), recorded with the low gain ($10^6$ V/A) current-differential system. The gain of the differential signal amplification was 100 V/V. The pressure differential applied to the micropore was −36 mBar and the temperature during the experiment was 30.0 °C.

Agglomeration could also be minimised by using lower concentrations of the electrolyte. This would allow the translocation of single particles to be observed, resulting in the increased accuracy of the sizing. Figure 4.23 shows the transients used to record a 220 ± 17.6 nm Ø particle translocating through a ≈ 450 nm Ø pore. Once again, the small dimensions of the pore restricted the liquid flow, resulting in relatively few translocations being seen. However, the use of lower electrolyte concentrations seemed successful, with a visible translocation showing a current signal of 22 ± 2 nA, which corresponds to a resistance change of 400 ± 7.3 kΩ. The visibility of this signal was clear despite the lower background current given by the lower electrolyte concentration.

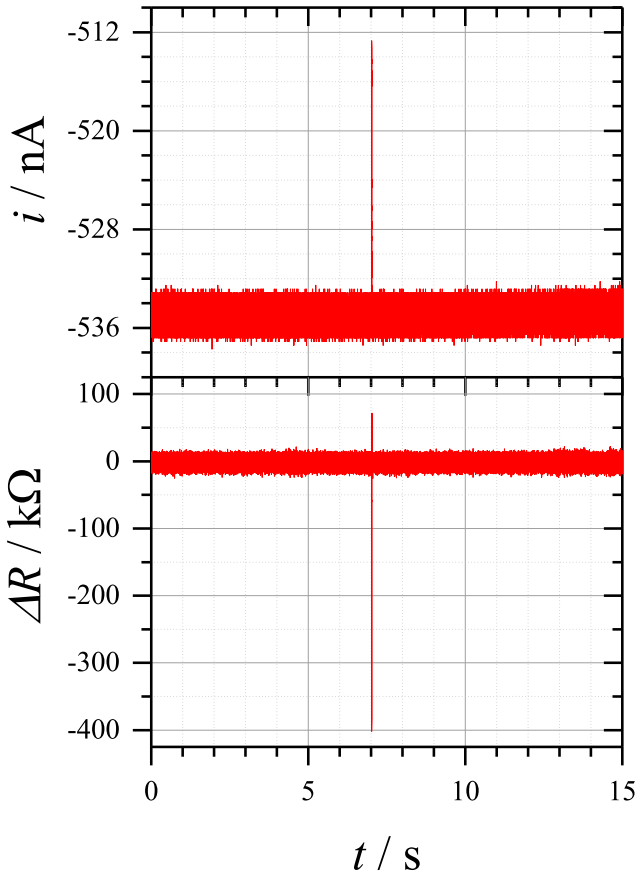


**Figure 4.23:** Current and differential transients recorded at −5 V *vs.* Ag/AgCl with a ≈ 450 nm Ø conical nanopore in aerobic 100 mM KCl. The plots show the translocation of 220 ± 17.6 nm Ø nanoparticles ($1.4 \times 10^{10}$ particles $mL^{-1}$), recorded with the low gain ($10^6$ V/A) current-differential system. The gain of the differential signal amplification was 100 V/V. The pressure differential applied to the micropore was −56 mBar and the temperature during the experiment was not recorded.

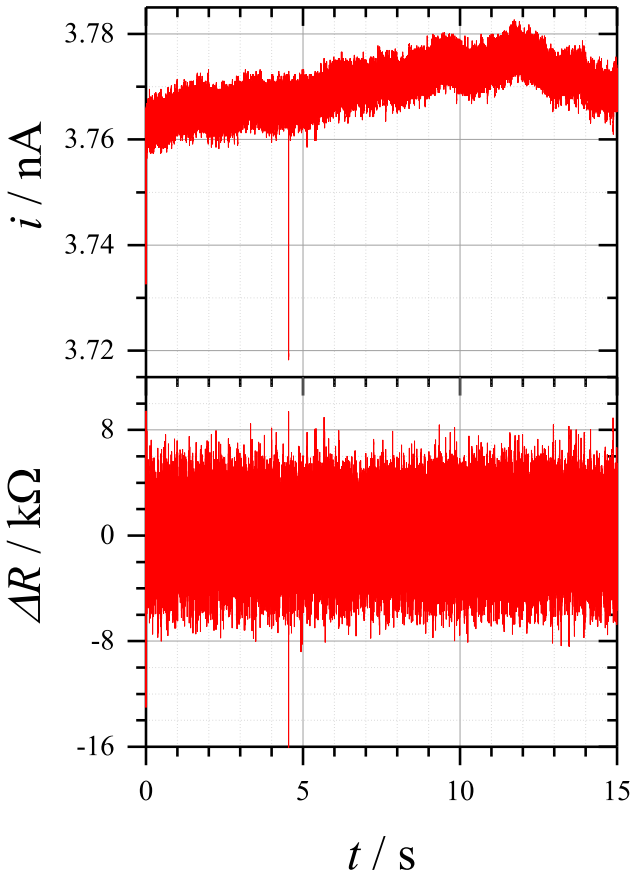


**Figure 4.24:** Current and differential transients recorded at −220 mV *vs.* Ag/AgCl with a ≈ 520 nm Ø conical nanopore in aerobic 10 mM KCl. The plots show the translocation of 220 ± 17.6 nm Ø nanoparticles ($1.4 \times 10^{10}$ particles $mL^{-1}$), recorded with the high gain ($10^9$ V/A) current-differential system. The gain of the differential signal amplification was 10000 V/V. The pressure differential applied to the micropore was −53 mBar and the temperature during the experiment was 21.5 °C.

Attempts to further decrease the electrolyte concentration resulted in background currents too low to be recorded with a $10^6$ V/A current follower, and in translocation signals that were too small to be observed. Therefore, the amplification of the current follower was increased to $10^9$ V/A, allowing smaller signals to be detected. Figure 4.24 shows the transients used to record the translocation of 220 ± 17.6 nm Ø particles through a ≈ 520 nm Ø nanopore. A current signal of 45 ± 10 pA was observed, corresponding to a resistance change of 750 ± 310 kΩ. Note that lower voltages were applied in order to avoid saturation from the batteries at ≈ 5 nA. Large amounts of noise were seen in the differential transient, and the change in resistance was inconsistent with the value determined

by chronoamperometry. This suggested that the $10^9$ V/A amplification was suitable for increasing the current follower sensitivity, but was incompatible with the differential signal generator. The pore also suffered from a low number of translocations as a result of the reduced pore dimensions. However, switching polarity showed that there were still no observable electroosmotic forces, despite the presence of strong ion rectification. The study of nanoparticles/nanobubbles with smaller nanopores therefore seemed to naturally come with the downside of fewer translocations.

## 4.5 Coulter counting through micropipettes

Nanopores prepared from the chemical etching of W nanoelectrodes were chosen for their durability, as well as for the ability to characterise the nanoelectrodes prior to etching. However, the use of pipette pulling to generate nanopores has recently become widespread, providing the advantages of reproducibility and a low aspect ratio. The Coulter counting of nanoparticles was performed with pulled pipettes in order to determine whether they were more effective at recording the translocation of nanoparticles.

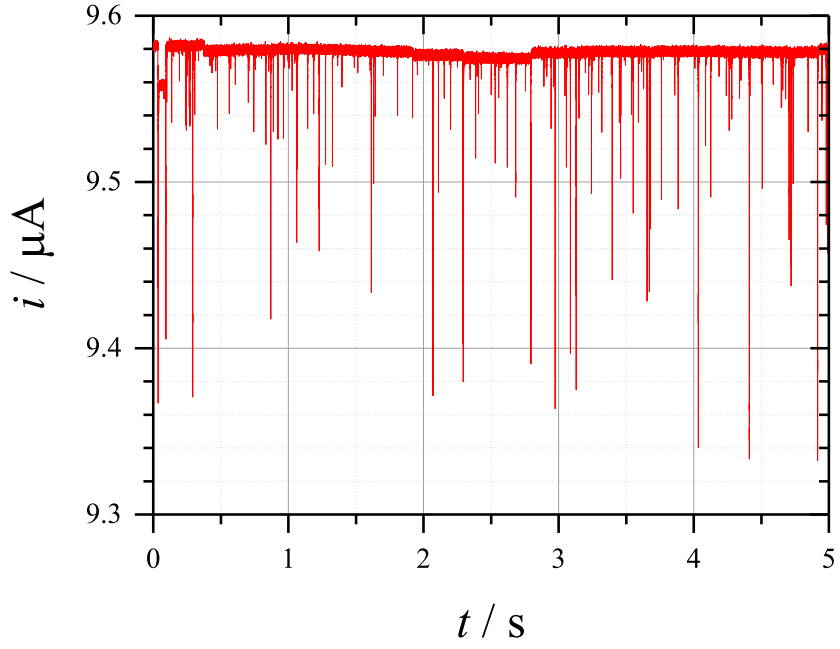


**Figure 4.25:** Current transient recorded at −4 V *vs.* Ag/AgCl with a ≈1000 nm Ø conical nanopipette in aerobic 1 M KCl. The plot shows the translocation of 900 ± 12 nm Ø nanoparticles ($7.5 \times 10^7$ particles $mL^{-1}$), recorded with the low gain ($10^6$ V/A) current-differential system. The pressure differential applied to the micropore was −94 mBar and the temperature during the experiment was 23.0 °C.

Figure 4.25 shows the current transient used to record the translocation of 900 ± 12 nm Ø particles through a ≈1000 nm Ø pulled pipette. Prior to recording this transient, optical microscopy was used to estimate the pipette dimensions, but the proximity of this pipette to the resolution limit caused inaccuracies in this assessment. Without a method to determine the diameter of the pipette, the voltammetry of the pipette in electrolyte could only be used to determine the background resistance. This was in stark contrast to the wire etching nanopores, which could be studied using voltammetry before and after the etching process. The transient in Figure 4.25 exhibited numerous translocations, but they varied greatly in magnitude, indicating the translocation of several particles at once. This was most likely caused by a combination of the high concentration of electrolyte employed, which would have promoted agglomeration of the particles, and the geometry of the pipette, which appeared to be less acute than the nanopores generated by wire etching, thereby increasing the flow rate[161].

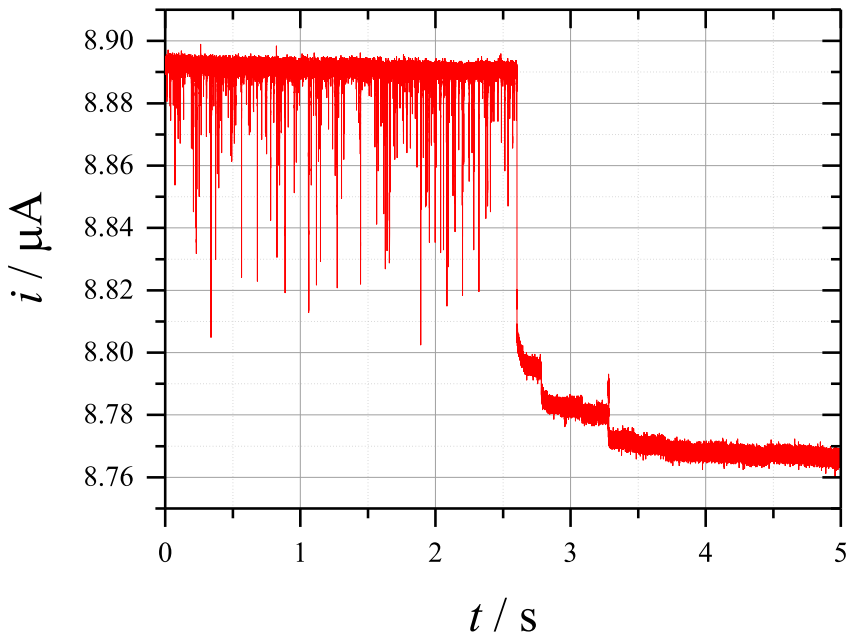


**Figure 4.26:** Current transient recorded at −4 V *vs.* Ag/AgCl with a ≈1000 nm Ø conical nanopipette in aerobic 1 M KCl.The plot shows the translocation of 370 ± 14.8 nm Ø nanoparticles ($2.7 \times 10^9$ particles $mL^{-1}$), recorded with the low gain ($10^6$ V/A) current-differential system. The pressure differential applied to the micropore was −94 mBar and the temperature during the experiment was 23.0 °C.

The current transient shown in Figure 4.26 was used to record the translocation of 370 ± 14.8 nm Ø particles through the ≈1000 nm Ø pipette. There was still a wide variance on the signal magnitude, but the increased concentration of particles still resulted in more translocations. This led to a blocking event after 2.5 s, indicated by the sudden and permanent drop in current. These results show that although pipettes do not appear to suffer from the poor flow rate that has been shown to affect the wire etching nanopores, they still are disrupted by the agglomeration of charged particles in high concentration electrolyte. The same precautions of reducing electrolyte concentration and using smaller pipettes would inevitably result in the low current signals and unstable background currents that were witnessed on the wire etching nanopores. Therefore, it is believed that the pulled pipettes offer no particular advantage to the use of these nanopores in Coulter counting, and indeed could be less suitable due to their fragility.

## 4.6 Chapter 4 conclusions

The apparatus required for the Coulter counting of nanobubbles was successfully tested with the translocation of particles through well-defined cylindrical micropores. These translocations were recorded using a conventional chronoamperometry method and an alternative differential method, shown here to give greater signal-to-noise ratios. The change in pore resistance during particle translocation agreed well with theoretical and simulated values, proving the apparatus was capable of accurate sizing. Furthermore, the measurement of fast translocations (0.3 ms) through conical micropores showed the apparatus had a high time resolution. Nanopores were prepared by the complete removal of the electrode material from W nanoelectrodes, and characterised by the translocation of nanoparticles. Simulations were then compared to these translocations and used to estimate the geometry of the pores. However, several problems were encountered during the translocation of nanoparticles through nanopores. High concentrations of electrolyte caused particle agglomeration, but reducing the concentration and pore diameter to address this resulted in lower background currents and less visible signals. The use of more sensitive apparatus successfully improved signal visibility, but the smaller pore diameters had also resulted in fewer translocations, which made characterisation more difficult. Nevertheless, the accuracy and high time resolution exhibited by the Coulter counting apparatus made it applicable in the detection of nanobubbles.

# 5 Coulter counting of transient nanobubbles

Acoustic waves can be used to induce sinusoidal pressure fluctuations in a liquid and, with sufficient pressure amplitudes, can cause the formation of bubbles by acoustic cavitation[12]. The use of ultrasonic waves (*i.e.* typically above 20 kHz) to induce acoustic cavitation has previously been employed for microbubble production[157,164], and the same method has also been reported to reliably generate bulk nanobubbles[37,38]. Since the effects of acoustic waves on the dynamics of bubbles is well understood, this method of bulk nanobubble generation has a significant advantage over less well defined methods. However, the *in situ* observation of bubbles generated ultrasonically is mostly performed with microscopy and high-speed camera techniques. Whilst these techniques are capable of characterising microbubble formation, they are unsuitable for the study of nanobubbles. The Coulter counting method demonstrated in Chapter 4 could be combined with these techniques to provide better characterisation of the formation of nanobubbles. Whilst the Coulter counting of microbubbles has been previously reported[6,157], this method has yet to be applied to nanobubbles. Figure 5.1 illustrates how the Coulter counting technique could be used to characterise bulk nanobubbles.

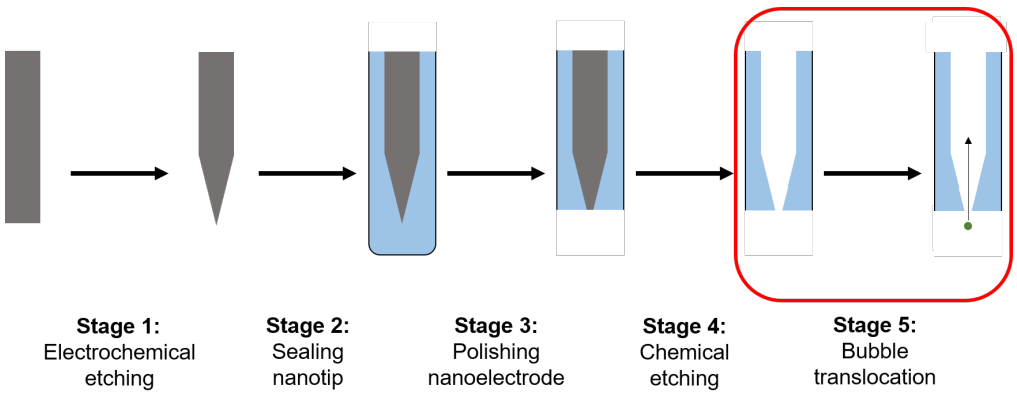


**Figure 5.1:** Stages in the project required to record the Coulter counting of nanobubbles. The focus of this chapter, highlighted by the red box, is the generation of microbubbles and nanobubbles by acoustic cavitation in aqueous electrolytes. These bubbles are subsequently detected by Coulter counting through cylindrical micropores and conical nanopores respectively.

This chapter discusses the Coulter counting of ultrasonically generated nanobubbles through the nanopores prepared in Chapter 4. The translocation of the nanobubbles is shown to be highly sensitive to the cell design, so the translocation of microbubbles is first tested in order to determine the optimal parameters for bubble detection. Evidence that the translocations are indeed bubbles is provided by high-speed imaging of the bubble motion and hydrophone data of the acoustic environment within the electrolyte. These show the oscillation of microbubbles during translocation, which can be linked to the acoustic environment within the cell.

## 5.1 Methods for characterising the ultrasonication of electrolytes

Before the Coulter counting technique was employed, conventional characterisation methods were used to ensure the ultrasonication of electrolytes was capable of generating bubbles. High-speed camera videos were used to monitor the formation and motion of bubbles at the piston-like emitter (PLE) which produced the ultrasonic waves.

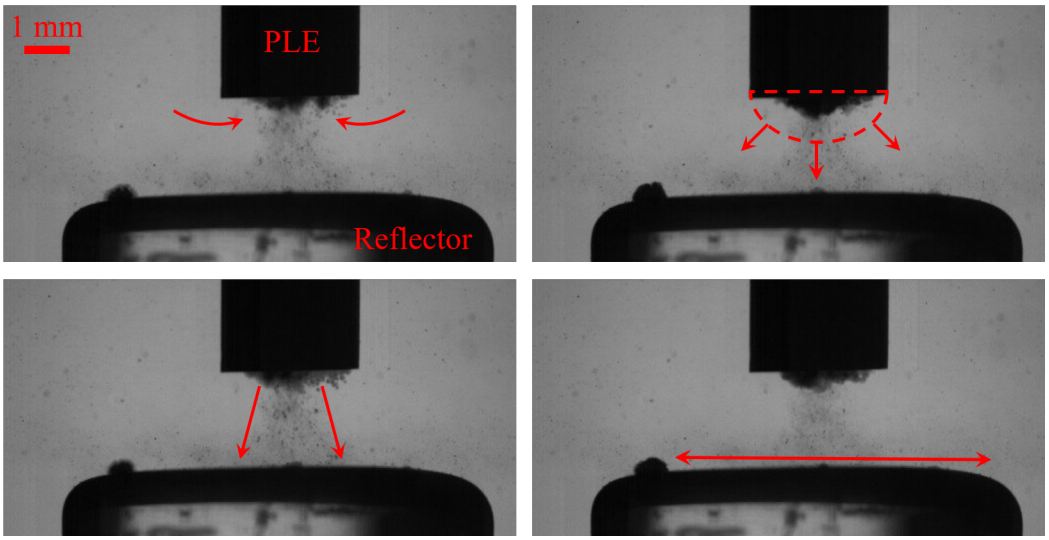


**Figure 5.2:** High-speed camera images of the bubble activity directly underneath the piston like emitter (PLE) during the ultrasonication of 10 mM KCl with the PLE driven at an output power of 6 $W_{RMS}$. Clockwise from the top left, the images show: bubbles in the bulk of the solution migrating towards the bubble cluster at the PLE; the expansion of the bubble cluster; the collapse of the bubble cluster and the ejection of finer bubbles towards the glass reflector; and the reformation of the bubble cluster, with the recently ejected bubbles gathering on the glass reflector to make their own clusters that can travel across the reflector. The images were recorded at a frame rate of 20000 FPS, making them 50 $\mu$s apart.

The still frames displayed in Figure 5.2 show a cluster of bubbles under the tip of the PLE, and show how this cluster evolved during the ultrasonication process. The tip of the PLE oscillated in a vertical motion, thereby acting as a sound source. This motion was driven by a piezoelectric transducer provided with 6 $W_{RMS}$ of electrical energy (as reported by the instrumentation). Bubble activity below the PLE was observed as a result of this motion, and enabled the formation of a bubble cluster in this area[163]. This cluster was seen to grow and collapse on the surface of the PLE at a frequency that was determined from the separation of the frames to be $\approx$ 6 kHz, which was a fourth of the ultrasonic frequency used to drive the PLE. Bubbles were also observed to become trapped on the glass reflector after moving away from PLE tip. Note that this reflector was placed under the PLE as it was found to improve the reproducibility of bubble translocation, as will be shown later.

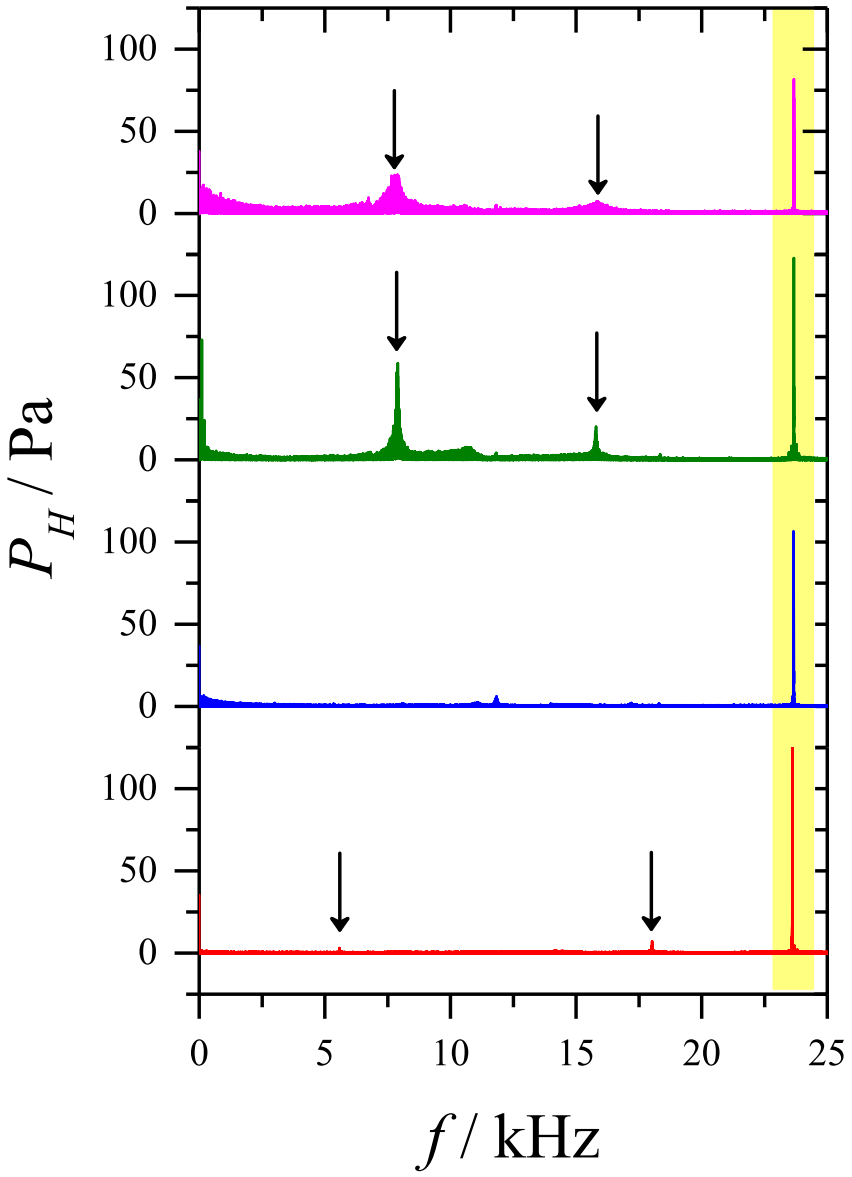


**Figure 5.3:** Fast Fourier transform of the hydrophone data recorded during the ultrasonication of 10 mM KCl with the PLE driven at output powers of: (RED) 2 $W_{RMS}$; (BLUE) 6 $W_{RMS}$; (GREEN) 12 $W_{RMS}$; and (PINK) 18 $W_{RMS}$. The yellow band highlights the drive frequency of the PLE (22 – 24 kHz), whilst the black arrows point out possible sub-harmonic frequencies caused by the oscillation of bubble clusters under the PLE. The hydrophone was held level with the tip of the PLE, with a horizontal displacement of 10 mm.

The hydrophone data shown in Figure 5.3 describes the frequency components present in the electrolyte during ultrasonication. In all cases, a large acoustic pressure was observed at $22-24$ kHz, corresponding to the frequency of the PLE oscillation. However, additional pressures were also detected in the electrolyte during the application of higher powers to the transducer. These pressures appeared at $\approx 7.5$ and 15 kHz, which suggested they were sub-harmonics at a third of the driving frequency. These sub-harmonics were consistent with the collapse of the bubble cluster observed in Figure 5.2 and have also been related to the generation of fine bubble clouds similar to those seen in Figure 5.2[163]. The application of different powers to the transducer can affect the pressure wave in the liquid, and therefore the inertial collapse of the bubble cluster too. This might explain why sub-harmonic oscillation was seen at some powers, but not others. However, the acoustic pressures observed in Figure 5.3 were smaller than those that have been previously reported[157]. This could be due to shielding between the PLE and the hydrophone.

## 5.2 Optimal cell design for the detection of microbubbles

The sub-harmonic collapse of the bubble cluster under the PLE was shown to produce clouds of fine bubbles. Coulter counting through micropores could be used in order to detect any microbubbles generated during this collapse. However, it was first necessary to determine the best conditions for generating these microbubbles. Therefore, different parameters in the cell design were varied, in order to see the effect on microbubble translocation.

The horizontal position of the PLE was varied so that its relationship with the glass reflector could be investigated, as shown in Figure 5.4. When both the PLE and the micropore were above the reflector, numerous translocations were observed. These were attributed to the formation of microbubbles between the PLE and the reflector. Similar observations were made when the PLE was held above the reflector, but the micropore was not. However, significantly fewer translocations were observed when only the micropore was held above the reflector. This highlights the importance of the reflector in the detection of microbubbles. The reflector effectively acts to trap bubbles under the PLE, resulting in an increase in the bubble activity between the PLE and the reflector. This result also

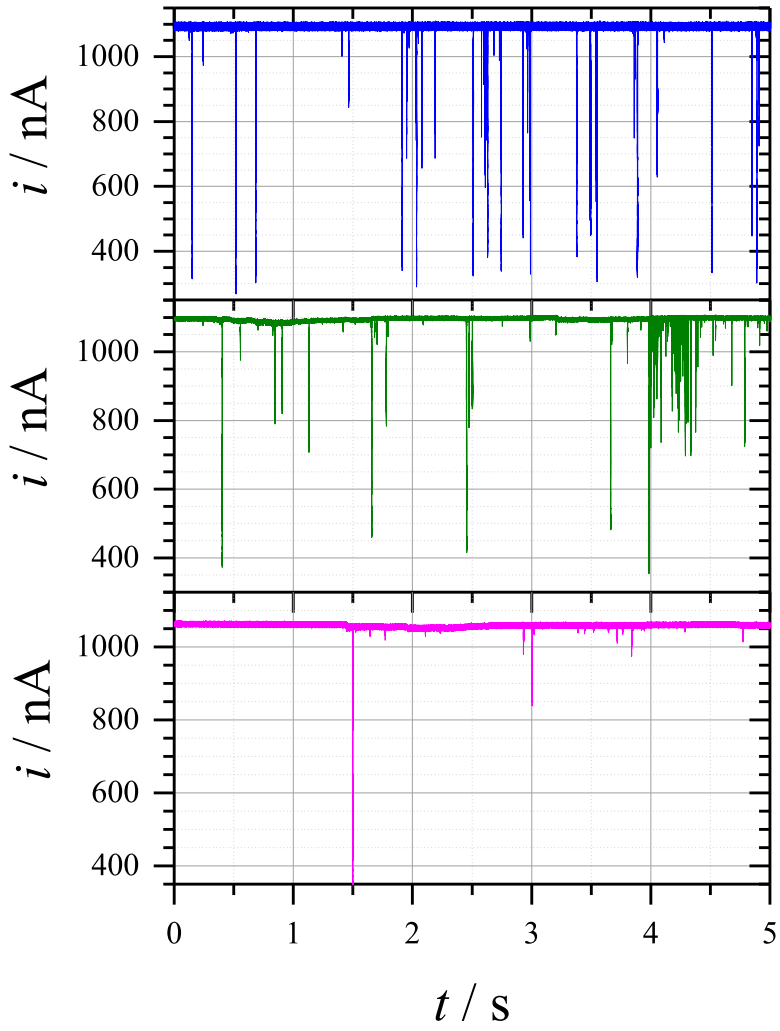


**Figure 5.4:** Current transients recorded at +5 V *vs.* Ag/AgCl with a 40 $\mu$m Ø cylindrical micropore in aerobic 10 mM KCl. Each plot shows the translocation of microbubbles generated ultrasonically with a PLE driven at 2 $W_{RMS}$. The micropore was held level with the tip of the PLE, with a horizontal displacement of 2 mm, and was positioned so that the glass reflector was directly under: (BLUE) only the PLE; (GREEN) both the PLE and the micropore; and (PINK) only the micropore. The pressure differential applied to the micropore was −72 mBar and the temperature during the experiment was 26.7 °C.

indicated that the direct translocation of bubbles in the cluster was not as likely to cause the same translocations. After determining the importance of the reflector in increasing bubble activity in the region, all future translocations were recorded with both the PLE and the micropore directly above the reflector.

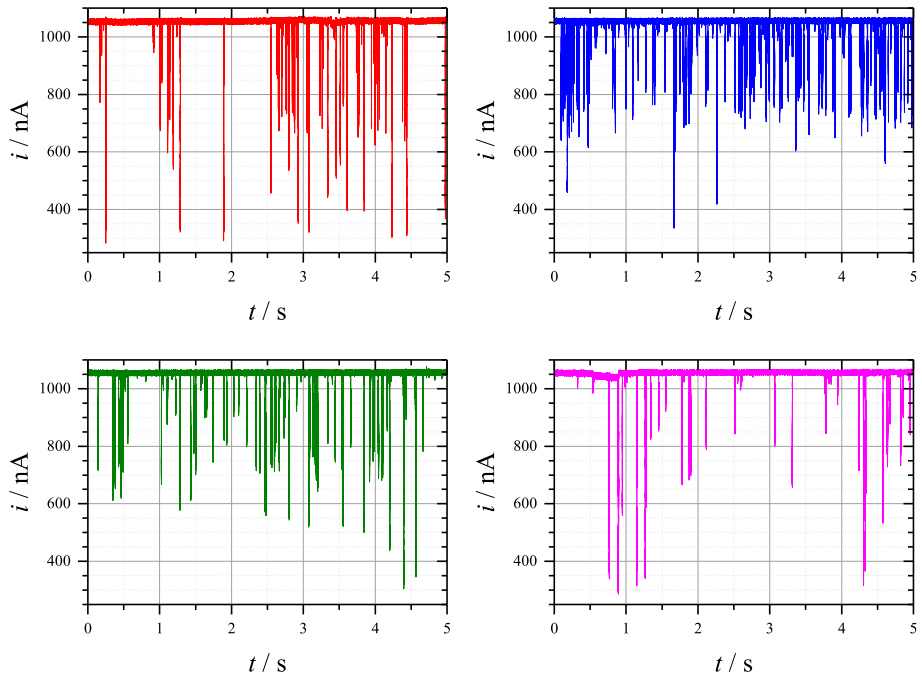


**Figure 5.5:** Current transients recorded at +5 V *vs.* Ag/AgCl with a 40 $\mu$m Ø cylindrical micropore in aerobic 10 mM KCl. Each plot shows the translocation of microbubbles generated ultrasonically with a PLE driven at 2 $W_{RMS}$. The micropore was held level with the tip of the PLE at (RED) 1 mm; (BLUE) 2 mm; (GREEN) 3 mm; and (PINK) 4 mm above the glass reflector, with a horizontal displacement of 1 mm. The pressure differential applied to the micropore was −76 mBar and the temperature during the experiment was 25.2 °C.

Given that the reflector effectively increased the bubble activity under the PLE, enlarging the vertical distance between the PLE and reflector was predicted to reduce the quantity of microbubble translocations. The current transients in Figure 5.5 showed that this was indeed the case, with fewer events observed when the PLE was far away from the reflector. This seemed to confirm the importance of the reflector in the production of microbubbles. Therefore, the PLE was kept within a vertical distance of 2.5 mm of the reflector for the rest of the project.

In order to determine where best to measure the microbubble translocations, the

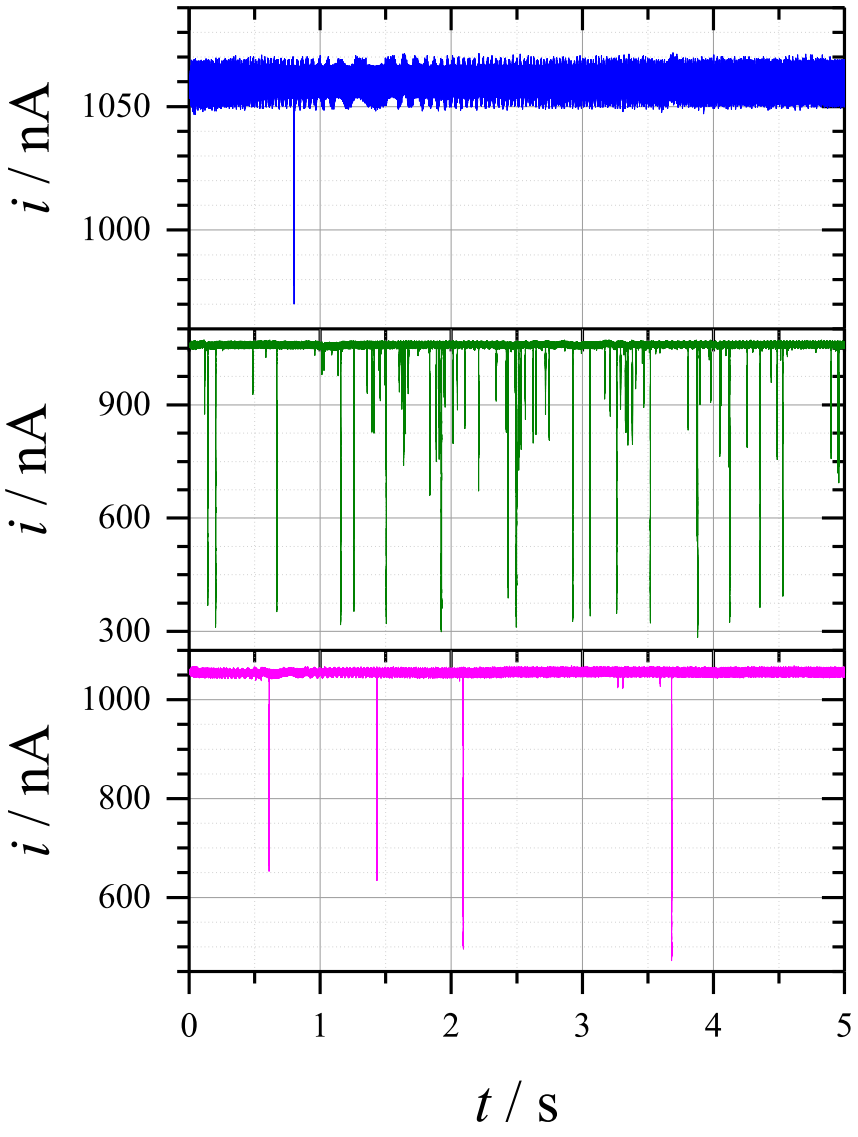


**Figure 5.6:** Current transients recorded at +5 V *vs.* Ag/AgCl with a 40 $\mu$m Ø cylindrical micropore in aerobic 10 mM KCl. Each plot shows the translocation of microbubbles generated ultrasonically with a PLE driven at 2 $W_{RMS}$. The micropore was held: (TOP) 1.5 mm below; (MIDDLE) level with; and (BOTTOM) 1.5 mm above the tip of the PLE, with a horizontal displacement of 1 mm. The pressure differential applied to the micropore was −76 mBar and the temperature during the experiment was 25.2 °C.

micropore was positioned at different vertical distances from the PLE, which was kept stationary. Figure 5.6 showed the current transients recorded with the micropore below, level with, and above the tip of the PLE. The largest quantity of microbubble translocations were observed when the pore was level with the PLE. When the pore was moved away from the PLE, the number of events declined dramatically, suggesting the microbubbles are only present close to the PLE. The different cell design parameters that were tested in these experiments highlighted the locality of the microbubbles around the PLE and the importance of the glass reflector in increasing bubble activity in this area. However, these are only preliminary results and the exact nature of the microbubble population during ultrasonication needs further study.

## 5.3 Characterisation of microbubbles by Coulter counting

The highest quantity of microbubble translocations was observed with the PLE, micropore, and reflector in the positions detailed above. This allowed the characterisation of microbubbles to be performed with Coulter counting, with particular focus on the experimental conditions that may have affected bubble stability.

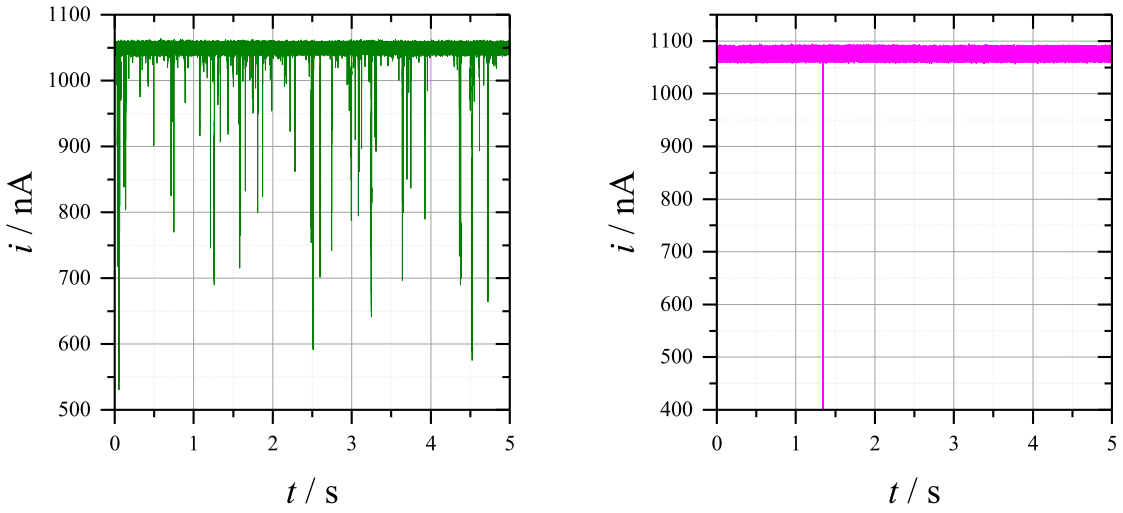


**Figure 5.7:** Current transients recorded at +5 V *vs.* Ag/AgCl with a 40 $\mu$m Ø cylindrical micropore in aerobic 10 mM KCl. Both plots show the translocation of microbubbles generated ultrasonically with a PLE driven at 2 $W_{RMS}$. The micropore was held level with the tip of the PLE, with horizontal displacements of (GREEN) 1 mm and (PINK) 4 mm. The pressure differential applied to the micropore was −72 mBar and the temperature during the experiment was 24.9 °C.

Figure 5.7 shows the current transients used to record microbubble translocations observed at varying horizontal distances between the PLE and the micropore. The translocations attributed to ultrasonically generated microbubbles varied in magnitude, with many of the signals showing magnitudes of ≈ 500 nA. Although there were numerous smaller translocation signals, the largest signals were interesting because they were indicative of microbubbles that were of similar dimensions to the micropore. Even at the lowest amplification gains, this caused the signal from the differential systems to become saturated, suggesting the chronoamperometry method used in Chapter 4 was more suitable for recording microbubble translocations. As shown in Figure 5.7, the increased separations between the PLE and the micropore resulted in the fewest translocations, seemingly

confirming the locality of the microbubbles to the cluster at the PLE.

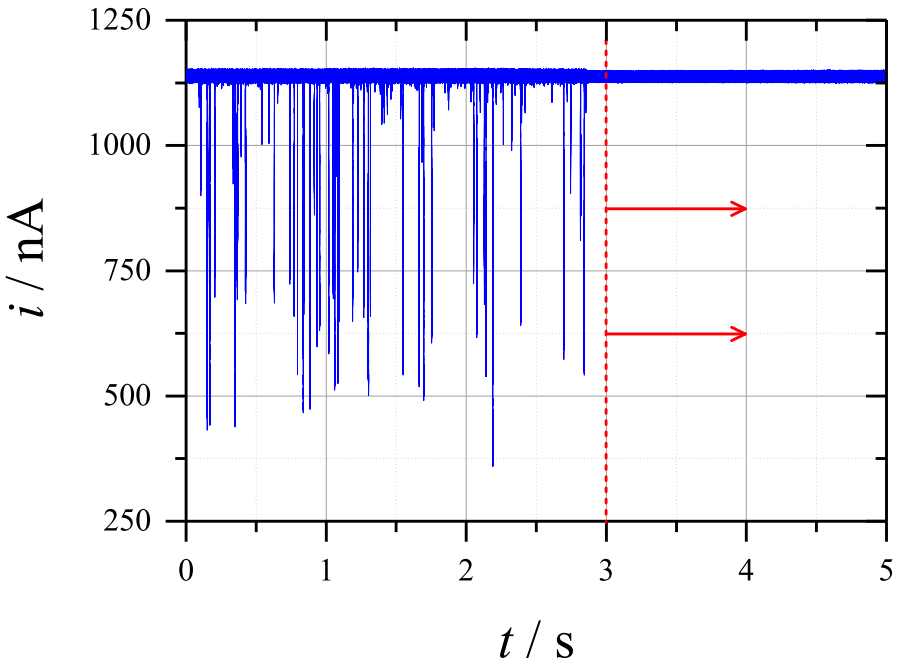


**Figure 5.8:** Current transient recorded at +5 V *vs.* Ag/AgCl with a 40 $\mu$m Ø cylindrical micropore in aerobic 10 mM KCl. The plot shows the translocation of microbubbles generated ultrasonically with a PLE driven at 2 $W_{RMS}$. After the time indicated by the red dashed line, the ultrasonication was terminated in order to determine the lifetime of the ultrasonically generated microbubbles. The micropore was held level with the tip of the PLE, with a horizontal displacement of 1 mm. The pressure differential applied to the micropore was −70 mBar and the temperature during the experiment was 28.0 °C.

The apparent dependence of the microbubbles on the PLE cluster was further examined by turning the ultrasonic source off during Coulter counting. This would prevent further cavitation, stopping the microbubble generation and allowing the lifetime of the microbubbles to be examined. As shown in Figure 5.8, numerous microbubble translocations were observed whilst the electrolyte was being ultrasonicated, but no events were seen after this ultrasonication was terminated. This indicates a lack of microbubble stability outside of the acoustic environment provided by the PLE, which could also explain the locality of the microbubbles to the cluster. It was therefore determined that the microbubbles being generated at the PLE cluster were both transient in nature and local to the PLE. This could indicate a reduction in the bubble concentration, or a contradiction

with the reported stability of micro/nanobubbles generated by ultrasonication, but in any case did not seem to invalidate the characterisation of bubbles by Coulter counting.

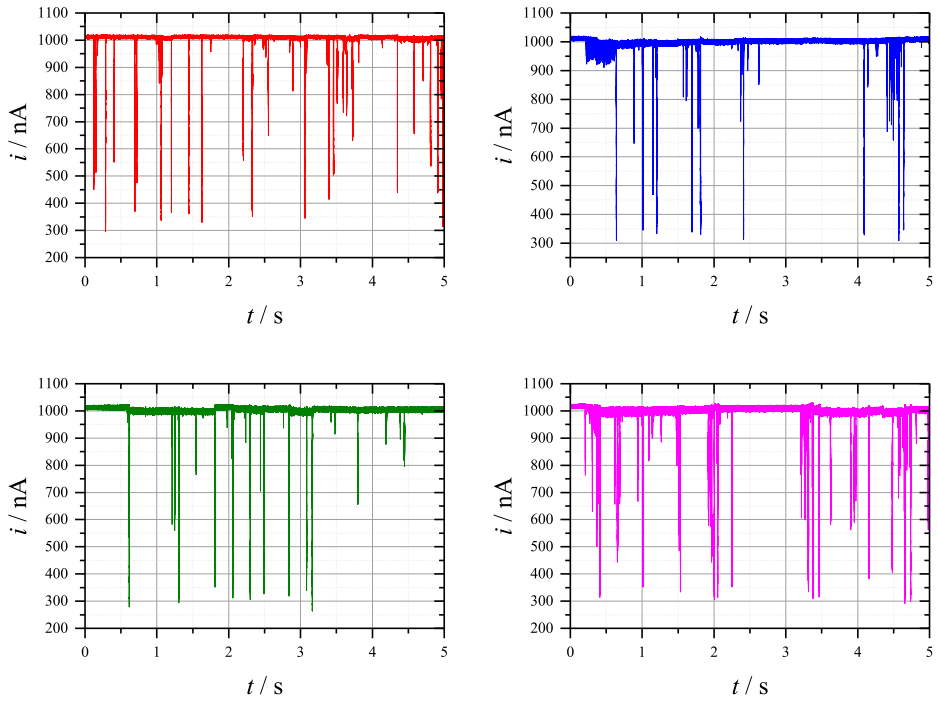


**Figure 5.9:** Current transients recorded at +5 V *vs.* Ag/AgCl with a 40 $\mu$m Ø cylindrical micropore in aerobic 10 mM KCl. Each plot shows the translocation of microbubbles generated ultrasonically with a PLE driven at: (RED) 2 $W_{RMS}$; (BLUE) 6 $W_{RMS}$; (GREEN) 12 $W_{RMS}$; and (PINK) 18 $W_{RMS}$. The micropore was held level with the tip of the PLE, with a horizontal displacement of 1 mm. The pressure differential applied to the micropore was −75 mBar and the temperature during the experiment was 23.3 °C.

The effects of the PLE cluster dynamics were tested by increasing the electrical power applied to the PLE transducer. Increased powers resulted in larger oscillations of the PLE tip, which caused greater pressure amplitudes in the acoustic wave under the PLE[163]. This could affect the frequency of the inertial collapse of the PLE cluster. However, the current transients in Figure 5.9 did not show any evidence of a difference in the microbubble generation. The quantity and magnitude of the translocations did not appear to differ, although the highest power did show slightly wider translocations, which might suggest the translocation of several bubbles through the pore in quick succession.

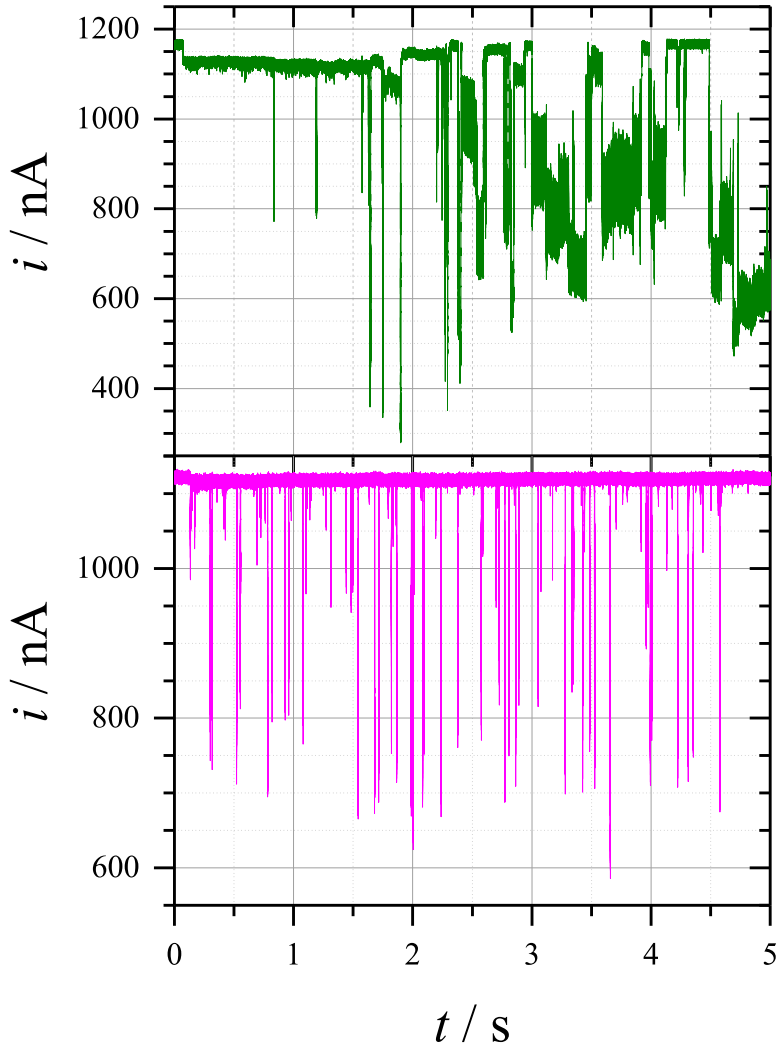


**Figure 5.10:** Current transients recorded at +5 V *vs.* Ag/AgCl with a 40 $\mu$m Ø cylindrical micropore in aerobic 10 mM KCl. Both plots show the translocation of microbubbles generated ultrasonically with a PLE driven at 2 $W_{RMS}$. The micropore was held level with the tip of the PLE, with a horizontal displacement of 1 mm. The pressure differential applied to the micropore was (TOP) −15 mBar and (BOTTOM) −75 mBar and the temperature during the experiment was 27.8 °C.

The microbubbles were also shown to behave differently during their translocation under different pressure differentials. As shown in Figure 5.10, the translocation of microbubbles under high pressure differentials was rapid and produced relatively small signals. Conversely, the translocations under low pressure differentials took longer and were significantly larger in magnitude. The varying signal magnitude could only be explained by the acoustic oscillation of the microbubbles during translocation. This oscillation would

vary the volume of electrolyte displaced by the bubble, thereby varying the signal magnitude. These oscillations were more easily observed at low pressure differentials due to the long translocation times at reduced flow rates experienced by the micropore. Note that no such effect was observed during the translocation of microparticles at different pressure differentials.

## 5.4 Microbubble oscillations during translocation

This microbubble oscillation was of particular interest, as it proved the translocations were definitely caused by microbubbles rather than particles which may have formed during erosion of the PLE. Furthermore, it provided more insight on the influence of the acoustic wave on the microbubbles. High-speed camera videos were recorded in order to further examine the translocation of microbubbles at various pressure differentials.

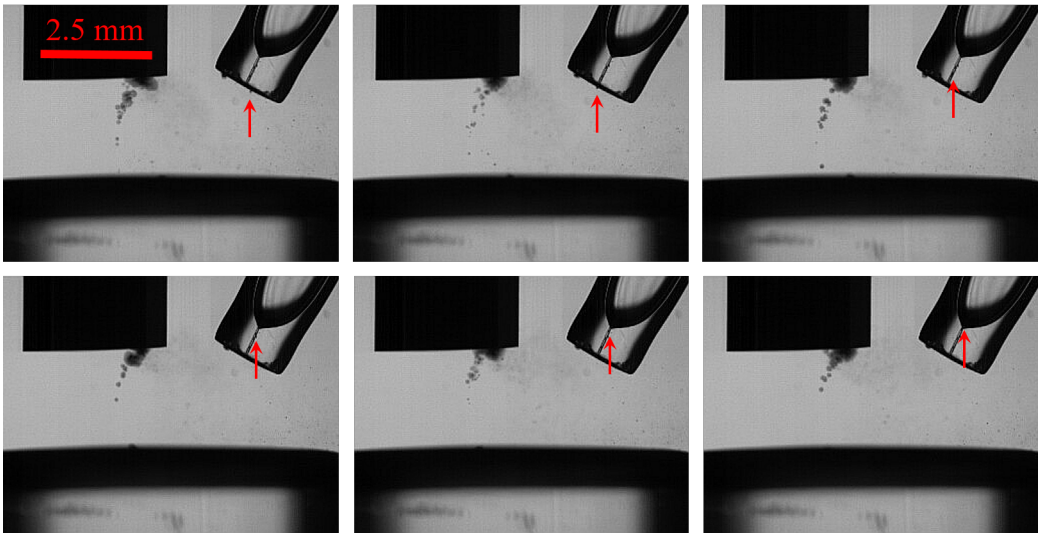


**Figure 5.11:** High-speed camera images showing the low pressure translocation of a microbubble through a 40 $\mu$m Ø cylindrical micropore in 10 mM KCl. The red arrows indicate the position of the microbubble in each of the frames which, using a frame rate of 20000 FPS, were recorded every 50 $\mu$s. The microbubble was generated ultrasonically with a PLE driven at 2 $W_{RMS}$. The pressure differential applied to the micropore was −15 mBar and the temperature during the experiment was 27.8 °C.

The still frames displayed in Figure 5.11 showed the translocation of a microbubble under the influence of a low pressure differential. The position of this microbubble in each

of the frames is indicated by a red arrow. The bubble originated on the surface of the micropore and was seen to move around this surface before it translocated through the pore. During translocation, the bubble appeared to oscillate in size, which was consistent with the current oscillations seen in Figure 5.10. The observation of this oscillation was made possible by the relatively long duration of the translocation, which was calculated to have taken place over $\approx 0.25$ ms. This was significantly slower than the events recorded under high pressure differentials. In order to record the oscillations with more time resolution, the Coulter counting was repeated, but was recorded with an oscilloscope instead.

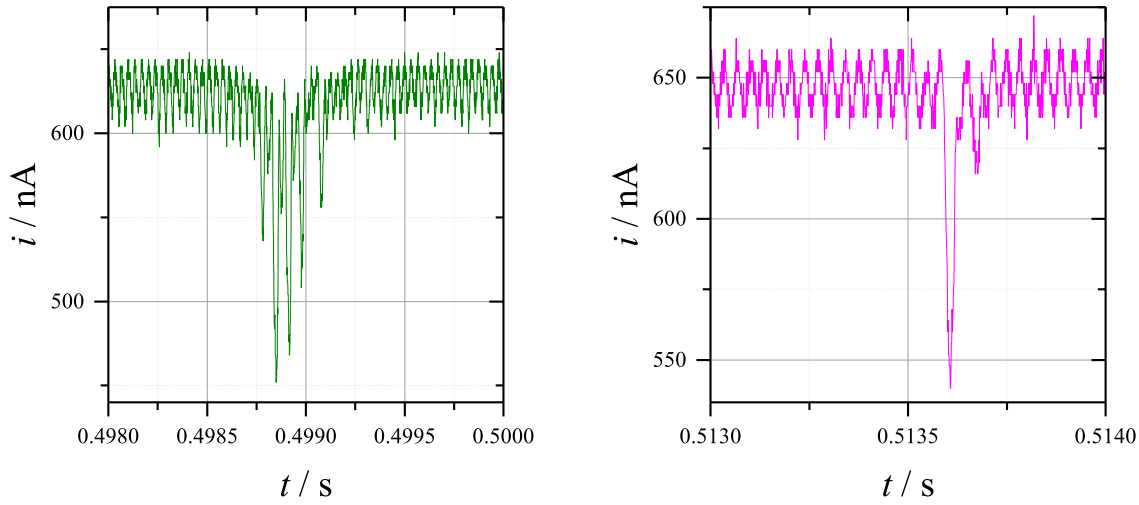


**Figure 5.12:** Part of current transients recorded at +5 V *vs.* Ag/AgCl with a 25 $\mu$m Ø cylindrical micropore in aerobic 10 mM KCl. Both plots show high resolution ($10^6$ Hz) oscilloscope measurements of the translocation of microbubbles generated ultrasonically with a PLE driven at 2 $W_{RMS}$. The micropore was held level with the tip of the PLE, with a horizontal displacement of 1 mm. The pressure differential applied to the micropore was (LEFT) −17 mBar and (RIGHT) −70 mBar and the temperature during the experiment was 27.8 °C.

Figure 5.12 shows the current transients of microbubble translocations, recorded under varying pressure differentials with an oscilloscope capable of $10^6$ Hz data acquisition rates. Under high pressures, the translocation of microbubbles was rapid, taking place over less than 0.1 ms. This was insufficient time to record the oscillation of the bubble, resulting in the appearance of a single sharp peak. Conversely, the events recorded under low pressures lasted for $\approx 0.5$ ms, allowing the several oscillations of the bubble to be observed. Note that the variations in current were largest as the bubble entered the pore ($\approx 150$ nA), but diminished as the bubble continued to translocate. This suggested

a strong influence of the acoustic wave on the bubble, but also the loss of this acoustic pressure at greater distances within the pore structure.

The frequency of these current oscillations can be analysed in order to determine the behaviour of the microbubble during translocation and link it to the acoustic environment in the electrolyte. Figure 5.13 shows a current transient with several microbubble translocations that were observed to exhibit current oscillations. This was compared to the fast Fourier transform of the current transient, which showed a background noise corresponding to the drive frequency of the PLE at 22.5 kHz. However, the translocation of the microbubbles caused the frequency of the current oscillations to be observed. The smallest of the translocations showed the clearest frequency analysis, with the current oscillating at $\approx 7.5$ and 15 kHz. This was determined to be a $f/3$ sub-harmonic of the drive frequency of the PLE, which is consistent with the hydrophone data in Figure 5.3. This signal was the clearest because the larger translocations in Figure 5.13 were observed to be 'slugs' of bubbles rather than individual spherical bubbles. These 'slug' bubbles filled a large portion of the pore with gas, making the current less susceptible to the influence of the acoustic wave. Note that these slugs were more often observed at high powers, which is consistent with the observations of Figure 5.9.

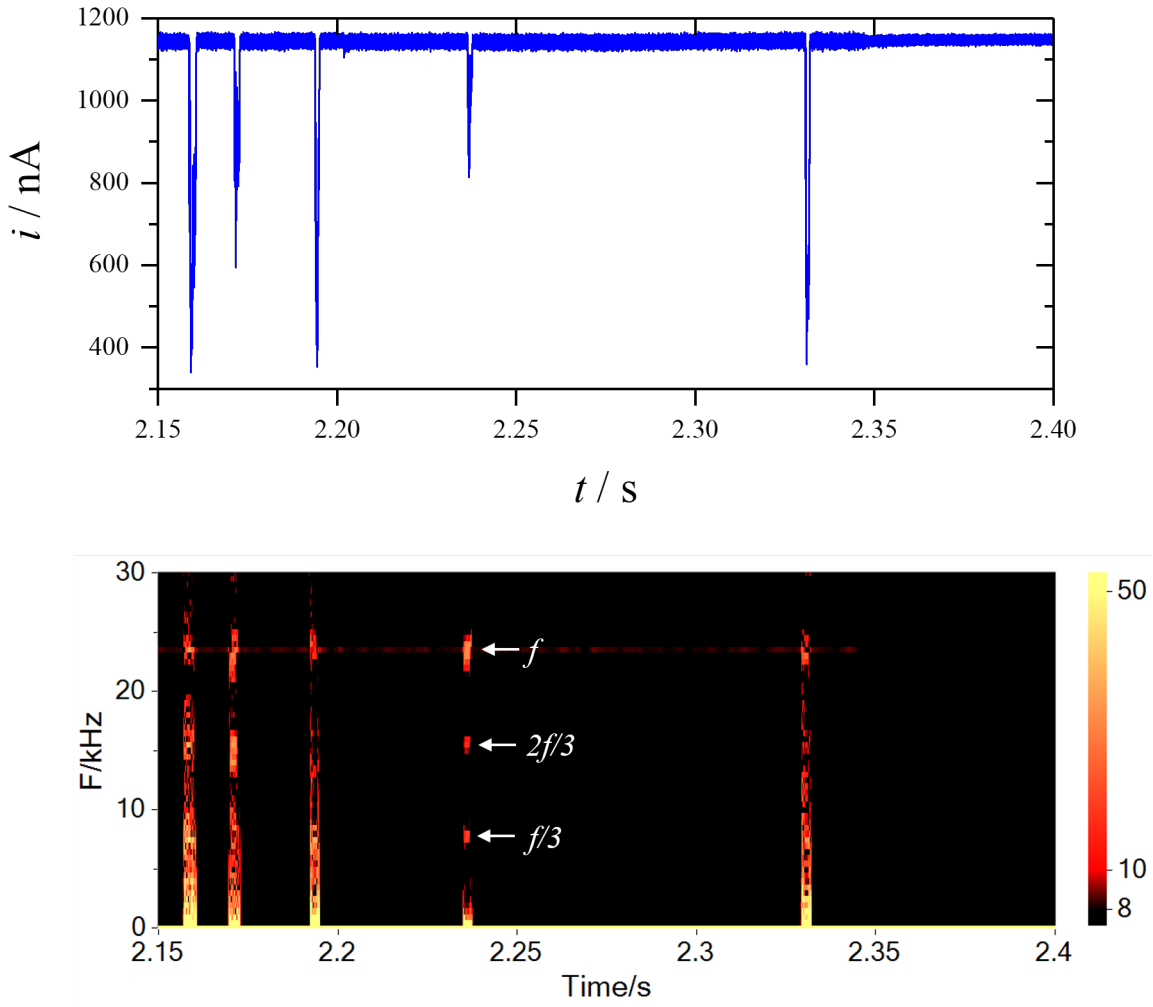


**Figure 5.13:** Plot showing the fast Fourier transform of the frequency components present in a current transient recorded at +5 V *vs.* Ag/AgCl with a 40 $\mu$m Ø cylindrical micropore in aerobic 10 mM KCl. The frequency components come from the translocation of microbubbles generated ultrasonically with a PLE driven at 18 $W_{RMS}$, which oscillate under the influence of the acoustic field within the electrolyte. The micropore was held level with the tip of the PLE, with a horizontal displacement of 1 mm. The pressure differential applied to the micropore was −70 mBar and the temperature during the experiment was 27.8 °C. The annotations on the plot refer to the sub-harmonic frequencies of the microbubble oscillation where $f$ refers to the frequency of the ultrasonic source. The scale bar on the right represents nA.

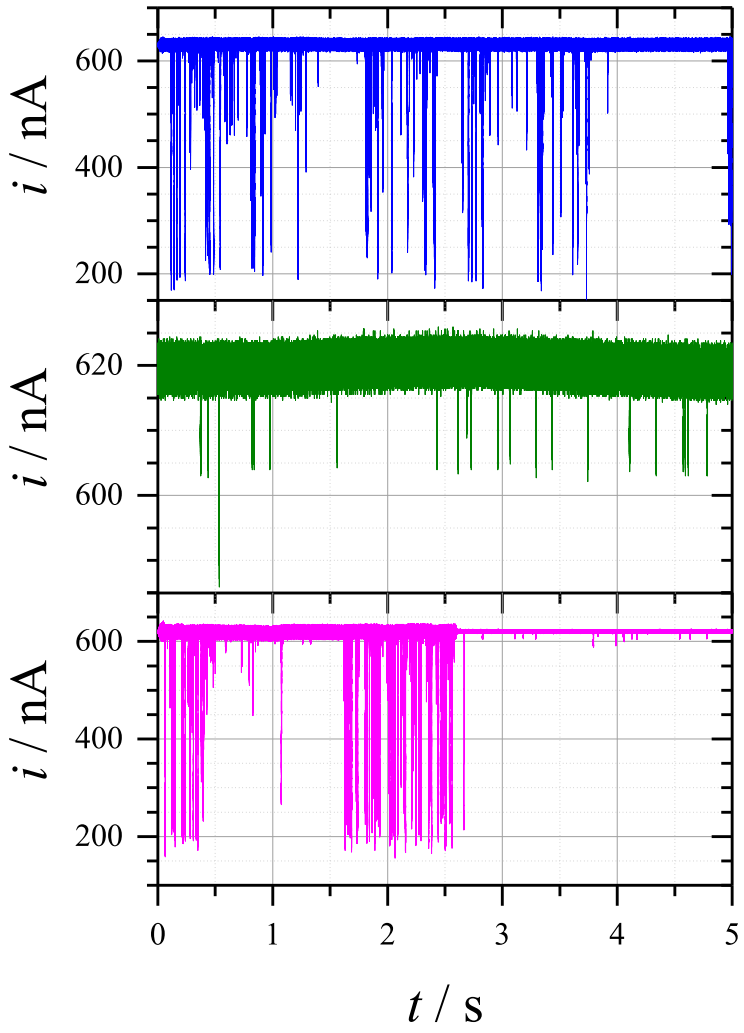


**Figure 5.14:** Current transients recorded at +5 V *vs.* Ag/AgCl with a 25 $\mu$m Ø cylindrical micropore in aerobic 10 mM KCl. The plots show the translocation of: (TOP) microbubbles generated ultrasonically with a PLE driven at 2 $W_{RMS}$; (MIDDLE) 18.8±1.5 $\mu$m Ø microparticles ($4 \times 10^4$ particles $mL^{-1}$); and (BOTTOM) both microbubbles and microparticles. The micropore was held level with the tip of the PLE, with a horizontal displacement of 1 mm. The pressure differential applied to the micropore was −80 mBar and the temperature during the experiment was 27.8 °C.

The addition of microparticles to the electrolyte further highlighted the unique behaviour of the microbubbles during translocation. The current transients displayed in Figure 5.14 showed that the particles were easy to distinguish from the microbubbles, as they were monodisperse and did not not exhibit any current oscillations. Furthermore, they could be observed after the ultrasonication had been terminated, whereas the tran-

sient microbubbles were unstable outside the influence of the acoustic wave. This contrast proved that the Coulter counting was still a valid technique for microbubble characterisation, despite the transient nature of the bubbles.

## 5.5 Characterisation of nanobubbles by Coulter counting

After the transient microbubbles generated during the ultrasonication of electrolytes had been sufficiently characterised, focus was turned to the possibility of nanobubble detection. It was not known whether the inertial collapse of the PLE cluster was capable of generating nanobubbles, so the Coulter counting was repeated, but with the micropore replace by one of the nanopores described in Chapter 4. Note that the PLE, nanopore, and reflector were kept in the positions detailed in section 5.2.

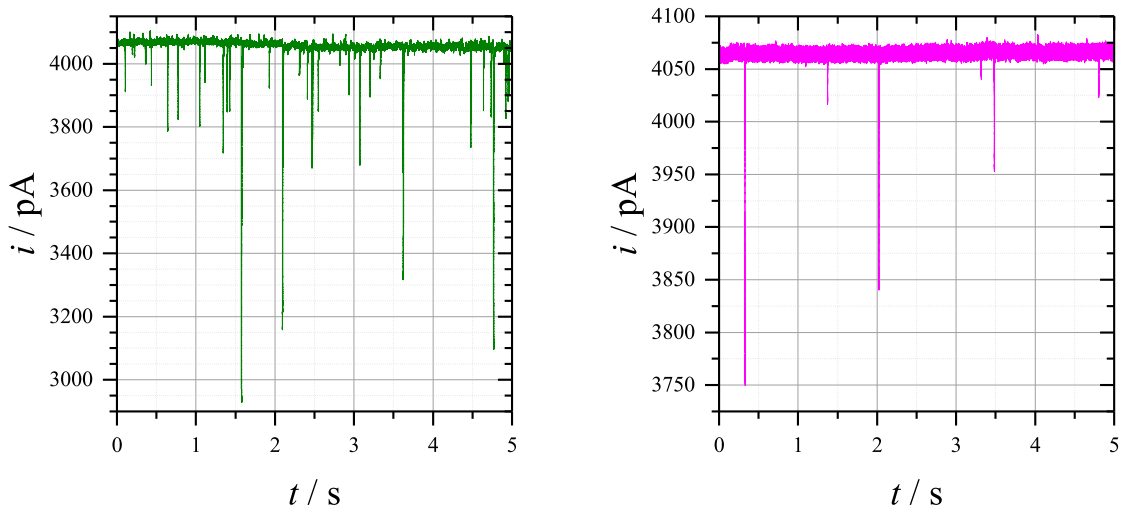


**Figure 5.15:** Current transients recorded at +280 mV *vs.* Ag/AgCl with a 430 nm Ø conical nanopore in aerobic 10 mM KCl. Both plots show the translocation of nanobubbles generated ultrasonically with a PLE driven at 2 $W_{RMS}$. The nanopore was held level with the tip of the PLE, with horizontal displacements of (GREEN) 1 mm and (PINK) 4 mm. The pressure differential applied to the nanopore was −77 mBar and the temperature during the experiment was 28.2 °C.

Figure 5.15 shows the current transients used to record the possible translocation of ultrasonically generated nanobubbles. These transients were recorded with varying horizontal distances between the PLE and the nanopore. Numerous translocations were

observed when the nanopore was held close to the PLE, with the magnitude of these translocations varying widely and the presence of some signals up to $\approx 1000$ pA in magnitude. When the pore was held further away from the PLE, the quantity of these translocations declined dramatically. This was consistent with the observations made during the translocation of microbubbles, suggesting the inertial collapse of the PLE cluster was also capable of producing large concentrations of polydisperse nanobubbles. High-speed camera videos showed the formation of a bubble on the surface of the nanopore, which appeared to move over the pore at the same time translocations were observed. This was similar to the effect observed with microbubble translocation. However, it should be noted that the translocation of microbubbles through the nanopore would have caused significantly larger and longer lasting signals, indicating the translocations in Figure 5.15 were more likely to be nanobubbles. The dependence on distance from the PLE suggested that these nanobubbles also displayed the locality to the PLE cluster that was observed with microbubbles.

This locality to the PLE cluster was further investigated by terminating the ultrasonic source during Coulter counting. As shown in Figure 5.16, several possible nanobubble translocations were observed whilst the electrolyte was being ultrasonicated, but no further translocations were seen after the ultrasonication was terminated. This observation was inconsistent with the possible detection of nanoparticles formed during the erosion of the PLE, as such nanopoarticles would still be suspended in the solution long after the ultrasonication was stopped. However, it was consistent with the formation of transient nanobubbles during the sonication, which was similar to the effect observed during microbubble translocation.

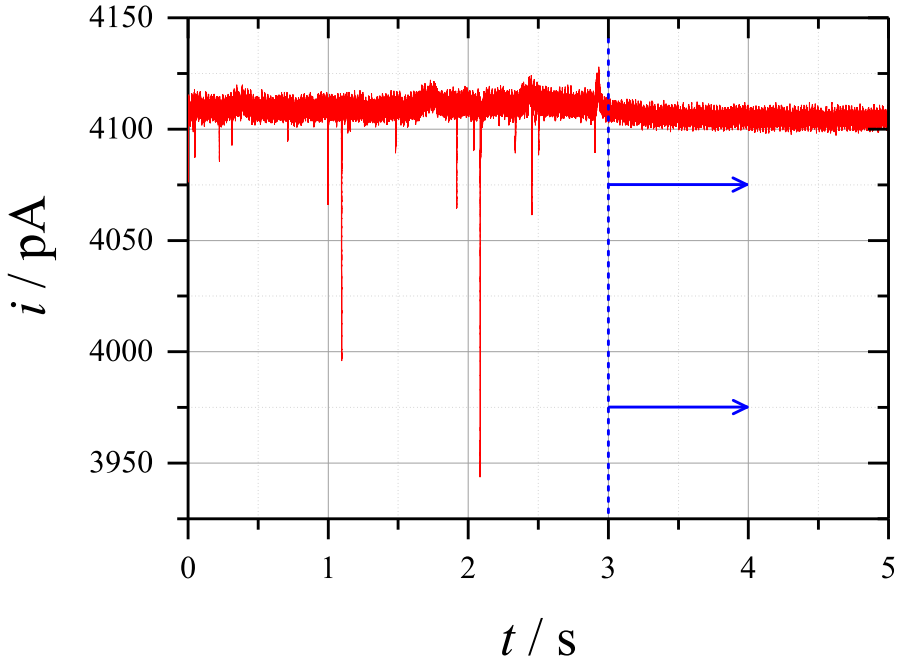


**Figure 5.16:** Current transient recorded at +280 mV *vs.* Ag/AgCl with a 430 nm Ø conical nanopore in aerobic 10 mM KCl. The plot shows the translocation of nanobubbles generated ultrasonically with a PLE driven at 2 $W_{RMS}$. After the time indicated by the blue dashed line, the ultrasonication was terminated in order to determine the lifetime of the ultrasonically generated nanobubbles. The nanopore was held level with the tip of the PLE, with a horizontal displacement of 1 mm. The pressure differential applied to the nanopore was −77 mBar and the temperature during the experiment was 28.2 °C.

These experiments suggested that the nanobubbles were local to the PLE and could not exist for long outside the influence of the acoustic wave. However, the long term stability of nanobubbles has been reported, and is said to occur through contamination of the bubble interface[38,59]. This reduces the surface tension of the liquid and therefore slows down the diffusion of gas from the bubble. Surfactants were therefore added to the electrolyte in order to deliberately stabilise the ultrasonically generated nanobubbles in the absence of the acoustic wave. However, even with the addition of surfactants, no translocations were seen in the the current transient after ultrasonication was terminated, as shown in Figure 5.17. Whilst this contradicted the reported stability of bulk nanobubbles, it did not necessarily invalidate the use of Coulter counting to detect nanobubbles.

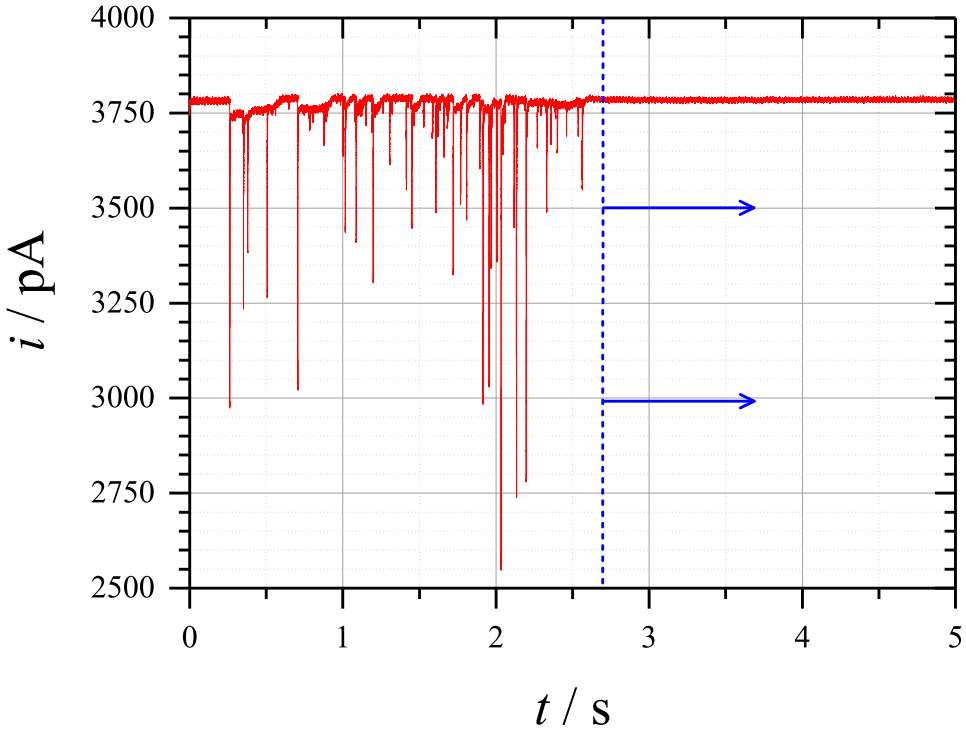


**Figure 5.17:** Current transient recorded at +280 mV *vs.* Ag/AgCl with a 430 nm Ø conical nanopore in aerobic 10 mM KCl + 1% Triton X-100. The plot shows the translocation of nanobubbles generated ultrasonically with a PLE driven at 2 $W_{RMS}$. The nanopore was held level with the tip of the PLE, with a horizontal displacement of 1 mm. The pressure differential applied to the nanopore was −77 mBar and the temperature during the experiment was 25.6 °C.

The sub-harmonic collapse of the PLE cluster was shown to make little difference to the ultrasonic generation of microbubbles. In order to determine the effect this collapse frequency had on nanobubble generation, higher powers were applied to the PLE. The current transients shown in Figure 5.18 showed that the effect of power was more pronounced in nanobubble generation, with a larger quantity of translocations observed at the highest power setting. This suggested the increased concentration of nanobubbles produced by the PLE collapse, which could be a result of the more efficient inertial cavitation observed at higher powers.

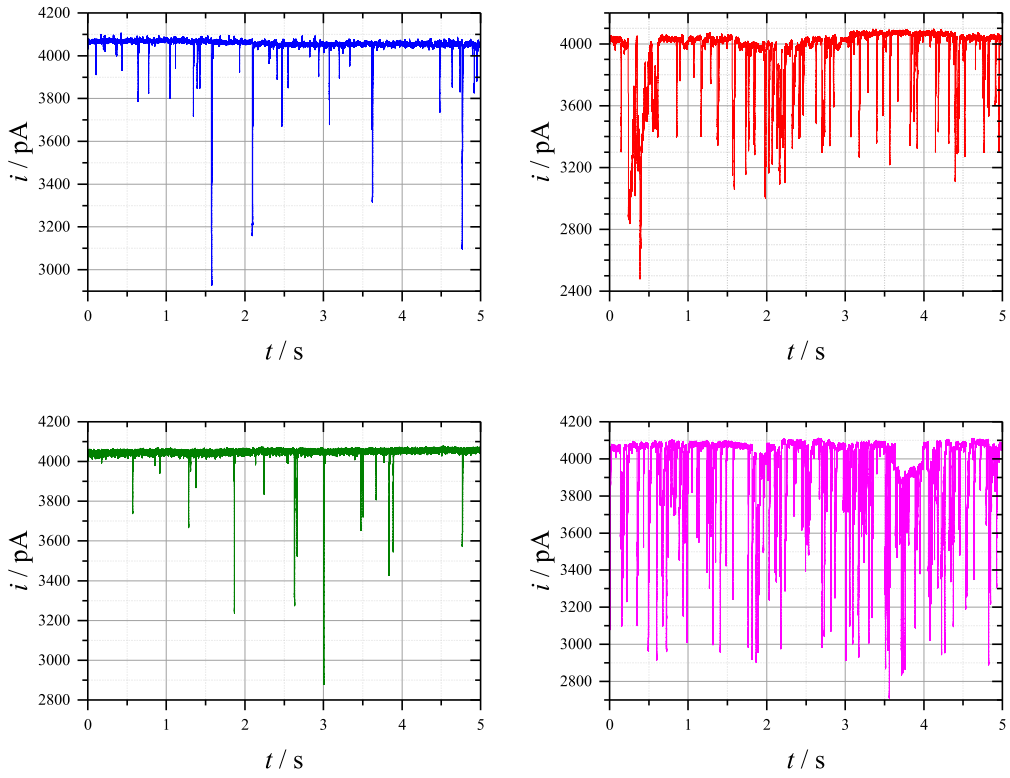


**Figure 5.18:** Current transients recorded at +280 mV *vs.* Ag/AgCl with a 430 nm Ø conical nanopore in aerobic 10 mM KCl. Each plot shows the translocation of nanobubbles generated ultrasonically with a PLE driven at: (RED) 2 $W_{RMS}$; (BLUE) 6 $W_{RMS}$; (GREEN) 12 $W_{RMS}$; and (PINK) 18 $W_{RMS}$. The nanopore was held level with the tip of the PLE, with a horizontal displacement of 1 mm. The pressure differential applied to the nanopore was −77 mBar and the temperature during the experiment was 28.2 °C.

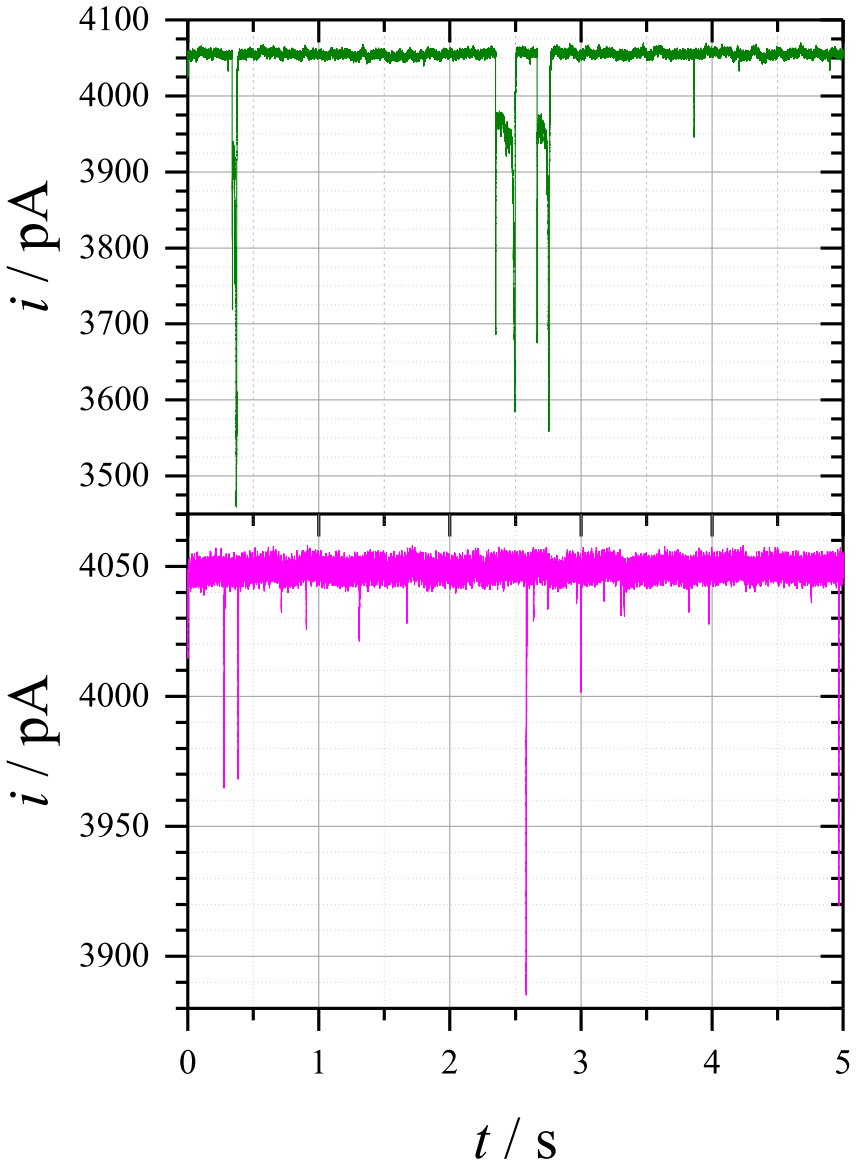


**Figure 5.19:** Current transients recorded at +280 mV *vs.* Ag/AgCl with a 430 nm Ø conical nanopore in aerobic 10 mM KCl. Both plots show the translocation of nanobubbles generated ultrasonically with a PLE driven at 2 $W_{RMS}$. The nanopore was held level with the tip of a PLE, with a horizontal displacement of 1 mm. The pressure differential applied to the nanopore was (TOP) −15 mBar and (BOTTOM) −72 mBar and the temperature during the experiment was 28.3 °C.

The behaviour of the nanobubbles during their translocation was investigated by recording the Coulter counting under various pressure differentials. As shown in Figure 5.19, high pressure differentials resulted in the fast translocation of the nanobubbles,

causing the formation of sharp peaks. Conversely, low pressure differentials caused the nanobubbles to translocate over longer timescales, resulting in wider signals. However, the oscillation of nanobubbles during translocation was not observed. This was attributed to the insufficient pressure amplitude of the acoustic wave, which needs to be significantly higher in order to cause size oscillations in the nanobubbles. This is consistent with the dynamics of acoustic bubbles, in which a nanobubble is predicted to have an increased cavitation threshold.

The possible nanobubble translocations shown in these results need to be further investigated in order to confirm the validity of applying the Coulter counting method to nanobubbles. However, by comparing these results to the observation of well-defined microbubble translocations, it is highly likely that the translocations are indeed caused by ultrasonically generated nanobubbles.

## 5.6 Bubble translocation through micropipettes

The use of pulled micropipettes to record nanoparticle translocation was discussed in Chapter 4, and was shown to offer no particular advantage to the use of nanopores made by the etching of W nanoelectrodes. Coulter counting of bubbles was also recorded through these micropipettes, in order to see if the translocations differed in any way to those through the nanopores made by W etching.

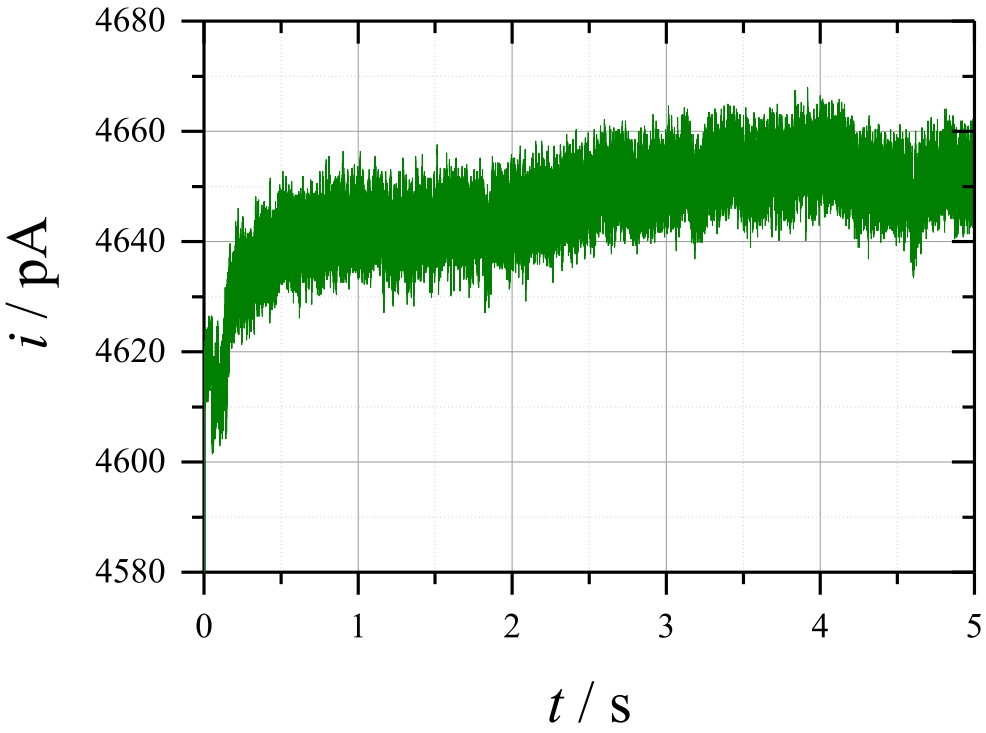


**Figure 5.20:** Current transient recorded at +87 mV *vs.* Ag/AgCl with a 2.5 $\mu$m Ø conical pulled micropipette in aerobic 10 mM KCl. The plot shows the lack of translocations despite bubbles being generated ultrasonically with a PLE driven at 2 $W_{RMS}$. The micropipette was held level with the tip of the PLE, with a horizontal displacement of 1 mm. The pressure differential applied to the micropipette was −78 mBar and the temperature during the experiment was 23.1 °C.

As shown in Figure 5.20, no translocations were observed through the pipette during the ultrasonication of the electrolyte. This is in contrast to the numerous translocations observed through the micro/nanopores made by wire etching. Furthermore, hydrophone data and high-speed camera videos recorded throughout the ultrasonication showed a

significant amount of bubble activity shown in the cell, which was seemingly not detected by the micropipette. The images from the high-speed camera even showed bubble clusters moving up the body of the pipette under the influence of the acoustic wave. Similar bubble clusters were seen on the surface of micro/nanopores and were linked to the translocation of bubbles.

The lack of bubble translocations may be explained by the motion of bubbles on the surface of the pores. Bubbles were observed to skate around the surface of pores that were set in a thick surround of glass, with the occasional movement of the bubbles over the pore enabling their detection. However, there was no such surface on the pipette structure for the bubbles to move in this way. Therefore, it was thought that introducing a flat surface next to the pipette would allow bubbles to get closer, enabling their detection by Coulter counting. A polished glass rod was positioned next to the pipette, as shown in the set-up illustrated in Figure 5.21.

As shown in Figure 5.22, the positioning of this glass rod enabled small translocations of $\approx 150$ pA to be seen through the micropipettes. This seemingly confirmed the idea that the translocation of bubbles required the presence of a surface for the bubbles to move around on. These small translocations were attributed to the emission of finer bubbles from the oscillation of the bubble on the surface of the rod, which was possibly due to the influence of the acoustic wave. Larger signals due to the translocation of bubble 'slugs' were not observed, since the bubble on the glass rod could not move directly over the pipette. Whilst this showed translocations could be performed with pipettes, the results obtained with the micro/nanopores prepared by etching were considerably better quality. The use of pipettes did however shed some light on how ultrasonically generated bubbles could be detected by Coulter counting. The fine bubbles ejected by the inertial collapse of PLE cluster were collected by the reflector, keeping bubble activity in this region high. This resulted in bubbles on the surface of the pores, which oscillated and moved under the influence of the acoustic wave. This oscillation produced small micro/nanobubbles, which were detected as they translocated through the pores, and microbubbles, which caused bubble 'slugs' as they moved over the pore.

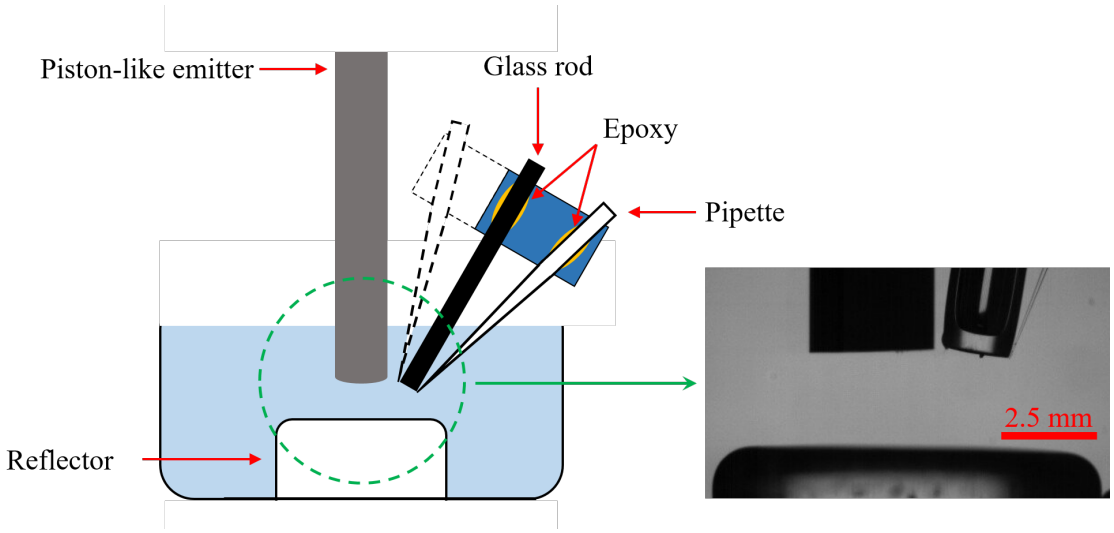


**Figure 5.21:** Design of the pulled micropipette modification used to improve the translocation of ultrasonically generated bubbles. The micropipette was glued onto a glass microscope slide, allowing the tip of the micropipette to be placed next to a glass rod, which was also glued onto the glass slide. This glass rod acted as a surface for the formation of tertiary bubble clusters, which then released detectable bubbles close to the micropipette. The dashed lines indicate the alternative position of the modified micropipette after a 180° rotation, allowing the micropipette to be positioned closer or further away from the PLE. A high-speed camera image of this modified micropipette set-up is shown.

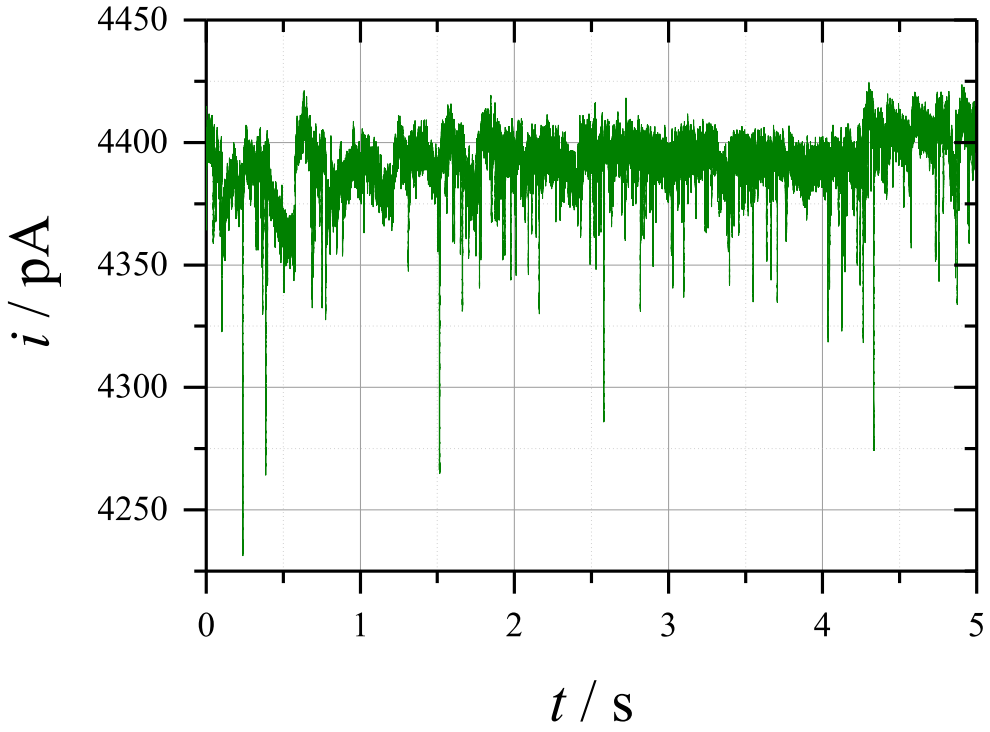


**Figure 5.22:** Current transient recorded at +87 mV *vs.* Ag/AgCl with a 2.5 $\mu$m Ø conical pulled micropipette in aerobic 10 mM KCl. The plot shows the translocation of bubbles being generated ultrasonically with a PLE driven at 2 $W_{RMS}$. The micropipette was positioned next to a polished glass rod, which was held level with the tip of the PLE, with a horizontal displacement of 1 mm. The pressure differential applied to the micropipette was −78 mBar and the temperature during the experiment was 23.1 °C.

## 5.7 Chapter 5 conclusions

The ultrasonication of electrolytes with a titanium piston-like emitter was shown to produce large populations of bubbles, which formed a cluster that repeatedly expanded and collapsed in an inertial cavitation mechanism. This expansion/collapse cycle was shown to occur at sub-harmonic frequencies of the PLE, which contributed to the formation of fine bubble clouds. This system produced surface confined microbubbles, which were detected by Coulter counting through cylindrical micropores and observed using high-speed camera techniques. These microbubbles showed significant oscillations during translocation. which was related to the acoustic environment in the electrolyte, providing key evidence that the translocations were bubbles. Similar observations were made with nanopores, except that the oscillations were not possible at the low frequencies employed.

The micro/nanobubbles observed by Coulter counting were determined to be transient in nature and local to the bubble cluster under the PLE. Whilst this contradicts the reports of stable nanobubbles, the Coulter counting technique was shown to be effective, and could easily be applied to other generation methods.

# 6 Conclusions and future work

The contradiction between well established bubble dynamics and the experimentally observed stability of nanobubbles is the source of much controversy. Furthermore, the lack of suitable techniques that can explain this stability has led to widespread skepticism in the existence of nanobubbles. However, with mounting experimental evidence showing their observation, the current consensus is that nanobubbles do exist in some form. To better understand why these nanobubbles appear to be stable, more suitable methods of nanobubble detection and characterisation are required. The work in this thesis has proposed the use of Coulter counting to provide a new method of characterising bulk nanobubbles.

The nanopores required for the Coulter counting of bulk nanobubbles were obtained by the complete etching of nanoelectrodes. Therefore, a wire etching procedure for the fabrication of W nanoelectrodes was reported in this work. The use of W as an electrode material was first examined using microelectrodes. These were able to record well-behaved steady state voltammetry for redox compounds, and exhibited little interference from background processes. Furthermore, these microelectrodes showed the corrosion of W under certain conditions, allowing the electrochemical etching of W to be performed in alkaline solutions. This etching process was used to produce sharp W tips, which were shown by electron microscopy to have conical/exponential geometries with full cone angles ranging between $2 - 4°$. The sealing of these tips in glass capillaries led to the formation of inlaid W nanodisc electrodes, which were shown to exhibit similar characteristics to the W microelectrodes. However, the W nanoelectrodes often required sufficient conditioning and cleaning before they could display steady state voltammetry, suggesting other processes were occurring on the W surface. This was also observed with chronoamperometry recorded on the W nanoelectrodes, which did not follow the theoretical fittings at shorter timescales. The origin of these additional processes was not fully determined during the course of this project, and needs to be investigated in further work.

The apparatus required for Coulter counting was established before any nanobubble translocations were recorded. Microparticle translocations through well-defined cylindrical micropores were used to characterise the apparatus, and were recorded using a conventional chronoamperometry method and an alternative differential method, which was shown to give greater signal-to-noise ratios. The ability of this Coulter counting apparatus was evaluated by comparison with both theory and simulations of particle translocation, and with the fast translocation of microparticles through conical micropores. Through these methods, the apparatus was determined to be capable of accurately sizing microparticles with a high time resolution. Glass nanopores set in a thick surround of glass were prepared by the chemical etching of the W nanoelectrodes. Nanoparticle translocations were successfully recorded through these nanopores and were consistent with simulated translocations, indicating the suitability of the nanopores for the Coulter counting of nanobubbles. However, the reduced flow rate experienced by nanopores that were smaller in diameter prevented more detailed characterisation. Future work in this area should be concerned with improving the number of translocations recorded at low diameters. Recent literature has shown this being achieved by exerting fine control over the pressure or electrophoretic driving force. Furthermore, different pore geometries that might increase the flow rate could be investigated, through control of the electrochemical W microwire etching procedure.

After demonstrating the Coulter counting of nanoparticles through glass nanopores, attention was turned to the characterisation of nanobubbles. Ultrasonication of electrolyte solutions was shown to produce large bubble clusters at the tip of a piston-like emitter. The continuous growth and collapse of this cluster produced microbubbles that were detected by Coulter counting through cylindrical micropores. These microbubbles were shown to be transient in nature and local to the PLE. Furthermore, they were shown to oscillate under the influence of the acoustic wave as they translocated, causing variations in the current signal. This behaviour was even recorded using a high-speed camera and showed that the detection of bubbles by Coulter counting was possible. Later experiments with pipettes showed that the translocation of micro/nanobubbles was linked to the oscillation of bubbles on the surface of the pores. The Coulter counting through nanopores was then used to confirm the presence of transient nanobubbles within the ultrasonicated electrolyte. Further work is needed to understand the exact process by which ultrasonically generated nanobubbles can be detected, but these results clearly indicate the successful use of Coulter counting to detect bulk nanobubbles. This technique could be combined

with other characterisation methods to provide more information on the formation and stability of nanobubbles, generated either by ultrasonication or an alternative methods like electrolysis.

# 7 References


(1) C. G. J. Bisperink and A. Prins, *Colloids and Surfaces A: Physicochemical and Engineering Aspects*, 1994, **85**, 237–253.

(2) M. A. Shafi, J. G. Lee and R. W. Flumerfelt, *Polymer Engineering and Science*, 1996, **36**, 1950–1959.

(3) J. Rubio, M. L. Souza and R. W. Smith, *Minerals Engineering*, 2002, **15**, 139–155.

(4) S. F. Jones, G. M. Evans and K. P. Galvin, *Advances in Colloid and Interface Science*, 1999, **80**, 27–50.

(5) F. Lugli and F. Zerbetto, *Physical Chemistry Chemical Physics*, 2007, **9**, 2447–2456.

(6) D. C. Grulke, N. A. Marsh and B. A. Hills, *British Journal of Experimental Pathology*, 1973, **54**, 684–691.

(7) E. C. Unger, T. O. Matsunaga, T. McCreery, P. Schumann, R. Sweitzer and R. Quigley, *European Journal of Radiology*, 2002, **42**, 160–168.

(8) E.-J. Lee, Y.-H. Kim, H.-S. Kim and A. Jang, *Environmental Science and Pollution Research*, 2015, **22**, 8451–8459.

(9) M. Alheshibri, J. Qian, M. Jehannin and V. S. J. Craig, *Langmuir*, 2016, **32**, 11086–11100.

(10) R. Sander, *Atmospheric Chemistry and Physics*, 2015, **15**, 4399–4981.

(11) T. G. Leighton, *The Acoustic Bubble*, Academic Press, London, 1st, 1997.

(12) F. R. Young, *Cavitation*, Imperial College Press, London, 2nd, 1999.

(13) L. Parkinson, R. Sedev, D. Fornasiero and J. Ralston, *Journal of Colloid and Interface Science*, 2008, **322**, 168–172.

(14) S. Ljunggren and J. C. Eriksson, *Colloids and Surfaces A: Physicochemical and Engineering Aspects*, 1997, **129-130**, 151–155.

(15) P. S. Epstein and M. S. Plesset, *The Journal of Chemical Physics*, 1950, **18**, 1505–1509.

(16) R. T. Ferrell and D. M. Himmelblau, *Journal of Chemical and Engineering Data*, 1967, **12**, 111–115.

(17) M. S. Plesset and A. Prosperetti, *Annual Review of Fluid Mechanics*, 1977, **9**, 145–185.

(18) E. A. Neppiras, *Physics Reports*, 1980, **61**, 159–251.

(19) J. R. T. Seddon, D. Lohse, W. A. Ducker and V. S. J. Craig, *ChemPhysChem*, 2012, **13**, 2179–2187.

(20) D. Sette and F. Wanderlingh, *Physical Review*, 1962, **125**, 409–417.

(21) N. F. Bunkin and F. V. Bunkin, *Soviet Physics: Journal of Experimental and Theoretical Physics*, 1992, **74**, 271–278.

(22) E. T. Degens, R. P. von Herzen, H.-K. Wong, W. G. Deuser and H. W. Jannasch, *Geologische Rundschau*, 1973, **62**, 245–277.

(23) B. D. Johnson and R. C. Cooke, *Science*, 1981, **213**, 209–211.

(24) K. Ebina, K. Shi, M. Hirao, J. Hashimoto, Y. Kawato, S. Kaneshiro, T. Morimoto, K. Koizumi and H. Yoshikawa, *PLoS ONE*, 2013, **8**, e65339.

(25) B. E. Oeffinger and M. A. Wheatley, *Ultrasonics*, 2004, **42**, 343–347.

(26) M. Argenziano, G. Banche, A. Luganini, N. Finesso, V. Allizond, G. R. Gulino, A. Khadjavi, R. Spagnolo, V. Tullio, G. Giribaldi, C. Guiot, A. M. Cuffini, M. Prato and R. Cavalli, *International Journal of Pharmaceutics*, 2017, **523**, 176–188.

(27) Y. Wang, X. Li, Y. Zhou, P. Huang and Y. Xu, *International Journal of Pharmaceutics*, 2010, **384**, 148–153.

(28) J. Zhu, H. An, M. Alheshibri, L. Liu, P. M. J. Terpstra, G. Liu and V. S. J. Craig, *Langmuir*, 2016, **32**, 11203–11211.

(29) A. Ghadimkhani, W. Zhang and T. Marhaba, *Chemosphere*, 2016, **146**, 379–384.

(30) M. Fan, D. Tao, R. Honaker and Z. Luo, *Mining Science and Technology*, 2010, **20**, 159–177.

(31) S. Calgaroto, A. Azevedo and J. Rubio, *International Journal of Mineral Processing*, 2015, **137**, 64–70.

(32) V. Leroy and T. Norisuye, *ChemPhysChem*, 2016, **17**, 2787–2790.

(33) W. N. Wang and R. Totterman, *Internat. Pat.*, **WO 2014/184585**, 2014.

(34) K. Terasaka, A. Hirabayashi, T. Nishino, S. Fujioka and D. Kobayashi, *Chemical Engineering Science*, 2011, **66**, 3172–3179.

(35) M. Fan, D. Tao, R. Honaker and Z. Luo, *Mining Science and Technology*, 2010, **20**, 1–19.

(36) P. R. Gogate and A. B. Pandit, *AIChE Journal*, 2000, **46**, 1641–1649.

(37) J.-Y. Kim, M.-G. Song and J.-D. Kim, *Journal of Colloid and Interface Science*, 2000, **223**, 285–291.

(38) S.-H. Cho, J.-Y. Kim, J.-H. Chun and J.-D. Kim, *Colloids and Surfaces A: Physicochemical and Engineering Aspects*, 2005, **269**, 28–34.

(39) N. Nirmalkar, A. W. Pacek and M. Barigou, *Langmuir*, 2018, **34**, 10964–10973.

(40) I. Dalmolin, E. Skovroinski, A. Biasi, M. L. Corazza, C. Dariva and J. V. Oliveira, *Fluid Phase Equilibria*, 2006, **245**, 193–200.

(41) J. Qiu, Z. Zou, S. Wang, X. Wang, L. Wang, Y. Dong, H. Zhao, L. Zhang and J. Hu, *ChemPhysChem*, 2017, **18**, 1345–1350.

(42) A. Häbich, W. Ducker, D. E. Dunstan and X. Zhang, *Journal of Physical Chemistry B*, 2010, **114**, 6962–6967.

(43) A. S. Najafi, J. Drelich, A. Yeung, Z. Xu and J. Masliyah, *Journal of Colloid and Interface Science*, 2007, **308**, 344–350.

(44) K. Kikuchi, H. Takeda, B. Rabolt, T. Okaya, Z. Ogumi, Y. Saihara and H. Noguchi, *Journal of Electroanalytical Chemistry*, 2001, **506**, 22–27.

(45) K. Kikuchi, S. Nagata, Y. Tanaka, Y. Saihara and Z. Ogumi, *Journal of Electroanalytical Chemistry*, 2007, **600**, 303–310.

(46) K. Kikuchi, A. Ioka, T. Oku, Y. Tanaka, Y. Saihara and Z. Ogumi, *Journal of Colloid and Interface Science*, 2009, **329**, 306–309.

(47) K. Kikuchi, Y. Tanaka, Y. Saihara, M. Maeda, M. Kawamura and Z. Ogumi, *Journal of Colloid and Interface Science*, 2006, **298**, 914–919.

(48) V. B. Svetovoy, R. G. P. Sanders, T. S. J. Lammerink and M. C. Elwenspoek, *Physical Review E - Statistical, Nonlinear, and Soft Matter Physics*, 2011, **84**, 035302.

(49) K. Ohgaki, N. Q. Khanh, Y. Joden, A. Tsuji and T. Nakagawa, *Chemical Engineering Science*, 2010, **65**, 1296–1300.

(50) Z. Xing, J. Wang, H. Ke, B. Zhao, X. Yue, Z. Dai and J. Liu, *Nanotechnology*, 2010, **21**, 145607.

(51) T. Uchida, S. Oshita, M. Ohmori, T. Tsuno, K. Soejima, S. Shinozaki, Y. Take and K. Mitsuda, *Nanoscale Research Letters*, 2011, **6**, 1–9.

(52) T. Uchida, S. Liu, M. Enari, S. Oshita, K. Yamazaki and K. Gohara, *Nanomaterials*, 2016, **6**, 1–10.

(53) K. Kikuchi, Y. Tanaka, Y. Saihara and Z. Ogumi, *Electrochimica Acta*, 2006, **52**, 904–913.

(54) F. Y. Ushikubo, T. Furukawa, R. Nakagawa, M. Enari, Y. Makino, Y. Kawagoe, T. Shiina and S. Oshita, *Colloids and Surfaces A: Physicochemical and Engineering Aspects*, 2010, **361**, 31–37.

(55) H. Kobayashi, S. Maeda, M. Kashiwa and T. Fujita, Proceedings of SPIE, ed. N. Aya, N. Iki, T. Shimura and T. Shirai, Tokyo, 2014, vol. 9232, 0S1–0S6.

(56) T. P. Burg, M. Godin, S. M. Knudsen, W. Shen, G. Carlson, J. S. Foster, K. Babcock and S. R. Manalis, *Nature*, 2007, **446**, 1066–1069.

(57) K. Yasui, T. Tuziuti, W. Kanematsu and K. Kato, *Langmuir*, 2016, **32**, 11101–11110.

(58) K. Yasui, T. Tuziuti and W. Kanematsu, *Physical Review E*, 2016, **94**, 013106.

(59) F. Jin, J. Ye, L. Hong, H. Lam and C. Wu, *Journal of Physical Chemistry B*, 2007, **111**, 2255–2261.

(60) S. O. Yurchenko, A. V. Shkirin, B. W. Ninham, A. A. Sychev, V. A. Babenko, N. V. Penkov, N. P. Kryuchkov and N. F. Bunkin, *Langmuir*, 2016, **32**, 11245–11255.

(61) N. F. Bunkin, A. V. Shkirin, P. S. Ignatiev, L. L. Chaikov, I. S. Burkhanov and A. V Starosvetskij, *Journal of Chemical Physics*, 2012, **137**, 054706.

(62) J. H. Weijs, J. R. T. Seddon and D. Lohse, *ChemPhysChem*, 2012, **13**, 2197–2204.

(63) J. Israelachvili and R. Pashley, *Nature*, 1982, **300**, 341–342.

(64) H. K. Christenson and P. M. Claesson, *Science*, 1988, **239**, 390–392.

(65) J. L. Parker, P. M. Claesson and P. Attard, *Journal of Physical Chemistry*, 1994, **98**, 8468–8480.

(66) L. Meagher and V. S. J. Craig, *Langmuir*, 1994, **10**, 2736–2742.

(67) S.-T. Lou, Z.-Q. Ouyang, Y. Zhang, X.-J. Li, J. Hu, M.-Q. Li and F.-J. Yang, *Journal of Vacuum Science & Technology B: Microelectronics and Nanometer Structures*, 2000, **18**, 2573–2575.

(68) N. Ishida, T. Inoue, M. Miyahara and K. Higashitani, *Langmuir*, 2000, **16**, 6377–6380.

(69) X. H. Zhang, A. Khan and W. A. Ducker, *Physical Review Letters*, 2007, **98**, 136101.

(70) D. Seo, S. R. German, T. L. Mega and W. A. Ducker, *Journal of Physical Chemistry C*, 2015, **119**, 14262–14266.

(71) G. Liu, Z. Wu and V. S. J. Craig, *Journal of Physical Chemistry C*, 2008, **112**, 16748–16753.

(72) H. Chen, H. Mao, L. Wu, J. Zhang, Y. Dong, Z. Wu and J. Hu, *Biofouling*, 2009, **25**, 353–357.

(73) G. Liu and V. S. J. Craig, *ACS Applied Materials and Interfaces*, 2009, **1**, 481–487.

(74) Z. Wu, H. Chen, Y. Dong, H. Mao, J. Sun, S. Chen, V. S. J. Craig and J. Hu, *Journal of Colloid and Interface Science*, 2008, **328**, 10–14.

(75) E. Karatay, A. S. Haase, C. W. Visser, C. Sun, D. Lohse, P. A. Tsai and R. G. H. Lammertink, *Proceedings of the National Academy of Sciences*, 2013, **110**, 8422–8426.

(76) D. C. Tretheway and C. D. Meinhart, *Physics of Fluids*, 2004, **16**, 1509–1515.

(77) Y. Wang and B. Bhushan, *Soft Matter*, 2010, **6**, 29–66.

(78) D. Li, D. Jing, Y. Pan, B. Bhushan and X. Zhao, *Langmuir*, 2016, **32**, 11287–11294.

(79) Z. Che and P. E. Theodorakis, *Journal of Colloid and Interface Science*, 2017, **487**, 123–129.

(80) V. S. J. Craig, *Soft Matter*, 2011, **7**, 40–48.

(81) S. Yang and A. Duisterwinkel, *Langmuir*, 2011, **27**, 11430–11435.

(82) X. H. Zhang, A. Quinn and W. A. Ducker, *Langmuir*, 2008, **24**, 4756–4764.

(83) X. H. Zhang, X. Zhang, J. Sun, Z. Zhang, G. Li, H. Fang, X. Xiao, X. Zeng and J. Hu, *Langmuir*, 2007, **23**, 1778–1783.

(84) M. Liu, W. Zhao, S. Wang, W. Guo, Y. Tang and Y. Dong, *ChemPhysChem*, 2013, **14**, 2589–2593.

(85) H. An, B. H. Tan, Q. Zeng and C.-D. Ohl, *Langmuir*, 2016, **32**, 11212–11220.

(86) L. Luo and H. S. White, *Langmuir*, 2013, **29**, 11169–11175.

(87) S. R. German, M. A. Edwards, Q. Chen and H. S. White, *Nano Letters*, 2016, **16**, 6691–6694.

(88) L. Zhang, Y. Zhang, X. Zhang, Z. Li, G. Shen, M. Ye, C. Fan, H. Fang and J. Hu, *Langmuir*, 2006, **22**, 8109–8113.

(89) Q. Chen, H. S. Wiedenroth, S. R. German and H. S. White, *Journal of the American Chemical Society*, 2015, **137**, 12064–12069.

(90) H. Ren, S. R. German, M. A. Edwards, Q. Chen and H. S. White, *The Journal of Physical Chemistry Letters*, 2017, **8**, 2450–2454.

(91) L. Wang, X. Miao and G. Pan, *Langmuir*, 2016, **32**, 11147–11154.

(92) W. Walczyk and H. Schönherr, *Langmuir*, 2013, **29**, 620–632.

(93) S. Karpitschka, E. Dietrich, J. R. T. Seddon, H. J. W. Zandvliet, D. Lohse and H. Riegler, *Physical Review Letters*, 2012, **109**, 066102.

(94) D. R. Evans, V. S. J. Craig and T. J. Senden, *Physica A*, 2004, **339**, 101–105.

(95) M. Holmberg, A. Kühle, J. Garnæs, K. A. Mørch and A. Boisen, *Langmuir*, 2003, **19**, 10510–10513.

(96) H. An, B. H. Tan and C.-D. Ohl, *Langmuir*, 2016, **32**, 12710–12715.

(97) N. Hain, D. Wesner, S. I. Druzhinin and H. Schönherr, *Langmuir*, 2016, **32**, 11155–11163.

(98) B. H. Tan, H. An and C.-D. Ohl, *Physical Review Letters*, 2017, **118**, 054501.

(99) L. Zhang, B. Zhao, L. Xue, Z. Guo, Y. Dong, H. Fang, R. Tai and J. Hu, *Journal of Synchrotron Radiation*, 2013, **20**, 413–418.

(100) E. R. White, M. Mecklenburg, S. B. Singer, S. Aloni and B. C. Regan, *Applied Physics Express*, 2011, **4**, 055201.

(101) F. Hui, B. Li, P. He, J. Hu and Y. Fang, *Electrochemistry Communications*, 2009, **11**, 639–642.

(102) S. R. German, Q. Chen, M. A. Edwards and H. S. White, *Journal of The Electrochemical Society*, 2016, **163**, H3160–H3166.

(103) Y. Liu and X. Zhang, *The Journal of Chemical Physics*, 2017, **146**, 164704.

(104) S. Maheshwari, M. van der Hoef, X. Zhang and D. Lohse, *Langmuir*, 2016, **32**, 11116–11122.

(105) P. Attard, *The European Phsyical Journal Special Topics*, 2013, 1–22.

(106) X. Zhang, M. H. Uddin, H. Yang, G. Toikka, W. Ducker and N. Maeda, *Langmuir*, 2012, **28**, 10471–10477.

(107) P. Attard, M. P. Moody and J. W. G. Tyrrell, *Physica*, 2002, **314**, 696–705.

(108) J. R. T. Seddon, H. J. W. Zandvliet and D. Lohse, *Physical Review Letters*, 2011, **107**, 116101.

(109) H. Peng, G. R. Birkett and A. V. Nguyen, *Advances in Colloid and Interface Science*, 2015, **222**, 573–580.

(110) M. P. Brenner and D. Lohse, *Physical Review Letters*, 2008, **101**, 214505.

(111) X. H. Zhang, N. Maeda and V. S. J. Craig, *Langmuir*, 2006, **22**, 5025–5035.

(112) W. A. Ducker, *Langmuir*, 2009, **25**, 8907–8910.

(113) H. Teshima, T. Nishiyama and K. Takahashi, *The Journal of Chemical Physics*, 2017, **146**, 014708.

(114) P. Attard, *Langmuir*, 2016, **32**, 11138–11146.

(115) J. H. Weijs and D. Lohse, *Physical Review Letters*, 2013, **110**, 054501.

(116) X. Zhang, D. Y. C. Chan, D. Wang and N. Maeda, *Langmuir*, 2013, **29**, 1017–1023.

(117) Y. Liu and X. Zhang, *The Journal of Chemical Physics*, 2014, **141**, 134702.

(118) D. Lohse and X. Zhang, *Reviews of Modern Physics*, 2015, **87**, 981–1035.

(119) J. R. T. Seddon, O. Bliznyuk, E. S. Kooij, B. Poelsema, H. J. W. Zandvliet and D. Lohse, *Langmuir*, 2010, **26**, 9640–9644.

(120) H. Tarábková and P. Janda, *Journal of Physics: Condensed Matter*, 2013, **25**, 184001.

(121) X. H. Zhang, N. Maeda and J. Hu, *Journal of Physical Chemistry B*, 2008, **112**, 13671–13675.

(122) L. Zhang, X. Zhang, C. Fan, Y. Zhang and J. Hu, *Langmuir*, 2009, **25**, 8860–8864.

(123) K. Yasui, T. Tuziuti, W. Kanematsu and K. Kato, *Physical Review E*, 2015, **91**, 033008.

(124) J. R. T. Seddon, E. S. Kooij, B. Poelsema, H. J. W. Zandvliet and D. Lohse, *Physical Review Letters*, 2011, **106**, 056101.

(125) H. An, G. Liu and V. S. J. Craig, *Advances in Colloid and Interface Science*, 2015, **222**, 9–17.

(126) X. Wang, B. Zhao, J. Hu, S. Wang, R. Tai, X. Gao and L. Zhang, *Physical Chemistry Chemical Physics*, 2017, **19**, 1108–1114.

(127) D. W. M. Arrigan, *Analyst*, 2004, **129**, 1157–1165.

(128) R. W. Murray, *Chemical Reviews*, 2008, **108**, 2688–2720.

(129) C. G. Zoski, *Electroanalysis*, 2002, **14**, 1041–1051.

(130) D. Pletcher, *A First Course in Electrode Processes*, The Royal Society of Chemistry, Cambridge, 2nd, 2009.

(131) R. Chen, K. Hu, Y. Yu, M. V. Mirkin and S. Amemiya, *Journal of The Electrochemical Society*, 2016, **163**, H3032–H3037.

(132) P. Elsamadisi, Y. Wang, J. Velmurugan and M. V. Mirkin, *Analytical Chemistry*, 2011, **83**, 671–673.

(133) P. Sun, Z. Zhang, J. Guo and Y. Shao, *Analytical Chemistry*, 2001, **73**, 5346–5351.

(134) P. Sun, F. O. Laforge, T. P. Abeyweera, S. A. Rotenberg, J. Carpino and M. V. Mirkin, *Proceedings of the National Academy of Sciences*, 2008, **105**, 443–448.

(135) J. I. Yeh and H. Shi, *Wiley Interdisciplinary Reviews: Nanomedicine and Nanobiotechnology*, 2010, **2**, 176–188.

(136) D. O. Wipf, A. C. Michael and R. M. Wightman, *Journal of Electroanalytical Chemistry*, 1989, **269**, 15–25.

(137) R. B. Morris, D. J. Franta and H. S. White, *Journal of Physical Chemistry*, 1987, **91**, 3559–3564.

(138) M. P. Nagale and I. Fritsch, *Analytical Chemistry*, 1998, **70**, 2908–2913.

(139) M. P. Nagale and I. Fritsch, *Analytical Chemistry*, 1998, **70**, 2902–2907.

(140) R. M. Penner, M. J. Heben, T. L. Longin and N. S. Lewis, *Science*, 1990, **250**, 1118–1121.

(141) Y. Shao, M. V. Mirkin, G. Fish, S. Kokotov, D. Palanker and A. Lewis, *Analytical Chemistry*, 1997, **69**, 1627–1634.

(142) B. B. Katemann and W. Schuhmann, *Electroanalysis*, 2002, **14**, 22–28.

(143) J. L. Amphlett and G. Denuault, *Journal of Physical Chemistry B*, 1998, **102**, 9946–9951.

(144) K. L. Adams, M. Puchades and A. G. Ewing, *Annual Review of Analytical Chemistry (Palo Alto Calif)*, 2008, **1**, 329–355.

(145) M. V. Mirkin, F.-R. F. Fan and A. J. Bard, *Journal of Electroanalytical Chemistry*, 1992, **328**, 47–62.

(146) C. J. Slevin, N. J. Gray, J. V. MacPherson, M. A. Webb and P. R. Unwin, *Electrochemistry Communications*, 1999, **1**, 282–288.

(147) V. P. Menon and C. R. Martin, *Analytical Chemistry*, 1995, **67**, 1920–1928.

(148) A. Mardegan, P. Scopece, F. Lamberti, M. Meneghetti, L. M. Moretto and P. Ugo, *Electroanalysis*, 2012, **24**, 798–806.

(149) Y. Saito, *Review of Polarography*, 1968, **15**, 177–187.

(150) W. H. Coulter, *US Pat.*, **US2656568**, 1953.

(151) P. R. Birkin, S. Linfield, G. Denuault, R. Jones, J. J. Youngs and E. Wain, *ACS Sensors*, 2019, **4**, 2190–2195.

(152) W.-J. Lan, D. A. Holden, J. Liu and H. S. White, *The Journal of Physical Chemistry C*, 2011, **115**, 18445–18452.

(153) S. R. German, L. Luo, H. S. White and T. L. Mega, *Journal of Physical Chemistry C*, 2013, **117**, 703–711.

(154) R. W. DeBlois and C. P. Bean, *Review of Scientific Instruments*, 1970, **41**, 909–916.

(155) J. L. Anderson and J. A. Quinn, *Review of Scientific Instruments*, 1971, **42**, 1257–1258.

(156) W. R. Smythe, *Physics of Fluids*, 1964, **7**, 633–638.

(157) T. M. Foley, Ph.D. Thesis, University of Southampton, 2014.

(158) B.-F. Ju, Y.-L. Chen and Y. Ge, *Review of Scientific Instruments*, 2011, **82**, 013707.

(159) R. J. White, B. Zhang, S. Daniel, J. M. Tang, E. N. Ervin, P. S. Cremer and H. S. White, *Langmuir*, 2006, **22**, 10777–10783.

(160) W.-J. Lan, D. A. Holden, B. Zhang and H. S. White, *Analytical Chemistry*, 2011, **83**, 3840–3847.

(161) K. McKelvey, M. A. Edwards and H. S. White, *Journal of Physical Chemistry Letters*, 2016, **7**, 3920–3924.

(162) T. G. Leighton, *Progress in Biophysics and Molecular Biology*, 2007, **93**, 3–83.

(163) P. R. Birkin, D. G. Offin, C. J. B. Vian and T. G. Leighton, *Journal of the Acoustical Society of America*, 2011, **130**, 3379–3388.

(164) W. Lauterborn and T. Kurz, *Reports on Progress in Physics*, 2010, **73**, 1–88.

(165) N. Nioradze, R. Chen, J. Kim, M. Shen, P. Santhosh and S. Amemiya, *Analytical Chemistry*, 2013, **85**, 6198–6202.

(166) B. Sakmann and E. Neher, *Single-Channel Recording*, Spinger, New York, 2nd, 1995.

(167) B. Zhang, J. Galusha, P. G. Shiozawa, G. Wang, A. J. Bergren, R. M. Jones, R. J. White, E. N. Ervin, C. C. Cauley and H. S. White, *Analytical Chemistry*, 2007, **79**, 4778–4787.

(168) M. V. Mirkin and B. R. Horrocks, *Analytica Chimica Acta*, 2000, **406**, 119–146.

(169) P. Schmuki, *Journal of Solid State Electrochemistry*, 2002, **6**, 145–164.

(170) R. D. Conner, R. B. Dandliker and W. L. Johnson, *Acta Materialia*, 1998, **46**, 6089–6102.

(171) M. Pourbaix, *Atlas of Electrochemical Equilibria in Aqueous Solutions*, NACE International (National Association of Corrosion Engineers), Houston, 2nd, 1974, p. 644.

(172) Z.-F. Huang, J. Song, L. Pan, X. Zhang, L. Wang and J.-J. Zou, *Advanced Materials*, 2015, **27**, 5309–5327.

(173) H. Zheng, J. Z. Ou, M. S. Strano, R. B. Kaner, A. Mitchell and K. Kalantar-Zadeh, *Advanced Functional Materials*, 2011, **21**, 2175–2196.

(174) M. E. Abdelsalam, G. Denuault, M. A. Baldo and S. Daniele, *Journal of Electroanalytical Chemistry*, 1998, **449**, 5–7.

(175) T. Tuvić, I. Pašti and S. Mentus, *Russian Journal of Physical Chemistry A*, 2011, **85**, 2399–2405.

(176) M. E. Abdelsalam, G. Denuault, M. A. Baldo, C. Bragato and S. Daniele, *Electroanalysis*, 2001, **13**, 289–294.

(177) M. Anik and K. Osseo-Asare, *Journal of The Electrochemical Society*, 2002, **149**, B224–233.

(178) Y. Wang, J. G. Limon-Petersen and R. G. Compton, *Journal of Electroanalytical Chemistry*, 2011, **652**, 13–17.

(179) P. Sun and M. V. Mirkin, *Analytical Chemistry*, 2006, **78**, 6526–6534.

(180) J. T. Cox and B. Zhang, *Annual Review of Analytical Chemistry*, 2012, **5**, 253–72.

(181) P. J. Mahon and K. B. Oldham, *Analytical Chemistry*, 2005, **77**, 6100–6101.

(182) C. Beriet and D. Pletcher, *Journal of Electroanalytical Chemistry*, 1994, **375**, 213–218.

(183) J. E. B. Randles and K. W. Somerton, *Transactions of the Faraday Society*, 1952, **48**, 937–950.

(184) T. Sun, P.-Y. Blanchard and M. V. Mirkin, *Analytical Chemistry*, 2015, **87**, 4092–4095.

(185) B. Zhang, Y. Zhang and H. S. White, *Analytical Chemistry*, 2004, **76**, 6229–6238.

(186) J. Velmurugan and M. V. Mirkin, *ChemPhysChem*, 2010, **11**, 3011–3017.

(187) C. C. Harrell, Y. Choi, L. P. Home, L. A. Baker, Z. S. Siwy and C. R. Martin, *Langmuir*, 2006, **22**, 10837–10843.

(188) T. Ito, L. Sun, R. R. Henriquez and R. M. Crooks, *Accounts of Chemical Research*, 2004, **37**, 937–45.

(189) R. B. McCleskey, *Journal of Chemical & Engineering Data*, 2011, **56**, 317–327.

(190) L. Luo, S. R. German, W.-J. Lan, D. A. Holden, T. L. Mega and H. S. White, *Annual Review of Analytical Chemistry*, 2014, **7**, 513–535.

(191) W. R. Smythe, *Review of Scientific Instruments*, 1972, **43**, 817–818.

(192) G. R. Willmott and B. E. T. Parry, *Journal of Applied Physics*, 2011, **109**, 094307.

(193) E. A. Heins, Z. S. Siwy, L. A. Baker and C. R. Martin, *Nano Letters*, 2005, **5**, 1824–1829.

(194) S. Tseng, S.-C. Lin, C.-Y. Lin and J.-P. Hsu, *Journal of Physical Chemistry C*, 2016, **120**, 25620–25627.

(195) W.-J. Lan, C. Kubeil, J.-W. Xiong, A. Bund and H. S. White, *Journal of Physical Chemistry C*, 2014, **118**, 2726–2734.

(196) S. R. German, T. S. Hurd, H. S. White and T. L. Mega, *ACS Nano*, 2015, **9**, 7186–7194.

(197) M. A. Edwards, S. R. German, J. E. Dick, A. J. Bard and H. S. White, *ACS Nano*, 2015, **9**, 12274–12282.

# 8 Appendix

## 8.1 Example calculations

**Analysis of nanoelectrodes by voltammetry:**

Using the limiting current recorded by steady state cyclic voltammetry in 5 mM $Ru(NH_3)_6Cl_3$, the radius of a nanoelectrode can be determined using Equation 3.11, which is repeated below.

$$i_{lim} = 4nFDca$$

For the 360 nm Ø electrode shown in Figure 4.16 (estimating the limiting current as 200 pA after taking the slope into account):

$$2 \times 10^{-10}\ \text{A} = 4\ \times\ 1\ \times\ 96485\ \text{C mol}^{-1}\ \times\ 5.71 \times 10^{-6}\ \text{cm}^2\ \text{s}^{-1}\ \times\ 5 \times 10^{-6}\ \text{mol dm}^{-3}\ \times\ a$$

$$a = \frac{2 \times 10^{-10}\ \text{A}}{4\ \times\ 1\ \times\ 96485\ \text{C mol}^{-1}\ \times\ 5.71 \times 10^{-6}\ \text{cm}^2\ \text{s}^{-1}\ \times\ 5 \times 10^{-6}\ \text{mol dm}^{-3}}$$

$$a = 1.82 \times 10^{-5}\ \text{cm} = 182\ \text{nm}$$

**Analysis of nanopores by voltammetry:**

Using the resistance of the pore, as assessed by cyclic voltammetry of the pore in 1 M KCl, and the radius of the pore from the cyclic voltammetry recorded with the nanoelectrode before chemical etching, the half cone angle of the nanopore can be determined using Equation 4.2, which is repeated below.

$$R_p = \frac{1}{\kappa r_p}\left(\frac{1}{\pi \tan(\theta)} + \frac{1}{4}\right)$$

For the 360 nm Ø pore shown in Figure 4.16 (taking the resistance from the larger current of the slightly rectified response):

$$2 \times 10^6\ \Omega = \frac{1}{10.83\ \text{S m}^{-1}\ \times 1.82 \times 10^{-7}\ \text{m}}\ \times\ \left(\frac{1}{\pi \tan(\theta)} + \frac{1}{4}\right)$$

$$2 \times 10^6\ \Omega\ \times\ 10.83\ \text{S m}^{-1}\ \times 1.82 \times 10^{-7}\ \text{m} = \left(\frac{1}{\pi \tan(\theta)} + \frac{1}{4}\right)$$

$$\pi \tan(\theta) = \frac{1}{3.69}$$

$$\theta = 4.98^\circ$$

**Error propagation in calculation of change in resistance during translocation:**

There is an error associated with the change in resistance calculated from the change in current measured through a pore during particle translocation. This error is derived from the error in the current, given by the amount of noise recorded during the experiment. For example, in Figure 4.4 the background current was measured as 1088 nA and the noise was $\approx 8$ nA, making the error on the current $1088 \pm 4$ nA. This same error is present during translocation, so the measured translocation signal of 1083 nA has an error of $1083 \pm 4$ nA. When calculating the change in resistance, the following formula is used:

$$\Delta R = R_2 - R_1$$

$$\Delta R = \frac{V_{app}}{i_2} - \frac{V_{app}}{i_1}$$

where $\Delta R$ is the change in resistance; $V_{app}$ is the voltage applied to the pore; $i_1$ is the background current; and $i_2$ is the current during translocation. In the case of Figure 4.4, this is:

$$\Delta R = \frac{5\text{V}}{1083\text{nA}} - \frac{5\text{V}}{1088\text{nA}}$$

$$\Delta R = 21216.94\Omega$$

Inclusion of the errors in the current leads to a maximum change in resistance of:

$$\Delta R = \frac{5\text{V}}{1079\text{nA}} - \frac{5\text{V}}{1092\text{nA}}$$

$$\Delta R = 55165.72\Omega$$

And a minimum change in resistance of:

$$\Delta R = \frac{5\text{V}}{1087\text{nA}} - \frac{5\text{V}}{1084\text{nA}}$$

$$\Delta R = -12730.12\Omega$$

Therefore, the error in the change in resistance can be given as:

$$\Delta R = 21216.94 \pm 33947.05\Omega$$

This error is unreasonable because it is larger than the actual value of the change in resistance. This is due to the poor signal to noise ratio of the translocations witnessed in Figure 4.4.

**Error propagation in cone angle measurements:**

The general error in a function with the form $y = f(x, z, ...)$ can described by the formula below.

$$S_y = \left[\left(\frac{\partial y}{\partial x} \times \partial x\right)^2 + \left(\frac{\partial y}{\partial z} \times \partial x\right)^2 + ....\right]^{1/2}$$

For Equation 4.2, the error in the pore resistance can be calculated by the following formulas.

$$R_p = \underbrace{\frac{1}{\kappa r_p}}_{\beta} \times \underbrace{\left(\frac{1}{\pi \tan(\theta)} + \frac{1}{4}\right)}_{\alpha}$$

$$Error\ in\ R_p = \left[\left(\frac{-\alpha \partial r_p}{\kappa r_p^2}\right)^2 + \left(\frac{-\beta \partial \theta}{\sin^2 \theta}\right)^2\right]^{1/2}$$

This error propagation can be observed in the figure below.

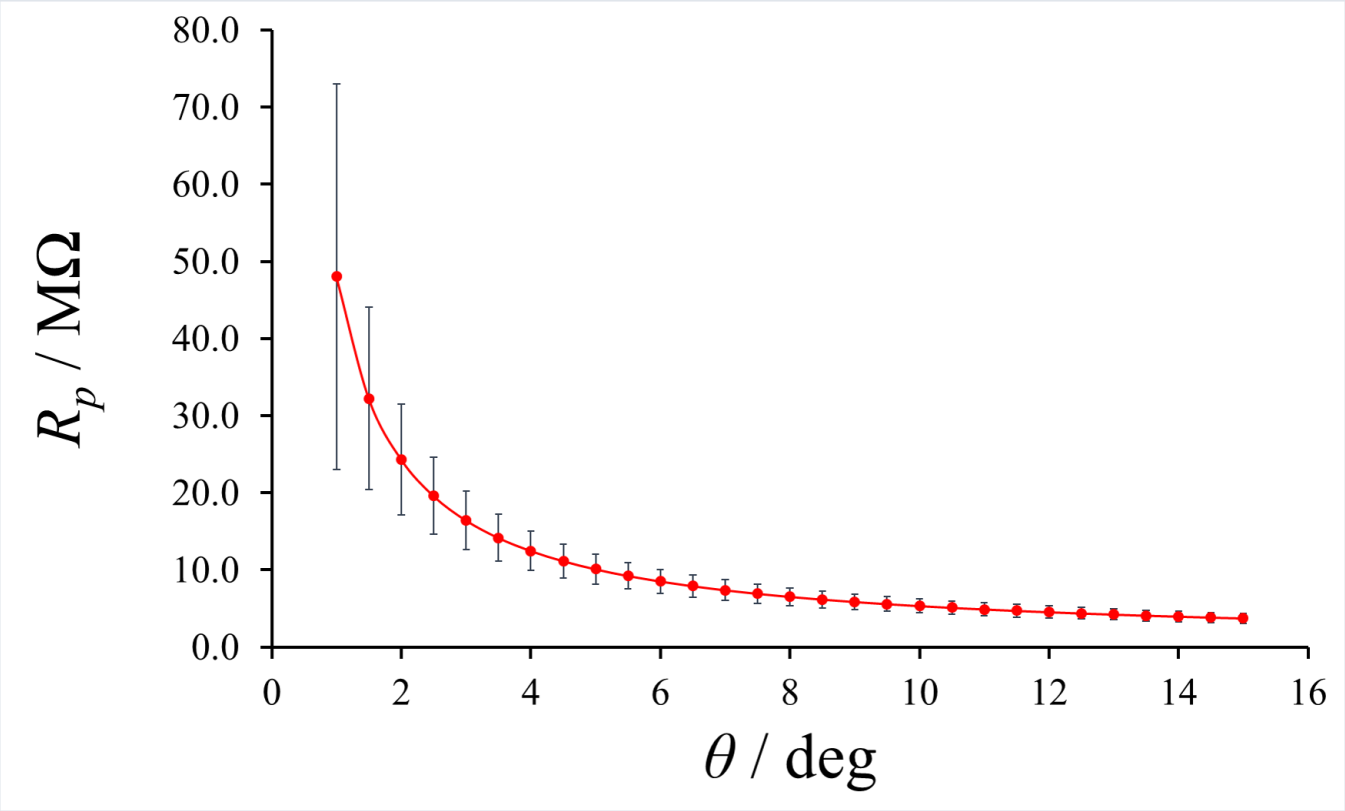


**Figure 8.1:** Plot showing how the propagation of errors in the cone angle error can affect the value of the pore resistance determined by Equation 4.2.

## 8.2 List of solutions

The following list contains the details of every solution used throughout the project. All of the solutions were prepared using 18.2 MΩ cm deionised water from a Suez Select Fusion water dispenser. Glassware was cleaned using a 5–10% solution of Decon 90 in deionised water for at least 24 hours, after which the glassware was rinsed thoroughly with deionised water and left to air dry under cover.

- 100 mM $H_2SO_4$ (0.56 mL), pH 1, in $H_2O$ (100 mL)
- 100 mM $K_2SO_4$ (1.7424 g), pH 7, in $H_2O$ (100 mL)
- 100 mM NaOH (0.4 g), pH 13, in $H_2O$ (100 mL)
- 5 mM $Ru(NH_3)_6Cl_3$ (0.0387 g) + 100 mM $K_2SO_4$ (0.4356 g), pH 3.5, in $H_2O$ (25 mL)
- 2 M NaOH (8 g) in $H_2O$ (100 mL)
- 10% w/v $H_3PO_4$ ($\approx$ 1 g) + $H_2O$ (9 mL)
- 10 mM $K_3Fe(CN)_6$ (0.0823 g) + 200 mM $Sr(NO_3)_2$ (1.05815 g), pH $\approx$ 7, in $H_2O$ (25 mL)
- ECF-60 + E3 Brightener (10 mL)
- 1:3 by volume of $H_2O_2$ (2.5 mL) + HCl (7.5 mL)
- 250 mM $K_2S_2O_8$ (0.6758 g) + 2 M NaOH (0.8 g) in $H_2O$ (10 mL)
- 1 M KCl (7.454 g) in $H_2O$ (100 mL)
- 18.8 $\mu$m Ø polystyrene spheres ($\approx$ 0.042 g, $\approx 7.2 \times 10^4$ particles $mL^{-1}$) + 10 mM KCl (0.0031 g) in $H_2O$ (4.18 mL)
- 4.9 $\mu$m Ø polystyrene spheres ($\approx$ 0.031 g, $\approx 7.2 \times 10^4$ particles $mL^{-1}$) + 1 M KCl (1.4908 g) in $H_2O$ (20 mL)
- 600 nm Ø polystyrene spheres ($\approx$ 0.03 g, $\approx 1 \times 10^7$ particles $mL^{-1}$, 25× diluted) + 1 M KCl (0.7454 g) in $H_2O$ (10 mL)

- 18.8 + 11 $\mu$m Ø particles ($\approx 7.2 \times 10^5$ particles $mL^{-1}$) + 10 mM KCl (0.0075 g) in $H_2O$ (10 mL)
- 100 nm Ø polystyrene spheres ($\approx$ 0.025 g, $\approx 2.1 \times 10^9$ particles $mL^{-1}$, 50× diluted) + 1 M KCl (0.7454 g) in $H_2O$ (10 mL)
- 220 nm Ø polystyrene spheres ($\approx$ 0.03 g, $\approx 1.4 \times 10^{10}$ particles $mL^{-1}$) + 1 M KCl (0.7454 g) in $H_2O$ (10 mL)
- 220 nm Ø polystyrene spheres ($\approx$ 0.03 g, $\approx 1.4 \times 10^{10}$ particles $mL^{-1}$) + 100 mM KCl (0.0745 g) in $H_2O$ (10 mL)
- 220 nm Ø polystyrene spheres ($\approx$ 0.03 g, $\approx 1.4 \times 10^{10}$ particles $mL^{-1}$) + 10 mM KCl (0.0075 g) in $H_2O$ (10 mL)
- 900 nm Ø polystyrene spheres ($\approx$ 0.03 g, $\approx 7.5 \times 10^7$ particles $mL^{-1}$) + 1 M KCl (0.7454 g) in $H_2O$ (10 mL)
- 370 nm Ø polystyrene spheres ($\approx$ 0.03 g, $\approx 2.7 \times 10^9$ particles $mL^{-1}$) + 1 M KCl (0.7454 g) in $H_2O$ (10 mL)
- 10 mM KCl (0.0745 g) in $H_2O$ (100 mL)
- 10 mM KCl (0.0745 g) + 0.1% Triton$^{TM}$ X-100 v/v (100 $\mu$L) in $H_2O$ (99.9 mL)
- 10 mM KCl (0.0745 g) + 10 mM HCl (0.056 mL) in $H_2O$ (100 mL)
- 10 mM KCl (0.0745 g) + 10 mM NaOH (0.04 g) in $H_2O$ (100 mL)

## 8.3 Derivation of equations used in differential Coulter counting systems

**Resistor bridge differential system:**

The background current flowing through a resistor bridge (formed by placing a dummy resistor in series with a pore) can be determined using Ohm's law:

$$i_1 = \frac{V_{app}}{\theta_R}$$

where $i_1$ s the background current; $V_{app}$ is the applied voltage; and $\theta_R$ is the combined resistance of the pore ($R_p$) and the dummy resistor ($R_d$). When a particle translocates through the pore, $R_p$ is changed, and this formula becomes:

$$i_2 = \frac{V_{app}}{\theta_R + \Delta R}$$

where $i_2$ is the current during translocation and $\Delta R$ is the change in pore resistance during translocation. The applied voltage must drop to ground over the two resistors, so if both resistors have similar values then the voltage measured in between the resistors must be half the applied voltage. However, when the resistance of the pore changes, the voltage dropped over the pore also changes and the voltage in between the resistors is altered. This voltage is called the sensing voltage, $V_{sen}$. The change in the sensing voltage is therefore related to the change in the current passed through the circuit using:

$$\Delta V_{sen} = (i_1 - i_2) \times R_d$$

$$\Delta V_{sen} = \frac{V_{app} \Delta R R_d}{{\theta_R}^2 + \theta_R \Delta R}$$

By assuming the change in resistance will be small in comparison to the combined

resistance of the resistor bridge (i.e. $\Delta R \ll R_p + R_d$), this can be simplified to:

$$\Delta V_{sen} = \frac{V_{app} \Delta R R_d}{{\theta_R}^2}$$

During the operation of the differential signal generator, this change in voltage is amplified using the following formula:

$$V_{out} = X_{DiS} \times \Delta V_{sen}$$

where $V_{out}$ is the output signal of the resistor bridge differential system and $X_{DiS}$ is the amplifier gain. This can be implemented into the derivation of $\Delta V_{sen}$, with the inclusion of a correction factor ($\xi$) that accounts for signal loss through parasitic capacitance and sub-optimal performance in the various op-amps used in the circuitry:

$$\Delta R = \frac{{\theta_R}^2 V_{out}}{\xi V_{app} R_d X_{DiS}}$$

**Current differential system:**

In the absence of particle translocation, the current flowing through the pore can be determined using Ohm's Law:

$$i_1 = \frac{V_{app}}{R_p}$$

where $i_1$ s the background current; $V_{app}$ is the applied voltage; and $R_p$ is the background resistance. During translocation, the resistance of the pore is changed, altering the measured current in the process:

$$i_2 = \frac{V_{app}}{R_p + \Delta R}$$

where $i_2$ is the current during translocation and $\Delta R$ is the change in pore resistance during translocation. The change in current that occurs during translocation is amplified by the value of the resistor in the current follower feedback loop, giving a change in voltage:

$$\Delta V = (i_1 - i_2) \times R_{CF}$$

where $\Delta V$ is the change in voltage recorded from the current follower and $R_{CF}$ is the value of the resistor in the current follower feedback loop. This can be rearranged:

$$\Delta V = V_{app} \times R_{CF}\Big(\frac{1}{R_p} - \frac{1}{R_p + \Delta R}\Big)$$

$$\Delta V = V_{app} \times R_{CF}\Big(\frac{R_p + \Delta R - R_p}{{R_p}^2 + R_p \Delta R}\Big)$$

By assuming the change in resistance will be small in comparison to the resistance of the pore (i.e. $\Delta R \ll R_p$), this can be simplified to:

$$\Delta V = \frac{V_{app} R_{CF} \Delta R}{{R_p}^2}$$

During the operation of the differential signal generator, this change in voltage is amplified using the following formula:

$$V_{DiS} = X_{DiS} \times \Delta V$$

where $V_{DiS}$ is the output signal of the current-differential system and $X_{DiS}$ is the amplifier gain. This can be implemented into the derivation of $\Delta V$, with the inclusion of a correction factor ($\xi$) that accounts for signal loss through parasitic capacitance and sub-optimal performance in the various op-amps used in the circuitry:

$$\Delta R = \frac{{R_p}^2 V_{DiS} \xi}{V_{app} R_{CF} X_{DiS}}$$

## 8.4 Detailed circuit diagrams

**Electrochemical W etching circuit:**

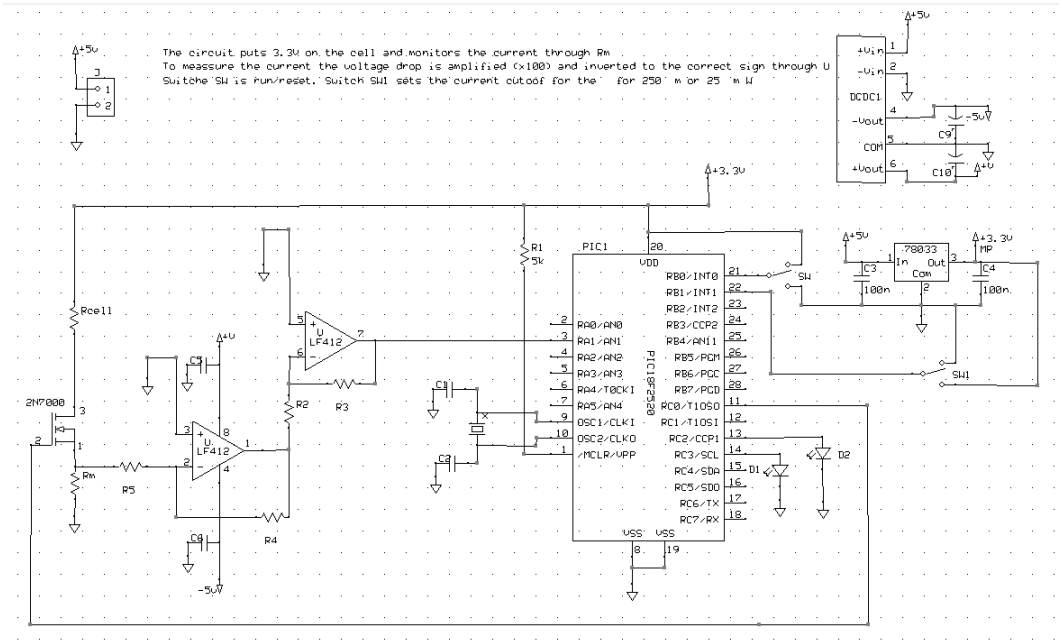


**Figure 8.2:** Detailed circuit diagram for the electrochemical W etching circuit.

**Nanoelectrode polishing breakthrough circuit:**

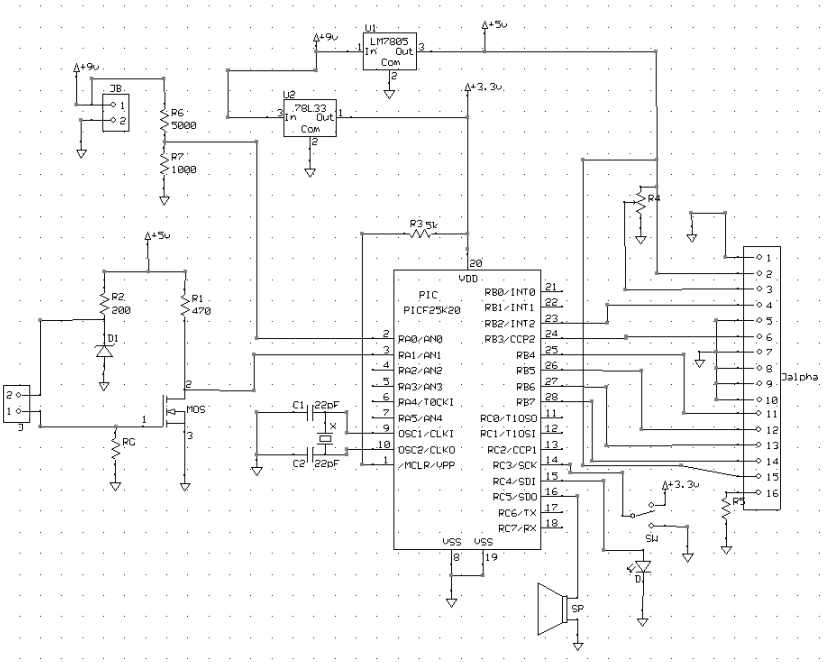


**Figure 8.3:** Detailed circuit diagram for the W nanoelectrode polishing breakthrough circuit.

**Differential signal generator circuit:**

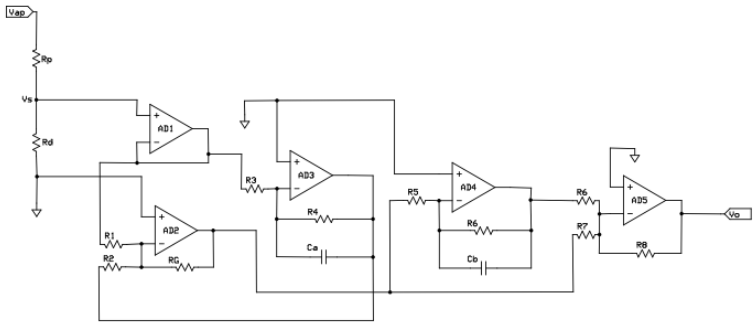


**Figure 8.4:** Detailed circuit diagram for the differential signal generator.

## 8.5 Increased mass transport observed on W nanoelectrodes

**Cyclic voltammetry of W nanoelectrodes in $Ru(NH_3)_6Cl_3$:**

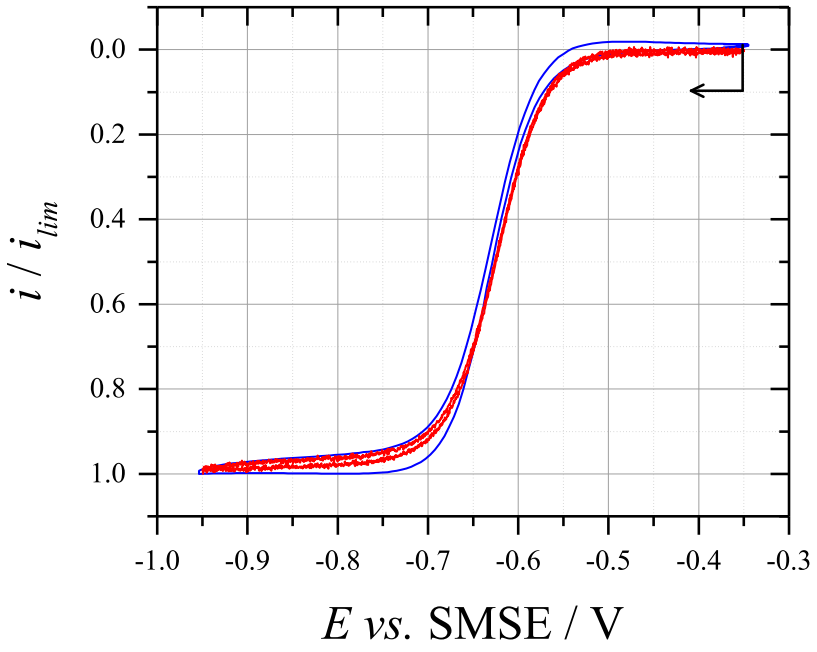


**Figure 8.5:** Normalized cyclic voltammograms recorded at 5 mV $s^{-1}$ with (BLUE) a 25 $\mu$m Ø W microelectrode, and (RED) a 116 nm Ø W nanoelectrode, in degassed 5 mM $Ru(NH_3)_6Cl_3$ + 0.1 M $K_2SO_4$ (pH 3.5). Each voltammogram was normalised with respect to its limiting current at −0.95 V *vs.* SMSE. The arrow indicates the initial potential and the scan direction.

**Cyclic voltammetry of W nanoelectrodes in $K_3Fe(CN)_6$:**

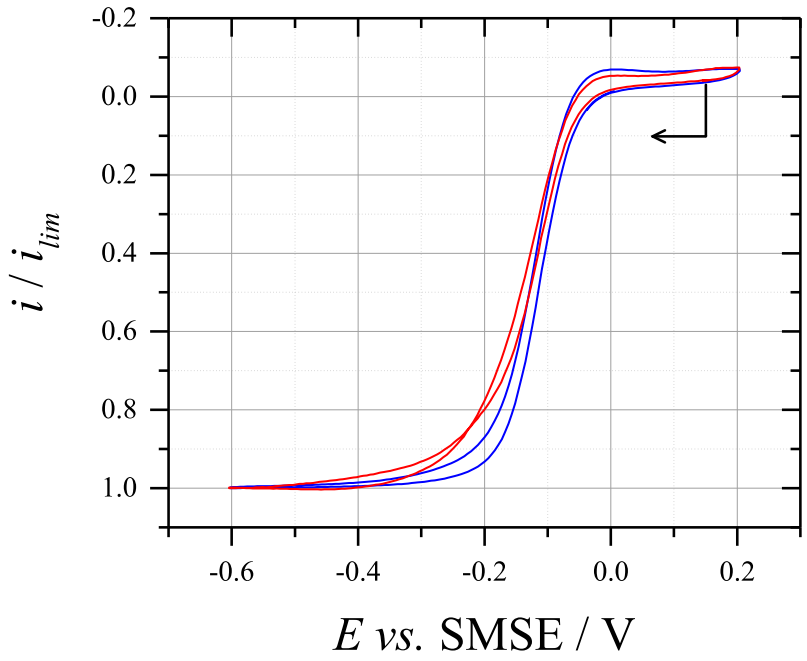


**Figure 8.6:** Normalized cyclic voltammograms recorded at 5 mV $s^{-1}$ with (BLUE) a 25 $\mu$m Ø W microelectrode, and (RED) a 400 nm Ø W nanoelectrode, in anaerobic 10 mM $K_3Fe(CN)_6$ + 0.2 M $Sr(NO_3)_2$ (pH 7). Each voltammogram was normalised with respect to its limiting current at −0.6 V *vs.* SMSE. The arrow indicates the initial potential and the scan direction.

## 8.6 Distortions seen on W nanoelectrodes

**Origin of the resistive current from glass conductivity**:

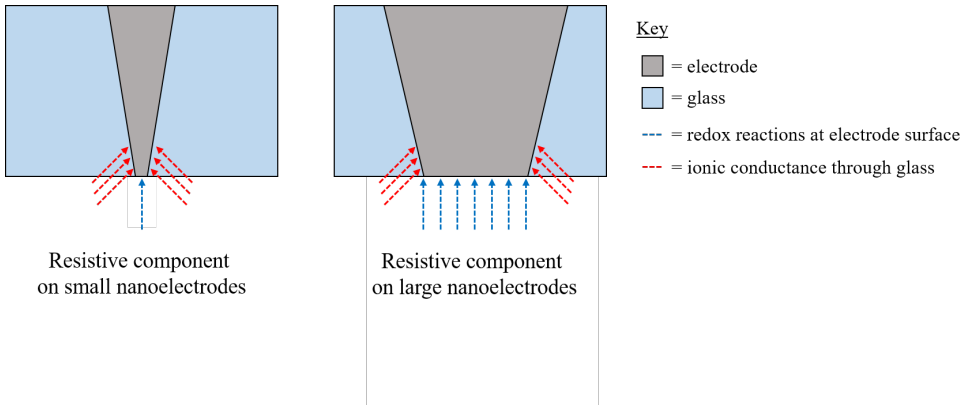


**Figure 8.7:** Possible explanation for the superimposition of a resistive component onto the cyclic voltammogram of a W nanoelectrode sealed in soda glass. The blue dashed arrows represent the current recorded from the redox reactions of $Ru(NH_3)_6Cl_3$, whilst the red dashed arrows represent the contribution from ion conductance through the glass sheath. As the electrode radius increases, the current contributions from glass conductivity become small in comparison to the current from the redox reaction, leading to less of an effect.

**High-speed cyclic voltammetry of W microelectrodes in $Ru(NH_3)_6Cl_3$:**

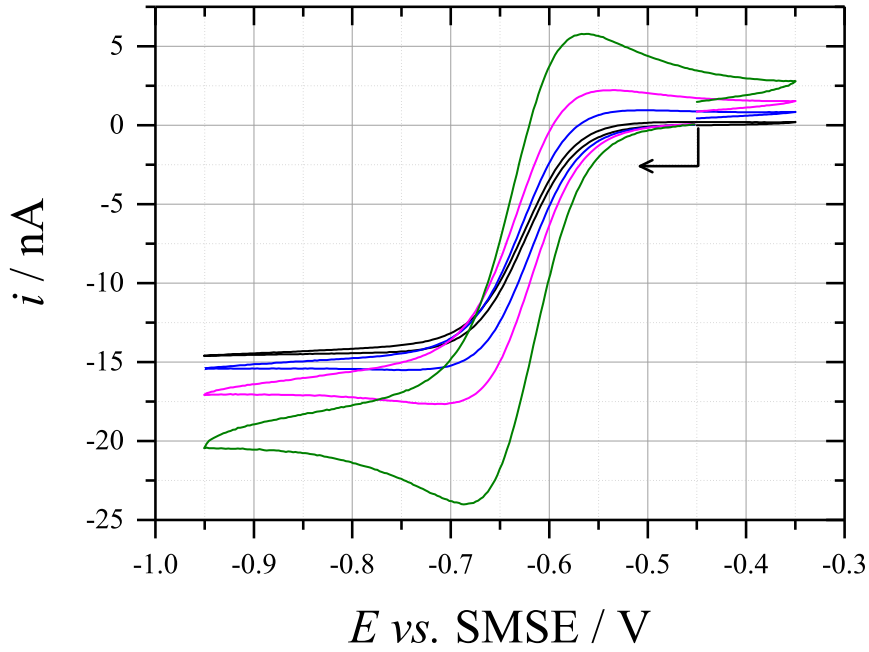


**Figure 8.8:** Cyclic voltammograms recorded at: (BLACK) 5 mV $s^{-1}$; (BLUE) 50 mV $s^{-1}$; (PINK) 250 mV $s^{-1}$; and (GREEN) 1000 mV $s^{-1}$ with a 25 $\mu$m Ø W microelectrode in anaerobic 5 mM $Ru(NH_3)_6Cl_3$ + 0.1 M $K_2SO_4$ (pH 3.5). The arrow indicates the initial potential and the scan direction.

**High-speed cyclic voltammetry of W nanoelectrodes in $Ru(NH_3)_6Cl_3$:**

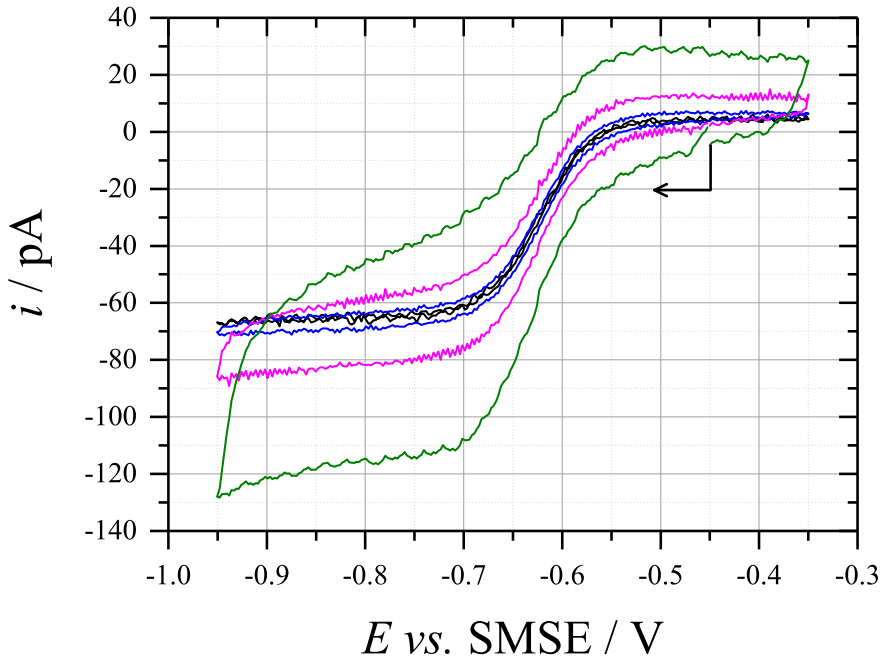


**Figure 8.9:** Cyclic voltammograms recorded at: (BLACK) 5 mV $s^{-1}$; (BLUE) 50 mV $s^{-1}$; (PINK) 250 mV $s^{-1}$; and (GREEN) 1000 mV $s^{-1}$ with a 125 nm Ø W nanoelectrode in anaerobic 5 mM $Ru(NH_3)_6Cl_3$ + 0.1 M $K_2SO_4$ (pH 3.5). The arrow indicates the initial potential and the scan direction.

## 8.7 Characterisation of the Coulter counting apparatus

**Blocking event in a cylindrical micropore:**

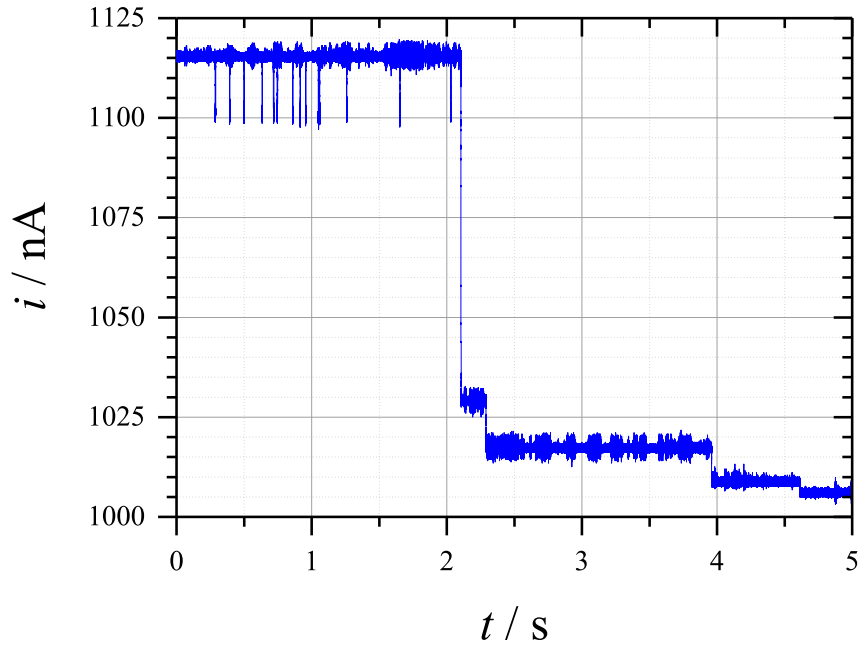


**Figure 8.10:** Current transient recorded at −5 V *vs.* Ag/AgCl with a 40 $\mu$m Ø cylindrical micropore in aerobic 10 mM KCl. The plot shows a blocking event during the translocation of 24.9 $\mu$m Ø microparticles ($4\times10^4$ particles $mL^{-1}$), recorded with the currentfollower system. The pressure differential applied to the micropore was −44 mBar and the temperature during the experiment was 26.1 °C.

**Observations of the chemical etching procedure on W microwires:**

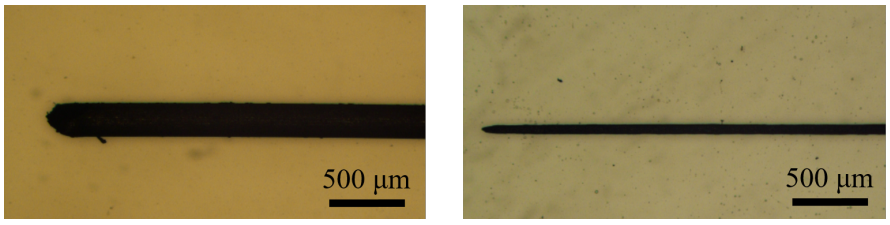


**Figure 8.11:** Optical microscope images of a 250 $\mu$m Ø W microwire before (LEFT) and after (RIGHT) chemically etching in 250 mM $K_2S_2O_8$ + 2 M NaOH for 2 hours. Each image was recorded at 2× magnification.

**Comparison of particle translocations through cylindrical and conical micropores**

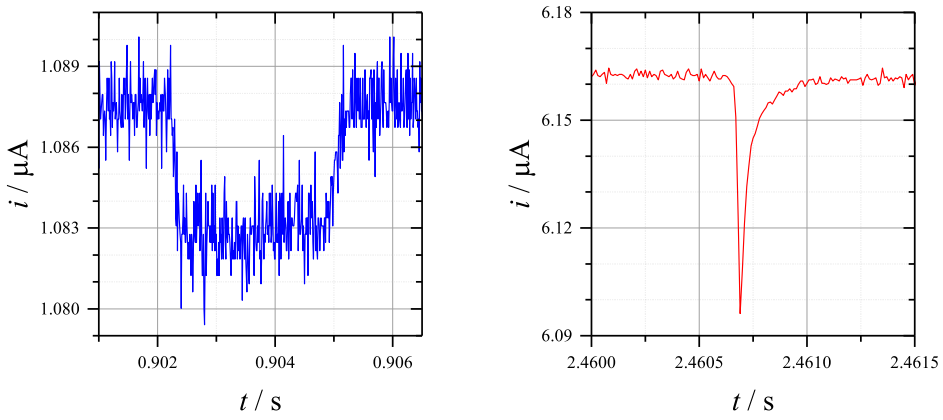


**Figure 8.12:** Current transients comparing the signal shape of particle translocations recorded through cylindrical and conical micropores with the low gain ($10^6$ V/A) current follower system. The transients were recorded at: (LEFT) $-5$ V *vs.* Ag/AgCl with a 40 $\mu$m Ø cylindrical micropore in aerobic 10 mM KCl, during the translocation of 18.8 $\mu$m Ø microparticles ($4 \times 10^4$ particles mL$^{-1}$) under a $-43$ mBar pressure differential; and (RIGHT) $-1$ V *vs.* Ag/AgCl with a 8 $\mu$m Ø conical micropore in aerobic 1 M KCl, during the translocation of 4.9 $\mu$m Ø microparticles ($4.6 \times 10^5$ particles mL$^{-1}$) under a $-36$ mBar pressure differential.

## 8.8 Simulation details

Particle translocations through both micropores and nanopores were simulated using **COMSOL Multiphysics**. All models were started by selecting a new model wizard file and then selecting the **2D Axisymmetric** dimension. This assumed the pore being modelled was symmetric around a rotational axis through its center.

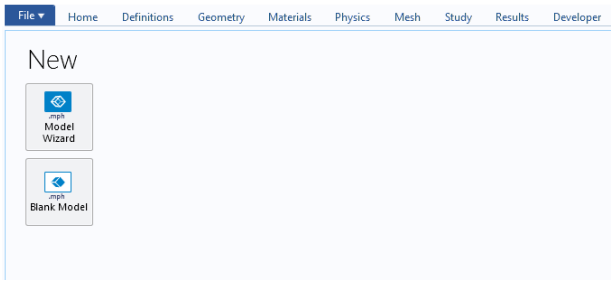


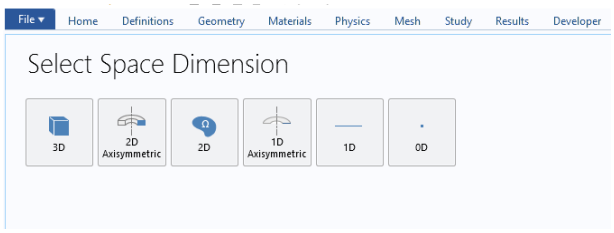


In order to simulate the passage of current through the pore, the **Primary Current Distribution** physics interface was used. In order to simplify the simulation, a stationary study option was used. This kept all variables constant throughout the simulation, meaning any changes had to be performed using a parametric sweep. This however ignores any contribution to translocation time from pressure induced flow.

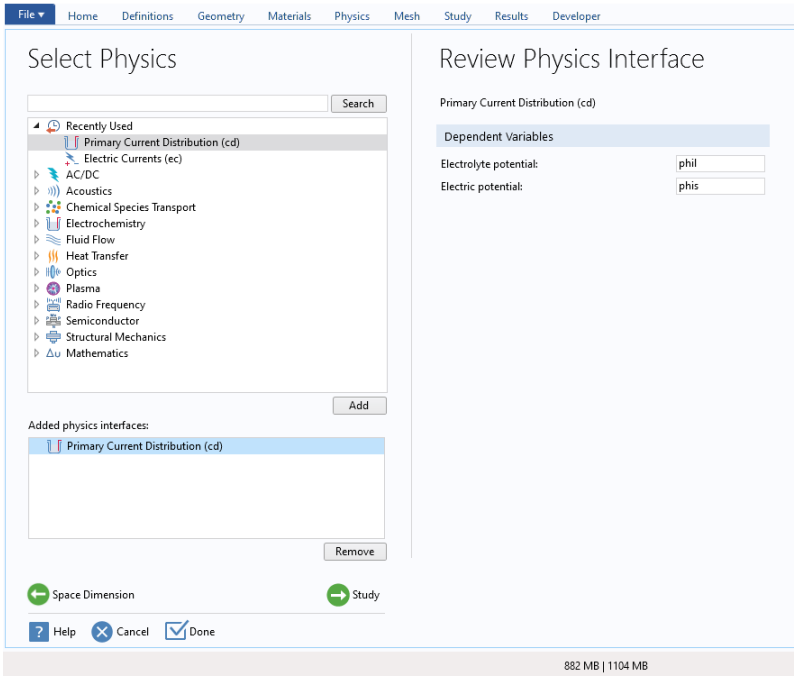
File
Home
Definitions
Geometry
Materials
Physics
Mesh
Study
Results
Developer
Select Physics
Search
Recently Used
Primary Current Distribution (cd)
Electric Currents (ec)
AC/DC
Acoustics
Chemical Species Transport
Electrochemistry
Fluid Flow
Heat Transfer
Optics
Plasma
Radio Frequency
Semiconductor
Structural Mechanics
Mathematics
Add
Added physics interfaces:
Primary Current Distribution (cd)
Remove
Space Dimension
Study
Help
Cancel
Done
Review Physics Interface
Primary Current Distribution (cd)
Dependent Variables
Electrolyte potential:
phil
Electric potential:
phis
882 MB | 1104 MB

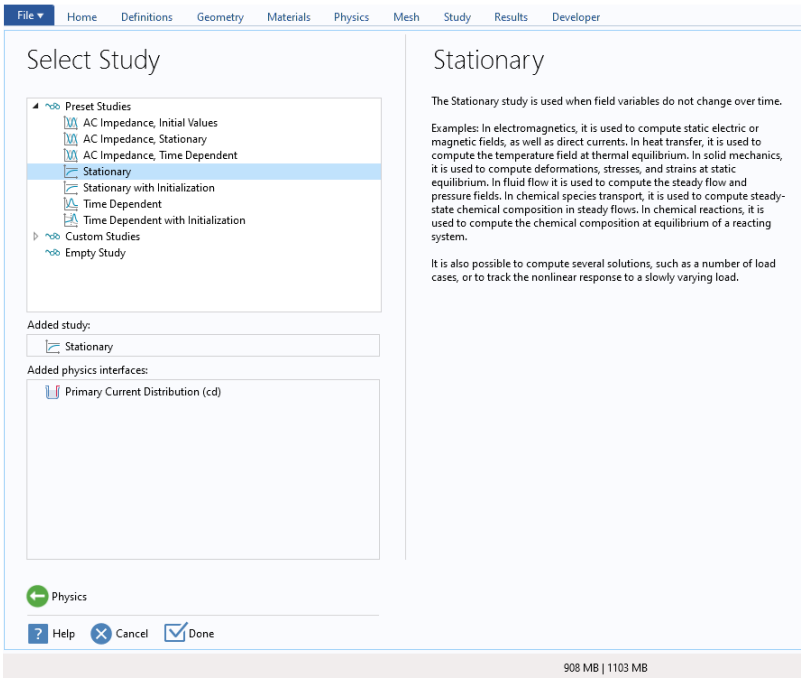
File
Home
Definitions
Geometry
Materials
Physics
Mesh
Study
Results
Developer
Select Study
Preset Studies
AC Impedance, Initial Values
AC Impedance, Stationary
AC Impedance, Time Dependent
Stationary
Stationary with Initialization
Time Dependent
Time Dependent with Initialization
Custom Studies
Empty Study
Added study:
Stationary
Added physics interfaces:
Primary Current Distribution (cd)
Physics
Help
Cancel
Done
Stationary
The Stationary study is used when field variables do not change over time.
Examples: In electromagnetics, it is used to compute static electric or magnetic fields, as well as direct currents. In heat transfer, it is used to compute the temperature field at thermal equilibrium. In solid mechanics, it is used to compute deformations, stresses, and strains at static equilibrium. In fluid flow it is used to compute the steady flow and pressure fields. In chemical species transport, it is used to compute steady-state chemical composition in steady flows. In chemical reactions, it is used to compute the chemical composition at equilibrium of a reacting system.
It is also possible to compute several solutions, such as a number of load cases, or to track the nonlinear response to a slowly varying load.
908 MB | 1103 MB

**Simulations of pore/particle diameter:**

The following example shows the settings used to simulate the change in resistance incurred by the growth of a particle inside a cylindrical micropore. This was used to investigate the relationship between particle to pore ratio and the signal magnitude (i.e. Figure 4.6). Note that the pore diameter was kept constant, allowing the background resistance to be subtracted from resistances measured during simulation. To begin the simulation, several parameters were defined, including pore dimensions, particle positions and experimental conditions.

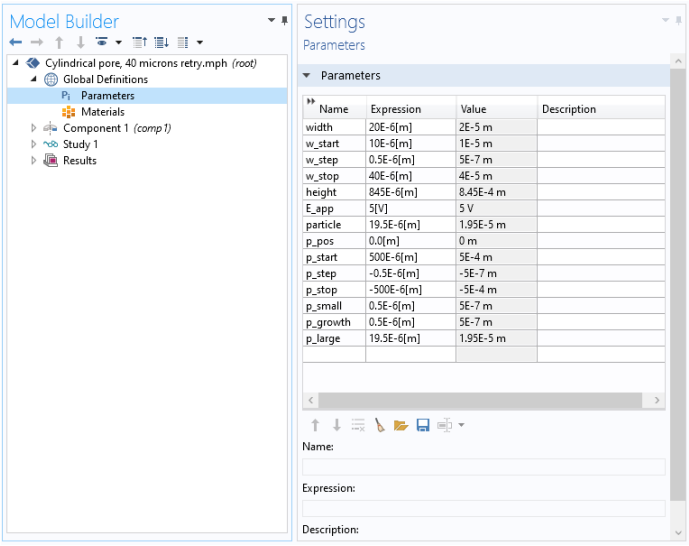


These parameters were then used to build a geometrical model of the pore. Three rectangles were built to represent the micropore:

- **Rectangle 1**; *Width* = width (20 $\mu$m); *Height* = height (845 $\mu$m); *Base* = Corner; $r$ = 0; and $z$ = -height/2
- **Rectangle 2**; *Width* = 1 mm; *Height* = 1 mm; *Base* = Corner; $r$ = 0; and $z$ = height/2
- **Rectangle 3**; *Width* = 1 mm; *Height* = 1 mm; *Base* = Corner; $r$ = 0; and $z$ = -1-(height/2)

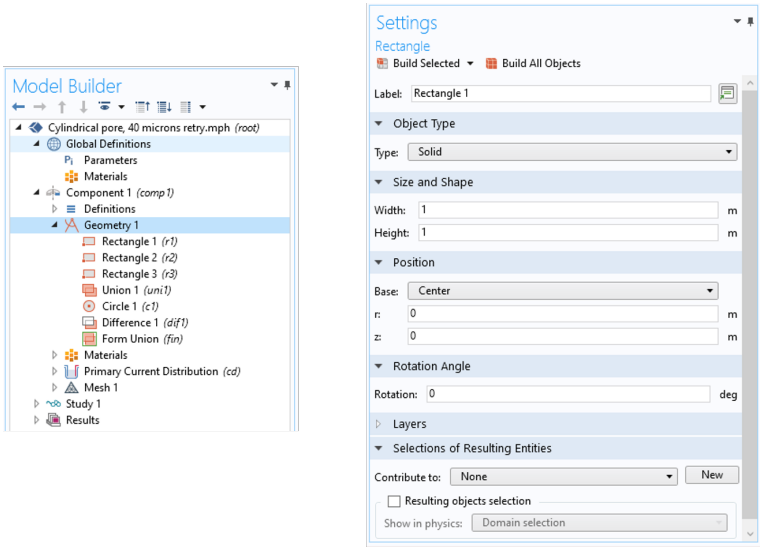


A union was formed between these rectangles, forming a pore structure with a microchannel (Rectangle 1) and two large reservoirs (Rectangles 2 and 3). A circle was added to represent the particle, with dimensions of: Radius = particle (19.5 $\mu$m); Base = Center; $r = 0$; and $z = \mathrm{p_{pos}}$ (0). This circle was subtracted from the rectangles using a difference operation.

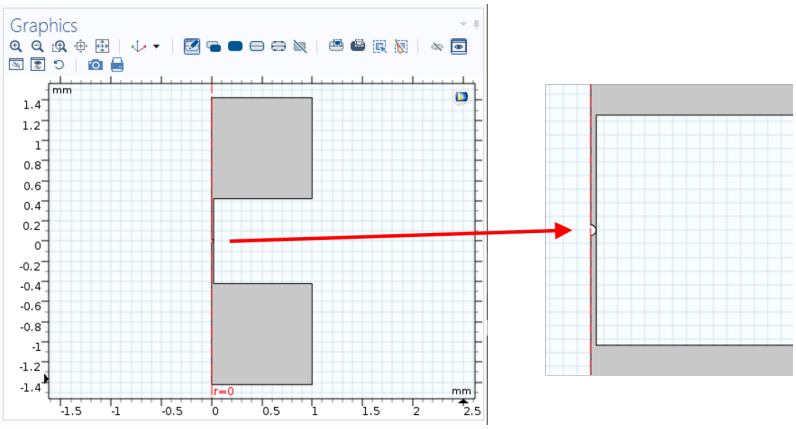


The three rectangles were set as the electrolyte using the materials tab, and the conductivity of the chosen electrolyte was entered manually. This assumed that any current could only pass through the electrolyte; the particle and glass template were not assigned a material and were therefore left as voids which no current could pass through. This may introduce slight errors in the simulation, but seemed to produce better results.

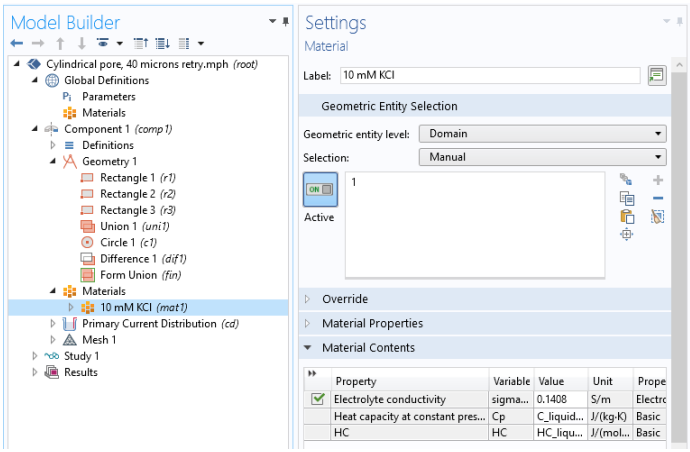


The boundaries of the reservoirs were selected to represent the electrodes placed on either side of the pore. On one side of the pore, boundary 6 was given an electric potential of $E_{app}$ (5 V), whilst on the other side, boundary 2 was given an electric potential of 0 V.

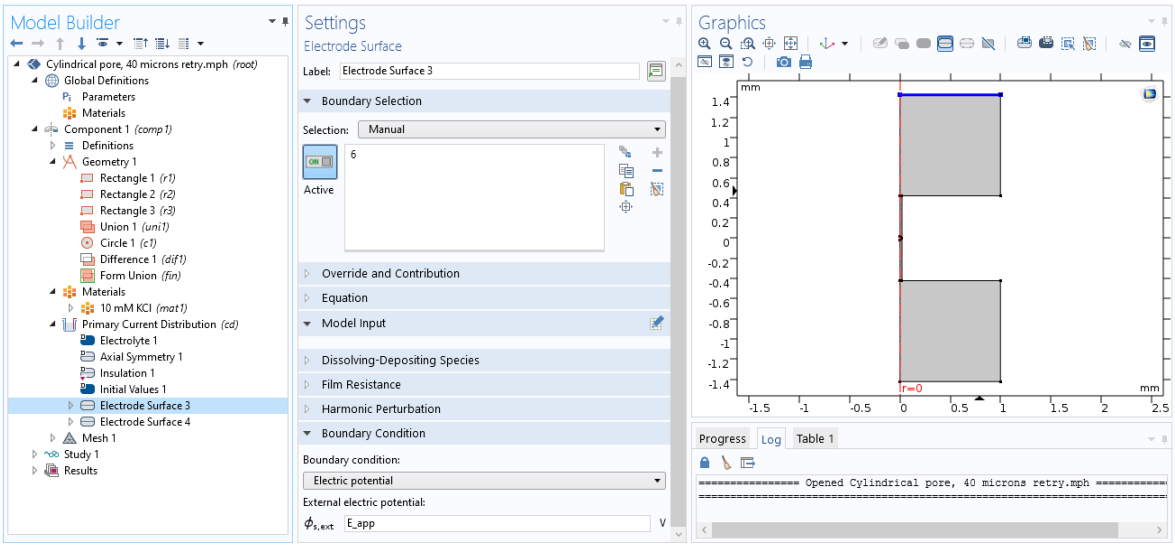


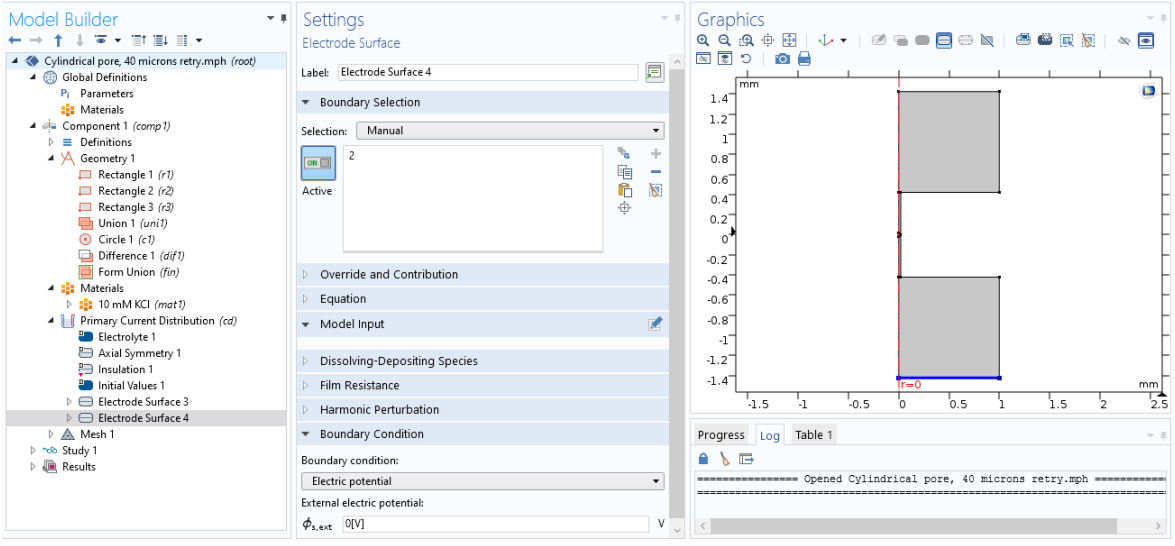

A new definition was established, allowing the current recorded across boundary 6 to be integrated using an operation named **inel**.

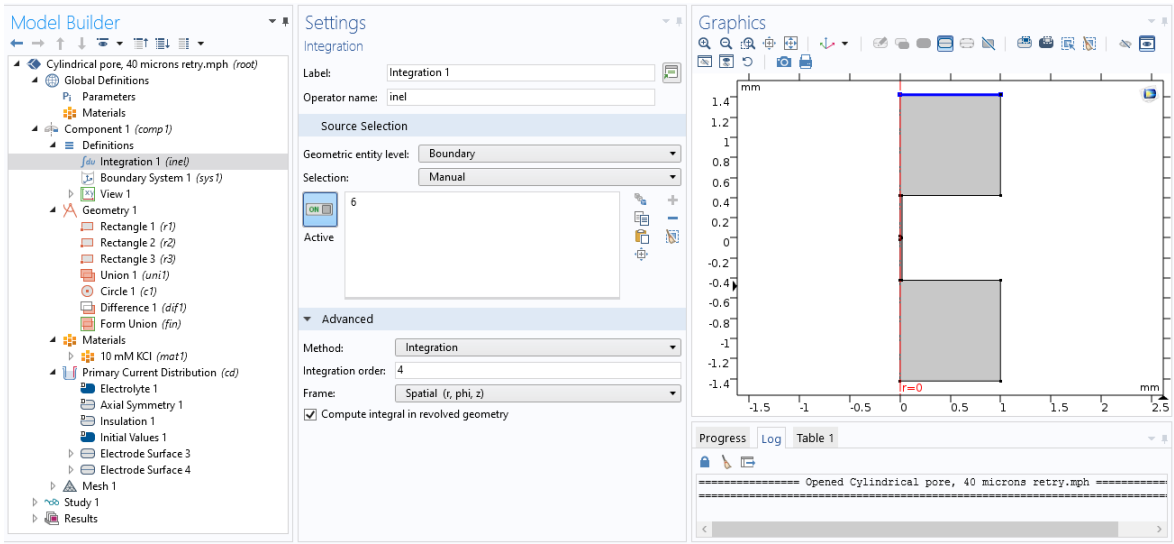


This allowed the current across the pore to be measured as a function of the potential difference between the two boundaries. The entire area of the three rectangles was split into a triangular mesh, with the current being calculated for each cell within the mesh. However, by default the pore received the same treatment as the reservoirs, meaning the cells were the same size regardless of their location and therefore the channel section contained fewer cells. To correct this, a custom **Free Triangular** meshing was established, setting the size of the cells with respect to the parameters in:

- **Pore wall** (Size 1); *Max* = width/25 (0.8 $\mu$m); *Min* = width/50 (0.4 $\mu$m)
- **Pore openings** (Size 2); *Max* = width/25 (0.8 $\mu$m); *Min* = width/50 (0.4 $\mu$m)
- **Particle points** (Size 4); *Max* = width-particle/20 (0.025 $\mu$m); *Min* = width-particle/50 (0.01 $\mu$m)
- **Particle edges** (Size 5); *Max* = width-particle/5 (0.1 $\mu$m); *Min* = width/20 (0.025 $\mu$m)

This allowed the meshing to become more accurate in the confined dimensions of the pore, whilst allowing the larger reservoir area to keep a relatively large meshing. By linking the meshing on the particle to the difference between the particle and pore size,

the meshing was more accurate during simulations where large particle to pore ratios were used (although as the meshing became finer, the simulation time dramatically increased).

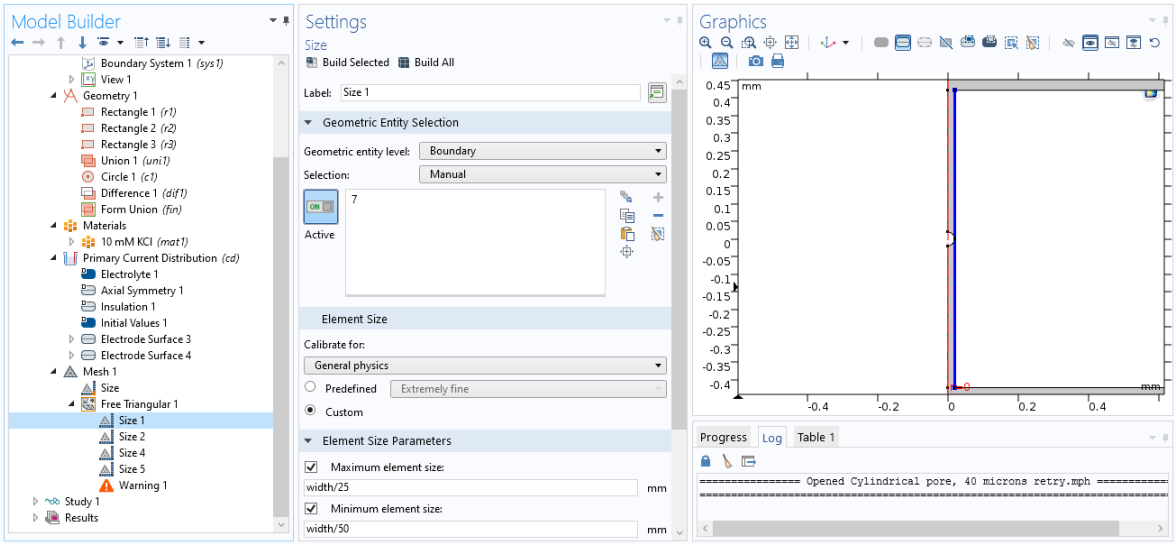


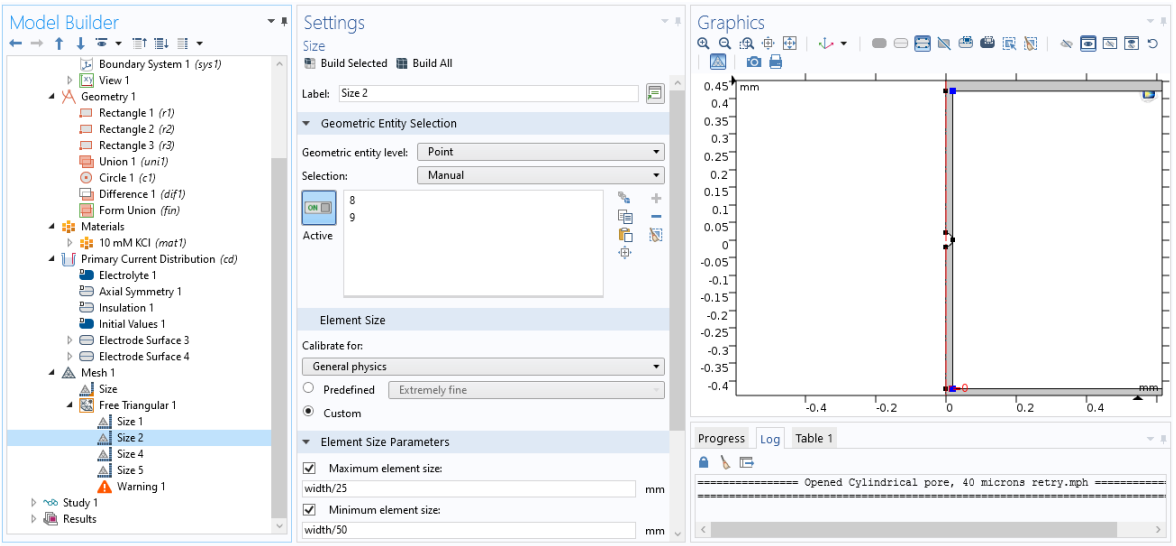


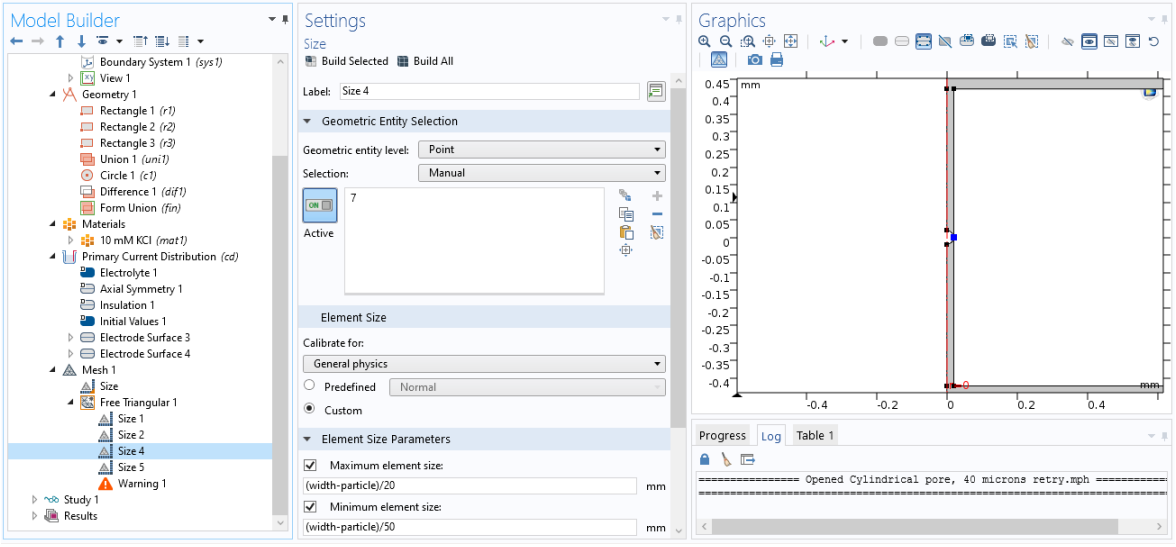

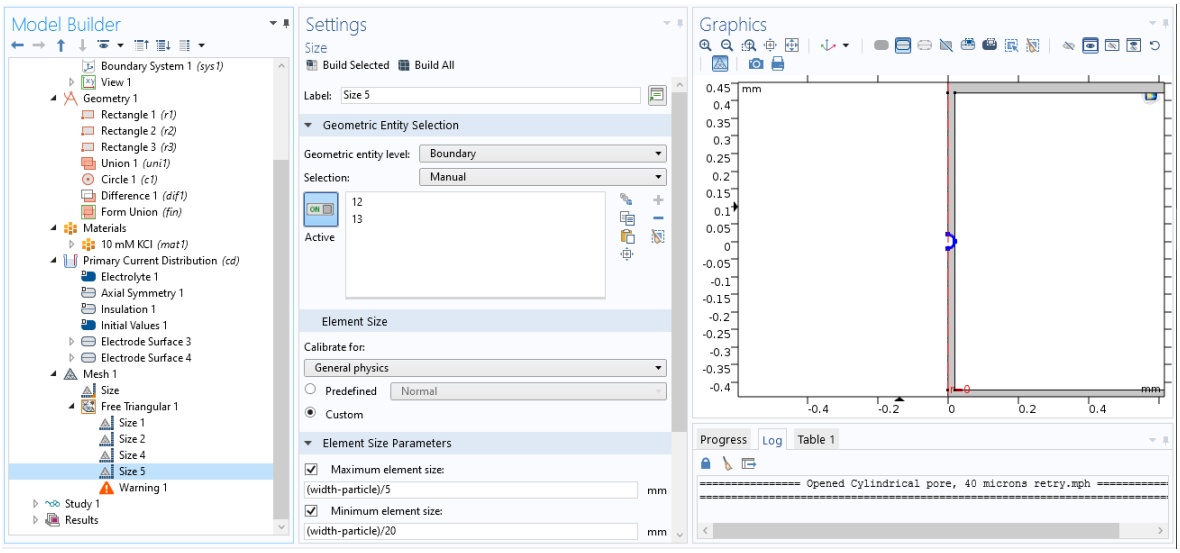


This simulation would allow the current passed across a pore to be measured when a particle was located in the centre of the channel. However, to model the relationship between the change in the resistance and the particle to pore ratio, a simulation in the absence of a particle would need to be subtracted from a simulation in which the particle is gradually increased in size. The former was easily achieved by temporarily deleting the particle, but the latter would require a parametric sweep of the particle radius. In a parametric sweep, several consecutive simulations are recorded, each with a change in one parameter. In the case of Figure 4.6, the particle radius was swept between a lower limit ($p_{small}$) of 0.5 $\mu$m and an upper limit ($p_{large}$) of 19.5 $\mu$m, in increments ($p_{growth}$) of 0.5 $\mu$m.

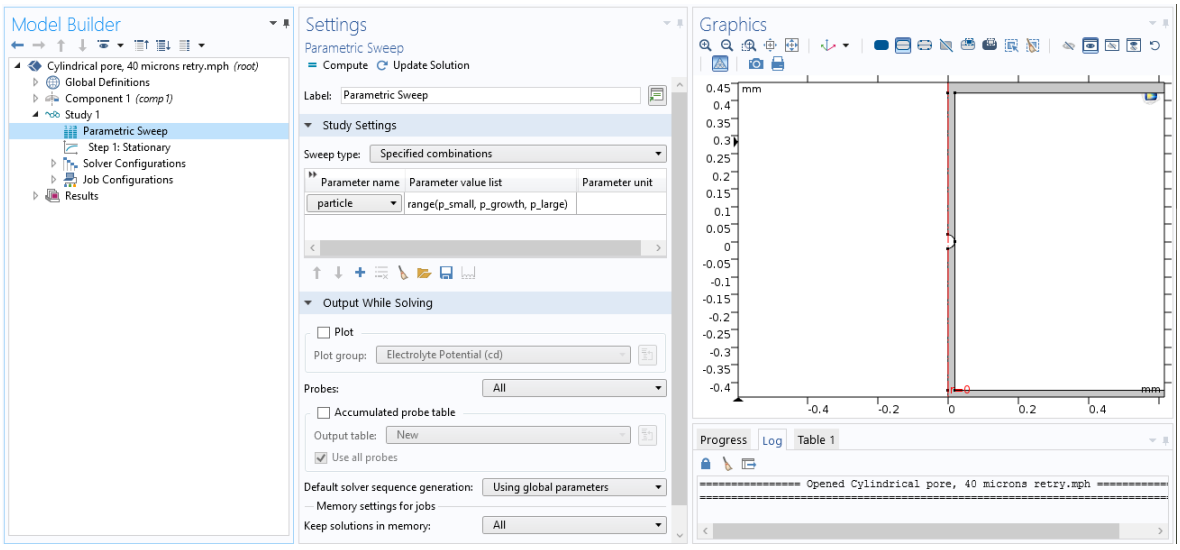

Once this parametric sweep was complete, the results could be analysed using the COMSOL Multiphysics software. Ignoring the default plots that the program generated, a new 1D plot was added. This was used to label the data and select which simulation results would be used. A graph was added to that plot, with the y axis showing the resistance measured through the pore and the x axis showing the particle size during the parametric sweep. The resistance was calculated using an expression dividing the applied voltage by the current integrated from boundary 6 using the **inel** operation.

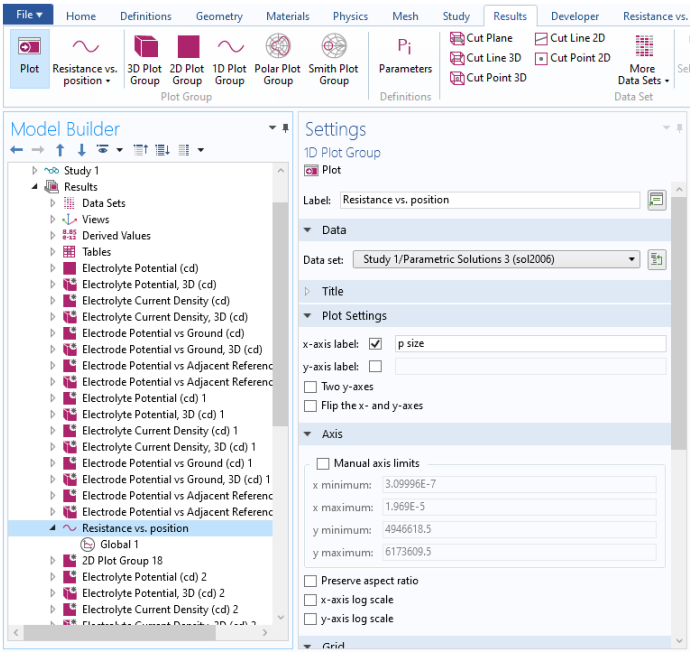


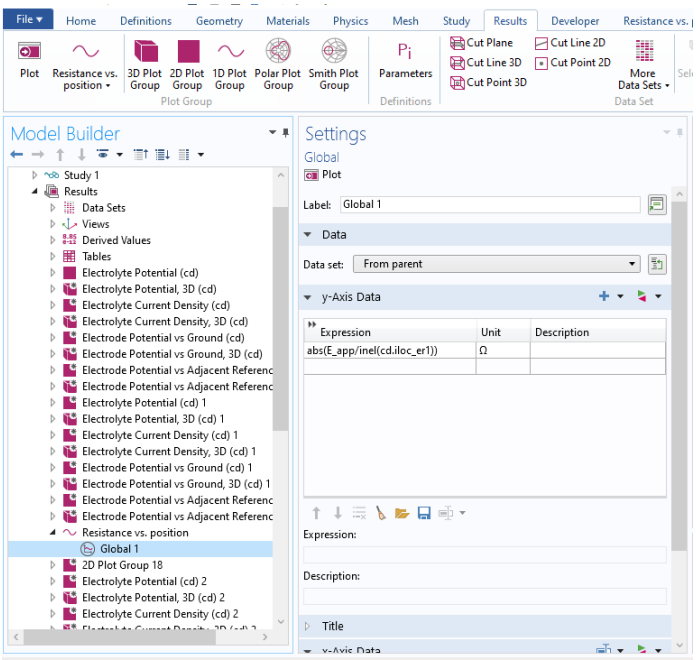

The results were then exported as a .txt file and analysed using Origin software.

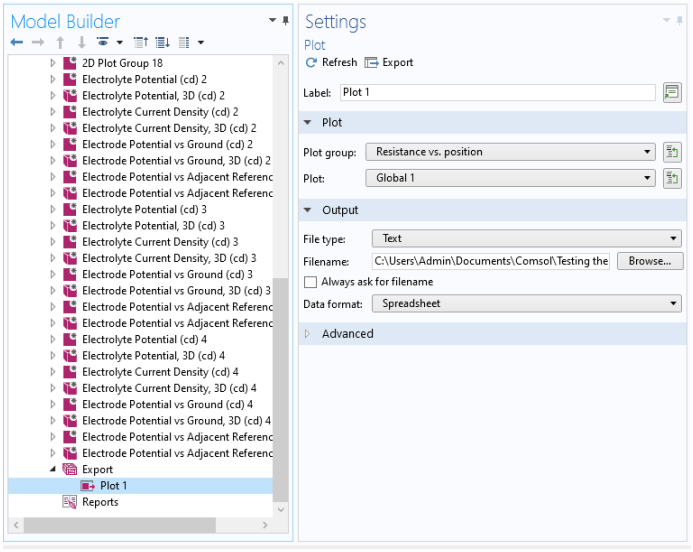

**Simulations of particle translocation:**

The simulation that allowed the translocation of nanoparticles to be modelled in Figures 4.18 + 4.19 only differs slightly from the one described above. The main difference is the geometry of the simulation, in which a polygon is place in between Rectangle 1 and one of the reservoirs. This polygon had several sections, allowing both the sharp tapering tip of the nanopore and the wider base to be modelled.

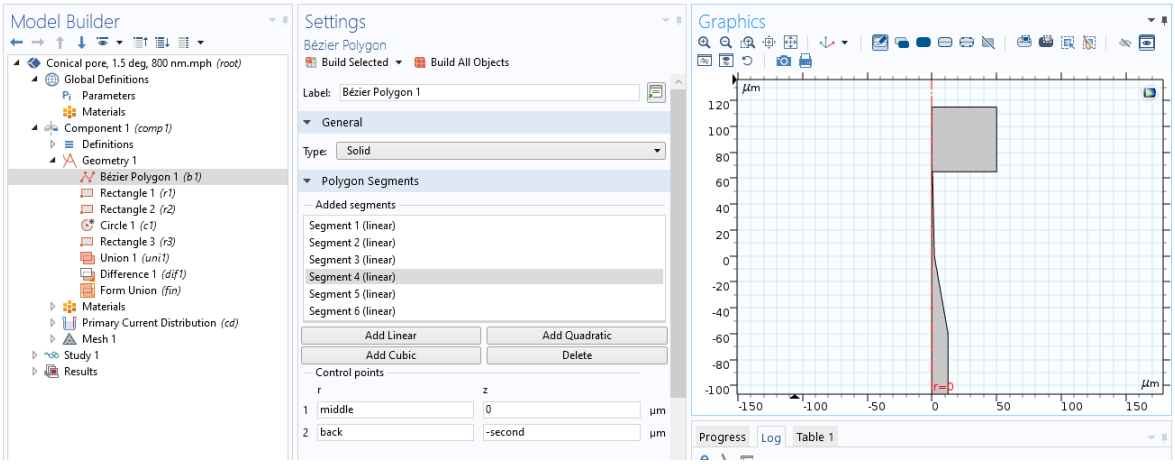


Using trigonometry, the precise length of each section of the polygon could be calculated. It should be noted that this approach allowed the conical part of the nanopore to be split into several segments, each of which could vary in cone angle and length. This also had the advantage of allowing different segments to have different levels of meshing, avoiding the highly demanding scenario of one long nanopore requiring the finest meshing possible. The following parameters were used to build the nanopore:

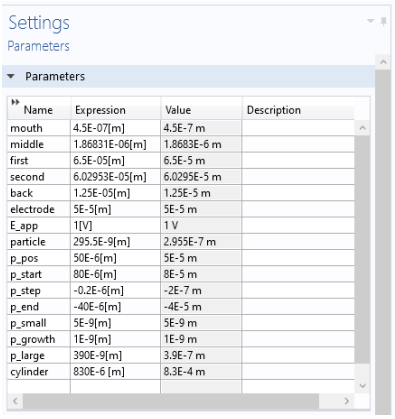


| Name | Expression | Value | Description |
|---|---|---|---|
| mouth | 4.5E-07[m] | 4.5E-7 m | |
| middle | 1.86831E-06[m] | 1.8683E-6 m | |
| first | 6.5E-05[m] | 6.5E-5 m | |
| second | 6.02953E-05[m] | 6.0295E-5 m | |
| back | 1.25E-05[m] | 1.25E-5 m | |
| electrode | 5E-5[m] | 5E-5 m | |
| E_app | 1[V] | 1 V | |
| particle | 295.5E-9[m] | 2.955E-7 m | |
| p_pos | 50E-6[m] | 5E-5 m | |
| p_start | 80E-6[m] | 8E-5 m | |
| p_step | -0.2E-6[m] | -2E-7 m | |
| p_end | -40E-6[m] | -4E-5 m | |
| p_small | 5E-9[m] | 5E-9 m | |
| p_growth | 1E-9[m] | 1E-9 m | |
| p_large | 390E-9[m] | 3.9E-7 m | |
| cylinder | 830E-6 [m] | 8.3E-4 m | |

The sections of the polygon had the following setting:

- **Segment 1**; *r1* = 0; *r2* = 0; *z1* = 0; and *z2* = first
- **Segment 2**; *r1* = 0; *r2* = mouth; *z1* = first; and *z2* = first
- **Segment 3**; *r1* = mouth; *r2* = middle; *z1* = first; and *z2* = 0
- **Segment 4**; *r1* = middle; *r2* = back; *z1* = 0; and *z2* = -second
- **Segment 5**; *r1* = back; *r2* = 0; *z1* = 0; and *z2* = -second
- **Segment 6**; *r1* = 0; *r2* = 0; *z1* = -second; and *z2* = 0

This geometry modelled a reservoir of electrolyte connected to the tip of the nanopore (low angle), which then widened out into the base of the nanopore (high angle) until it reached the channel (Rectangle 1) templated by a small section of microwire, which in turn was connected to the second reservoir. As previously mentioned, this segmented approach allowed different meshing to be applied to different parts of the nanopore structure:

- **First part of conical nanopore**; *Max* = mouth/20; *Min* = mouth/50
- **Second part of conical nanopore**; *Max* = middle/5; *Min* = middle/10
- **Particle**; *Max* = particle/20; *Min* = particle/50
- **Cylindrical channel**; *Max* = cylinder/2.5; *Min* = cylinder/5

Another difference is that in the case of Figures 4.18 + 4.19, the parametric sweep was made on the particle position rather than particle size. The particle position was swept between a lower limit ($p_{start}$) of 80 $\mu$m and an upper limit ($p_{end}$) of $-40$ $\mu$m, in increments ($p_{step}$) of 0.2 $\mu$m. This means that the simulated translocations are independent of external factors such as pressure differentials and potential fields, and cannot be related to translocation time without the inclusion of particle speed.